A Thesis Submitted for the Degree of PhD at the University of Warwick

http://go.warwick.ac.uk/wrap/77193

Library Declaration and Deposit Agreement

1. STUDENT DETAILS

Please complete the following:

Full name: …………………………………………………………………………………………….

University ID number: ………………………………………………………………………………

2. THESIS DEPOSIT

2.1 Under your registration at the University, you are required to deposit your thesis with the University in BOTH hard copy and in digital format. The digital copy should normally be saved as a single pdf file.

2.2 The hard copy will be housed in the University Library. The digital copy will be deposited in the University's Institutional Repository (WRAP). Unless otherwise indicated (see 2.6 below), this will be made immediately openly accessible on the Internet and will be supplied to the British Library to be made available online via its Electronic Theses Online Service (EThOS) service.
[At present, theses submitted for a Master's degree by Research (MA, MSc, LLM, MS or MMedSci) are not being deposited in WRAP and not being made available via EthOS. This may change in future.]

2.3 In exceptional circumstances, the Chair of the Board of Graduate Studies may grant permission for an embargo to be placed on public access to the thesis **in excess of two years**. This must be applied for when submitting the thesis for examination (further information is available in the *Guide to Examinations for Higher Degrees by Research*.)

2.4 If you are depositing a thesis for a Master's degree by Research, the options below only relate to the hard copy thesis.

2.5 If your thesis contains material protected by third party copyright, you should consult with your department, and if appropriate, deposit an abridged hard and/or digital copy thesis.

2.6 Please tick one of the following options for the availability of your thesis (guidance is available in the *Guide to Examinations for Higher Degrees by Research)***:**

☐ Both the hard and digital copy thesis can be made publicly available immediately

☐ The hard copy thesis can be made publicly available immediately and the digital copy thesis can be made publicly available after a period of two years (*should you subsequently wish to reduce the embargo period please inform the Library*)

☐ Both the hard and digital copy thesis can be made publicly available after a period of two years (*should you subsequently wish to reduce the embargo period please inform the Library*)

☐ Both the hard copy and digital copy thesis can be made publicly available after _______________ (insert time period in excess of two years). **This option requires the prior approval of the Chair of the Board of Graduate Studies (see 2.3 above)**

The University encourages users of the Library to utilise theses as much as possible, and unless indicated below users will be able to photocopy your thesis.

☐ I **do not** wish for my thesis to be photocopied

3. GRANTING OF NON-EXCLUSIVE RIGHTS

Whether I deposit my Work personally or through an assistant or other agent, I agree to the following:

- Rights granted to the University of Warwick and the British Library and the user of the thesis through this agreement are non-exclusive. I retain all rights in the thesis in its present version or future versions. I agree that the institutional repository administrators and the British Library or their agents may, without changing content, digitise and migrate the thesis to any medium or format for the purpose of future preservation and accessibility.

4. DECLARATIONS

I DECLARE THAT:

- I am the author and owner of the copyright in the thesis and/or I have the authority of the authors and owners of the copyright in the thesis to make this agreement. Reproduction of any part of this thesis for teaching or in academic or other forms of publication is subject to the normal limitations on the use of copyrighted materials and to the proper and full acknowledgement of its source.

- The digital version of the thesis I am supplying is either the same version as the final, hard-bound copy submitted in completion of my degree once any minor corrections have been completed, or is an abridged version (see 2.5 above).

- I have exercised reasonable care to ensure that the thesis is original, and does not to the best of my knowledge break any UK law or other Intellectual Property Right, or contain any confidential material.

- I understand that, through the medium of the Internet, files will be available to automated agents, and may be searched and copied by, for example, text mining and plagiarism detection software.

- At such time that my thesis will be made publically available digitally (see 2.6 above), I grant the University of Warwick and the British Library a licence to make available on the Internet the thesis in digitised format through the Institutional Repository and through the British Library via the EThOS service.

- If my thesis does include any substantial subsidiary material owned by third-party copyright holders, I have sought and obtained permission to include it in any version of my thesis available in digital format and that this permission encompasses the rights that I have granted to the University of Warwick and to the British Library.

5. LEGAL INFRINGEMENTS

I understand that neither the University of Warwick nor the British Library have any obligation to take legal action on behalf of myself, or other rights holders, in the event of infringement of intellectual property rights, breach of contract or of any other right, in the thesis.

Please sign this agreement and ensure it is bound into the final hard bound copy of your thesis, which should be submitted to Student Reception, Senate House.

Student’s signature: ....…… Date: ....

van der Waals Epitaxy in Graphene Heterostructures

by

Alexander James Marsden

Thesis

Submitted to the University of Warwick

for the degree of

Doctor of Philosophy

Physics

August 2015

Contents

List of Figures

List of Tables

Abbreviations

acTEM	Aberration Corrected Transmission Electron Microscope (Microscopy)
AFM	Atomic Force Microscope (Microscopy)
ARPES	Angle-Resolved Photoelectron Spectroscopy
CCD	Charge-Coupled Device
CVD	Chemical Vapour Deposition
DFT	Density Functional Theory
DNA	Deoxyribonucleic acid
EBSD	Electron Backscatter Diffraction
EDS	Energy Dispersive X-ray Spectroscopy
FFM	Friction Force Microscopy
FFT	Fast Fourier Transform
GO	Graphene Oxide
HHCF	Height-Height Correlation Function
HOPG	Highly Ordered Pyrolytic Graphite
HRTEM	High-Resolution Transmission Electron Microscope (Microscopy)
ITO	Indium tin oxide
ITRS	International Technology Roadmap for Semiconductors
LED	Light Emitting Diode
MFC	Mass Flow Controller
NEXAFS	Near Edge X-ray Absorption Fine Structure
OMBD	Organic Molecular Beam Deposition
OPV	Organic Photovoltaics

OTFT	Organic Field-Effect Transistors
p-6P	*p*-sexiphenyl
PMMA	Poly(methyl methacrylate)
QCM	Quartz Crystal Microbalance
rGO	Reduced Graphene Oxide
SAED	Selected Area Electron Diffraction
SEM	Scanning Electron Microscope (Microscopy)
STM	Scanning Tunneling Microscope (Microscopy)
TEM	Transmission Electron Microscope (Microscopy)
TMA	Trimesic Acid
TPA	Terephthalic Acid
UHV	Ultra High Vacuum
VOPc	Vanadyl-phthalocyanine
XPS	X-ray Photoelectron Spectroscopy

Acknowledgments

I owe a lot to many for the completion of this thesis and the work within.

First, I thank Dr Neil Wilson, who has guided and supported me throughout the whole PhD process. I am particularly grateful for the many hours he has spent with me over the past four years, especially considering how to difficult they are to come by.

Other academics have also helped me: Dr Diane Holland, for starting me off in research; Dr Ana Sanchez, for all the lessons in TEM; Dr Gavin Bell, for teaching me so much about synchrotrons and Star Wars; as well as Dr Richard Beanland, Dr. Giovanni Costantini, and Dr Jeremy Sloan.

The postdocs who have helped: Dr Keith Evans, for lessons in advanced supervisor management; Dr Peter Brommer; Dr Luis Alves Perdigao; Dr Luke Rochford; and Dr Reza Kashtiban.

I also greatly appreciate the support from the technicians: Steve York, Steve Hindmarsh and Rob Johnston, who demonstrate diligent patience every day!

I have also benefited from many friends throughout the past four years: Zac Laker, who has helped enormously in completing a lot of loose ends; Dr Adam Dyson; Dr Volker Keinhorst; Dr James Mudd; Jon Peters; and Grace Wood; as well as the many others (Mo, Cookie, Dawn, Mark, Ian, Ali, Alex, Sam, Daesung, Oreste, Ada, among many more).

I also thank my families. My parents have provided unreserved support since the very start, and helped pave the way for me to even attempt something like this. Thank you. Also, thanks in the same way to Richard and Terri. I also thank my sisters for trying to sound interested! I also wish to acknowledge my grandfathers, both of whom would have relished this opportunity given the chance.

And, finally, the biggest thanks of all goes to my wife, Hannah, who has been with me for every step of this journey. She has shown a special selflessness to support me throughout, and filled my life with comfort such that my mind is free to think. Thank you. I dedicate this to her, and the adventure we are about to undertake together.

Declarations

I declare that this thesis contains an account of my research work carried out at the Department of Physics, University of Warwick, between October 2011 and June 2015 under the supervision of Dr N. R. Wilson. The research reported here has not been previously submitted, wholly or in part, at this or any other academic institution for admission to a higher degree.

Parts of this thesis have been published by the author:

- Wilson, N. R., Marsden, A. J., Saghir, M., Bromley, C. J., Schaub, R., Costantini, G., White, T. W., Partridge, C., Barinov, A., Dudin, P., Sanchez, A. M., Mudd, J. J., Walker, M., Bell, G. R. *Weak mismatch epitaxy and structural feedback in graphene growth on copper foil.* Nano Res. **6**, 99 (2013)
- Marsden, A. J., Phillips, M. and Wilson, N. R. *Friction force microscopy: a simple technique for identifying graphene on rough substrates and mapping the orientation of graphene grains on copper.* Nanotechnology **24**, 255704 (2013)
- Marsden, A. J., Asensio, M.-C., Avila, J., Dudin, P., Barinov, A., Moras, P., Sheverdyaeva, P. M., White, T. W., Maskery, I., Costantini, G., Wilson, N. R., Bell, G. R. *Is graphene on copper doped?* Phys. status solidi - Rapid Res. Lett. **7**, 643 (2013)
- Marsden, A.J., Brommer, P., Mudd, J. J., Dyson, M. A., Cook, R., Asensio, M. C., Avila, J., Levy, A., Sloan, J., Bell, G. R., Wilson, N.R. *Effect of oxygen and nitrogen functionalization on the physical and electronic structure of graphene.* Nano Res. **8**, 2620 (2015)

Other parts of the thesis are to be published shortly:

- Marsden, A. J., Rochford, L., Wood, D., Ramadan, A. J., Laker, Z. P. L., Jones, T. S., Wilson, N. R. *Growth of large crystalline grains of vanadyl-phthalocyanine without epitaxy on graphene.* (Submitted to Adv. Func. Mater.)
- Marsden, A. J., Alves-Perdigao, L., Laker, Z. P. L., De Luca, O., Costantini, G., Wilson, N.R. *Monolayer to thin film transition in supramolecular assemblies on graphene.* (In preparation)

All the work presented here was completed by myself, except for the following:

- The ARPES data shown in section 3.2.6 and chapter 4 were aquired with the help of A. Barinov and P. Dudin from Elettra, and M. Ascensio, J. Avila, and A. Levy from Soleil.
- DFT calculations shown in 4.3, and those discussed in the text, were performed by P. Brommer.
- VOPc depositions in chapter 5 were done with the help of L. Rochford, as well as the XRD and further discussion.
- The TMA and TPA depositions in chapter 6 were performed by L. Alves Perdigao and O. De Luca.

Abstract

Graphene — a two-dimensional sheet of carbon atoms — has surged into recent interest with its host of remarkable properties and its ultimate thinness. However, graphene combined with other materials is starting to attract more attention. These heterostructures can be important for production routes, incorporating graphene into existing technologies, or for modifying its intrinsic properties. This thesis aims to examine the role of van der Waals epitaxy within these heterostructures.

First, the graphene-copper interaction during chemical vapour deposition of graphene is investigated. Graphene is found to grow with a mismatch epitaxy of $\pm 8^{\circ}$ relative to the [001] direction of the Cu(100) surface, despite a mismatch in symmetry and lattice parameter between two. Further, the electronic structure of both graphene and copper is unchanged by the interaction. This highlights the weak interaction between the two, owing to its van der Waals nature.

Functionalised graphene is another important heterostructure, and is intensively studied for both graphene production routes and for altering graphene's properties. Here, it is the change to the homogeneous graphene surface that makes it interesting for van der Waals epitaxy. The effect of functionalisation of graphene with atomic oxygen and nitrogen is presented next. In both cases, only small amounts of functionalisation (≈ 5 at%) is sufficient to significantly deteriorate the π-band structure of the graphene through localisation. For small amounts of nitrogen functionalisation, and greater amounts of oxygen functionalisation, extended topological defects are formed in the graphene lattice. Unlike epoxide oxygen groups, these disruptions to the pristine graphene are found to be irreversible by annealing.

Next, the interaction between graphene and the organic semiconducting molecule vanadyl-phthalocyanine (VOPc) is presented. As a result of the van der Waals nature of the graphene surface, VOPc molecules can form crystals microns in size when deposited onto a substrate with an elevated temperature of 155°C; at ambient temperatures, the crystals are only tens of nanometres across. In contrast, the functionalised graphene oxide surface prevents large crystal growth, even at elevated temperatures, because surface functionalities inhibit molecule diffusion. This highlights the importance of graphene as a substrate for molecular crystal growth, even when the growth is not epitaxial.

Finally, the supramolecular assembly of trimesic acid (TMA) and terephthalic acid (TPA) is presented. Despite their chemical similarity they display different behaviour as they transition from monolayers to three-dimensional structures: for TMA, the epitaxial chicken wire structure seen at a monolayer templates up through the layers as molecules stack, until a thickness of ≈ 20 nm, when random in-plane orientations appear; on the other hand, TPA forms a brickwork structure at the monolayer, which quickly transitions to fibre-like crystals with a bulk structure for the thin films. However, the TPA orientation is still determined by the epitaxy with the graphene substrate, although this is significantly weaker than for TMA.

Chapter 1

Introduction

1.1 Introduction

In this Information Age, technology is rapidly shrinking. This is driven by our desire to further incorporate technology into our daily lives. As just one example, computing power that 40 years ago could fill a room, now fits in the palm of a hand.

This feat has been motivated by Moore's Law, an observation-turned-challenge to make technology smaller. In 1965, Gordon Moore stated that the number of components on a printed circuit board had doubled at regular intervals, and that this would continue for "at least ten years" [1]. In fact, this has extended to the present day, with a doubling interval originally at one year, and more recently, two years. Furthermore, the observation became the driving force for targets set by the International Technology Roadmap for Semiconductors (ITRS).

However, the progress following Moore's Law is beginning to stall because it is becoming increasingly difficult to pack more computing power into smaller space; the materials and technologies that have been used so far are beginning to reach their limits [2].

In 2004, there was a huge boost to miniaturisation of technology. This came when Novoselov and Geim successfully managed to isolate, manipulate and then measure a single sheet of graphite only one atom thick — called graphene [3]. With the ability to isolate graphene came the possibility of making materials that were truly two-dimensional, which has inspired many possibilities of technology miniaturisation [4]. On top of this, graphene was shown to have many remarkable properties that have added to this excitement.

Although graphene has shown much promise, it is the prospect of combining graphene with other materials that has attracted more recent attention [5]. These heterostructures could help alter graphene's properties for certain applications, such as opening a band gap for transistors. They could also open routes to production, like using metal substrates to grow large-areas of graphene. Or graphene could be incorporated into existing technologies to enhance their performance, for instance in replacing the transparent conducting electrodes in solar cells.

This then poses many questions about how graphene interacts in these heterostructures, some of which are addressed here. How does graphene interact with metals during growth? How do atomic species change the properties of graphene? How do the organic semiconducting molecules used in organic electronics arrange on graphene?

This thesis examines how graphene interacts with metals, atoms and molecules. Specifically it explores how van der Waals forces within these heterostructures drive their formation. In some cases this presents as a van der Waals epitaxy between the two. Understanding these interactions will help bring graphene, and its heterostructures, into our technologies sooner.

1.2 Background

1.2.1 Graphene

Graphene is a two-dimensional sheet of sp^2 bonded carbon atoms. Its unit cell, shown in figure 1.1(a), is a rhombus with two non-equivalent carbon atoms (A and B) in its basis. The basis vectors of the unit cell are

$$a_1 = \left(\frac{\sqrt{3}a}{2}, \frac{a}{2} \right) \quad a_2 = \left(\frac{\sqrt{3}a}{2}, \frac{-a}{2} \right) \tag{1.1}$$

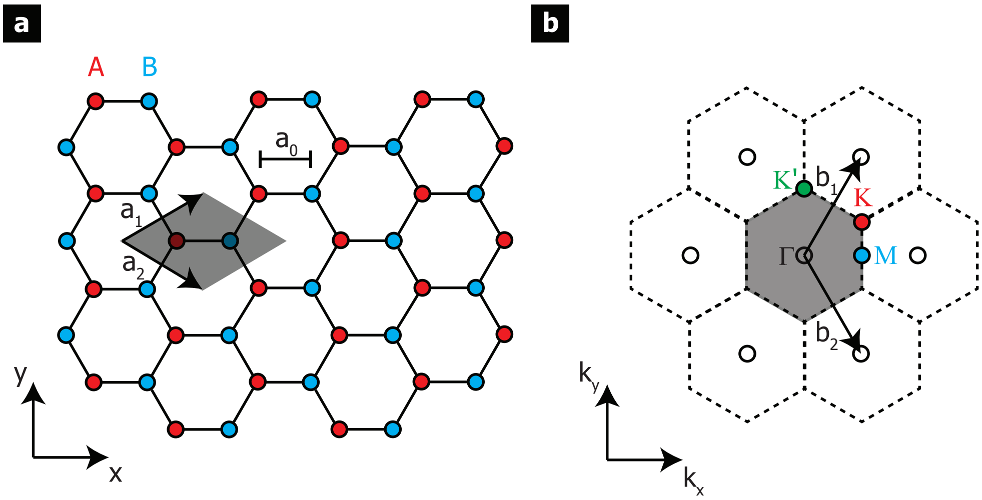

Figure 1.1: (a) the real space structure of graphene. The shaded area shows the unit cell, with two inequivalent carbon atoms, A and B. (b) the reciprocal lattice of graphene. Here the shaded region indicates the first Brillouin zone and the high symmetry points: Γ, M, K and K'. Adapted from [6].

where $a = \sqrt{3}a_0$ is the lattice constant and a_0 is the C-C bond length (0.142 nm). The corresponding reciprocal lattice vectors are

$$b_1 = \left(\frac{2\pi}{\sqrt{3}a}, \frac{2\pi}{a}\right) \quad b_2 = \left(\frac{2\pi}{\sqrt{3}a}, \frac{-2\pi}{a}\right) \tag{1.2}$$

and these are shown in figure 1.1(b). The high symmetry points are shown and have the vectors

$$\Gamma = (0,0) \quad K = \left(\frac{2\pi}{\sqrt{3}a}, \frac{2\pi}{3a}\right) \quad M = \left(\frac{2\pi}{\sqrt{3}a}, 0\right) \tag{1.3}$$

Electronic properties

The reciprocal lattice helps describe graphene's unique electronic structure. This can be calculated using a nearest-neighbour tight-binding model, which yields the following dispersion relation for graphene [7],

$$E(k_x, k_y) = \pm t\sqrt{3 + 2\cos\left(\sqrt{3}k_y a_0\right) + 4\cos\left(\frac{\sqrt{3}}{2}k_y a_0\right)\cos\left(\frac{3}{2}k_x a_0\right)} \tag{1.4}$$

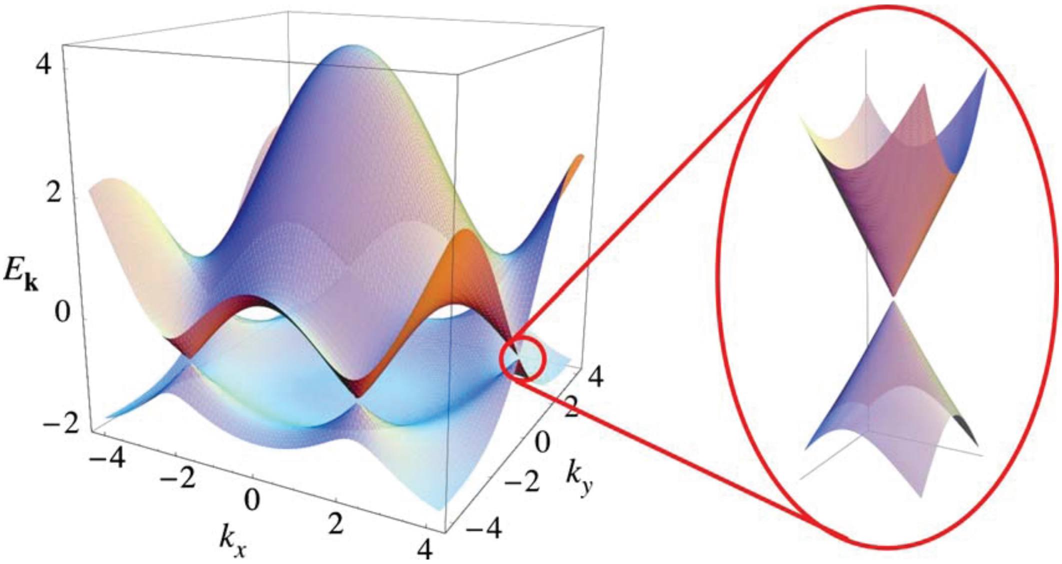

Figure 1.2: The electronic structure of graphene, showing the valence and conduction bands around the first Brillouin zone. On the right is a magnification around the K point, where the valence and conduction bands meet. This shows the linear dispersion around the so-called Dirac point. Taken from [7].

with t the hopping parameter.

The most notable feature in the band structure is the linear dispersion around the K point, where the valence and conduction bands meet. This is highlighted in figure 1.2. These points are referred to as Dirac points, and the cone shaped dispersion called Dirac cones, because of the nature of charge carriers in this region: the linear dispersion means they behave as if they are Dirac fermions, quantum mechanically described by the relativistic Dirac equation.

Around the K point a nearest-neighbour tight-binding model accurately predicts the graphene band structure and so can be used to measure the properties of graphene based on this structure. The linear dispersion around K can be approximated to,

$$E(q) \approx \pm v_F|q| + \mathcal{O}\Big((q/K)^2\Big) \tag{1.5}$$

with $q = K - k$, the momentum relative to the K point. Here v_F is the Fermi velocity which is given by

$$v_F = \frac{3ta_0}{2} \tag{1.6}$$

with t the hopping parameter as before. Around the K point, the density of states ($\rho(E)$) is then,

$$\rho(E) = \frac{2A_c}{\pi}\frac{|E|}{v_F^2} \tag{1.7}$$

where $A_c = 3\sqrt{3}a^2/2$ is the area of the unit cell. For undoped graphene, the Fermi level sits at the Dirac point. On the other hand, for doped graphene, the shift in Fermi level will cause a change in carrier concentration per unit cell (n). This can be calculated using the above to give,

$$n = \frac{2}{\sqrt{3}\pi}\left(\frac{E_D - E_F}{t}\right)^2 \tag{1.8}$$

where $E_D - E_F$ is the energy of the Dirac crossing relative to the Fermi energy.

Optical properties

Another key graphene property is its transparency. It has an opacity of 2.3 ± 0.1 %, and a reflectance of < 0.1 % [8]. Further, the opacity is almost independent of the wavelength and every additional layer adds 2.3 % to the total opacity. This transparency makes graphene ideal for opto-electronic devices like photodetectors or photovoltaics.

Mechanical properties

Graphene's mechanical properties are also exceptional. A single sheet of graphene has an intrinsic strength of 42 ± 4 Nm^{-1} and an effective Young's modulus of 1.0 ± 0.1 TPa, which makes graphene the strongest material ever measured [9]. On top of this, graphene sheets can support themselves when suspended over trenches micrometers across. Sheets suspended like this can be used as resonators with a very low noise floor, suitable for extremely low mass and force detection [10].

Applications

When combined, these properties show huge promise for many applications, especially when coupled with its two-dimensional nature. The large surface area

($2630\ \mathrm{m^2g^{-1}}$, compared to $1315\ \mathrm{m^2g^{-1}}$ for single-walled carbon nanotubes and 10-$20\ \mathrm{m^2g^{-1}}$ for graphite [11]) makes it ideal for contact sensors for chemical detection [12]; coupled with this are low noise levels, essential for single-molecule sensitivity [13]. Large surface area also shows promise for energy storage [11]. A high mobility enables high-frequency electronics [14], such as transistors that can operate at 100 GHz [15]. Finally its transparency means graphene can replace the transparent conducting electrodes in photonic applications, making flexible LEDs and photovoltaics [16]. These are just a sample of many possible applications [17].

1.2.2 van der Waals materials

The discovery of graphene has sparked a new interest in the wider family of van der Waals materials. These are materials that are composed of two-dimensional sheets held together by van der Waals forces, like graphene sheets making up graphite. Examples include hexagonal boron nitride (hBN) and the transition metal dichalcogenides (e.g. MoS_2 and WSe_2).

These van der Waals materials have properties that can compliment those of graphene, while still being extremely thin (essentially two-dimensional). hBN, for example, is a wide-bandgap (5.97 eV) semiconductor [18]. And the family of metal dichalcogenides display a range of electronic properties in monolayer form: there are semiconductors like WS_2 and MoS_2, metals like NbS_2, and even superconductors like $TaSe_2$ and $NbSe_2$ [19].

While they have shown striking properties, it is the prospect of combining van der Waals materials that is now receiving the most attention [5], as demonstrated in figure 1.3. Graphene has already been successfully combined with hBN. Graphene devices fabricated on a hBN substrate showed mobilities comparable to those measured for freely-suspended graphene sheets [20], [21]. Further, encapsulating a graphene sheet in hBN or MoS_2 layers showed a 100-fold increase in mobility compared to other flat oxides like mica [22].

One remaining challenge with the van der Waals heterostructures is how they are produced. Currently they are made predominantly by exfoliating and stacking

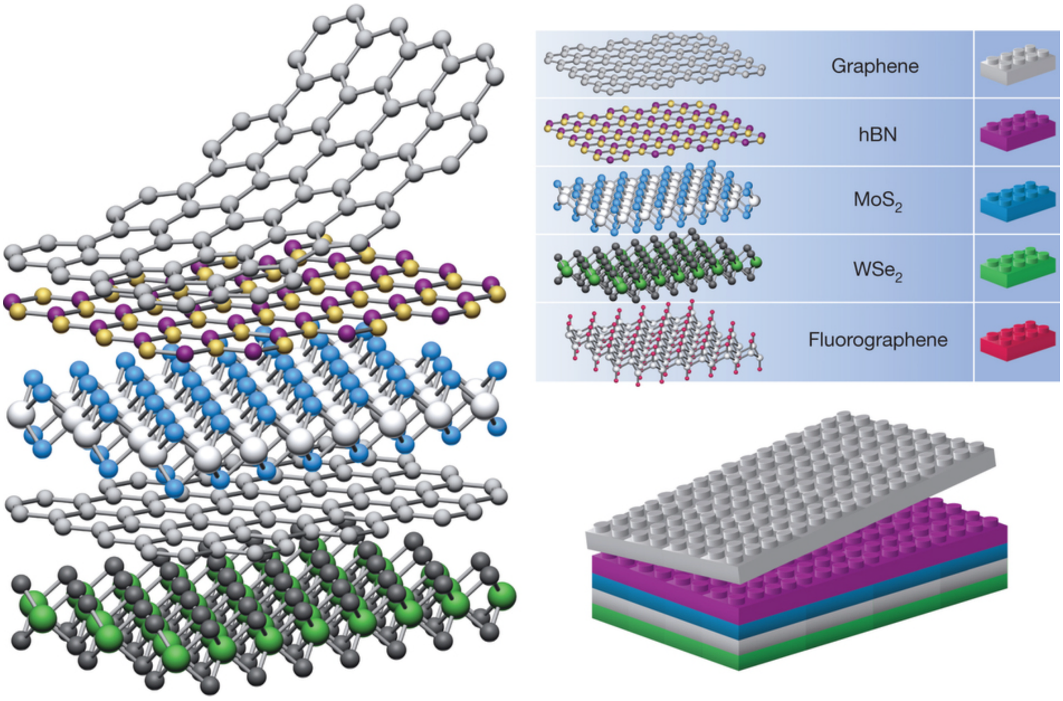

Figure 1.3: Some of the family of van der Waals materials. Stacking these different layers opens routes to many new heterostructures. Taken from [5].

the individual layers. This is time consuming and impractical for large scale applications. Growth methods are now being looked at as a way of combining graphene with other materials. It is these methods that motivate the study of the role of van der Waals epitaxy in van der Waals materials systems.

1.2.3 van der Waals epitaxy

Epitaxy — from the Greek of *epi*, meaning above, and *taxis*, an ordered manner — is the study of crystalline films grown on crystalline substrates. Heteroepitaxy, where the film and substrate are different materials, has been the foundation of the semiconductor industry, where device architectures are fabricated by epitaxially growing layers. In traditional epitaxial growth the dangling bonds of the film material satisfy the dangling bonds of the substrate material, as shown in figure 1.4. For this reason, the symmetry and relative lattice parameters of the two has a direct impact on the resulting interface. The difference in lattice parameter, called the lattice mismatch,

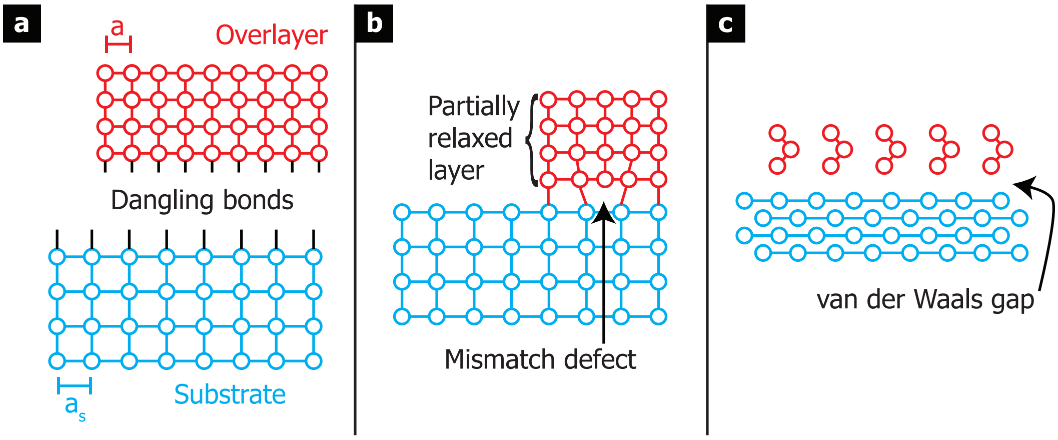

Figure 1.4: Schematic of epitaxial growth. In traditional epitaxy (a) the film and substrate bond covalently to satisfy the other's dangling bonds. Often the lattice parameter of the substrate does not match that of the film and so strain and dislocations are present (b). In contrast, in van der Waals epitaxy the film and substrate interact through weak van der Waals forces (c). Adapted from [23], [26].

is defined [23] as

$$f = \frac{a_s - a}{a} \tag{1.9}$$

where a is the lattice parameter of the film material and a_s that of the substrate. For lattice mismatches greater than 5 % the interface will display dislocations and stacking faults. These defects are generally deleterious to device performance [24]. For smaller mismatches the interface will be strained, and this again has an impact on the interface's properties [25].

In contrast to this 'traditional' epitaxy, with a covalently bonded film and substrate, in van der Waals epitaxy, the two interact through weak van der Waals forces. van der Waals epitaxy is typified by four conditions [23].

1. The film exhibits a consistent orientation relationship with the substrate
2. The lattice planes at the interface are incoherent and incommensurate
3. The interface shows no excessive strain induced by the epitxay
4. The epitaxy persists even for large lattice mismatches and different symmetries

This final condition — the relaxing of the lattice matching condition — is one of the main reasons for studying van der Waals epitaxy. Without the need to match lattice parameters or symmetries, there is greater freedom in choosing the film and substrate materials.

The combinations of materials can be classified into three categories: van der Waals films on conventional substrates; conventional films on van der Waals substrates; and structures where both the film and substrate are van der Waals materials.

For van der Waals materials on conventional substrates, one area that has benefited is the growth of crystalline nanowires. Here the alignment and orientation of the wires has an impact on their photonic and electronic properties. Relaxing the lattice mismatch by exploiting van der Waals epitaxy has reduced defects in these wires and enabled more material options. Examples include FePc nanowires on glass [27] and cadmium chalcogenide on mica for photovoltaics [28].

This mismatch relaxing condition was also exploited when GaSe was grown in two-dimensional form via van der Waals epitaxy on mica [29]. The resulting heterostructures were used as photodiodes with a quantum efficiency of 23.6 %, a relatively large value for a two-dimensional layer.

van der Waals materials can also be used as substrates, and graphene provides the ideal example for studying van der Waals epitaxy. This has already been demonstrated for GaN [30], where high-quality GaN films were grown epitaxially on graphene for use as blue LEDs. Furthermore, because there was only a weak interaction between the GaN and the substrate, the GaN film could be transferred to other substrates, and the graphene reused for more growth. Graphene has also been used in the growth of highly aligned, vertical, InAs nanowires [31]. The weak interaction demonstrates another advantage of van der Waals epitaxy over traditional epitaxy.

Finally, van der Waals materials can be the film and substrate. An early example was growing GaSe on WSe_2 [32]. Despite a lattice mismatch of 14 %, films with perfect epitaxial alignment were grown. More recently, atomically thin MoS_2 has been grown on graphene, with evidence of epitaxy presenting as an MoS_2

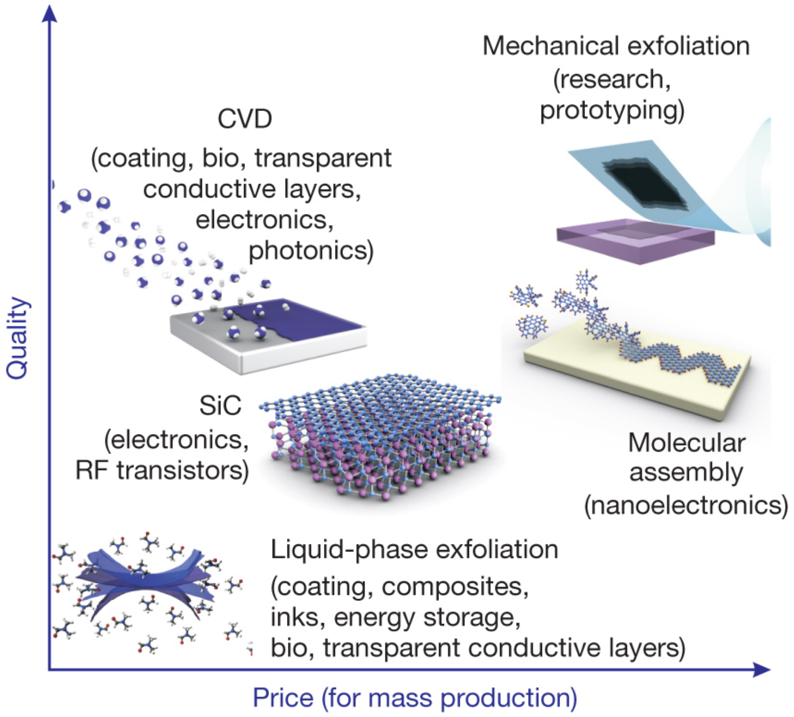

Figure 1.5: A comparison of the quality and the price for different graphene production routes. CVD has become the most popular route to cheap, large-area graphene with good quality. Taken from [4].

orientation defined by the graphene underneath [33]. In another example, after growing MoS_2 on graphene in UHV, measurements of the electronic structure of both materials found that they were electronically decoupled from each other, even though the MoS_2 grew epitaxially [34]. This highlights the weak, van der Waals nature of this type of epitaxial growth. Currently, van der Waals heterostructures are most commonly created by stacking exfoliated layers [35], but growth methods like this would enhance scalability.

1.2.4 Graphene production

Although graphene displays remarkable properties, it is yet to become a disruptive technology. One reason for this is the challenge of production. Graphene production routes are summarised in figure 1.5, and each one has advantages and limitations.

The original exfoliation method involves removing flakes of graphite using adhesive tape and placing onto a substrate [3]. The same flakes are repeatedly exfoliated, so that they gradually become thinner. Ultimately, there will be some flakes that are atomically thin: graphene. The graphene produced in this way is high-quality, and has been used for many proof-of-concept studies. However, its limits lie in the labour intensive method of gradually peeling down, and finding, the single-layer flakes. The flakes are also microns in size, making them unsuitable for large-area applications.

Another way of exfoliating graphite is in the liquid phase. Here, graphite is sonicated or stirred until individual graphene sheets are separated and dispersed in a solvent. To assist the dispersion, the graphite can be chemically functionalised, like in the case of graphene oxide. This has the effect of drastically changing the graphene's properties, and this is discussed in more detail in section 1.2.6. On the other hand, graphite sheets can be exfoliated in liquid without the chemical functionalisation using high shear forces [36], preserving the graphene quality. In either case, limitations lie in the sheet size, which is often only microns across. However, these methods still show promise for graphene-based inks and coatings.

Another graphene production route is the sublimation of Si from SiC. Here, SiC wafers are heated to above $1000°$C in UHV. The face of the wafers lose Si through sublimation and the remaining carbon atoms arrange in a honeycomb lattice [37]. The resulting graphene is high-quality and covers large areas, but the cost from the substrate and method limits it to high-end applications.

Finally the last method discussed here is chemical vapour deposition (CVD) of graphene onto metal foils. This is currently the most industrially favourable graphene production method, because it yields large-area, high-quality graphene, cheaply.

1.2.5 Graphene CVD

In CVD graphene growth, carbon containing precursors are catalytically broken down by a substrate, and the carbon atoms arrange into the graphene lattice. The reaction is supported by heating the substrate and/or the precursors. This can be

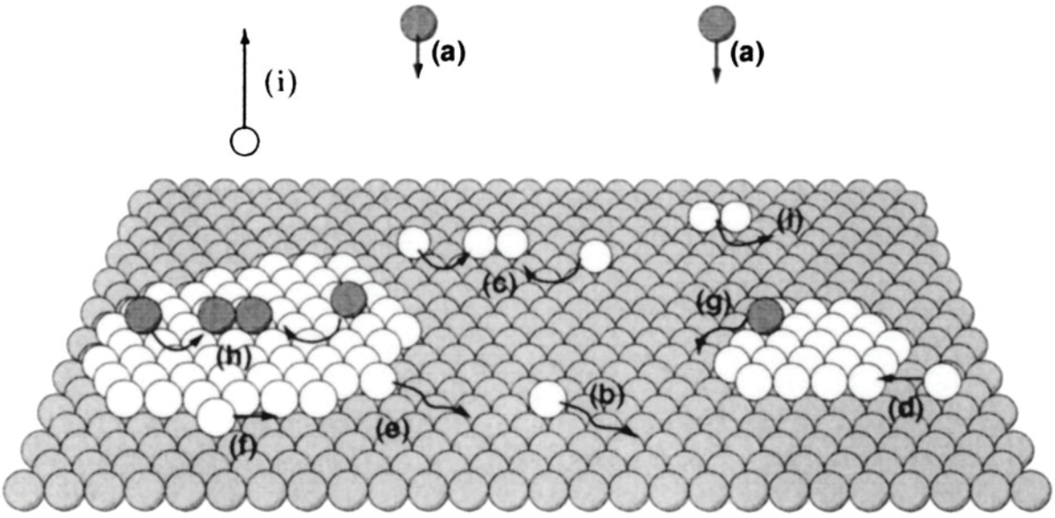

Figure 1.6: A summary of the processes in thin film growth. (a) absorption, (b) diffusion, (c) dimer formation, (d) aggregation, (e) detachment, (f) edge diffusion, (g) inter-layer diffusion, (h) dimer formation on second layers, (i) desorption, (j) dimer diffusion. Taken from [38].

done with thermal CVD, hot-walled, cold-walled or plasma enhanced CVD, along with others. Hot-walled, thermal CVD is the method used here.

Thin film growth

Graphene CVD proceeds via similar processes to those observed in conventional thin film growth. Thin film growth can be broken down into 10 important processes [38]: (a) the flux of growth units incident on the surface; (b) diffusion of these unit across the surface; the units can then attach together to start clusters (c), or can aggregate to an existing cluster (d); once attached, they can detach (e) or move along edges (f); growth units can deposit on top of islands and diffuse or detach onto the bottom surface (g), or form second-layer clusters (h); growth units can desorb from the surface (i); and finally, aggregated units can diffuse around the surface (j). These processes are summarised in figure 1.6.

Which of these processes are important depends on the graphene growth mechanism. Graphene growth on transition metals is typically described by one of two different mechanisms [39]: the first is precipitation, where carbon dissolved into the bulk precipitates to the surface after cooling, forming the graphene lattice [40]; or adsorption, where carbon diffuses across the surface, before aggregating into the graphene sheet. Which growth mechanism dominates is substrate dependant. For graphene grown on copper as used here, the adsorption mechanism dominates.

In the adsorption mechanism for thin film growth of graphene, the growth processes are generally the same, but with some key differences. The first is an extra process that occurs after surface adsorption: the catalytic decomposition of the carbon precursor into carbon atoms by the transition metal surface [41]. Because of this step, carbon species that have landed on an already formed island do not decompose, and so cannot nucleate a second layer.

Graphene is often observed to grow second layers, but these do not grow on top of the existing layer [42]. For the adsorption mechanism, the second layers form from carbon species that migrate underneath the existing graphene layer. These then nucleate and form a second island, likely at the same nucleation site as the top layer. This island can then grow while there are carbon atoms available.

Graphene growth

Thermal CVD on metals was first used to grow graphite in 1966, by exposing a Ni substrate heated to $900°$C to methane [43]. Later, in 1992, single layers of graphite were observed by STM on Pt(111) surface after it was exposed to ethylene while heated at $530°$C [44]. After the isolation of graphene in 2004, CVD was revisited as a route to monolayer graphene production. This was advanced by the discovery that large-area, uniform films of graphene could be grown on metal substrates, despite step edges, as shown for ethylene decomposition on Ir [45].

Other metals have now been investigated for CVD growth of graphene. Amongst all the choices of metallic substrates demonstrated for graphene CVD, copper has become the most popular [46]. This is because it is cheap, unlike platinum or gold. It is also because it has a low solubility of carbon, unlike nickel (which has a carbon solubility of ≈ 0.9 at% at $900°$C, compared to copper's < 0.001 at% [47]), where precipitation from the bulk during cooling makes growing monolayer graphene difficult [40]; in contrast, for copper, after the substrate is graphene-covered, the breakdown of carbon is stopped, which terminates the growth [41].

Just like the choice of substrate, there are choices available for carbon precursors. Liquid sources, like hexane [48] and toluene [49], have been used, along with solid sources, like PMMA and polystyrene [50]. However, gaseous sources have become the most popular and of these, methane has become the most common. CVD of methane onto copper foils produces high-quality graphene cheaply, and has already been scaled up to 30 inch sheets [51].

Despite progress in graphene CVD, problems remain in the quality, which is affected mainly by the grain structure. CVD graphene is polycrystalline, with separate islands nucleating across the foil and growing and merging to form a complete film that contains grain boundaries. It is these grain boundaries that fail first under external forces [52], [53], and are expected to scatter charge carriers [54], reducing the electrical performance. Minimising the number of grain boundaries is a priority of CVD graphene research.

Grain boundaries can be minimised in two ways: first, by increasing the grain size, and second, by exploiting an epitaxial relationship so grains share common orientations and remove misorientated grain boundaries [55], [56].

If independently nucleating grains do not share common orientations, the grain size of the graphene film will be directly related to the number of nucleated grains. In the extreme, a single crystal of graphene could be grown if nucleation was suppressed to a single point, and this grain then allowed to develop into the final film. Suppressing nucleation by removing nucleation sites has made progress [56] since CVD was first demonstrated. Among possible strategies, electropolishing the copper surface [49], growing onto a molten copper substrate [57], and using oxygen to remove any existing carbon nucleation sites before growth [58] have all increased the graphene grain size. Currently grains around 5 millimetres are now possible [59], [60].

At the same time, an epitaxial relationship between graphene and copper could exist [61]. For other substrates this has already been seen, like growth on SiC [37]. But there are still questions for graphene grown on copper. On the Cu(111) face, epitaxial growth has been seen [62], helped by the matching symmetry and small lattice mismatch ($f = 3.5$ %). However, the cheap technologically relevant foils show other crystallographic faces, like Cu(100) [63] where the lattice parameters and symmetry do not match. This lack of lattice matching presents the first opportunity to study van der Waals epitaxy in the graphene/copper heterostructure, and is the focus of chapter 3.

1.2.6 Covalent functionalisation of graphene

Other than CVD graphene, chemically assisted exfoliation is another promising production route. This yields only small flakes of graphene, but in large volumes with solution processability, and has shown promise for composites and coatings. The most common chemical exfoliation route is graphene oxide (GO). To make GO, graphite powder is heavily oxidised (often using a modified version of Hummer's original method [64]) and then sonicated and stirred in a solvent to separate and disperse individual sheets [65].

The structure of these oxidised sheets is debated, with some of the proposed models shown in figure 1.7. The exact structure of GO depends on the oxidation conditions and on the graphite precursor [66]. Accompanying the oxidised graphene sheets are much smaller graphene sheets (nanometres across) that are heavily functionalised with oxygen groups. These smaller sheets, called oxidative debris, adhere non-covalently to the graphene sheets [67]. This debris can be removed by 'base-washing' (heating the GO in NaOH and separating the aggregate out), and the result is termed base-washed GO. This base-washed GO has a higher C:O ratio of 4:1 compared to 2:1 for 'as produced' GO, suggesting the functionalised graphene backbone is not as decorated as bulk measurements would suggest [67].

The oxygen groups that are attached to the graphene backbone are generally detrimental to graphene's properties. The disruption they cause to the sp^2 bonded network makes GO an insulator [65]. This has hindered GO as a large-scale produc-

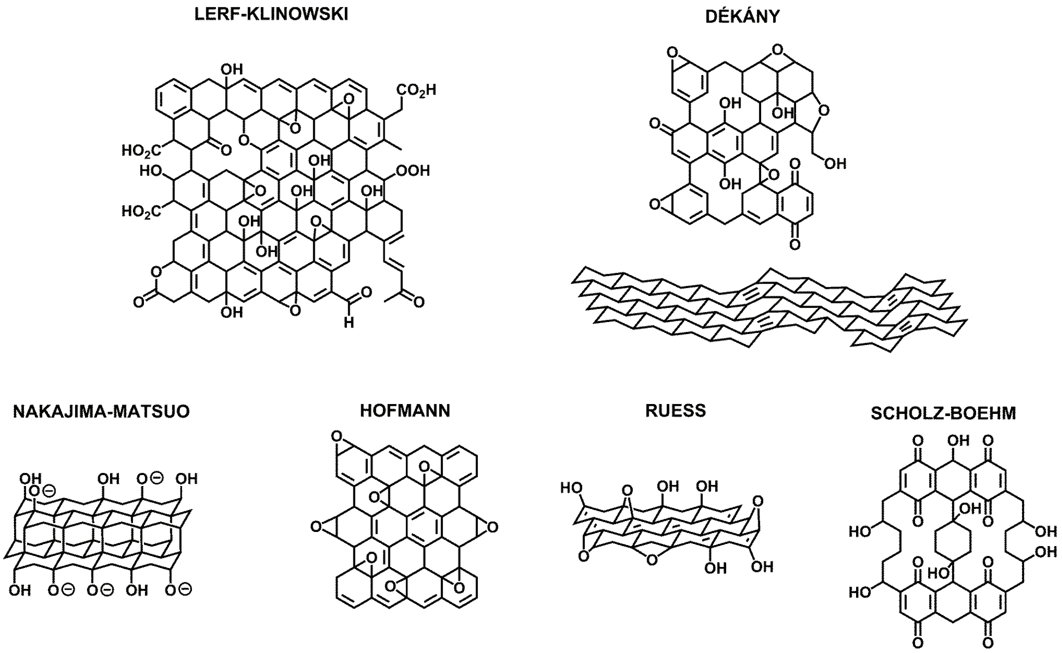

Figure 1.7: Proposed structural models for graphene oxide. The Lerf-Klinowski and Dékány models are examples of what is now the most accepted. The lower examples are earlier suggestions. Taken from [66].

tion route for graphene-based electronic applications.

However, reducing graphene oxide has shown promise. Here, reduction either by chemical methods (such as hydrazine vapour) or heating — or by a combination of the two — yields GO that that has a higher C:O ratio than as produced GO. This reduced GO (rGO) has better electronic quality [68], [69], and has successfully been used in devices. For example, in transparent conducting electrodes [70] and FETs [71]. These reduction methods are not fully understood and are yet to recover perfect graphene [72]. A step to understanding oxygen functionalisation of graphene is presented in chapter 4.

Covalent functionalisation could also be used to tune graphene's properties. For example, hydrogenated graphene becomes an insulator [73]. Nitrogen dopants have also attracted much attention. Adding nitrogen to graphene creates active regions that catalyse oxygen reduction reactions or that facilitate attaching nanoparticles [74], [75]. Further nitrogen doping offer opportunities to tune graphene's electronic properties. N-doped graphene films doubled the discharge capacity of Li-ion batteries when used instead of pristine graphene electrodes [76], and a field effect transistor (FET) fabricated with N-doped graphene displayed n-type behaviour and a 0.16 eV band gap [77]. Understanding the effect of the covalently attached nitrogen is also discussed in chapter 4.

Lastly, covalent functionalisation of graphene also provides opportunities to study van der Waals epitaxy. In section 1.2.5, two important processes identified in thin film growth were surface diffusion of growth units and nucleation. Both of these will proceed differently on a graphene surface that has been functionalised compared to pristine graphene. Currently GO and rGO are the most widely used graphene materials because they are cheap to produce, and so it is important to understand how the functionalisation affects thin film growth on these substrates. This starts by establishing the key differences between graphene and its functionalised counterparts.

1.2.7 Molecular heterostructures

Organic semiconductors

While covalent functionalisation offers many opportunities, another set of graphene heterostructures receiving significant interest are organic molecular overlayers [78]. This is because some organic molecules display semiconducting behaviour and electronics based on these are heralded to reduce the financial and environmental cost of the electronics industry [79]–[81]. Organic semiconductors (OSCs) are cheap, processable, and have shown performance capabilities in organic photovoltaics (OPVs) [82], organic thin film transistors (OTFTs) [81], and organic light-emitting diodes [83] approaching that of their inorganic counterparts.

Graphene provides the ideal substrate for these molecules, for example, as the transparent conducting electrodes in organic photovoltaics [84], [85], and so there is considerable interest in understanding thin film growth of OSCs on graphene.

To deposit molecules onto a substrate, organic molecular beam deposition (OMBD) has become increasingly popular [86]. This is where organic molecules are

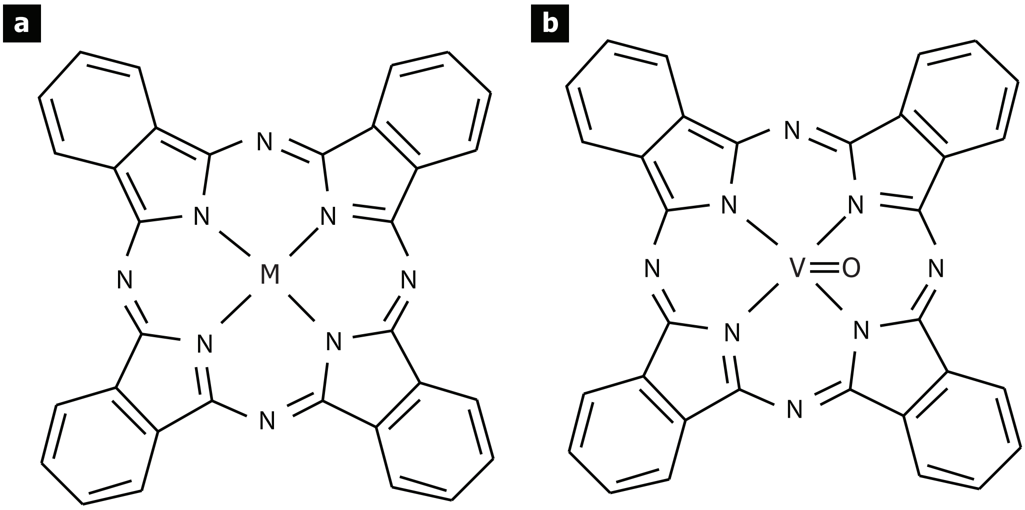

Figure 1.8: (a) Structure of a metallophthalocyanine, where M represents either a metal or a metal functional group. (b) vanadyl-phthalocyanine (M=VO). The functional group sticks out of the phthalocyanine plane. Adapted from [89], [90].

evaporated from a crucible that is pointed at the target substrate, all in UHV. OMBD has advantages over other deposition methods (like self-assembly from solutions): the rate and time of growth can be carefully tuned to give layer thickness control. On top of this, OMBD is performed in UHV, meaning substrates can be kept atomically clean.

For OMBD, the molecule-substrate interaction is critical [87]. Because both the molecules and graphene lack dangling bonds, these interactions are often driven by van der Waals forces. The growth mechanism of the resulting thin films follow the same processes as outlined in section 1.2.5, but with the growth units now molecules rather than atoms.

One of the most promising organic molecular systems for electronics are the metallophthalocyanines (MPc) [88]. They consist of four isoindole units with a metal (or metal group) in the centre, as shown in figure 1.8(a). These molecules fall into two categories: planar phthalocyanines, which have a single atom in the centre (e.g. CuPc, ZnPc), and so are almost flat; or non-planar phthalocyanines, which have a functional group at the centre, and so display an out-of-plane dipole (e.g. vanadyl-phthalocyanine, VOPc).

VOPc, shown in figure 1.8(b), is the phthalocyanine studied here. It was first used in dyes and inks because it is optically active in the visible range. Now this activity motivates their incorporation into OPVs as the active layer, where the photogenerated current originates [89]. VOPc also shows promise for (OTFTs) [91].

For VOPc and other phthalocyanines, their performance in the active layer depends on the morphology of the crystal structure after deposition. This structure should promote efficient charge transport in the desired current direction [81]: for OPVs, this is perpendicular to the substrate [92]; for OTFTs, on the other hand, this is parallel to the substrate [81]. Charge is most efficiently transported in the π-π stacking direction for disc-like molecules, like VOPc [81]. Controlling the growth of semiconducting molecules to encourage a π-π stacking direction perpendicular to the substrate (face-on orientation) is crucial for OPV performance [93]. For OTFTs, the edge-on orientation would be optimal.

In addition to crystal structure, the extent of the crystallinity will have an impact on device performance. Single crystals will perform better than polycrystalline films. This is primarily because boundaries between grains can trap or scatter charge carriers, reducing the efficiency of the charge transport [94].

The deposition substrate also has an impact on morphology and crystallinity. In many organic electronics, the substrates are amorphous — like indium tin oxide (ITO) for OPVs and SiO_2 for OTFTs. Films of disc-like molecules deposited onto these substrates are often of poor quality [95].

However, order-inducing layers deposited onto the amorphous substrate before deposition are a route to controlling the growth morphology. As an example, VOPc was deposited onto an order-inducing layer of *p*-sexiphenyl (*p*-6P) on Al_2O_3, which resulted in an increase in film crystallinity and crystal size [91]. Ultimately, these changes caused a 100-fold increase in the mobility. This 'weak epitaxial growth' [95] demonstrates how important van der Waals epitaxy is in these systems.

Graphene has also shown promise as the order-inducing substrate. CVD graphene was transferred onto an ITO substrate before deposition of $Cl_{16}AlPc$ [96]

resulting in greater crystallinity. STM was used to study FePc on graphene grown on Ru(0001) [97]. In this case, the molecules arranged in a Kagome lattice, providing an interesting chance to study the magnetic properties of these structures.

At the same time, other 2D substrates are being explored as substrates for OSCs [98]. One of these is GO because of its ease and scalability of production highlighted in section 1.2.6. Thin films of F_{16}CuPc deposited onto GO formed islands that were 10 to 20 nm across and displayed a polycrystalline ring in diffraction patterns [99]. GO paper has also been functionalised with ZnPc in an attempt to combine these two materials, which has shown promise for optoelectronics [100], [101]. ZnPc has also been used to exfoliate graphite directly [102]. The structure of OSCs on GO compared to graphene provides an opportunity to study van der Waals epitaxy in these materials.

Along with changing the growth substrate material to control morphology, changing the substrate temperature can also be used. Increasing the substrate temperature increases the mobility of the molecules on the surface. This higher diffusion rate encourages growth units to aggregate to an existing cluster rather than nucleate their own. This increases the island size of the molecular crystals.

This has been demonstrated for VOPc, where depositing onto quartz at $90°$C resulted in crystals that were hundreds of nanometres across, as opposed to tens of nanometres across when deposited onto a substrate at $30°$C [90]. The same is true for VOPc deposited onto CuI; at $26°$C crystals were tens of nanometres across, increasing to micrometres across at $155°$C [103]. Elevated temperatures also helped increase the crystallinity of VOPc on *p*-sexiphenyl (*p*-6P) [91].

It is clear that the semiconducting molecules are affected by the crystallinity of the substrate, and its temperature during deposition. Although growing organic crystals on graphene has been investigated, the substrate temperature effect has not. Further, the effect of the non-uniform surface of graphene oxide is not fully understood. Examining how substrate temperature affects VOPc growth on graphene, and how this changes for GO, is the focus of chapter 5.

Supramolecular chemistry

Supramolecular chemistry is the study of structures composed of molecules or ions that are held together by non-covalent forces like van der Waals forces and hydrogen bonds. It forms a large part of biological chemistry and nanotechnology, as just some examples [104].

There are two main branches of supramolecular chemistry. The first is host-guest chemistry. This is where one molecule or ion (the guest) fits inside another molecule (the host), where the host is normally significantly larger than the guest. These types of interactions are often used to trap small molecules in lattices, and these structures can also act as sensors [104].

The other branch of supramolecular chemistry is self-assembly. Here discrete molecules arrange with spatial organisation, either with or without a substrate. These structures interact through non-covalent forces, both between molecules and between the molecules and substrate. Because of these forces, they provide another opportunity for studying van der Waals epitaxy with molecules.

Many biological processes rely on self-assembly. It plays a role in the most essential of them all: the replication of deoxyribonucleic acid (DNA). Here, hydrogen bonds between the nucleobases of the two strands of the double helix can be broken and reformed easily during replication. If these bonds were covalent, vast amounts of energy would be required and the process would be infeasible [104].

Supramolecular assembly is also studied as a route to nanomaterials. Self-assembly is the foundation of bottom-up fabrication. This presents many opportunities to produce nanotechnology that is compact and cheap to produce because the structures form spontaneously [105]. Wires, switches, and rectifiers are all possible to form by self-assembly, just by choosing the right molecular precursors [104].

The substrate plays an important role in self-assembly. The most commonly used substrates are highly-oriented pyrolytic graphite (HOPG) and Au(111), primarily because they are easy to prepare and use [106]. In these cases, substrate driven interactions have a profound effect on the resulting assembly.

As a van der Waals surface, graphene provides an ideal choice of substrate

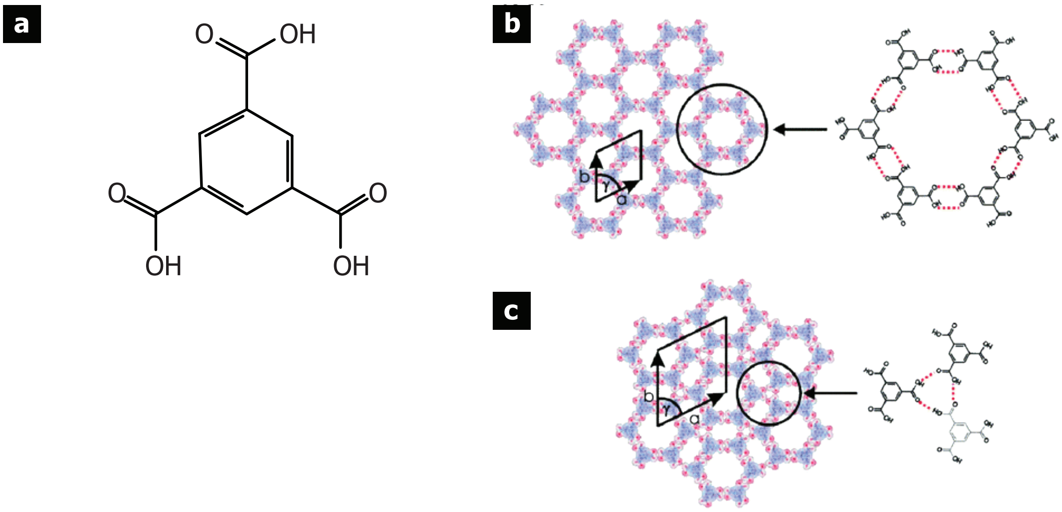

Figure 1.9: (a) chemical structure of TMA. TMA forms two network structures: (b) the chicken-wire structure, and (c) the flower structure. Taken from [110].

for supramolecular assembly. Perylene tetracarbox-ylic diimide (PTCDI) when deposited onto epitaxial graphene forms rows that run parallel to the high-symmetry directions of the moiré-like substrate [107]. As another example, tetratetracontane (TTC) also forms rows when deposited onto graphene [108]. In this case, the interaction between TTC and graphene is strong enough to bend the graphene surface when it is suspended on water layers.

Trimesic acid (TMA) and terephthalic acid (TPA) are two aromatic molecules that have been intensively studied for supramolecular assembly. Here hydrogen bonds form between the carbonyl and alcohol groups on the vertices of the molecules and extended networks are the result. For TMA, shown in figure 1.9(a), these networks have been seen in two forms: the chicken-wire (panel (b)) and the flower structure (panel (c)). Both of these structures have been seen on graphite under UHV [109] and at the solid-liquid interface [110]. On the other hand, for TPA, a brickwork pattern is seen (shown in figure 1.10). This has been seen on graphite [111] and Pt(111) [112], both at the solid-liquid interface.

As before, graphene provides an ideal substrate for studying supramolecular assembly for TMA and TPA. For TPA, the same brickwork structure as for graphite is observed on CVD graphene grown on Pt(111) [113]. Here they observed a 3×4 TPA

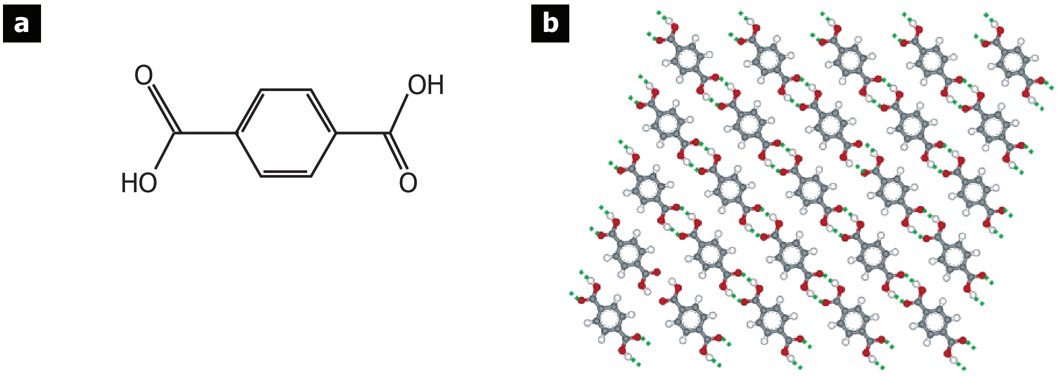

Figure 1.10: (a) chemical structure of TPA and (b) the 'brickwork' network structure that it forms. Taken from [111].

superstructure over the graphene lattice, and that this structure was seen in all six equivalent graphene directions. This is another example of van der Waals epitaxy of organics on graphene.

Molecular Metrology

When studying supramolecular assembly on surfaces, scanning tunnelling microscopy (STM) is most commonly used [106], [114]. With STM, the 2D structure is obtainable at the atomic scale, and so can provide detailed information for monolayer growth or below. However, less information is available about the out-of-plane structure. This has left questions about how the monolayer growth proceeds to thin film growth.

To study multilayers of these molecules, spectroscopy can be used. This has been shown for TPA on graphene using near-edge X-ray absorption fine structure (NEXAFS) [115]. However, these are indirect techniques and so interpretation is difficult.

Electron microscopy has been used to study self-assembly. Historically, these have often been in two areas: self-assembly of metal nanoparticles, where the large contrast and beam-stable particles are well suited to electron microscopy [116], [117]; and electron microscopy has also been used to study self-assembly of biological and polymer materials. The latter of these requires careful exposure to the beam to prevent damage to the specimen [118], and has benefited from improvements in low-voltage TEM [119].

Recently, electron microscopy has also been used to understand molecular thin films of OSCs. For example, scanning TEM (STEM) has been used to study grain boundaries in molecular crystals of chlorinated copper phthalocyanine ($Cl_{16}CuPc$) [120]. In addition, high-resolution TEM (HRTEM) was used to study the molecular interface of a $CuPc/C_{60}$ active layer in an OPV [121].

CVD graphene provides the ideal TEM support to study molecular layers because it contributes virtually no contrast to images. On top of this, the organic molecules can be directly deposited [99], which removes any degradation of the film during the transfer process, or during focused ion beam (FIB) lift-out preparation [122]. Therefore, electron microscopy is also used to help understand VOPc growth on graphene in chapter 5, and in chapter 6 to directly study der Waals epitaxy for TMA and TPA on graphene.

Overall, graphene has shown huge promise for the next generation of technologies, and it is graphene-based heterostructures that are currently receiving the most attention. Whether the heterostructures are studied to further production methods — like graphene grown on copper, or chemically assisted exfoliation — or as a result of deliberate modification — like adding atomic species and molecular overlayers — there are still unknowns. Understanding how graphene interacts in these heterostructures is essential.

1.3 Scope of this thesis

In this thesis, graphene heterostructures are examined using microscopy and surface science techniques in an attempt to understand their physical, chemical and electronic structures, and the interactions that drive them. Weak, van der Waals interactions with graphene result in a rich variety of thin film growth phenomena in these heterostructures.

First, in chapter 3, the graphene-copper interaction is investigated by observing how graphene grows on copper via CVD. The graphene grows with an orientation preference across millimetres of copper foil, which points to an epitaxial relationship between the two. Furthermore, the electronic structure of graphene on copper shows a pristine band structure suggesting this interaction is weak, pointing to an interaction driven by van der Waals epitaxy.

The unchanged band structure of graphene on copper provides the model system for studying the next heterostructure: graphene combined with atomic species. This is the focus of chapter 4. Here, graphene is dosed with atomic oxygen and nitrogen in ultra-high vacuum. The chemical changes on dosing are followed with XPS and the structural changes with TEM. These changes are then linked to changes in the electronic structure with ARPES. Finally, the reversibility of these changes are probed by attempting to remove the functional groups by annealing. These results give an important insight into the differences between graphene and chemically modified graphene.

After this, graphene in molecular heterostructures is presented in the remaining two chapters. First, in chapter 5, the formation of crystallites of vanadyl-phthalocyanine is studied. Using elevated temperatures during deposition produces crystallites of micron size. The crystallography is measured with acTEM. Further, the islands are significantly smaller on a functionalised graphene surface of GO, demonstrating the potential of the homogeneous graphene surface for promoting high-quality, OSC thin film growth.

The second molecular overlayer system is TMA and TPA presented in chapter 6. TEM is used to investigate the structural transition from supramolecular assembly of monolayers to three-dimensional thin films. For TMA, van der Waals epitaxy causes two preferred orientations of a chicken-wire structure relative to graphene that template through to ≈ 20 nm. After this, the same chicken-wire structure is seen but with random in-plane orientations. On the other hand, TPA forms a characteristic brickwork structure at the monolayer that quickly transitions to a bulk structure seen for thin films. Despite demonstrating a bulk structure, van der Waals epitaxy is still seen, but with much weaker ordering.

Chapter 2

Experimental methods

2.1 Graphene growth and transfer

2.1.1 Graphene growth

In this thesis graphene is grown onto copper foils from methane via chemical vapour deposition (CVD). This was first demonstrated in 2009 [46] and the procedure has evolved over the project. Outlined here are typical experimental parameters and an explanation of those evolutions.

A photograph and schematic of the CVD system are shown in figure 2.1. A quartz tube in a tube furnace is pumped from one end, while at the other mass flow controllers (MFCs) introduce hydrogen and methane. A nitrogen valve is also present for venting. Within this outer quartz tube is another quartz tube to load the foils, which sit in the centre of the furnace. The furnace and MFCs are LabVIEW controlled to ensure reproducible growth conditions.

The growth procedure is as follows: first the foils (Alfa Aesar, product # 13382, purity 99.5 %) are cleaned by sonicating in acetone, rinsing in isopropanol, followed by drying in nitrogen ((1) in the sample preparation overview, figure 2.2). They are then loaded into the quartz tube and the system pumped. After reaching the base pressure of $< 1\text{x}10^{-3}$ mbar, hydrogen is flowed at 10-20 standard cubic centimetres per minute (sccm), raising the pressure to $2\text{x}10^{-2}$ mbar. The furnace

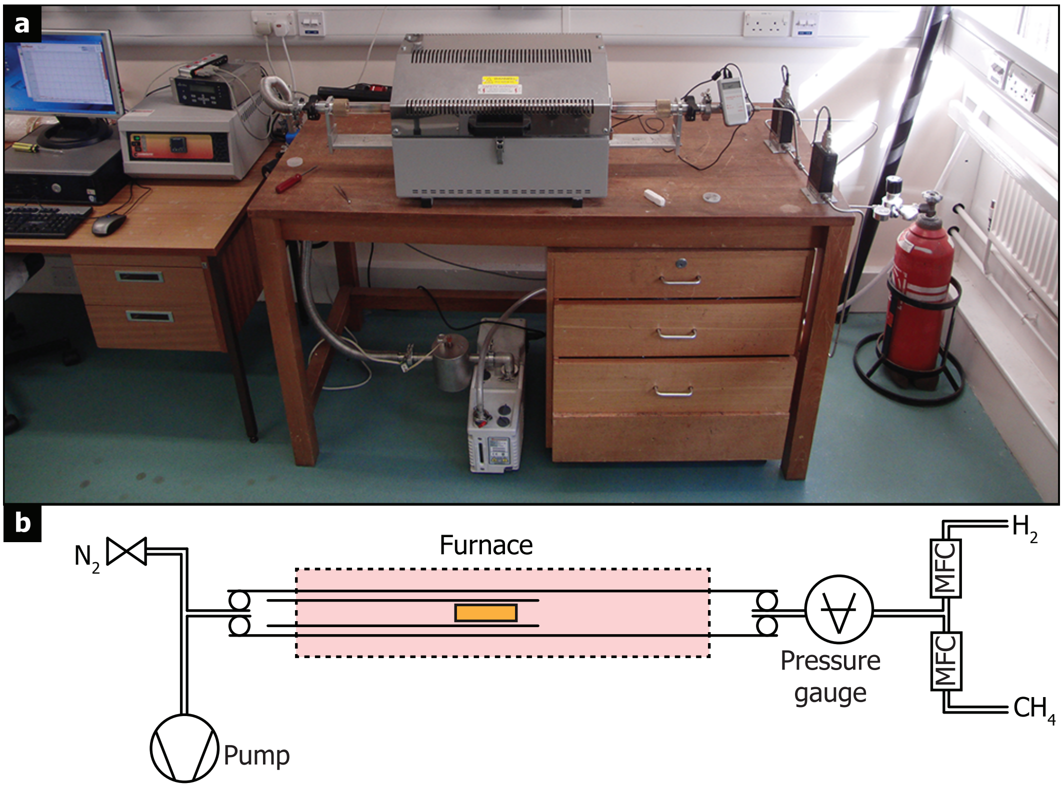

Figure 2.1: Photograph (a) and schematic diagram (b) of the CVD system at Warwick.

is heated at 15°C / min to 1000°C, where the foils are annealed for 20 minutes. To start the growth, 2–10 sccm methane is introduced for 10-30 minutes, after which the flow is stopped. The hydrogen is kept on while the furnace cools and only stopped below 150°C, when the foils are removed (2).

Later batches of copper foil were coated with an anti-corrosion layer by the supplier, which prevented graphene growth. This is not removed with the cleaning procedure and so a higher purity foil was tried (Alfa Aesar, product # 10950, purity 99.999 %). With these the growth proceeded differently: more methane was needed to achieve a full coverage (35 sccm for 10 minutes) and the methane flow was continued at a reduced rate (5 sccm) while the system cooled to prevent etching of the graphene.

While graphene grew effectively on higher purity foils, it was expensive, costing 85 p/cm^2 as opposed to 3 p/cm^2. By now processes had been developed to remove the anti-corrosion coating. One of these was electropolishing [49]. This removes the top few hundred nanometres of copper, along with the coating. The process is as follows: the target foil is placed in an electrolyte bath (containing 50 mL orthophosphoric acid, 1 g urea, 50 mL ethanol, 50 mL isopropanol and 10 mL deionised water) and attached to the anode of a power supply. To the cathode is attached a larger copper foil, also placed in the bath. Applying 5 V for ten seconds (with a current of approximately 2 A) removes the surface layer. The electrolyte solution is rinsed off the foil with deionised water and isopropanol, after which they are cleaned as before. Growing a complete graphene film on electropolished foils required a lower methane flow (2 sccm for 10 minutes) but methane was still required during cooling.

2.1.2 Graphene transfer

It is sometimes necessary to transfer graphene from copper to other substrates or supports; the most notable example here is to suspend graphene over grids for transmission electron microscopy (TEM). Just like for the growth, the transfer procedure has been developed over time. An outline is presented here and exact details are in

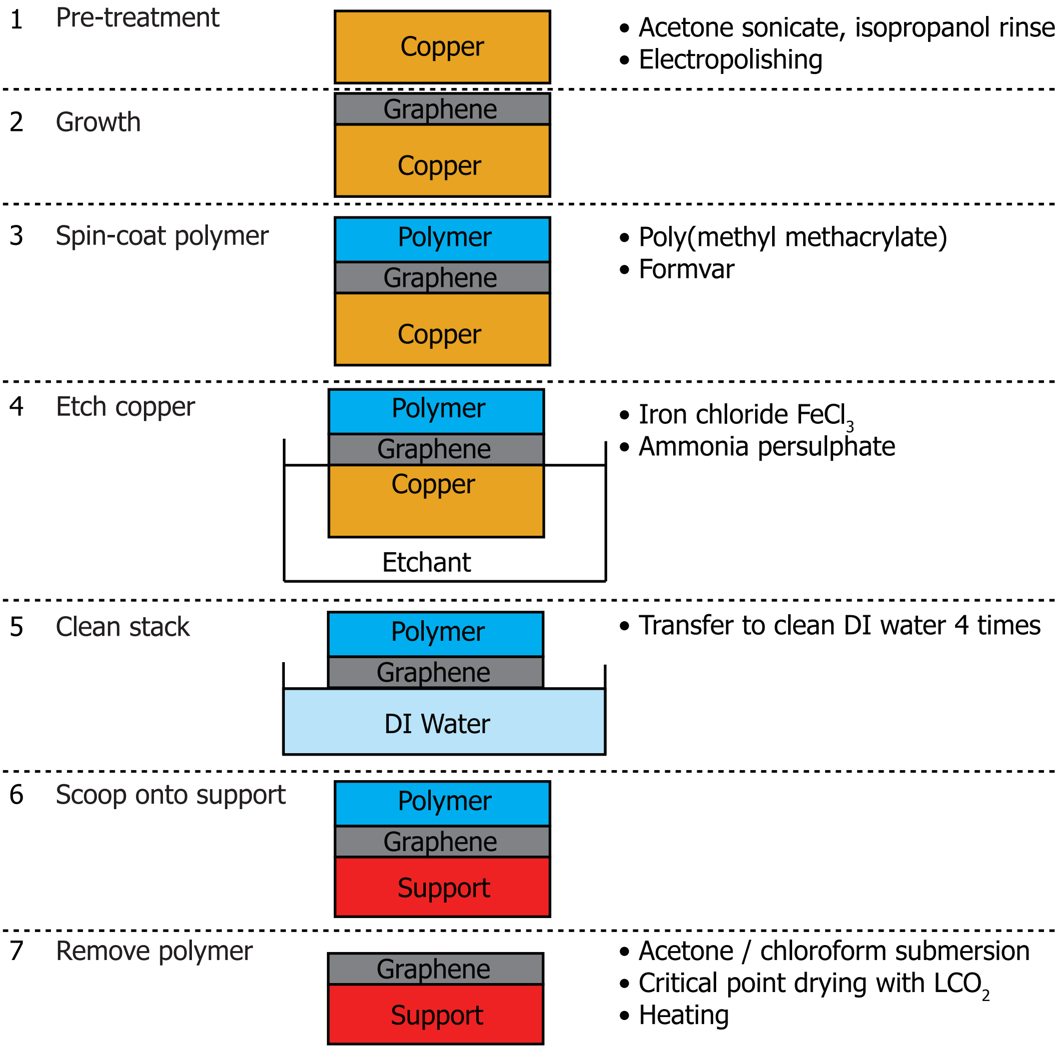

Figure 2.2: Schematic overview of sample preparation. Listed on the right are possible alternatives for each step.

their respective chapters.

The transfer procedure starts with graphene coated copper foils (2 in figure 2.2). First these are spin coated (0.1 s ramp, 3000 rpm, 45 s dwell) with a polymer support (3). Next, the copper is chemically etched with either iron chloride or ammonia persulphate, the latter leaving less contamination on the stack (4). This leaves a polymer coated graphene stack floating in etchant. These stacks are scooped and placed into deionised water using a glass slide, and this is repeated to fresh deionised water four times to remove any etchant (5). Once the stack is clean, it is scooped (6) using the target substrate (the TEM grid, for example). After this has dried in air, the final step is to remove the polymer support (7), and it is this step that has required the most development.

The common method for removing polymer is with solvents. For silicon substrates, this involves immersing in the solvent, rinsing and drying. However, this is not possible for TEM grids because surface tension caused by evaporating solvent will tear the freely suspended graphene. This difficulty is overcome using a critical point dryer (CPD). Here grids are placed in a small chamber while they are submerged in solvent. Liquid carbon dioxide, which has a practically achievable critical point of $31°$C and 1072 psi, replaces the solvent in the chamber through a series of fills and purges. Drying at this critical point results in no surface tension and suspended graphene films remain intact.

Despite submersion in solvents, the method above does not produce graphene grids clean enough for high-resolution TEM (HRTEM). To address this, one strategy was to try a different polymer support at stage (3). The original polymer was the commonly used poly(methyl methacrylate) (PMMA). On the other hand, in TEM grid manufacturing, formvar is used, which is substantially removed using chloroform. Formvar (34 mg/ml, dissolved in chloroform) was spin coated onto graphene coated copper foils with the same parameters as for PMMA. To clean, instead of submersion in acetone before critical point drying, they are submersed in chloroform then acetone: it is not possible to CPD from chloroform because it is not miscible with liquid carbon dioxide.

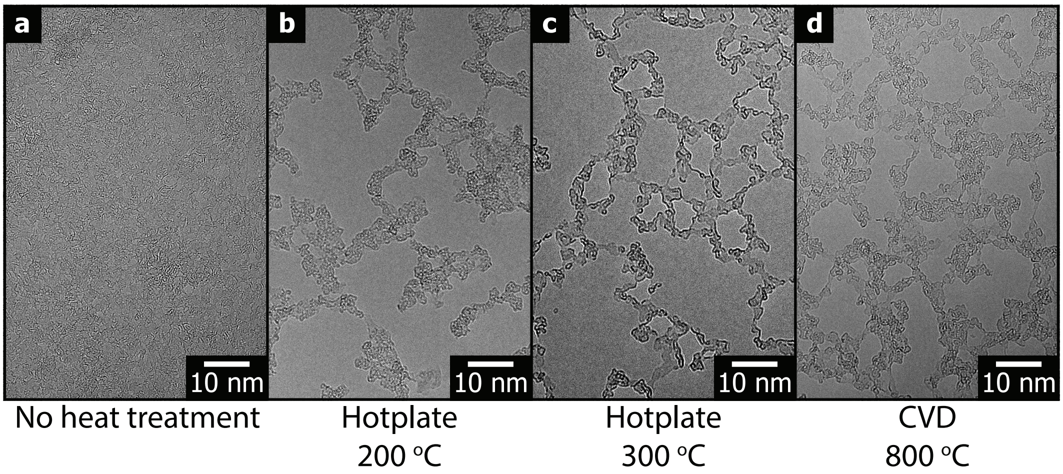

Figure 2.3: Effect of thermal treatment on graphene TEM grid cleanliness. Without heat treatment, the polymer residue is significant and no exposed graphene can be seen. 200°C hotplate treatments produce substantial clean areas, however, at 300°C holes have been etched into the film. Using higher temperatures (800°C) in the CVD does not give noticeably cleaner grids. Each treatment lasted for two hours.

Using formvar results in cleaner graphene grids, but still not clean enough for HRTEM. For further improvements, in the final stage of cleaning the grids are heated in two possible ways. The first is to return the transfer to the CVD system to heat to 800°C under 20 sccm hydrogen for two hours. The second is to heat in air on a hotplate at 200°C for the same amount of time. The latter of these is most commonly used because it is less time-consuming and does not appear to introduce defects into the graphene. On the hotplate at higher temperatures, however, etched holes appear in the film. Figure 2.3 shows the effect of these heating methods.

2.1.3 Graphene oxide

In some parts of this thesis, graphene oxide (GO) is studied and, in contrast to the intensive graphene transfer procedure, preparing GO TEM supports is straightforward. GO is produced using the modified Hummer's method [64], [70], which yields a GO paper which can be dispersed into deionised water. To coat a TEM support, first the GO solution is diluted to around 0.02 mg/ml. The GO concentration has a direct effect on the number of GO layers deposited and can be adjusted; 0.02

mg/ml will normally yield 50 % coverage of single-layer GO sheets. Second, a lacy or holey carbon support film is treated with air plasma (100 W, 1 minute), making the surface hydrophilic and helping the GO disperse uniformly. Finally, a single drop of GO is cast onto the grid and left to dry in air.

2.2 Microscopy

2.2.1 Optical

Next, the experimental techniques are presented, starting with microscopy. The drive of microscopy is to visualise objects undetectable by the naked eye. Optical microscopy uses lenses to form images from visible light and was the method first used to observe isolated graphene [3]. In this case, the challenge came not from the dimensions of the graphene sheets, but from the contrast: graphene is 97 % transparent in the visible range. To overcome this, the interference effect between the graphene sheet and a thin, oxide layer on silicon was exploited, producing enhanced contrast [123].

Here, however, graphene is grown on copper foils and there is no interference effect. But optical microscopes can be used to study the grain structure of the copper foils, or to assist in sample preparation. A Zeiss Axio Imager.M1m optical microscope was used.

2.2.2 Scanning Electron Microscopy

Optical microscopy is limited by a fundamental principle of optics: the Rayleigh resolution criterion. This states the maximum distance separation, r_d, of two objects to be resolved [124].

$$r_d \approx \frac{0.61\lambda}{NA} \tag{2.1}$$

Where NA is the numerical aperture and λ the wavelength used. To resolve smaller features, smaller wavelengths are needed. Using radiation with shorter wavelengths than visible light is possible, but these are hindered by difficulties in lensing. Electrons are another option. These charged particles can be lensed effectively with electromagnetic fields and have a tunable wavelength (λ) dependent on the voltage (V) they are accelerated by

$$\lambda = \frac{h}{\sqrt{2m_0eV\left(1+\frac{eV}{2m_0c^2}\right)}} \tag{2.2}$$

Electrons are accelerated in the range of 1–300 keV where this relativistic case is needed.

The first electron microscope presented here is the scanning electron microscope (SEM) [125]. In an SEM electrons are accelerated to typically 1–20 kV and focused to a fine spot on the sample. The high energy electrons impinging on the surface release electrons and photons and these provide the signals for studying in the SEM. They are recorded as the electron beam spot is rastered over the sample and a map of the intensities provide the image.

The main signal used for imaging are secondary electrons. These are useful for seeing the grain structure of the copper foils as well as features not visible in optical microscopes. Another advantage is the contrast between graphene and copper. The graphene attenuates electrons escaping from the surface so those covered regions appear darker. Furthermore, areas with stacked graphene layers attenuate more and are darker still [126].

The next signal involves X-rays. Core electrons are removed by the electron beam and, as other electrons drop down to fill the hole, photons are released. The energy difference is quantised and characteristic of both the element and transition. The amount of an element in the sample can be related to the number of X-rays counted at a specific energy. Although accurate, quantitative information is challenging from energy dispersive spectroscopy (EDS) because factors like surface-angle affect the counts and are hard to control. Measuring X-ray counts as the beam is rastered can produce elemental maps.

The final signal considered here is backscattered electrons that satisfy diffraction conditions, called electron back-scattered diffraction (EBSD) [127]. The sample is tilted to 70° relative to the electron source, and a phosphor screen at 90° placed near the sample. Some of the incident electrons are inelastically scattered backwards by the sample, and some of these scattered electrons are incident on atomic planes at the sample surface that satisfy Bragg conditions. Because the energy loss during the inelastic scattering is small (15–25 eV), the wavelength is considered to be unchanged. However, the electrons are now incoherent, and so after diffraction they form Kikuchi bands rather than diffraction spots on the phosphor screen. The angles between Kikuchi bands is measured (usually through a Hough transform) and compared with reference angles for the specified material. In this way, the crystallographic structure is measured at that point and a map of the structure is produced by rastering the beam.

At Warwick a Zeiss Supra 55VP SEM is used, usually with 10 kV accelerating voltage. EDS spectra and EBSD maps were collected with an EDAX Genesis analytical system with EBSD detector.

2.2.3 Transmission Electron Microscopy

To resolve smaller features it is necessary to use a transmission electron microscope (TEM). The key differences between a TEM and an SEM are the larger accelerating voltages (80–300 kV) and the transmission rather than reflected geometry [128]. This geometry requires a thin sample and so clearly graphene is ideal. Details of the common TEM modes are presented here.

The primary imaging mode is bright field mode and the lens geometry is show in panel (a) of figure 2.4, and an example image in panel (b). There are two types of contrast mechanisms: mass-thickness contrast, where electrons are strongly scattered by the sample; and phase contrast, where the sample changes the phase of the electron wave. Phase contrast is applicable for a weak-phase object, which applies to the samples studied here, and so is described in more detail.

The electron wave ($\psi_{ep}(\mathbf{r})$) just after leaving the sample (called the exit-

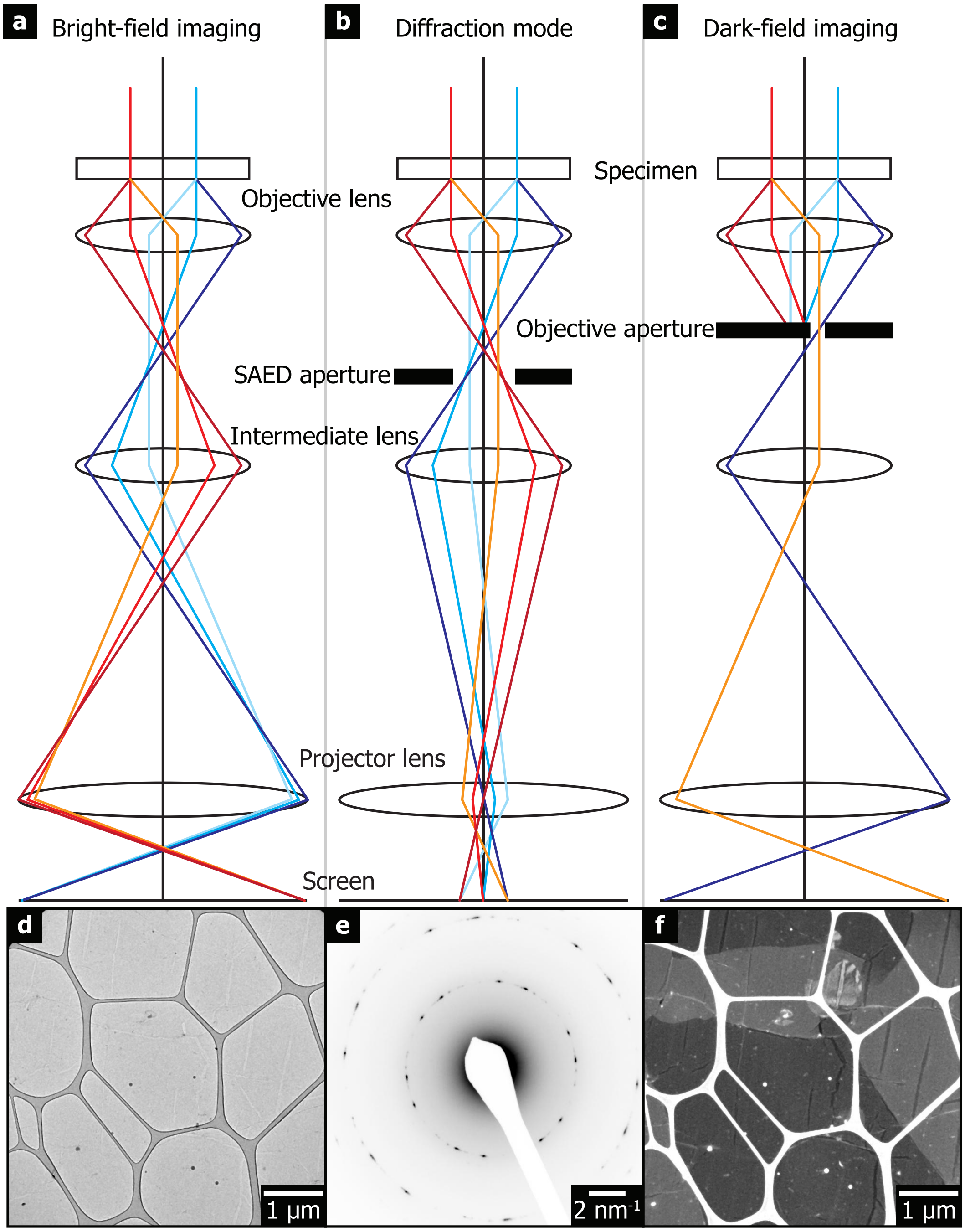

Figure 2.4: Schematic diagram of a transmission electron microscope (TEM) configured in the three modes used here. Bright field mode (a), diffraction (b) and dark field (c). Adapted from [128]. Panels (d), (e) and (f) show example images from each respective mode.

plane) can be described by [129]

$$\psi_{ep}(\mathbf{r}) = 1 - i\phi(\mathbf{r}) = 1 - \frac{i\pi}{\lambda U} V_t(\mathbf{r}) \tag{2.3}$$

where U is the accelerating voltage and $V_t(\mathbf{r})$ is the projected electrostatic crystal potential; that is, the potential from the crystal integrated over its thickness. Once through the sample, the electron wave passes through the objective lens. The effect this has on the wavefunction is a convolution with a transfer function $t(\mathbf{q})$

$$\psi(\mathbf{r}) = \mathcal{F}^{-1}[\psi_{ep}(\mathbf{q})t(\mathbf{q})] \tag{2.4}$$

where q is the two-dimensional vector of the spatial frequency spectrum and $\psi_{ep}(\mathbf{q}) = \mathcal{F}[\psi_{ep}(\mathbf{r})]$. The transfer function for a lens ($t_L(\mathbf{q})$) is written

$$t_L(\mathbf{q}) = \exp\left[\frac{-2\pi i}{\lambda}\chi(\mathbf{q})\right] \tag{2.5}$$

Where $\chi(\mathbf{q})$ is the aberration function. For conventional TEMs this is described by

$$\chi(\mathbf{q}) = \chi(q) = \frac{1}{2}q^2\lambda^2 C_1 + \frac{1}{4}q^4\lambda^4 C_3 \tag{2.6}$$

where the coefficient C_1 is called defocus, and C_3 called spherical aberration. Finally, the image is formed on a CCD by measuring the amplitude of the electron wave giving an intensity map $I(\mathbf{r})$

$$I(\mathbf{r}) = |\psi(\mathbf{r})|^2 \tag{2.7}$$

Unfortunately, the available resolution is still far from the theoretical. The limit is from spherical aberration (C_3) introduced by the electron lenses. To begin to approach the theoretical resolution (and so to see the atomic structure of graphene) TEMs have been developed with correctors to counteract the aberration, and this is the focus of the next section.

Aberration-Corrected TEM

In 1936 Schezer showed that rotationally symmetric lenses used in electron optics cause strong aberrations of the electron wave function [124]. This spherical aberration (C_3) limits the possible resolution of TEM to approximately 1 Å [130].

To fix this, the most common approach is to break the rotational symmetry by introducing combinations of quadrapoles, hexapoles and octopoles. These multipoles, combined called aberration correctors, introduce negative spherical aberration that counteracts the positive spherical aberration.

While this effectively counteracts spherical aberration, its removal causes other aberrations to become apparent. The aberration function must then take into account these aberrations and equation (2.6) becomes

$$\begin{aligned}\chi(\omega) = \Re\Big\{ & A_0\omega + \frac{1}{2}C_1\omega\overline{\omega} + \frac{1}{2}A_1\overline{\omega}^2 + B_2\omega^2\overline{\omega} + \frac{1}{3}A_2\overline{\omega}^3 \\ & + \frac{1}{4}C_3(\omega\overline{\omega})^2 + S_3\omega^3\overline{\omega} + \frac{1}{4}A_3\overline{\omega}^4 \Big\}\end{aligned} \tag{2.8}$$

where image shift (A_0) and first-order astigmatism (A_1) are now included here where they were left out of equation (2.6), and the higher order astigmatisms are also included. Here the complex scattering angle is now used $|\omega| = |\theta_x + i\theta_y| = \theta \approx \lambda q$ and $\overline{\omega}$ denotes the complex conjugate. The aberrations extend to even higher orders, but are only shown up to third-order because this is the highest that can be corrected on the JEOL ARM 200F at Warwick.

All the aberrations can be minimised along with spherical aberration by tuning the current through the correctors in a process outlined here called the Zemlintableau method [129]. To first measure the aberrations, the beam is tilted off the optic axis. Different order aberrations manifest as defocus (C_1) and first-order astigmatism (A_1), both of which can be measured from the FFT of an image of an amorphous area. By tilting around the axis, the full aberration profile is obtained [131], and the corrector currents are iteratively adjusted to minimise their impact.

Exit-wave reconstruction and simulation

More information is available from a TEM image if the effect of the objective lens (i.e. the lens aberrations) is removed to recover the electron wave just after it has left the sample ψ_{ep}. To recover this exit-wave, the spatial-frequency-dependence of the contrast transfer function $CTF(q)$ is used.

$$CTF(q) = -\sin\left(\frac{2\pi}{\lambda}\chi(q)\right) = -\sin\left(\frac{2\pi}{\lambda}\frac{1}{2}q^2\lambda^2C_1 + \frac{1}{4}q^4\lambda^4C_3\right) \tag{2.9}$$

Where the conventional aberration function (equation (2.6)) has been used for simplicity. The most practical method to recover the exit-wave is called the focus variation method. The principle is that by taking images at different defocus (C_1), information at different frequencies is transferred by the $CTF(q)$. The information from each defocus is then combined to reconstruct the exit-wave. This was done using a custom, exit-wave-reconstruction procedure written by Adam Dyson [132].

Even with the improvement in microscope resolution, and exit-wave reconstruction, TEM images can often be difficult to interpret. One solution to this problem is to simulate the exit-wave, or, furthermore, to include in the simulation the effect of the objective lens and camera to then compare to real images. In this thesis, simulations were performed using a custom routine (Adam Dyson [132]) based on the multi-slice method. In this procedure, the sample structure is first divided into fine planes normal to the electron beam. The transmission function for each plane (or slice) is calculated from the atomic positions in that slice, and these functions applied in turn to the electron wave. The result after the final slice is the exit-wave. To compare to real images, the transmission function of the objective lens is applied, the amplitude of the wave taken, which is then combined with noise introduced by the CCD.

Low-electron-dose techniques

One disadvantage of electron microscopes is the damage caused by the electron beam. Electrons cause damage through scattering with the sample [133], with the most relevant here being in two categories [134]: for conductors, knock-on damage, where atoms are displaced after elastic scattering from electrons; and for semiconductors and insulators, radiolysis, where charge cannot dissipate quickly after holes are created by inelastic scattering, and ionisation damage occurs. The damage mechanisms are affected by the choice of electron accelerating voltage [134]. For the conductor graphene, using 80 kV significantly reduces knock-on damage and normal imaging is possible.

For more delicate samples, the damage is still too great. The next option is to reduce the number of electron interactions by using a lower electron dose. These low-dose methods have been developed for delicate, biological samples. However, these techniques still expose the samples too much for some organic molecules, and have been developed further. Here, the advantage of thin films covering graphene that covers regularly spaced holes was exploited. The procedure is to expose one graphene covered hole to set the microscope to the correct conditions. Then, the beam is shifted away, the stage moved to the next hole, and, after the drift has settled, the region is exposed while the CCD is recording. Acceptable images are acquired immediately after exposure, but immediately after that, the sample is too damaged. The process can be repeated through each hole of the sample. Using these methods means no dose is used finding the correct area and setting the microscope, both of which expose the sample to electron dose.

An example of this for vanadyl-phthaloycanine (see chapter 5) is shown in figure 2.5. Just before exposure (a), the frame and its FFT show only noise features from the CCD. Just after the sample has been exposed (b), the crystalline structure of the molecules is apparent, as shown by spots in the FFT. Just 0.3 seconds later, the spots have been replaced by rings, which indicate amorphous material, demonstrating the rapid damage caused by the electron beam.

Electron diffraction and dark field TEM

It is also possible to study electron diffraction in a TEM. This is shown in panels (c) and (d) of figure 2.4. The intermediate lens strength is decreased so diffracted

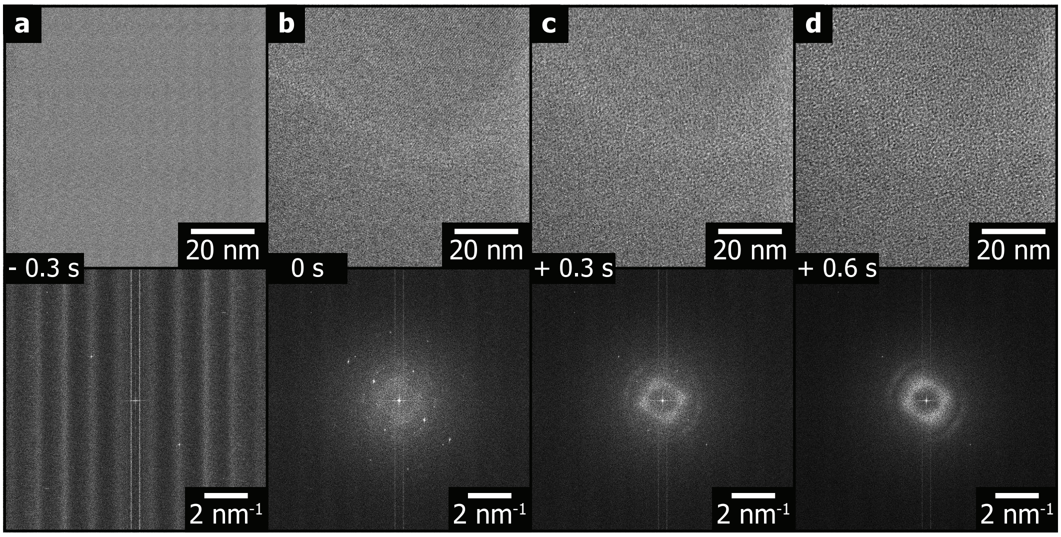

Figure 2.5: Example images from using the low-dose procedure. (a) is the frame captured just before exposure, with an FFT of this region below. The only features are from noise from the CCD. (b) is captured at exposure to the beam. Here, features from the crystalline molecules are visible. However, 0.3 and 0.6 s after exposure ((c) and (d)), amorphous rings are the only features in the FFT, showing how the beam has damaged the crystalline structure of the films.

beams are within the recording area. The diffracted intensity, I, is given by

$$I = \Phi\overline{\Phi} \tag{2.10}$$

where $\overline{\Phi}$ denotes the complex conjugate and

$$\Phi = f(\theta)\sum_{n}\exp[-i(\mathbf{k}-\mathbf{k}').\mathbf{r}_n] \tag{2.11}$$

where $f(\theta)$ is the scattering factor, $\mathbf{k}$ and $\mathbf{k}'$ are the incident and scattered electron wavevectors and $\mathbf{r}_n$ are the atom positions. Diffraction peaks appear when the wavevectors satisfy $\mathbf{k}-\mathbf{k}' = \mathbf{G}_{hkl}$ where $\mathbf{G}_{hkl}$ is the reciprocal lattice vector. For graphene, electron diffraction reveals lattice spacing, in-plane orientation, and it is also possible to distinguish the number of layers from the intensity of diffracted beams [135]. Another advantage is the use of apertures to select the area of the sample to form the diffraction pattern from (selected-area electron diffraction (SAED)).

The final TEM mode used here is dark field imaging. Here images are formed from scattered beams only, selected with the objective aperture. An application for graphene is imaging using only electrons from diffraction spots from different in-plane orientations, and making a colour composite to show the graphene grain structure.

Three TEMs were used in this work. The JEOL 2000 FX is operated at 200 kV and was used for diffraction, and bright field and dark field imaging. The same is true for the JEOL 2100. Finally, the latest addition is the JEOL ARM 200F. This TEM contains two CEOS aberration correctors: one for image correction as discussed above; and the other for probe correction only relevant for scanning TEM (STEM), not used here. This microscope was operated at 80 kV to minimise beam damage. All images were recorded using Gatan Orius cameras.

2.2.4 Atomic Force Microscopy

The next two sections present scanning probe microscopy (SPM), where a fine probe is moved over a surface and the interaction between the two is monitored. A map of the scale of this interaction forms the image.

The most common SPM technique is atomic force microscopy (AFM) [136]. In AFM, the fine probe, attached to a spring-like cantilever, interacts with the surface through physical forces. The cantilever movement is measured through a reflected laser dot onto a quadrant photodiode, as shown in figure 2.6. Although many forces can be investigated in many modes, the most routine are topographic modes — those that map the sample height. This can be found using two schemes: contact mode and tapping mode.

In contact mode the tip is pressed against the surface causing the cantilever to deflect away through repulsive van der Waals forces. This deflection is kept constant by using a feedback loop on the height of the stage while the tip moves across the sample, giving a height map.

In tapping mode, instead of pressing the tip into the sample, the cantilever is oscillated above the surface. As the cantilever approaches the surface the oscillation

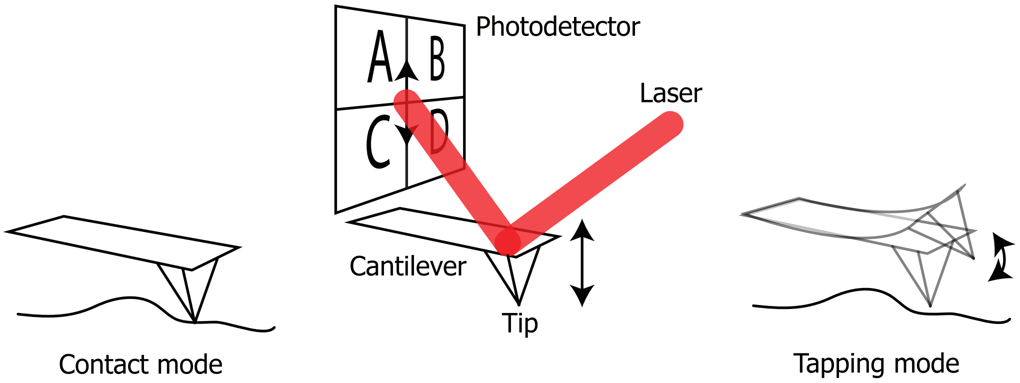

Figure 2.6: Schematic of the cantilever and photodiode in an AFM. The distance between the cantilever and the detector is much larger than shown here and a small cantilever movement causes a large spot movement.

amplitude is damped by the tip-sample interaction. The reduction in amplitude is kept constant through feedback on the stage height, again giving a height map. In contrast to contact mode, the forces are often not large enough to alter the surface, and so tapping mode is used to preserve delicate samples.

Both tapping and contact mode provide information about sample height. For graphene, detection from height alone is problematic, in particular on copper where the surface topography changes are much greater than the thickness of graphene. One possible solution is to detect graphene through a different force interaction. The next section looks at measuring the friction force between the tip and surface.

2.2.5 Friction Force Microscopy

Friction force microscopy gives a signal dependent on the local coefficient of friction across the sample surface [137]. The tip now moves perpendicular to the cantilever length, and lateral torsion of the lever is detected as lateral movement of the laser spot on the photodiode. A schematic of this is shown in panel (a) of figure 2.7. As the tip moves across a high-friction surface, the lever is deflected to high values; as the tip moves across a low-friction surface, lower values are recorded. This is shown in panel (b) of figure 2.7 and is referred to as the trace. For the retrace on

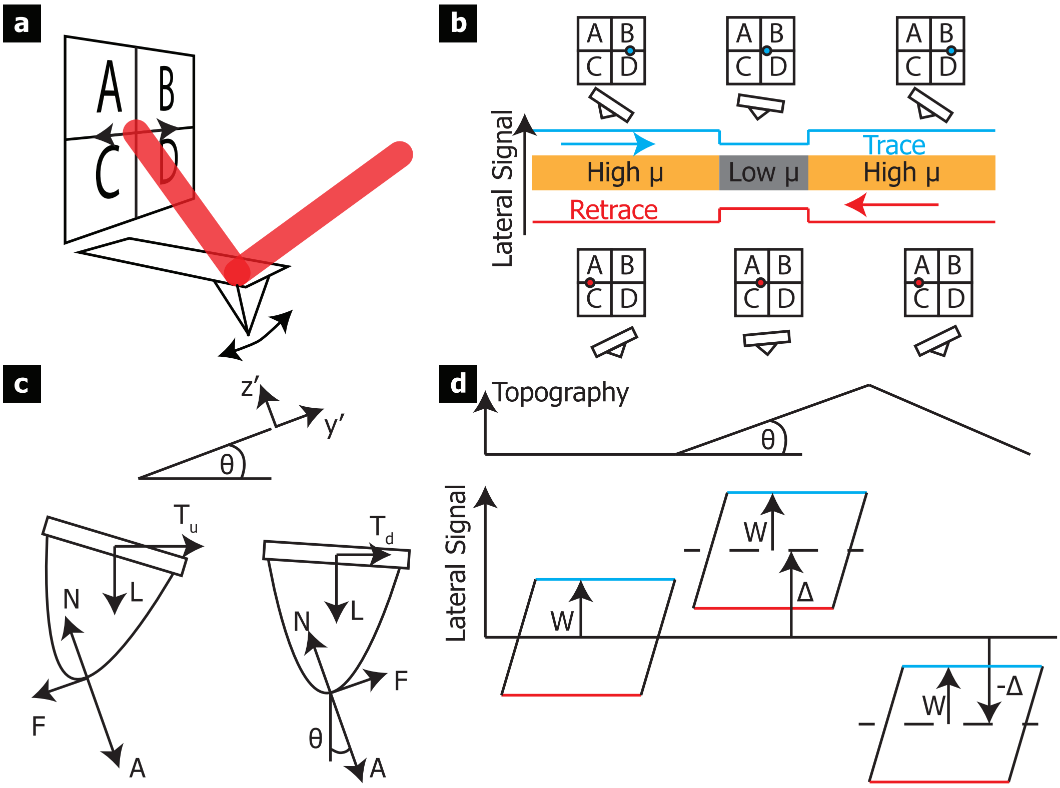

Figure 2.7: Schematic of how a friction force microscopy image is formed. (a) shows how lateral movement of the tip causes lateral movement on the photodiode, and then shown for different friction surfaces in (b). (c) is the free-body diagram of the tip moving up and down an inclined plane. (d) the effect this has on the lateral signal.

a high-friction surface, the spot is deflected to large, negative values, and on the low-friction to smaller values. This shows that the width of the friction loop (the difference between the trace and the retrace) is related to the coefficient of friction, μ. Using Amonton's Law gives

$$T = \mu(L + A)$$

where T is the torsional force, L is the load and A the adhesion of the tip to the surface.

The advantage of FFM is that, to a first approximation, topography changes do not affect the width of the friction loop; they only apply an offset to the centre.

To see this consider the free-body diagram of a tip moving on an inclined surface, shown in figure 2.7(c) [138]. The torsional force T on the tip as it moves up or down the slope is resolved as

$$T_{u/d} = \frac{Lsin\theta \pm \mu(Lcos\theta + A)}{cos\theta \mp \mu sin\theta} \tag{2.12}$$

where u and d represent moving up and down respectively. This can be expanded using Taylor series as

$$T_{u/d} = \pm\mu(L + A) + L\theta + \mu(L + A)\theta + \mathcal{O}(\theta^2) \tag{2.13}$$

Taking the difference of the up and down torsion forces — equivalent to finding the difference of the trace and retrace, hence the full width of the friction loop ($2W$ in figure 2.7)

$$2W = T_u - T_d = 2\mu(L + A) + \mathcal{O}(\theta^2) \tag{2.14}$$

While the torsional force depends strongly on the topography the friction force does not.

As an example, figure 2.8 shows FFM of a partially covered graphene on copper foil. Panel (a) shows the height image, where the striations from the cold-rolled copper are clear [49]. Panel (b) shows the deflection image (the difference between the deflection setpoint and actual value at that point), which again is dominated by topographic features. Panels (c) and (d) show the trace and retrace on the lateral signal. There are now contrast features in these images, in particular around flat regions, but the topography remains distinct. Finally, panel (e) shows the result of subtracting the trace from the retrace. As expected, the topographic contribution has been removed, and the contrast is wholly from the different coefficients of friction across the surface. Patches of darker, low-friction graphene [139] are clear on the higher-friction (copper-coloured) copper substrate. Panel (f) shows how the trace and retrace vary with topography, but also that the friction-loop width changes only with friction.

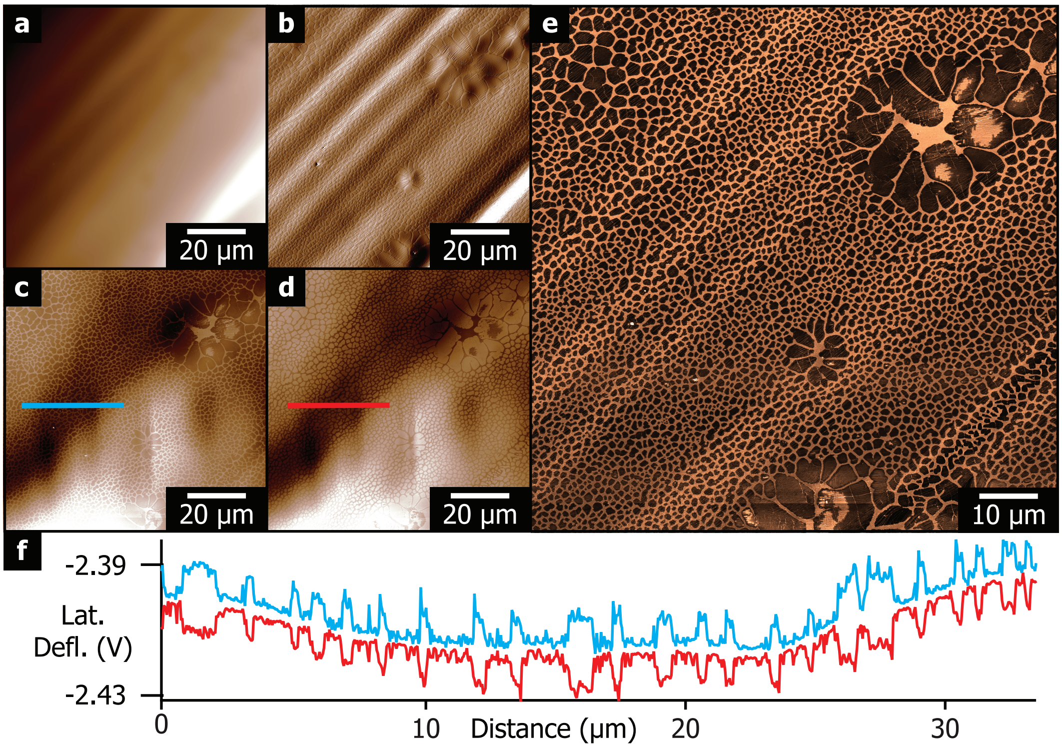

Figure 2.8: Formation of an FFM image. (a) is the height of a copper surface partially covered with graphene, (b) the deflection, (c) and (d) the trace and retrace respectively. (e) the FFM image formed from subtracting (c) and (d). (f) shows line profiles from the trace and retrace.

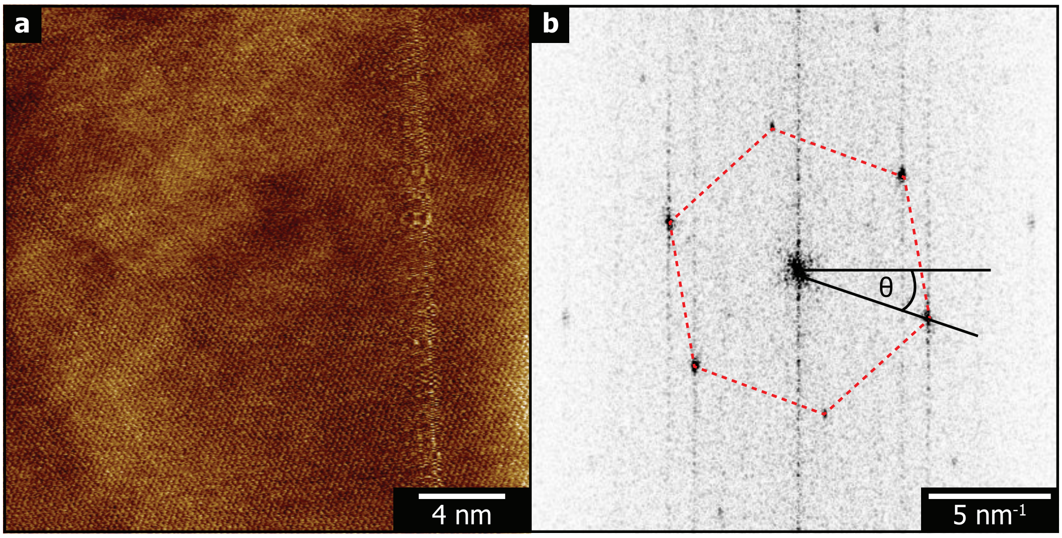

Figure 2.9: (a) lateral signal at the nanoscale. (b) FFT of (a) showing graphene orientation. Images taken by M. Phillips from Asylum Research.

Further to this imaging, the lateral forces can be probed at the nanoscale and can reveal the graphene structure. A tip sliding over the graphene surface at this scale will experience stick-slip friction at the atomic scale, where regular jumps from the tip moving over the surface lattice can be seen in the lateral signal [136]. Remarkably, this even works for large tips with multi-asperities [140] and so no special tip selection is required. Figure 2.9 shows the lateral trace signal from a 25 nm scan. The periodic features in the scan are more apparent in an FFT of the image, and this shows a hexagonal array of spots with graphene-like spacings. These can be used to find the local orientation of graphene, defined here by the angle θ.

In practice most of the work was done on an Asylum Research MFP3D, with closed loop stage, which is a key requirement when subtracting the trace from the retrace. This tips used were NSC 18 ($k = 2.8$ N/m, 75 kHz resonant frequency). For lattice orientation, an Asylum Research Cypher was used, the extra stability needed to see the lattice features. The same NSC 18 tips were used.

2.3 Surface Science Techniques

2.3.1 Ultra-high vacuum (UHV)

The earliest work on graphene overlayers (then called monolayer graphite) was conducted in a surface science setting [141], [142]. To study surfaces, techniques are generally employed in ultra-high vacuum (UHV) — that is, at pressures below 10^{-9} mbar. This is to ensure that surfaces are kept unaltered by adsorbates. Surprisingly, graphene grown on low-cost copper foils, prepared ex situ and not on an ideal single-crystal, can still be studied with these surface techniques. In this chapter, these techniques are outlined. For all of these, samples were grown ex situ and, once loaded into UHV, were treated with a one-hour anneal at around 200°C to remove surface adsorbates (unless specified differently).

2.3.2 Functionalisation and deposition

One advantage of UHV is the possibility of clean, controlled functionalisation. Here this is done with atomic species that are produced using two types of molecular crackers. First a thermal cracker, which contains a tungsten filament wrapped around a quartz gas inlet. The heated filament provides the energy required to separate the molecular bonds. Here this was using a Oxford Applied Research TC50 Thermal Gas Cracker. However, for some molecular species (like nitrogen) these sources do not provide enough energy to break the bonds. The second source creates a plasma from the gas, and the sample is placed downstream after a series of apertures that inhibit ions. For this a Tectra Gen II plasma source, operated in atomic source mode, was used.

As well as depositing atomic species, organic molecules can be deposited in UHV. The advantages are the same; it is clean and easily controllable with time. A crucible is filled with the organic molecules and is pointed towards the target substrate. When heated, molecules evaporate from the crucible and are deposited onto the substrate. The rate of deposition can be controlled by changing the temperature and quantified using a quartz crystal microbalance (QCM). Once the rate has stabilised, the substrate is inserted into the molecular beam. This process is called organic molecular beam deposition (OMBD) and is used here to deposit trimesic acid (TMA), terephthalic acid (TPA) and vanadyl-phthalocyanine (VOPc) onto graphene.

2.3.3 Low-Energy Electron Diffraction

Electron diffraction is an ideal tool for studying the crystallography of graphene, as shown in the TEM section. However, to perform electron diffraction in a TEM requires graphene to be transferred to an electron-transparent substrate. This process takes time, could damage the graphene and, ultimately, the graphene-copper registry is lost. It is possible to study electron diffraction in reflective geometry using low-energy electron diffraction (LEED). For this, no transfer is needed and so the substrate registry is available.

In a LEED setup, an electron gun points normal to the sample surface. Also normal to the surface is a fluorescent screen to detect the electrons. Between the screen and the surface are charged plates that remove any electrons that have lost energy while interacting with the sample. By screening these inelastically scattered electrons, only those satisfying diffraction conditions reach the screen. Using low-energy electrons (30–200 eV) keeps the diffraction surface specific.

2.3.4 X-ray Photoelectron Spectroscopy

The photoelectric effect is where electrons are liberated from a surface by incident light. When photons of energy $E = h\nu$ are incident on the surface they transfer energy to the material's electrons, which can escape the surface with energy

$$E_{e^-} = h\nu - BE - \phi \tag{2.15}$$

with ϕ the work function of the material and BE the binding energy. These binding energies are characteristic of the electron's environment, both of the element and the quantum numbers.

In X-ray photoelectron spectroscopy (XPS) monochromatic photons in the

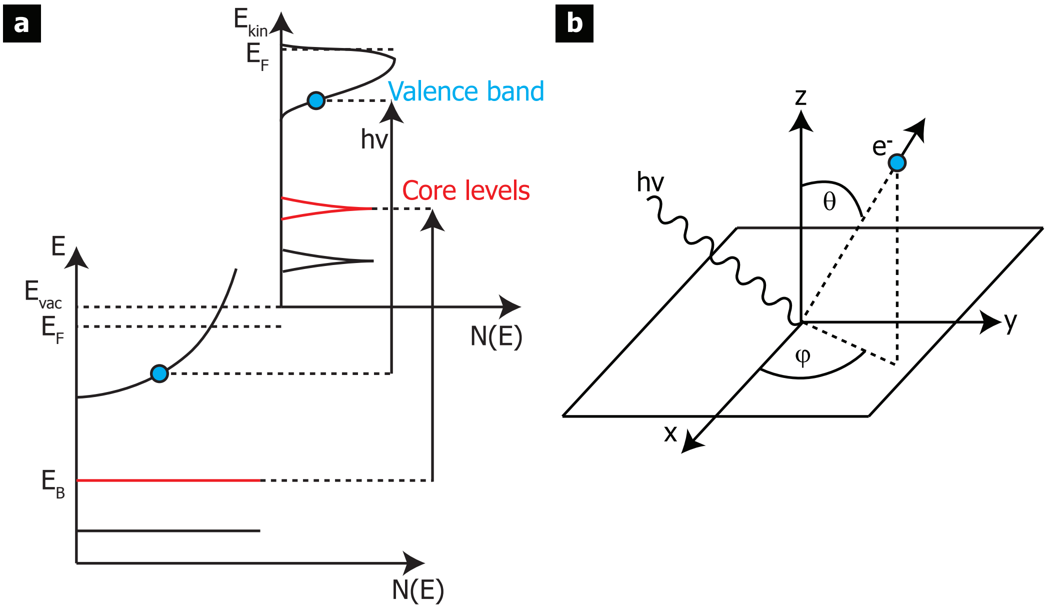

Figure 2.10: (a) energy levels in a solid, and the intensity they cause in a photoemission spectrum. (b) photoemission angles used in ARPES. Adapted from [143].

X-ray regime ($100 - 2000$ eV) are used. The liberated electrons are collected as a function of their energy by a hemispherical analyser. It is then possible to use the peak intensity (the number of electrons collected at that energy) as a relative measure of the amount of that element. A schematic of this core-level spectroscopy is shown in figure 2.10(a).

It is possible to perform XPS at synchrotron light sources. These have the advantage over lab sources of being brighter and often offer a tunable photon energy, which means the energy can be tuned to yield better interaction cross-sections. Both advantages result in a more efficient counting time. In this thesis XPS from Antares Beamline at the Soleil Synchrotron is used with a photon energy 700 eV and electrons collected with a Scienta R4000.

2.3.5 Angle-Resolved Photoemission Spectroscopy

The previous section explained how photons could liberate electrons from a surface and how the energy of these electrons could be related back to their energy in the material. However, electronic properties are determined not only by the electron energy, but also by their momentum. It is possible to find this momentum by measuring the electron's momentum outside the sample, and relating it back. This is done with angle-resolved photoemission spectroscopy (ARPES).

In ARPES, electrons are collected as a function of their energy, and of their emission angles θ and ϕ by rotating the sample (or detector) as shown in figure 2.10(b). These angles can be used to find the perpendicular and parallel components of the liberated electrons momentum, and, by the conservation of momentum and ignoring the photon's negligible momentum, give the components inside the material. The perpendicular component can be ignored in two-dimensional systems because dispersion out of the plane is negligible [143]. Then for the parallel component have

$$p_{||} = \hbar k_{||} = \sqrt{2mE_{kin}} sin\theta \tag{2.16}$$

Figure 2.11 demonstrates how ARPES can investigate the graphene band structure. Panel (a) shows the graphene Brillouin zone, with the K (and K'), Γ and M points shown. Also shown on here are the emission angles θ and ϕ. As shown in the above equation, increasing θ examines increasing k vectors. Phi rotates about the measurement surface normal, which for flat samples rotates around the centre of the Brillouin zone. In later chapters scans are referred to as, $\Gamma - K$, perpendicular to $\Gamma - K$, and a ϕ scan shown in figure 2.11(b).

For graphene on copper, a particular challenge remains in converting emission angles to k vectors, as shown in figure 2.11(c). The problem lies in that the local surface normal (the graphene plane normal, Γ) does not necessarily coincide with the measurement surface normal ($\theta = 0^o$) due to the copper topography. This means that equation (2.16) cannot always be used to convert θ into k. To measure doping and band gaps from the electronic structure, the exact momentum values around the K point are not needed, and so, in this case, the data will be presented as a function of emission angles. In the case where the momentum values are needed (for example, to measure the Fermi velocity) the θ offset will be accounted for before k-warping the data: this is most straightforwardly done for a $\Gamma - K$ scan where the Γ and K points can be identified and fixed at the known θ. The choice to

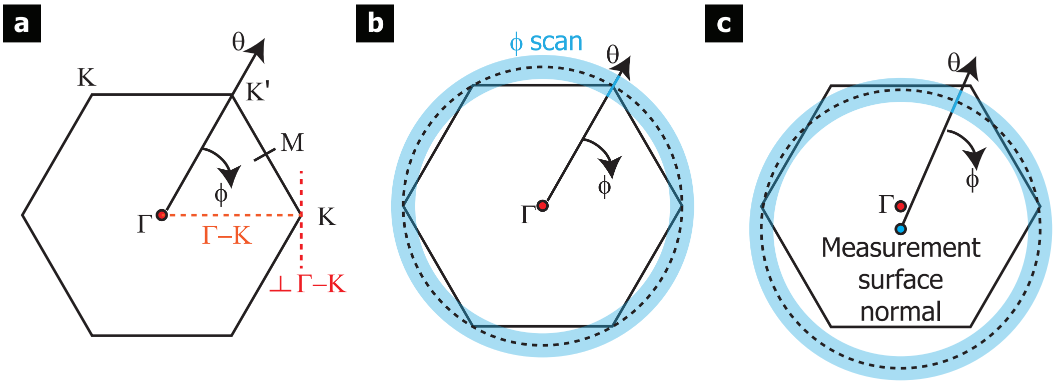

Figure 2.11: How angle-resolved photoemission can probe the graphene band structure. (a) shows the graphene Brillouin zone and real-space emission angles move through reciprocal space. The common $\Gamma - K$ scans are shown as well as the perpendicular $\Gamma - K$. (b) shows how the ϕ scan maps the Brillouin zone and (c) demonstrates how this is challenging for non-flat samples like graphene on copper.

perform k-warping is discussed in the relevant chapters.

It is also possible to perform ARPES with a photon beam that is around a micrometer in size, referred to as μARPES. This has the advantage of being able to examine an individual graphene grain, which are often of the order of micrometers across. The photon beam can be focused using a Schwarzschild objective, or by using zone plates. The disadvantage of these methods is that photon counts are reduced by focusing, and so are mostly used at synchrotron light sources.

ARPES measurements were done at Antares beamline [144] and also at the Spectromicroscopy beamline at the Elettra synchrotron in Italy. At Antares the same R4000 detector was used as for XPS but now with a photon energy of 100 eV. At Spectromicroscopy a custom-built electron detector was used with a photon energy of 74 eV.

Chapter 3

van der Waals Epitaxy in Graphene Growth on Copper

3.1 Introduction

Growing graphene on copper via chemical vapour deposition (CVD) is cheap, scalable, and produces large-area graphene of reasonable quality, and so has become the most-promising, industrially viable graphene production route for large-area electronic applications [4]. For CVD graphene, the remaining limitations lie in the quality. This is degraded by the polycrystalline nature of the graphene; the large sheet is composed of individually nucleating grains that merge and form boundaries [145], [146]. These grain boundaries fail first when stress is applied to graphene [147], and they also scatter electrons negatively impacting its electronic properties [148]. Therefore, it is essential to understand how graphene grows on copper in order to minimise these grain boundaries.

This chapter discusses evidence of an interaction between the graphene and copper during growth. This predominantly manifests itself as a graphene in-plane orientation preference relative to the copper surface orientations. On top of this, the copper substrate restructures only underneath the graphene overlayer and there is evidence that the copper crystallography influences the graphene growth rate. Despite the evidence of an epitaxial relationship between graphene and copper, the

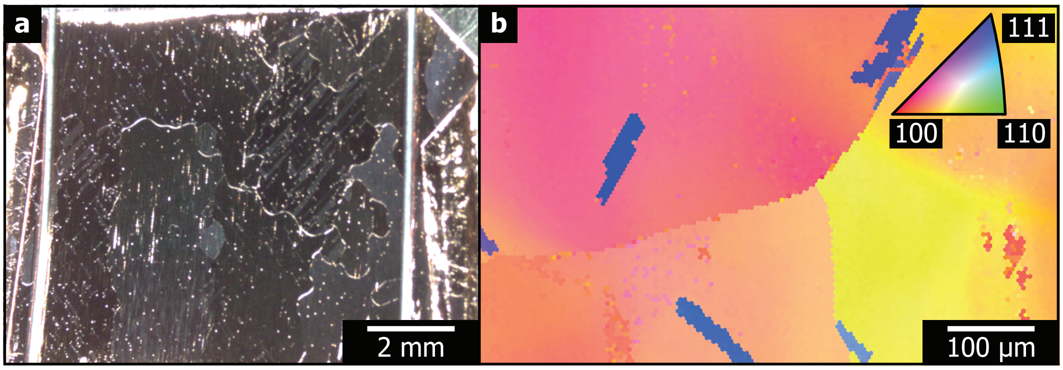

Figure 3.1: Optical (a) and EBSD (b) of copper foils after graphene growth. The copper grains are of the order of millimetres with a predominant crystallographic orientation of (100). Within these grains are microstripes of (111). These images were taken by M. Saghir.

interaction is weak: the final section presents the electronic structure of graphene on copper, which suggests the graphene is unaffected by the copper substrate. This weak, mismatch epitaxy is an example of van der Waals epitaxy in a graphene heterostructures.

3.2 Results and Discussion

3.2.1 Underlying copper structure

To have any understanding of the interaction between graphene and copper, it is first necessary to understand the underlying copper. The as-purchased foils are rough, polycrystalline copper with only small, randomly-orientated crystallographic grains. After annealing and growth the copper grains are much larger at millimeters across, as seen in the optical microscopy in figure 3.1(a). Further, EBSD can show the crystallographic orientation of these grains and a typical area is shown in 3.1(b). Different coloured pixels represent different crystallographic orientations at that point, with the pole figure colour scale shown at the top right. From this it is clear that the large grains are close to (100) with (111) microstripes embedded within.

The copper structure above is not necessarily that of all the foils treated in this way. As an example, figure 3.2 shows an optical image and EBSD map

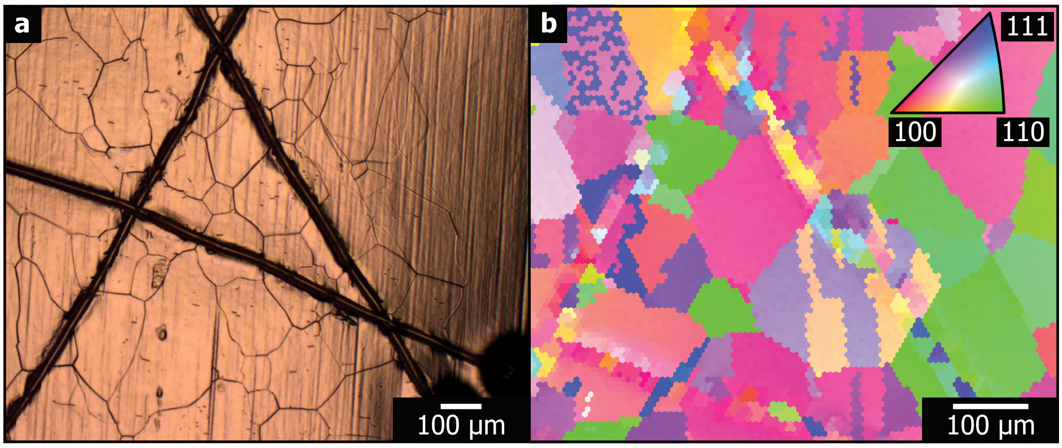

Figure 3.2: Optical (a) and EBSD (b) from the higher purity copper foils. The copper grains are smaller, and there is no dominant crystallography.

of ultrapure (99.9999% purity) copper foils after the same annealing and growth treatment. Now, the copper grain size is smaller (of the order of 100 μm) and there is no prominent crystallographic orientation. The explanation for the different copper structure for different foil types lies in how the foils are fabricated [149], and explains why different groups have observed different copper structures using similar treatments [150]. For the rest of this chapter the lower purity foils are used.

3.2.2 Interfacial restructuring under graphene

The first piece of evidence of a graphene-copper interaction comes from faceting of the copper surface only under graphene. Figure 3.3 shows a copper foil that is partially covered with graphene – achieved using a reduced growth time. Panel (a) shows friction force microscopy (FFM). There are regions of low friction (dark) on a high friction (light) background. The high friction areas show exposed copper substrate alongside the lower friction graphene. Panel (b) is the height scan of the same region. This shows a clear faceting of the copper underneath graphene. These facets are not seen on the bare copper.

This faceting is similar to that observed in other studies of graphene coated foils. Tian et al. [151] used STM to reveal 6 Å depressions spaced 5 nm apart. These were only seen under graphene coated regions, just as is seen here. Their explana-

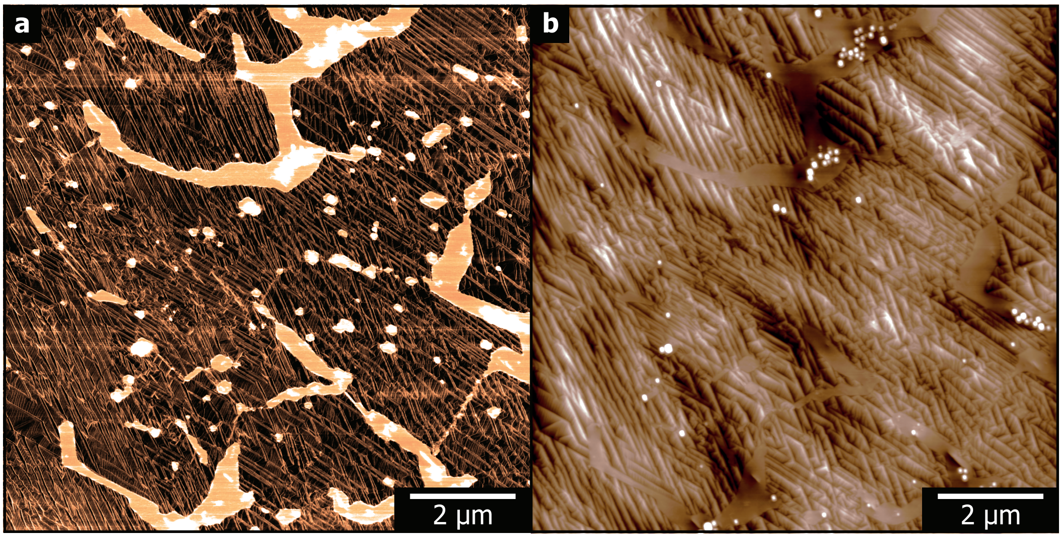

Figure 3.3: FFM (a) shows the presence of low-friction graphene, which is incomplete. Gaps in the graphene film expose the high-friction copper substrate. The height image of the same area (b) shows faceting of the copper, but only under graphene.

tion is that the restructuring is dislocation driven, with depressions introduced to relax tensile stress in the copper surface. The stress arises from the different signs on the coefficient of thermal expansion of the two materials: graphene expands on cooling, while copper contracts [39], [152].

The theory that strain relaxation would form the facets under the graphene would imply a strong interaction between the graphene and copper: the graphene would need to be strongly bound to the copper surface to deform it under the change in temperature. However, from SEM images, it is clear that wrinkles have formed in the graphene overlayer, which is evidence that the graphene can slide freely over the copper. Further, in other reports, graphene grows freely over copper step edges [153]. In section 3.2.6, evidence that the graphene is not strongly bound to the copper is shown, and so strain-induced relaxation seems unlikely.

A more likely explanation is that facets form in the copper as it attempts to minimise its surface energy. The graphene is clearly playing a role in this surface energy minimisation, and in metals especially, surface impurities inducing faceting is common [154]. Outside of the graphene covered regions, the surface is likely minimising to single-height steps, which appear much smoother [155].

The question remains of when the copper surface restructures. Recent reports have been able to examine graphene growth in-situ in an environmental SEM [156]. They were then able to directly see the copper surface faceting, not during growth, but as the copper surface was cooling. Above $750°$C, they see a smooth, graphene-coated copper surface that crystallises into pronounced facets at $600°$C. Above this temperature, the copper surface is highly mobile, and only below this does the surface solidify into facets.

3.2.3 Copper crystallography dependent growth speed

The next piece of evidence is different graphene growth speeds on different copper crystallographic surfaces. Figure 3.4 shows another partially covered graphene on copper surface. The presence of graphene is indicated in panel (a) by FFM. Panel (b) is an EBSD map of the same area, showing the end of a Cu(111) microstripe in a Cu(100) surface. From an overlay (shown in panel (c)) it is clear the coverage and island sizes are both larger on the Cu(111) than the Cu(100). The increased island size and coverage must lie with the copper crystallography because regions this close on the surface experience the same external conditions.

The currently accepted growth model for graphene on copper is that carbon species first adsorb onto the surface and decompose into carbon atoms. From here they migrate around the surface until they either attach to an existing graphene grain, nucleate their own grain, or desorb. Faster diffusion increases the probability of attaching to an existing cluster before nucleating or desorbing. This would manifest as larger graphene islands.

An increased diffusion on Cu(111) compared to Cu(100) would cause an increased island size on the Cu(111). This would be expected from calculations that show copper atoms themselves have a greater mobility on Cu(111) than Cu(100) [157]. Also, this would explain the increased number of smaller graphene islands on the Cu(100) as the lower mobility would increase the probability of nucleation.

This effect has also been reported before. Wood et al. [63] combined

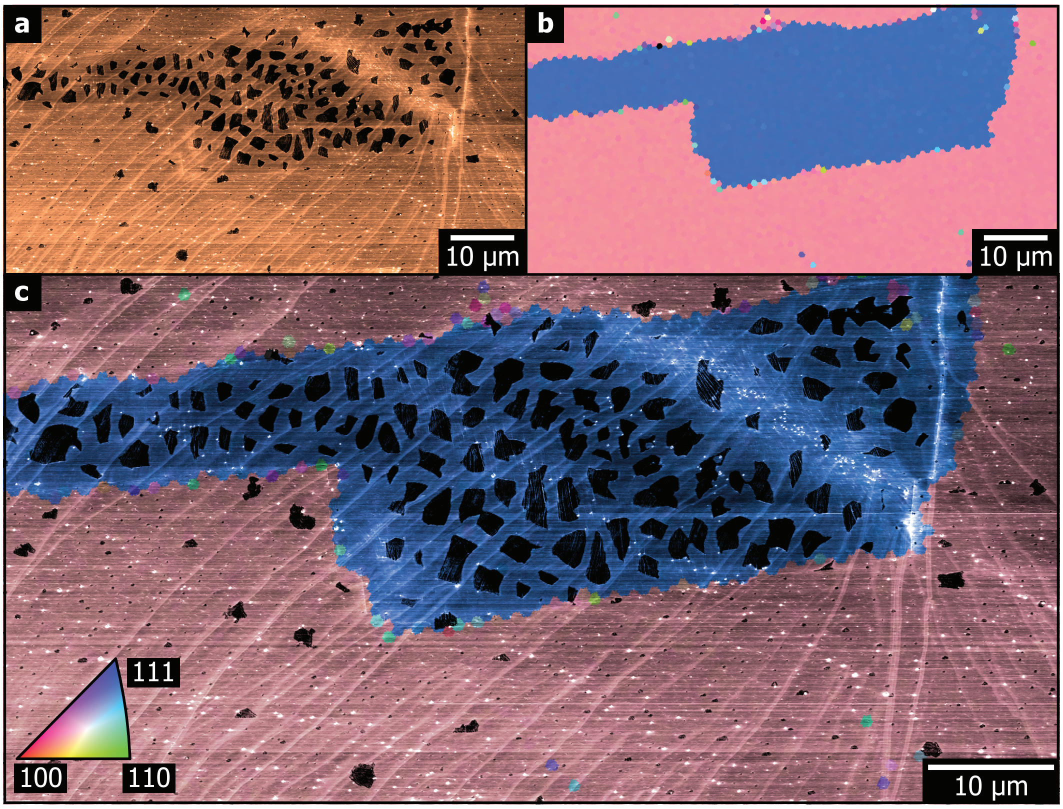

Figure 3.4: Copper crystallography dependent growth speed. (a) shows FFM of a partially covered graphene foil and (b) is EBSD, which shows the Cu(111) microstripe within Cu(100). Overlaying the two (c) shows that the graphene grain size and coverage are dependent on the crystallography.

SEM and EBSD to also note that the graphene growth rate is faster on Cu(111) than Cu(100) and again explained this with a greater mobility of carbon atoms on Cu(111) than Cu(100). Further to this, the anisotropic diffusion of carbon species for different facets affects the shape the graphene islands develop into [158]; another example of how the copper surface affects the growth.

3.2.4 Mismatch epitaxy

The final piece of evidence of a graphene-copper interaction is presented here: the preferred in-plane orientation (onwards just orientation) of graphene on copper. This orientation is examined on length scales from millimetres to micrometres.

A typical low-energy electron diffraction (LEED) pattern of a graphene coated copper foil is shown in figure 3.5(a). The spots in this diffraction pattern are labelled in (b). There is a pair (red and blue) of hexagonal spots centred on the middle of the pattern. These spots can be attributed to two orientations of graphene on a surface that is normal to the beam directions. There is also a second set of hexagonal spots (dashed) that are centred around a point on the right of the pattern. This set is from graphene that again has two orientations, but that is now on a copper surface whose normal is off the beam axis, i.e. on a tilted copper facet [58]. This copper surface causes a reflected beam spot labelled F1. Other reflection spots are also present from facets with different surface normals.

Panel (c) of figure 3.5 shows a diffraction pattern taken at a higher electron energy. The spots from graphene appear at a smaller radius, confirming they originate from diffraction. On the other hand, the facet spots (including F1) do not change. This confirms that these are reflections, where the changing wavelength has no effect. These facet reflections are consistent with the AFM results that showed a faceted copper surface.

Finally, panel (e), indexed in (f) shows the sample after a short treatment of ion-bombardment and annealing. The graphene diffraction spots are no longer visible, consistent with the removal of the graphene overlayer expected from this treatment. Instead, a square pattern is observed, consistent with diffraction from

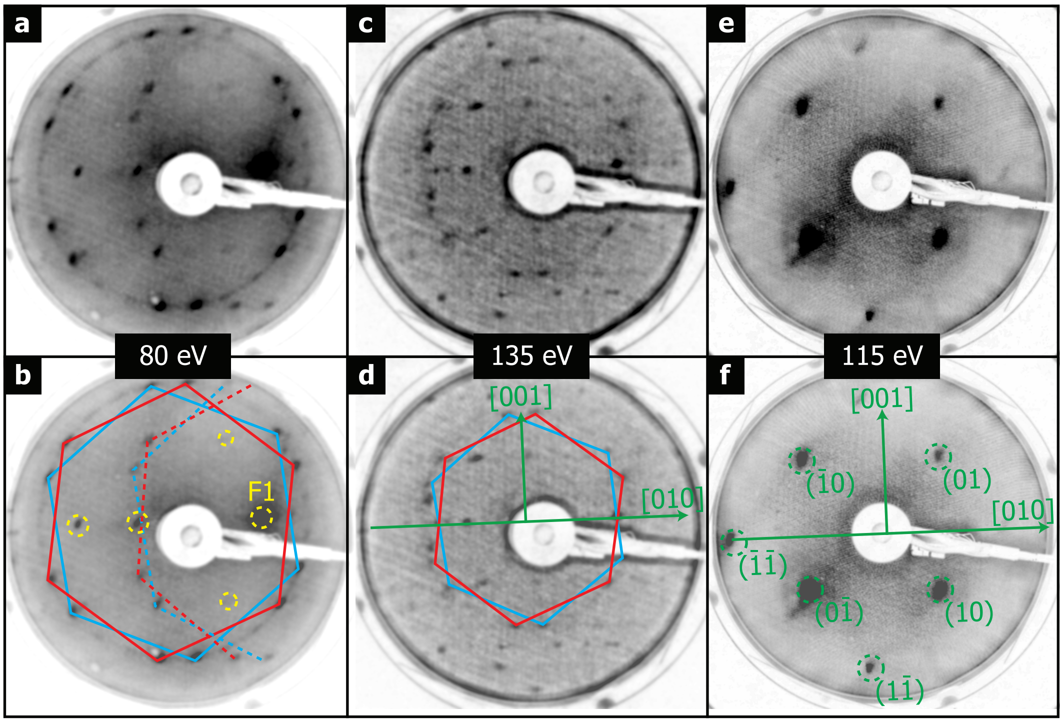

Figure 3.5: LEED from graphene on copper. (a) (indexed in (b)) shows graphene orientation preference. (b) (indexed in (d)) is at a higher energy, showing how facet reflections do not move with energy. Finally (e) (indexed in (f)) is LEED after ion-bombardment and annealing of the surface. Graphene is no longer present, and the Cu(100) pattern is indexed. LEED patterns taken by G. Bell.

the exposed Cu(100) surface. Seeing the copper diffraction spots reveals the high-symmetry directions. Because there is no sample rotation between the LEED patterns, these directions can be translated onto (b) and (d). This reveals a registry between the graphene and the copper. Specifically, the pair of graphene spots appear ±8° either side of the [001] direction. For a pair to appear either side of the [001] but not also on the [010] is unusual, and indicates some symmetry breaking of the Cu(100) square lattice. There are spots are present around the [010] but they are much weaker in intensity, meaning graphene in this orientation is not common across the surface.

The LEED presented above probes millimetre length scales, and it is possible to look at shorter length scales with electron diffraction in the TEM. Graphene is now transferred to a TEM grid as described in section 2.1. PMMA was used as a support and later removed with acetone vapours. Figure 3.6 shows a diffraction pattern from an area of graphene >50 μm across. The main feature is a pair of hexagonal spots with graphene-like spacings. This pattern is consistently seen when translating the sample, showing that this ordering is across larger length scales, agreeing with the LEED patterns. Further, radial profiles of the two diffraction patterns (LEED and TEM) are shown in panel (b) and the agreement is clear. There are two predominant graphene orientations that are separated by $(16 \pm 1)^\circ$.

3.2.5 Microscopic graphene grain structure

From the previous section it is clear that there are two preferred orientations for graphene growing on copper. The next question is about the microscopic structure of the graphene grains.

Figure 3.7 shows bright field TEM of a lacy carbon support after graphene has been transferred onto it. The support is clear as areas of darker contrast, as is the opaque diffraction aperture around the outside of the images. From this image, there is no clear evidence of the presence of graphene other than some amorphous carbon remnant from the transfer sitting over holes in the support.

To identify graphene, diffraction patterns from the left and right sides of

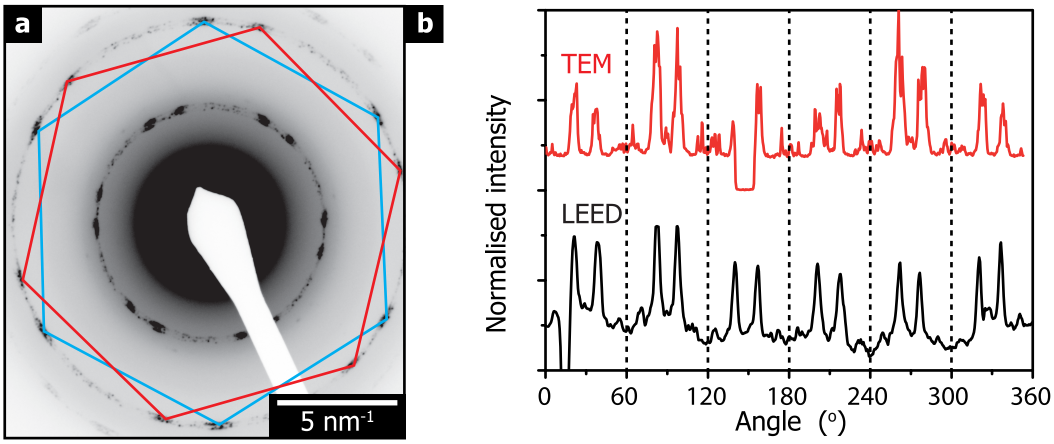

Figure 3.6: TEM diffraction from a large area. (a) shows the pattern with the same orientation preference as shown in LEED. This is highlighted in (b) with radial profiles of each diffraction pattern.

this image were taken and shown in panels (b) and (c). The selected-area electron diffraction patterns resemble the large area pattern shown in figure 3.6; they show the same hexagonal array of spots as well as the two preferred orientations, labelled on panel (b). Additionally, extra spots appearing in these patterns at graphene spacings show other orientations, but with much weaker intensity and so are a minority component.

Dark field TEM is used to visualise the graphene grain structure. Figure 3.8(a) shows a colour-composite, dark field image from the same area as that shown in figure 3.7(a). The two colours (red and blue) represent dark field images acquired with the objective aperture only allowing electrons from the areas of the diffraction pattern as indicated in figure 3.7(c). The graphene surface is mostly in two orientations, indicated here by most of the image showing red or blue. Areas that do not match either of the orientations do not contribute intensity.

While the surface shows two orientations it is not because there are only two graphene grains present, one of each orientation, or that both orientations lie on top of each other. In this area there are likely at least four separate grains, each around 2-5 μm across. The orientation of a grain can be confirmed by acquiring a SAED pattern from a smaller area within them. These are shown in panels (b) to (f).

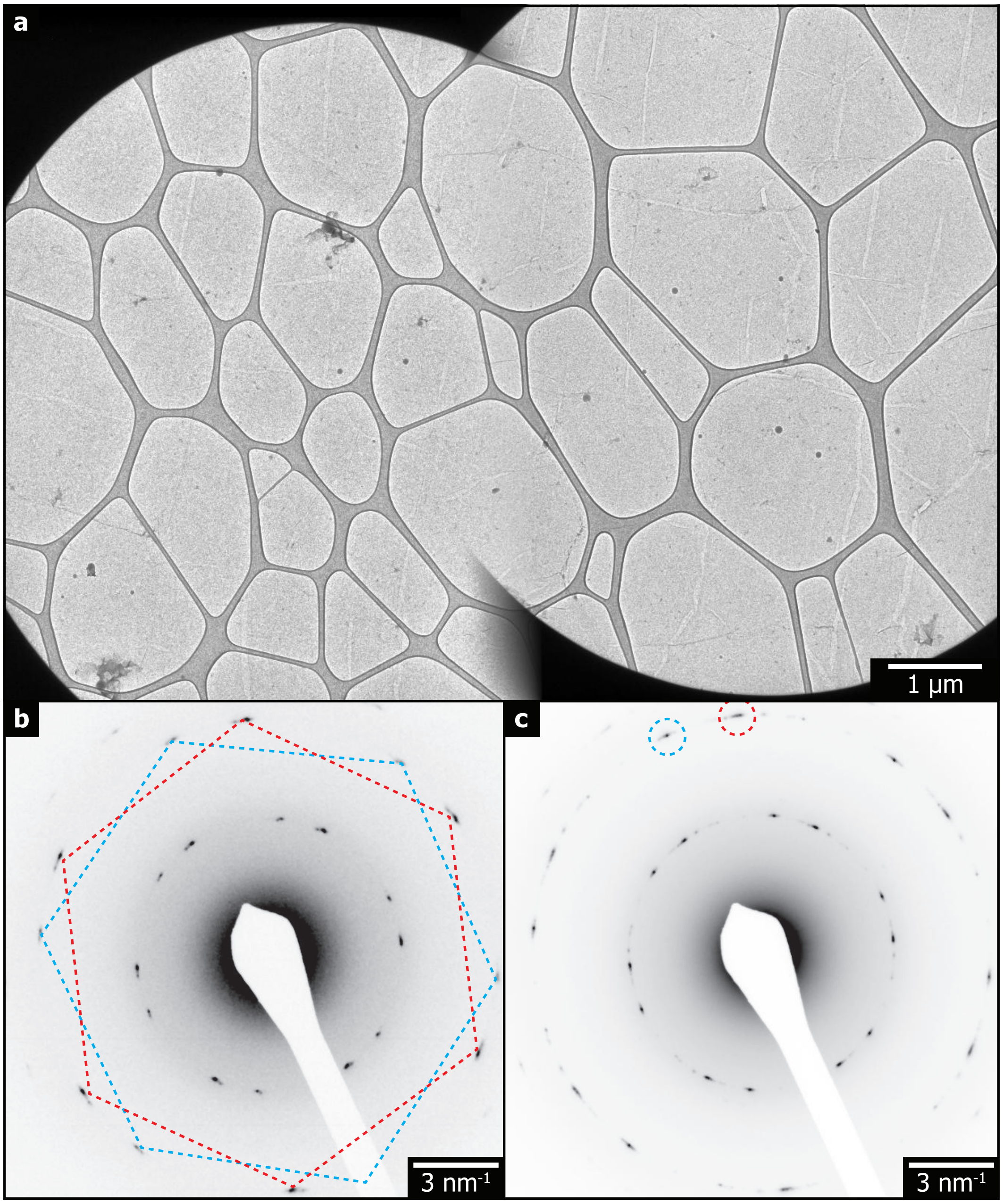

Figure 3.7: Bright field TEM of graphene. (a) shows the lacy carbon support with some transfer residue visible. (b) is a diffraction pattern from the left-hand-side of (a) and (c) the right-hand-side. These patterns also show the graphene orientation preference.

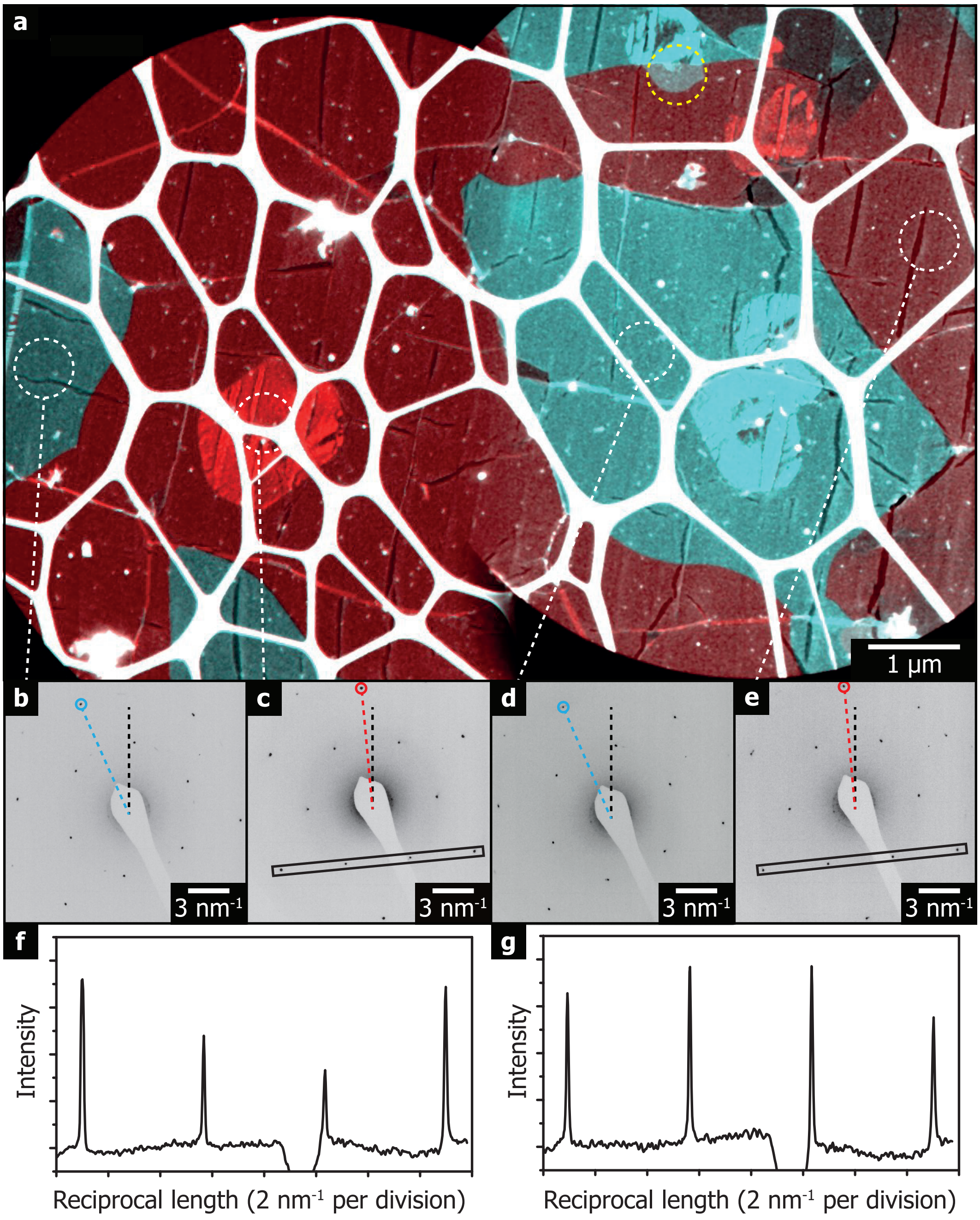

Figure 3.8: (a) shows dark field TEM of the same area shown in figure 3.7, with the graphene grain structure becoming clear. (b)-(e) show diffraction patterns within the grains confirming orientation. Finally (f) is a line profile from the bilayer region (from the box indicated in (c)), and (g) a line profile from the monolayer region (e).

The disconnected grains are assumed to have nucleated and grown independently. For them to have the same orientation suggests the underlying copper has a strong influence in determining this orientation.

The final feature of interest in these images are the patches of greater colour intensity. These correspond to bilayer graphene. This can be checked by taking SAED from the bilayer regions, shown in (f). A comparison of the outer spots (10) planes and the inner spots (01) planes is shown in (g) for bilayer and in (h) for single layer. The ratio of the inner pots to outer spot in the single layer region is ≈ 1 and for the bilayer region is ≈ 0.5. These ratio differences confirm the presence of AB-stacked bilayer. Because these dark field maps were acquired using the outer spots, bilayer regions appear with approximately 4 times the brightness [135]. There is also one region (highlighted in yellow) that shows a twisted bilayer, where the two graphene layers do not share the same orientation.

In the TEM studies, the grains can only be assumed to have nucleated independently because when the film is transferred to the grid it is already complete. It is possible to investigate the grain structure of incomplete films using FFM. Figure 3.9 shows a partially covered graphene coated copper foil. Panel (a) shows the height and (b) the friction signal. The low friction graphene grains are clearly resolved on the high friction copper surface. For panel (c), 20 nm images were acquired at regular intervals and these were used to measure the graphene orientation as described in section 2.2.5. The graphene orientation angle is then colour coded and shown on the grid; blank squares represent regions where an orientation could not be measured.

These results show two things. First, they confirm again the orientation preference of graphene on copper. This is most clearly shown with a histogram of the measured angles, shown in 3.9(e). There are two clear peaks, one at $(22 \pm 1)^\circ$ and the other at $(40 \pm 1)^\circ$; this is a separation of $(18 \pm 2)^\circ$, which is consistent with the diffraction measurements. The second point is that each graphene grain is just one orientation, the only exception being that labelled by a white arrow where two grains have presumably merged. This suggests graphene grains nucleate

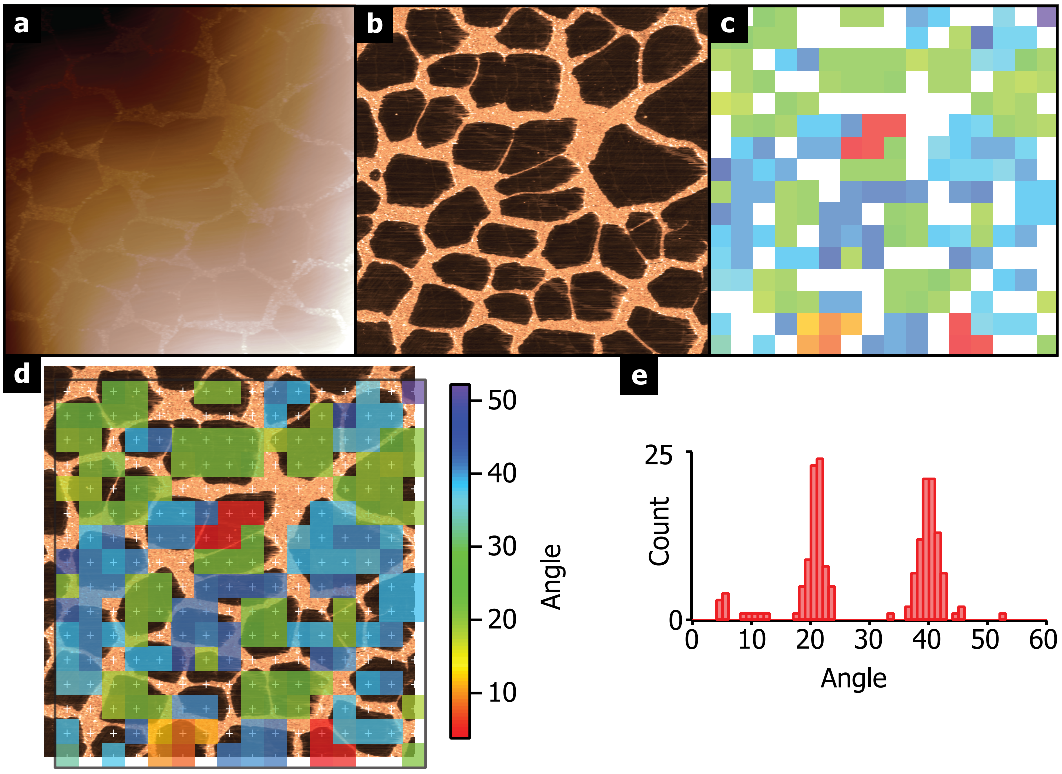

Figure 3.9: (a) shows a height image and (b) the FFM image of a partially covered graphene on copper foil. At regularly spaced points the surface orientation is measured, shown in (c), which is overlaid onto the FFM in (d). A histogram of the graphene orientation (e) shows the same orientation preference seen before. Images acquired by M. Philips, Asylum Research.

independently with their orientation and then grow and merge into a continuous sheet. This is important because there have been suggestions that the orientation preference could arise from grain boundary energy minimisation. This cannot be the case here. The isolated orientation dependence across such long ranges must be due to the copper surface.

So far the orientation preference in graphene grown on copper is clear, as is the fact that the copper plays a clear role. But the question remains as to what causes the orientation dependence. Most of the copper surface that graphene has grown on is vicinal Cu(100) with a square lattice, which is confirmed by EBSD and LEED. The graphene appears to contain two preferential orientations and these are mirrored around the [001] direction of the copper surface. However, this epitaxial arrangement cannot be from the Cu(100) surface, because the Cu(100) square lattice should cause four preferential orientations; two reflected around the [001] and another two around the symmetrically equivalent [010] direction.

The absence of the four-fold symmetry in the graphene orientation preference suggests the faceting of the copper surface plays an important role. The most dominant facet spot in the LEED (labelled F1 in figure 3.5) arises from a Cu(210) facet. In fact, most of the facet spot reflections lie on the [010] direction line and represent facets that take the general form of (n10). These (n10) facets have a rectangular unit cell and so would break the four-fold symmetry of the Cu(100) surface.

The impact the (n10) facets on the orientation dependence has been investigated elsewhere by growing graphene on single crystal Cu(110) [159]. LEED on these samples showed a striking similarity to those grown on polycrystalline copper here: the graphene again preferred two orientations, this time $\pm 5^\circ$ around the [001] direction of the rectangular Cu(110) unit cell. In this case it is clear how the mismatch epitaxy has arisen: the (11) diffraction peak of the Cu(110) surface is commensurate with the (10) diffraction peak of graphene. The second orientation then appears due to mirror symmetry of the copper surface.

The (n10) facets on the Cu(100) surface are likely responsible for the symmetry breaking that yields two preferences for the orientation. The facets only appear where graphene is present and the facets themselves could be responsible for the orientation that graphene takes. This suggests a structural feedback between the graphene and the facets.

On the other hand, as mentioned in section 3.2.2, there are in-situ experiments that suggest the facets crystallise when the copper surface cools [156]. This then complicates the idea of structural feedback between the facets and the graphene. One suggestion is that as graphene grows, it forms small (n10) facets on the surface, which in turn cause epitaxial alignment of the graphene overlayer. These small facets are not seen at high temperatures because the copper surface is so mobile. Then, as the surface cools, the copper is no longer mobile and so crystallises into the larger facets through energy minimisation. This could help explain how, although the copper surface does not appear to be faceted at higher temperatures, parts of the surface have taken the (n10) crystallography to cause the graphene-copper epitaxy.

In summary, graphene grown on copper contains predominantly two in-plane orientations. These are mirrored $\pm 8^\circ$ around the Cu[001] direction, with the symmetry breaking likely arising from the formation of (n10) facets. The next section examines the electronic structure of graphene that is grown on copper in an attempt to understand the strength of the graphene-copper interaction.

3.2.6 Graphene electronic structure

It is clear from the evidence presented in the previous section that there is an interaction between graphene and the copper surface. However, there is also evidence that the interaction is weak. For example, graphene grows as a continuous sheet over copper grain boundaries. To gain some insight into the strength of the graphene-copper interaction, ARPES is used to examine the electronic structure of graphene and to see if it is affected by the underlying copper.

Figure 3.10 shows ARPES from a graphene coated copper foil. The photon beam spot size is >100 μm, and so the result is the average of hundreds of graphene grains (similar to the TEM in figure 3.6). Panel (a) shows a constant energy slice at $E - E_F = -100$ meV with the x-y axes representing the emission angles. This shows a pair of spots, separated by 16°, that are repeated every 60°, consistent with the hexagonal array of the point-like Fermi surface expected for the K and K' points in the Brillouin zone. It is possible to take another slice at a lower energy, which is shown in panel (b) with $E - E_F = -600$ meV. Where there were spots before, there are now curves. These represent slices through the Dirac cone, confirming the presence of graphene. The curves are not closed loops, with intensity missing from the far side of the K point i.e. in the second Brillouin zone. This is caused by destructive interference between photoemitted electrons from the two graphene sublattices [160]. Finally, panel (c) shows cuts through the Dirac cones as indicated

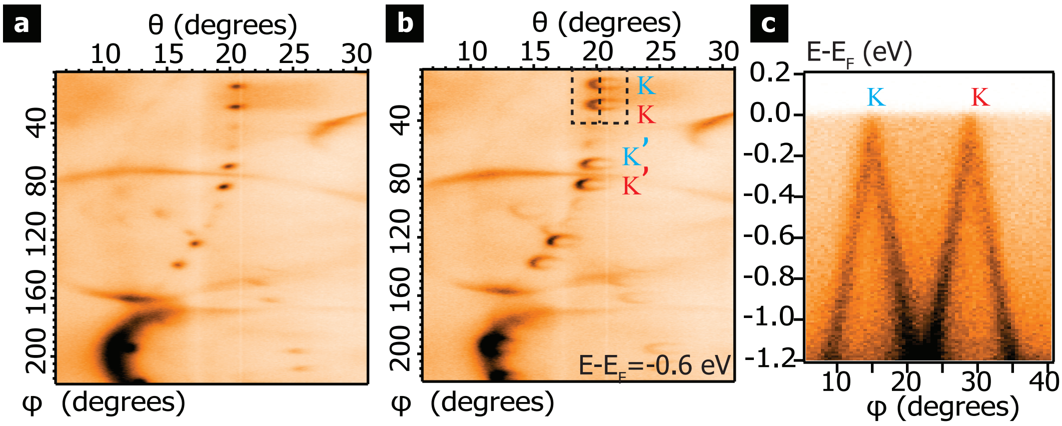

Figure 3.10: ARPES from graphene on copper. (a) shows a constant energy surface around the Fermi energy for graphene on copper, and (b) 0.6 meV below the Fermi energy. (c) is a constant $\theta = 20^o$ slice showing both Dirac cones, one for each orientation of graphene.

by dashed lines in (b), showing the pristine graphene band structure. The results here show again the orientation preference of graphene on copper. They also show the high electronic quality of the graphene, indicated by the sharpness of the bands.

To examine an individual graphene domain, μARPES can be used as described in section 2.3.5. A $\Gamma - K$ scan from within a single graphene domain is shown in figure 3.11. This is done by orienting ϕ in a $\Gamma - K$ direction, and then collecting spectra as a function of θ as described in section 2.3.5. The data have been k-warped with confidence using the features at Γ and K as reference points. The principal band of intensity between 2 and 4 eV are from the copper d states from the underlying foil. However, above and below these it is possible to see intensity from the graphene π band. Overlaying a tight binding model (equation 1.4) onto the figure shows a consistent match with the intensity, suggesting undoped, high-electronic-quality graphene, with hopping parameter $t = 3.3$ eV.

Further, by cutting perpendicular to the $\Gamma - K$ direction, it is possible to visualise both branches of the Dirac cone to verify the crossing. This is shown in figure 3.11(b). Again, the intensity is fit with a graphene tight-binding model. The branches meet at the Fermi level, which suggests no band gap and no charge transfer. It is, then possible to calculate the Fermi velocity (v_F) using equation 1.6 [7].

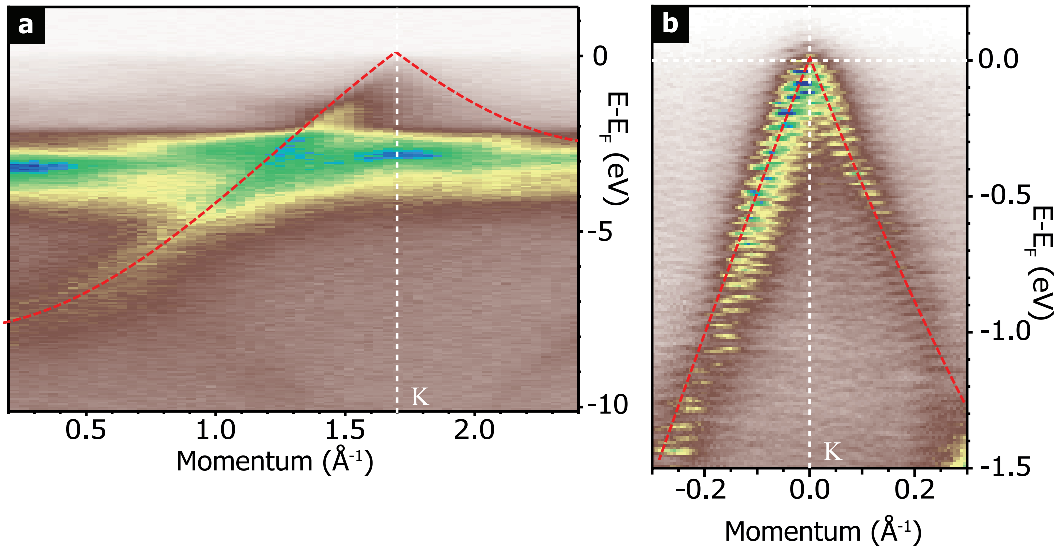

Figure 3.11: μARPES $\Gamma - K$ scan (a) of graphene on copper and (b) shows a cut perpendicular to this in reciprocal space so both branches of the Dirac cone are visible. A tight binding model calculation (red dash) and the K point (white dash) are indicated on both scans.

This gives $v_F = (3.3 \pm 0.3) \times 10^6$ ms^{-1}, which is consistent with other reports [7].

These results suggest that the graphene band structure is unchanged by the copper substrate and this suggests that if they do interact, it must be only be weakly. For no charge transfer from the metal is unexpected and contrary to other reports. For graphene on single crystal Cu(100) and Cu(111), both substrates interacted with the graphene and shifted the Fermi level up by ≈ 350 meV [161]. As well as this, they found a band gap of ≈ 250 meV.

To examine the lack of charge transfer seen for graphene here, the effect of pre-annealing was investigated, this being one of the main differences between what is reported here compared to elsewhere. This has a surprising effect on the graphene band structure as shown in figure 3.12. Panel (a) shows μARPES around the Fermi level of a graphene coated copper foil annealed to $200°$C. This shows a single, sharp line that continues uninterrupted to the Fermi level. This represents the available branch (the other being removed due to destructive interference) of a graphene Dirac cone. Panel (b) shows a graphene coated foil annealed to $500°$C. There is still a sharp line that reaches the Fermi level, but now there is an interruption around

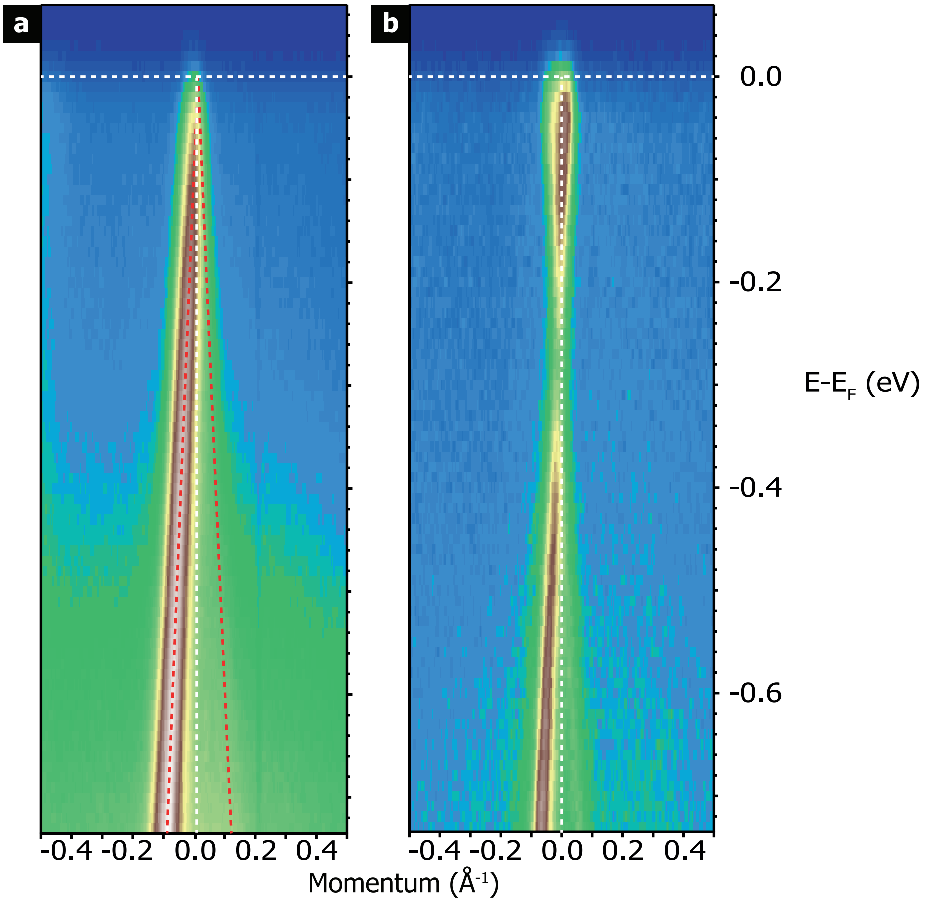

Figure 3.12: μARPES from 200°C (a) and 500°C (b) annealed graphene on copper. At lower temperatures, an undoped, pristine graphene band structure is observed. At higher temperatures, there is 350 meV n-doping and a band gap has opened.

350 meV. This shows two important things. First, the interruption indicates the opening of a band gap. By fitting the intensity above and below the break, a gap of 100 meV is measured. Second, the position of the break shows there is charge transfer to the graphene. Using the same fitting of the intensity, the centre of the gap is measured at 350 meV below the Fermi energy. This corresponds to electron (or n-) doping of the graphene by 350 meV. There is no noticeable change in the sharpness of the bands indicating that the graphene is still of a high quality.

Why charge transfer has occurred, and why a gap has opened up, only after a higher temperature anneal is not fully understood. One explanation is the removal of oxygen intercalated between graphene and copper, as proposed by Blume et al.

[162]. They used XPS to find a relationship between air annealing, and the binding energy of the C1s peak. The C1s peak shifts to a higher binding energy by 350 meV after air-exposed graphene is annealed in UHV. After exposure to air (and loaded again, but not annealed) this peak had returned to the lower binding energy. They linked these changes to changes in the O1s during the same treatment, and found that it was most likely linked to the removal of oxygen at high temperatures. This oxygen is assumed to be intercalated between the graphene and the copper.

The graphene on copper grown here does contain oxygen, as seen in XPS of these foils (discussed further in section 4.2.2). After annealing at $500°$C, the oxygen content (relative to carbon) is seen to decrease from (3.3 ± 0.6) % to (1.3 ± 0.3) %. This removal of oxygen could then enable coupling between the graphene and the copper, and then allow charge to transfer.

Also reported is growth of graphene on oxidised copper surfaces [163]. Here they found that graphene grown on an oxidised copper substrate was effectively decoupled from the copper surface, by observing a free-standing graphene band structure. In contrast, on Cu(111) an interaction was clear, with n-type doping of 380 meV. This further suggests that oxygen intercalation can decouple the graphene from the substrate.

One key difference between graphene grown on an oxidised copper surface and graphene grown here is the ordering of the oxygen on the copper. On the oxidised copper surface, the oxygen caused a reconstruction of the copper oxide surface [163]. This ordering showed clearly on LEED patterns on the surface and these reconstructions have been seen before when oxidising copper [164]. However, this ordering is not apparent here, suggesting that oxygen is not restructuring the surfaces when intercalated after growth.

In summary, the ARPES measurements reveal that, when treated to a $200°$C anneal, the graphene on copper band structure is unchanged by the presence of the copper; there is no electron transfer and no state-mixing that opens a band gap. One explanation for this is decoupling of the graphene by intercalated oxygen. For this to occur shows that the graphene layer is not strongly bonded to the copper.

The interaction seen throughout this chapter, therefore, must be a weak one.

3.3 Conclusions

CVD-graphene's degradation of properties due to its polycrystalline nature provides a limit on CVD as the ideal production route. This chapter outlined evidence of an interaction between the graphene and copper surface during the CVD growth. First, structural feedback caused faceting of the copper surface only underneath graphene. Second, partially covered films demonstrated different island sizes on different copper crystallographic orientation, suggesting a faster growth rate on Cu(111) than Cu(100). Finally, evidence of a preferred orientation of graphene was shown with separately nucleating grains forming with an orientation of $\pm 8^\circ$ around the copper [001] direction, which was influenced by the faceting of the copper surface.

The final part of the chapter discussed the electronic structure of graphene on copper, and gave evidence that the graphene is decoupled from the copper surface by observing no charge transfer and no mixing of the electronic states. This suggests that, despite a clear interaction between the graphene and the copper, it must be a weak one; the graphene is not bonded to the copper surface. This type of growth has been termed weak mismatch epitaxy, and is an example of van der Waals epitaxy in a graphene heterostructures.

These affects open up the possibility of modifying the copper surface as a route to controlling graphene growth. In particular, controlling the epitaxy would provide a direct route to controlling the graphene grain structure, and a way of improving the electronic quality. Here, however, this weak interaction yields graphene that would be a model system for studying graphene heterostructures, and this is the focus of the next chapters.

Chapter 4

Effect of oxygen and nitrogen functionalisation on the physical and electronic structure of graphene.

4.1 Introduction

In the previous chapter van der Waals epitaxy was demonstrated for pristine graphene grown on copper. However, graphene that is covalently functionalised is becoming increasingly interesting for two reasons [165]. First, it provides a route to altering graphene's properties. For example, nitrogen dopants in graphene result in an increase in electrolytic reactivity by producing activated regions that can catalyse oxygen reduction reactions, or that can anchor metal nanoparticles [74], [166]–[168]. The second reason is that graphene is unavoidably functionalised in some synthesis routes. The most common example is graphene oxide (GO), where oxygen groups are attached to the graphene surface to enable exfoliation and improve solubility [65]. To fully utilise chemically modified graphenes it will be important to understand how this functionalisation affects graphene.

For van der Waals epitaxy, chemical functionalisation could affect how graphene interacts. Chemical functionalisation will change graphene from the smooth, homogeneous surface to one where there are active sites. These active sites will change the focus from van der Waals forces when interacting with other species. Understanding how the functionalisation proceeds will be the first step to understanding how this different surface could affect van der Waals epitaxy.

Most attempts to study covalent functionalisation have focused on wet chemical or bulk methods: the GO synthesis method is all wet chemistry and nitrogen functionalisation is commonly achieved by including nitrogen containing compounds during CVD [75]. These methods often result in materials that are complex and so isolating individual effects is challenging. On top of this only coarse control of the stoichiometry is available.

On the other hand, greater control is available in gas phase reactions. In particular, functionalisation in UHV with atomic sources provides a clean and controlled route to covalently add atomic species [169]. Varying the exposure time controls the amount of functionalisation and, unlike high-energy ions in plasma treatments, atomic species do not heavily damage the surface.

In this chapter the graphene on copper model system demonstrated in chapter 3 is functionalised with atomic oxygen and nitrogen in UHV in order to understand how these atomic species alter graphene. The chemical and physical changes are examined with a combination of XPS and aberration-corrected TEM (acTEM). Then, the effect these changes have on the electronic structure are examined by ARPES. The final part of this chapter looks at the reversibility of the functionalisation.

For dosing with atomic species, two different sources were used, as described in section 2.3.2. All the dosing in this chapter was done using the Tectra Gen II plasma source (25 mA plasma current, gas pressure 6×10^{-5} mbar), except for the TEM results in figure 4.13, where a Oxford Applied Research TC50 Thermal Gas Cracker was used with 50 W power and a gas pressure of 6×10^{-6} mbar.

4.2 Results and Discussion

4.2.1 The graphene on copper model system

CVD-grown graphene displays an orientation preference across the copper surface, and its electronic structure is unchanged by the underlying copper. These combine to make it an ideal material for studying heterostructures. This principally lies in the ability to acquire high quality ARPES of a pristine graphene band structure. On top of that, the epitaxial growth means a macroscopic photon beam can be used to resolve discrete K points and not a blurred average of different orientations. This then eliminates the challenge of using a microscopic photon beam.

Another advantage of CVD grown graphene is the possibility of transferring the graphene to a TEM support. Figure 4.1 shows acTEM of graphene after transfer to a TEM grid. The hexagonal lattice of graphene is clear in (a) and in an FFT of this area, (b). Fourier filtering — where regions of the FFT matching a specific periodicity are masked to remove or emphasise information at those frequencies — is used to remove the contribution of the graphene lattice from the image, shown in (c). In the pristine graphene here, very little detail remains, indicating no defects in the graphene lattice. The only remaining contrast at the edge of the image is residue polymer from the transfer.

4.2.2 Epoxy formation on oxygen functionalisation

First, the chemical changes to the graphene after exposure to atomic oxygen are examined. CVD-grown graphene on copper foils were loaded into UHV and annealed at $200°$C for 1 hour. After taking measurements on the clean graphene, they were sequentially dosed with atomic species and measured again.

Figure 4.2 shows XPS of a graphene on copper foil after sequential dosing of 10 s, a further 20 s, and finally a further 30 s to give 60 s total dose. Panel (a) shows the C1s region. For pristine graphene, the spectrum is fit with a single Doniac-Sunjic peak at 284.3 ± 0.1 eV, which is characteristic of high-quality graphene [170]–[173]. Upon dosing, another peak at 286.0 ± 0.1 eV becomes apparent, which can be fit

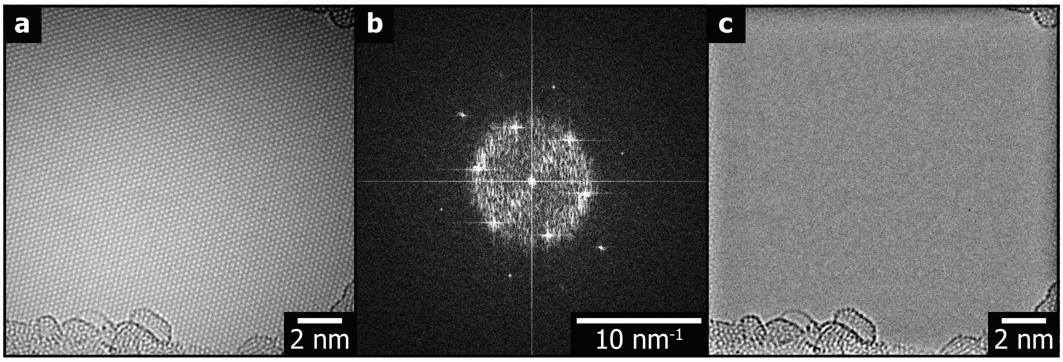

Figure 4.1: acTEM of pristine graphene. (a) shows TEM of a pristine graphene region and (b) the FFT of this region, showing the graphene hexagonal lattice. The lattice features can be removed by masking information from the FFT at the spatial frequencies of graphene, and then performing an inverse FFT (shown in (c)); here all that remains is the polymer residue from the transfer.

with a single Gaussian-Lorentzian convolution that increases with dose time. This peak can be assigned to carbon in an epoxide environment [169], [174]. The ratio of the areas of the two peaks gives a ratio of the amount of carbon that is in epoxide environment relative to the amount in a pristine graphene environment. The result is shown in panel (b). Here the amount of epoxide carbon increases almost linearly with dose time, to a maximum of approximately 10 % epoxide carbon after 60 s dosing. This corresponds to roughly 5 at% of epoxide to graphitic carbon — each epoxide group results in two carbons in epoxide environments, one at each end of the bridge. Finally, panel (c) shows the structure of an epoxide group attached to a graphene surface.

The chemical changes can also be followed by observing the O1s region. This, however, is complicated by the presence of oxygen on the surface before dosing. Figure 4.3(a) shows the O1s region of graphene on copper foil after the same sequential dosing. For the pristine sample, the majority of the intensity is in a peak at 529.9 ± 0.1 eV, assigned to oxygen associated with copper [162]. Oxidised copper could arise from exposed regions of the sample; the graphene can contain some cracks and this bare copper is certain to oxidise. By analysing the contrast in SEM images, it is possible to estimate that 1-2 % of the copper surface is exposed. There is also the possibility of oxygen that has intercalated under graphene contribut-

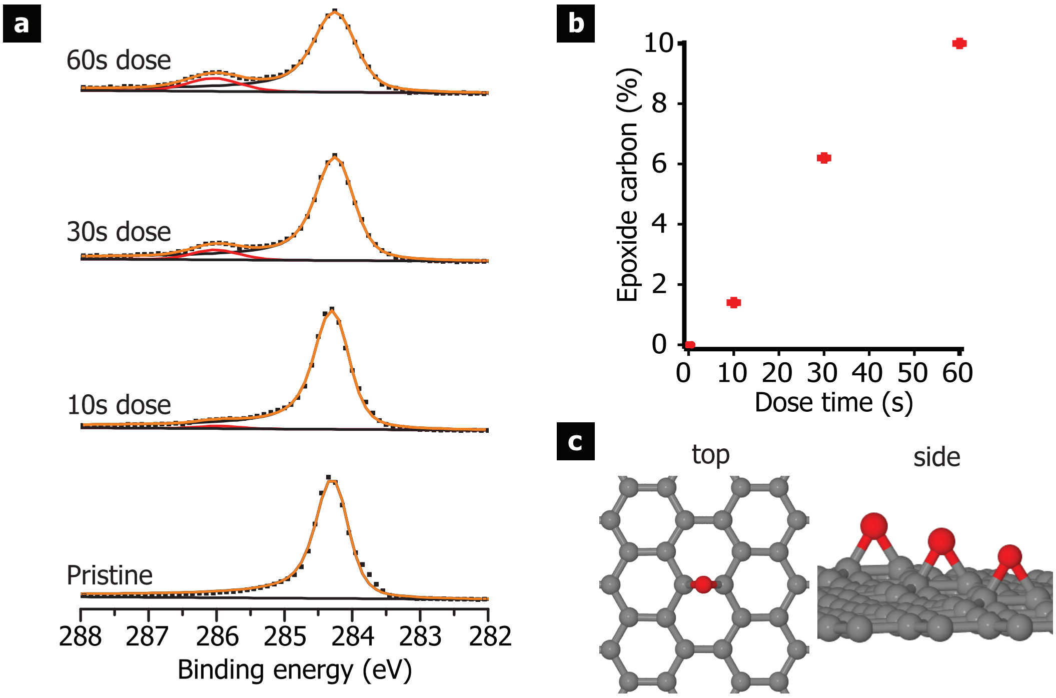

Figure 4.2: (a) shows changes in the C1s upon oxygen fuctionalisation. On dosing the single peak for pristine graphene is combined with a growing peak at higher binding energy. The ratio of these two peaks is shown in (b) and is identified as epoxide groups, shown schematically in (c). Structural models generated by P. Brommer.

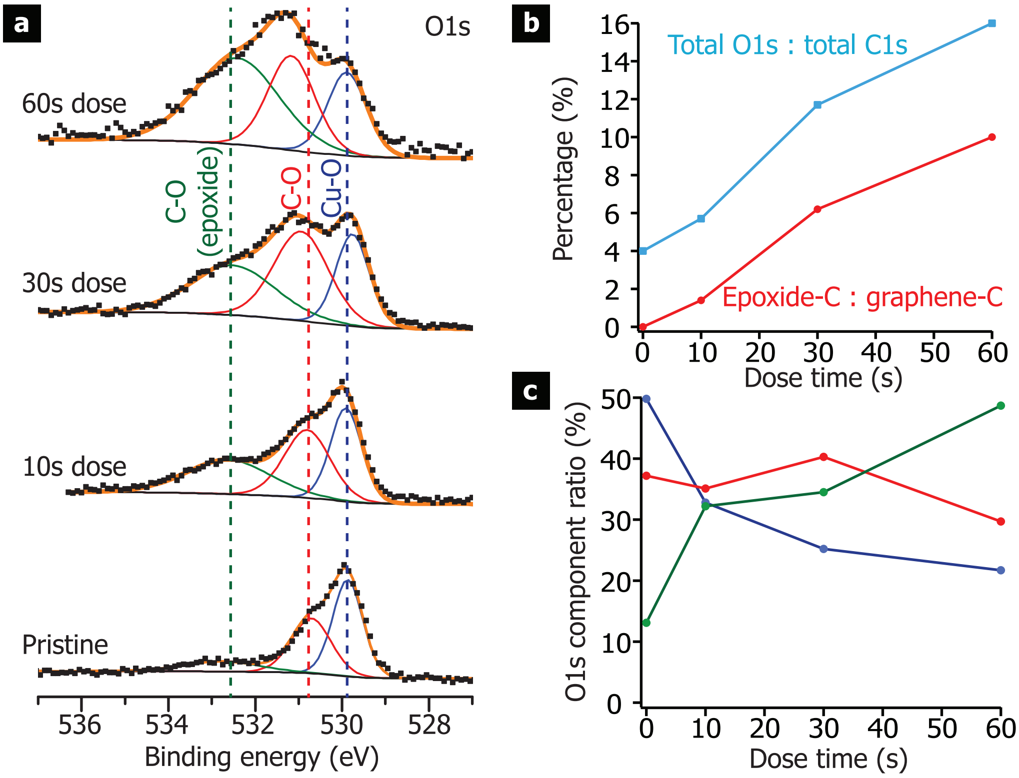

Figure 4.3: (a) shows the changes to the O1s on dosing with atomic oxygen. The changes are complicated by oxygen's presence for pristine graphene on copper. (b) shows the ratios of total O1s : total C1s and epoxide-C : graphene C increasing together, suggesting the extra oxygen is in the epoxide environment. (c) shows how the individual O1s components change. The green epoxide environment is the only component to increase consistently.

ing here. The other peaks, at higher binding energy, are often assigned to carbon bonded to oxygen environments. However, there is no evidence that this is bonded to graphene, as this would have been visible in the C1s region. This oxygen could be within small amounts of adventitious carbon [175] that has not been removed from the surface by cleaning.

Upon exposure, the most significant change is with the peak at 532.8 eV, which is at an energy often associated to oxygen in epoxide environments [176]. As well as this, there is also an increase in the peak at 530.7 eV, associated with carbon bonded to oxygen in other environments, including C=O. However, there is no evidence of C=O in the C1s (C=O should appear at 287.8 eV [176]). Panel

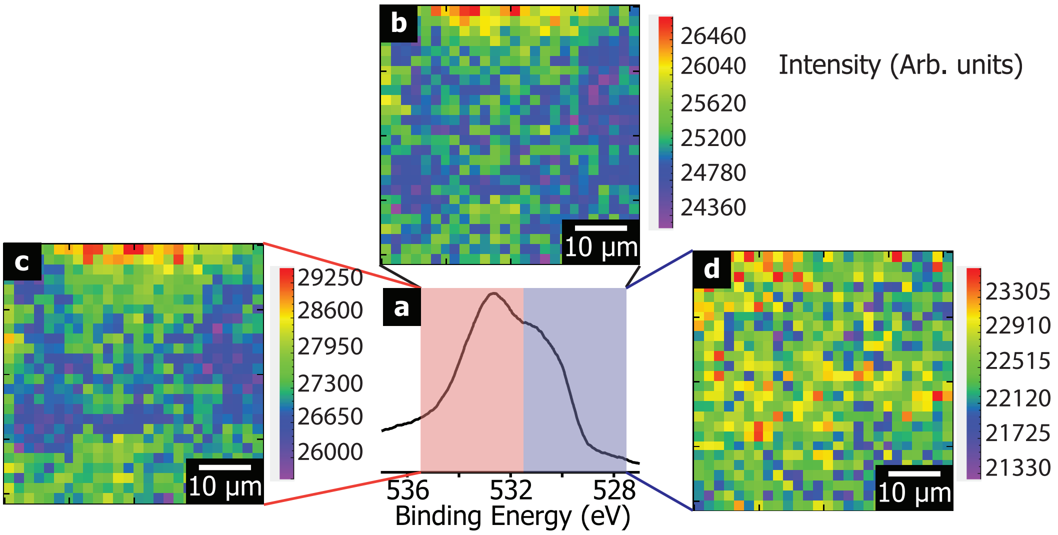

Figure 4.4: Scanning photoemission microscopy of graphene. (a) is the average O1s spectrum from this region. Forming a map by integrating the total spectrum is shown in (b); from the red region (mostly epoxide) in (c); and the blue region (mostly Cu-O and C-O from before dosing) in (d). The lack of structure in the images shows the uniformity of the oxygen functionalisation.

(b) shows how the ratio of total O1s to total C1s changes with dosing, along with the ratio of epoxide-C to graphene-C measured from the C1s. The comparable rate of change suggests a strong link between oxygen content and epoxide formation. Finally, panel (d) shows the ratio of the O1s components. The only one to increase consistently is the component at 532.8 eV — the epoxide environment. Combined, XPS from the C1s and O1s regions strongly suggest that the dominant effect when dosing with atomic oxygen is the formation of epoxide groups on the graphene surface.

The uniformity of the oxygen on the graphene on copper surface was examined with scanning photoemission microscopy (SPEM). In SPEM, the photon beam spot is focused to <1 μm, and spectra acquired while it is rastered across the surface by moving the sample. In this case, O1s spectra were taken at each point, integrated over the indicated regions and shown as maps in figure 4.4. These maps show no strong contrast features, suggesting that the epoxide groups are distributed uniformly across the graphene surface, consistent with previous reports [169].

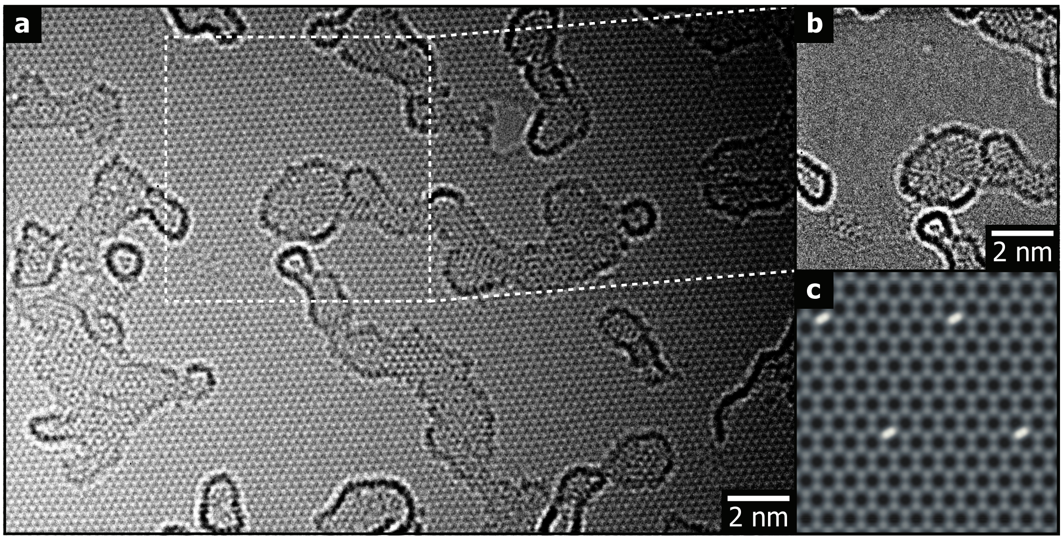

Figure 4.5: TEM of graphene dosed with 30 s of atomic oxygen. (a) shows the graphene lattice, and (b) the region in boxed in white with the lattice filtered. (c) is a simulation of an epoxide group.

acTEM was used to observe the structural changes in the graphene upon atomic oxygen dosing. Graphene was transferred to TEM grids before dosing to ensure no changes were caused by the transfer. A graphene coated TEM grid was dosed with 30 s atomic oxygen and the result is shown in figure 4.5. The graphene lattice is visible, as is the polymer residue. The surface is predominantly clear of defects except in the highlighted region. The filtered image is shown in (b), where this feature is much clearer. To help interpret this feature, an exit-wave simulation of four epoxide groups on a graphene surface is shown in (c). There is a close agreement between the two, suggesting that this could be an epoxide on the graphene surface. These features were not seen in most parts of the sample, resulting in a coverage lower than expected from the XPS. This is probably related to the mobility of the epoxide group under the electron beam, because it is so weakly bound to the graphene surface. This is discussed further in section 4.2.5.

4.2.3 Multi-environment nitrogen functionalisation

This next section looks at the changes in chemical and physical structure for dosing graphene with atomic nitrogen. Figure 4.6 shows the XPS for graphene dosed with

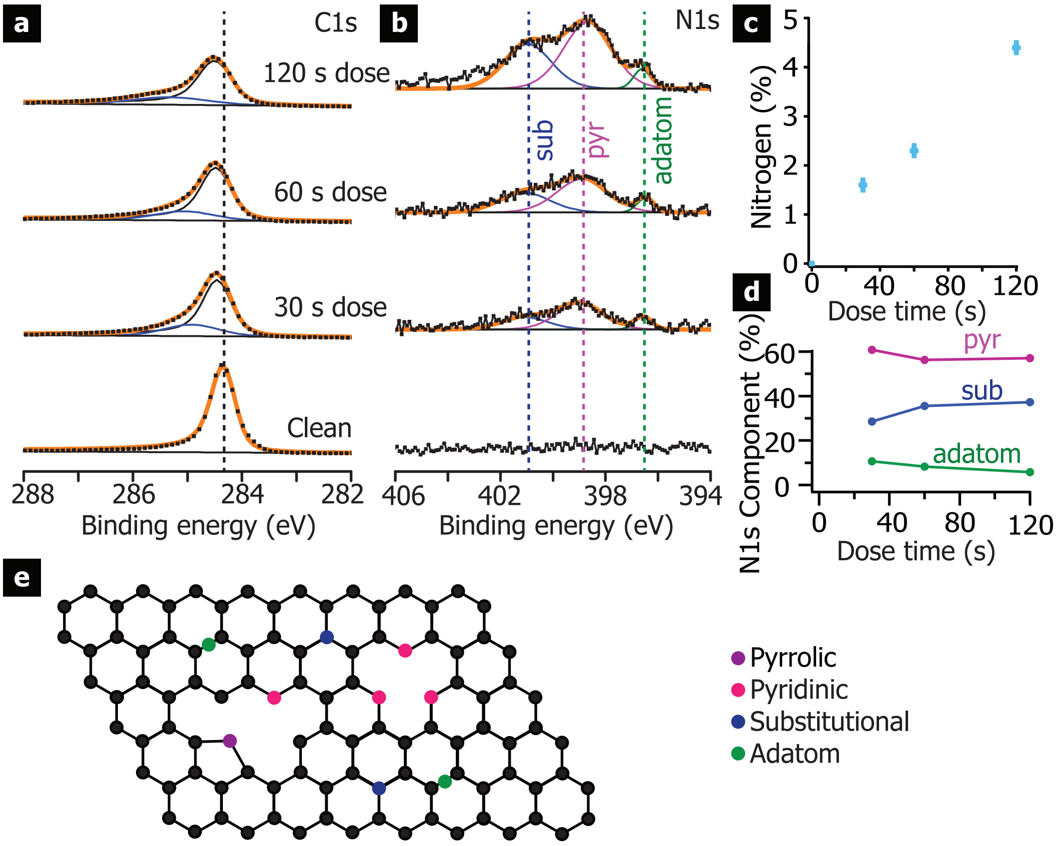

Figure 4.6: (a) is the C1s XPS region during dosing. Accompanying the graphene peak is another peak at higher binding energy, consistent with nitrogen-bonded carbon. The broadness indicates a range of environments. These are made clearer in the N1s XPS region in (b), with substitutional (blue), pyrrolic/pyridinic (pink) and adatom (green) nitrogen environments. The amount of nitrogen after each dose is shown in (c) and how the relative environments change is shown in (d).

atomic nitrogen for 30 s, a further 30 s, and finally a further 60 s to give a total dose of 120 s. Panel (a) shows the C1s region. As before, the pristine graphene is fit by a single Doniac-Sunjic peak at 284.4 ± 0.1 eV. Upon dosing, the spectra are no longer adequately fit by a single Doniac-Sunjic peak, but the increased intensity at higher binding energy can be accounted for by an extra peak. This peak increases in intensity, and broadens, with increasing dose. The graphene peak also broadens. This suggests that, unlike atomic oxygen, there is no single environment that the nitrogen belongs to, but a range of different environments. The region where the extra peak appears (285 eV) is consistent with carbon bonded to nitrogen [177].

Reference	Binding energy (eV)	
	Pyridinic	Pyrrolic
[178]	398.2	400.1
[179]	398.8	399.6
[180]	396.3	398.8
[181]	398.5 – 399	n/a
[166]	399	400
[74]	398.1 – 399.3	399.8 – 401.2

Table 4.1: Assignments of pyridinic and pyrrolic groups in the N1s region from the literature.

A clearer picture can be gained from the N1s region shown in 4.6(b). The clean graphene shows no evidence of nitrogen. Upon dosing, there is an increase in intensity that can be fit by 3 peaks: 400.9 ± 0.1 eV, assigned to nitrogen substituted into the graphene lattice; 396.6 ± 0.1 eV, assigned to nitrogen adatoms; and finally 398.7 ± 0.1 eV, assigned to both pyrrolic and pyridinic environments. These two environments are often separated into peaks at 400 eV for pyrrolic (a nitrogen atom in a five-membered ring), and 399 eV for pyridinic (one in a six-membered ring) [166]. Here they are kept together for the following reasons. The first is that there is some debate as to where the two peaks should appear. This is most clearly demonstrated in table 4.1, where there is little consensus on the exact binding energies. Further the signal-to-noise in the XPS is insufficient to unambiguously fit two separate peaks. Lastly, for the conclusions of this chapter, determining the relative amount of the pyrrole and pyridine is not essential: both relate to nitrogen atoms associated with vacancies in the graphene lattice.

To calculate the amount of nitrogen relative to carbon on the surface, the relative intensity in the N1s and C1s regions are compared, after correcting for their differing sensitivity factors. The result is shown in 4.6(c). The amount of nitrogen increases almost linearly with dose time, until, after 120 s of dosing, there is 4.4 at% nitrogen to carbon. Panel (d) shows the relative amount of the components of the N1s. These values vary only slightly during dosing, which suggest that each environment is formed at a comparable rate.

The XPS suggests defect-associated groups among the nitrogen functionalities and so acTEM is used to observe structural changes. Figure 4.7(a) shows acTEM of a graphene coated TEM grid after 30 s exposure to atomic nitrogen. The graphene lattice is clear, as well as polymer residue. There is also evidence of defects in the lattice, significantly more than for atomic oxygen dosing. These are more clearly seen again by Fourier filtering to remove the graphene lattice, which is shown in (b). Extended defective areas are revealed.

One particular defect is highlighted in green in 4.7(b). The image here is one of a stack taken at different defocus, and therefore an exit-wave image can be reconstructed for this area, which is shown in (c). With the help of a simulation (d), the structure can now be identified as a divacancy that has restructured into 5,7,5,7,5,7 rings [182], [183]. In other regions, defects like those seen in (e) are identified. Again with comparison to a simulation (f), these can be identified as monovacancies.

TEM clearly shows defects in the graphene lattice after dosing, but the question remains as to where the nitrogen is. Although TEM relies on Z-dependent contrast, conventional TEM imaging cannot distinguish nitrogen and carbon because they are too similar. Therefore, nitrogen substitutions cannot be identified, neither can the location of nitrogen within the defective regions.

However, some insight can be gained by calculating the energetically favourable structures using density functional theory (DFT). These calculations (performed by Peter Brommer, details in [184]) suggest nitrogen would be stable in structures shown in figure 4.8. For the nitrogen adatom, the most stable configuration is with the nitrogen over the bridge site; the same configuration as an epoxide group with oxygen. The substitutional nitrogen replaces the carbon in the graphene lattice and is stable in this configuration. Next, the configurations for a monovacancy and divacancy were investigated. Both of these were found to be stable in the pure carbon case. If nitrogen is included, the structure with the lowest energy for both the vacancy and divacancy are shown in the lower panels. The nitrogen is expected in these sites for each of these defects.

It is also clear from the TEM images that the defects appear to cluster within

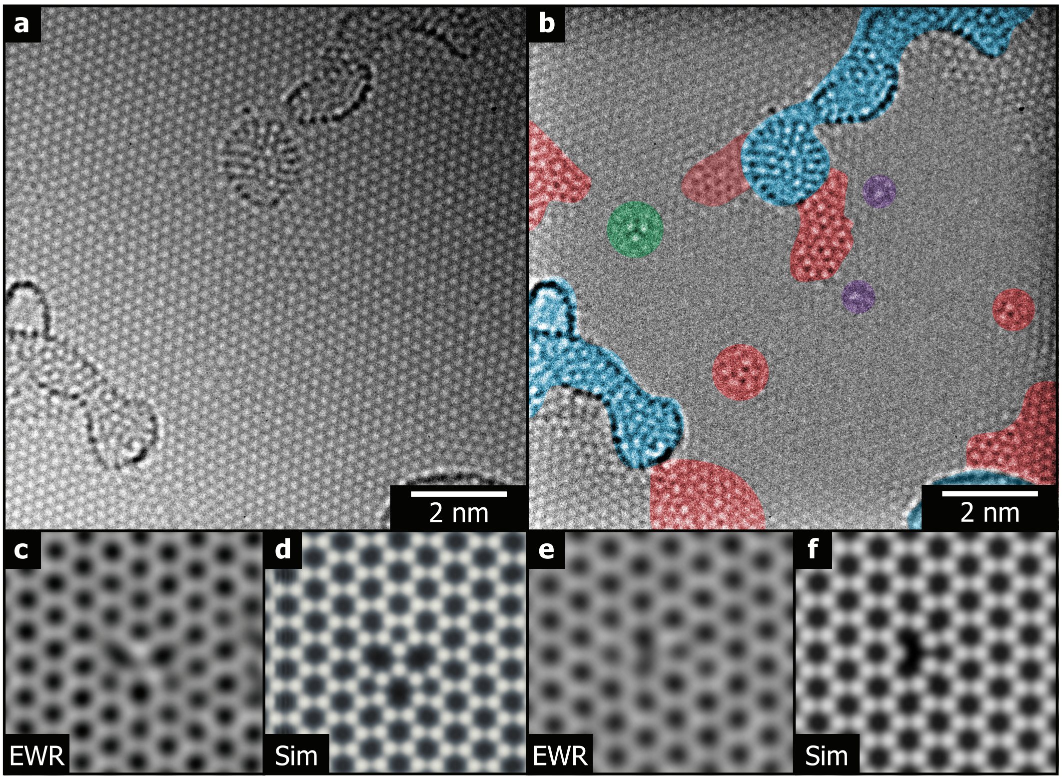

Figure 4.7: TEM of graphene after a 60 dose of nitrogen. (a) shows defective regions that are more apparent after Fourier filtering (b). Here polymer support (blue), extended topological defects (red), and a divacancy reconstruction (green) are clear, as well as some unrecognisable defects (purple). An exit-wave reconstruction of the divacancy is shown in (c) and a simulation of the stable structure calculated from DFT is shown in (d). In other regions, monovacancies are also visible, with one shown in (e), along with its exit-wave simulation (f). Simulations calculated by A. Dyson.

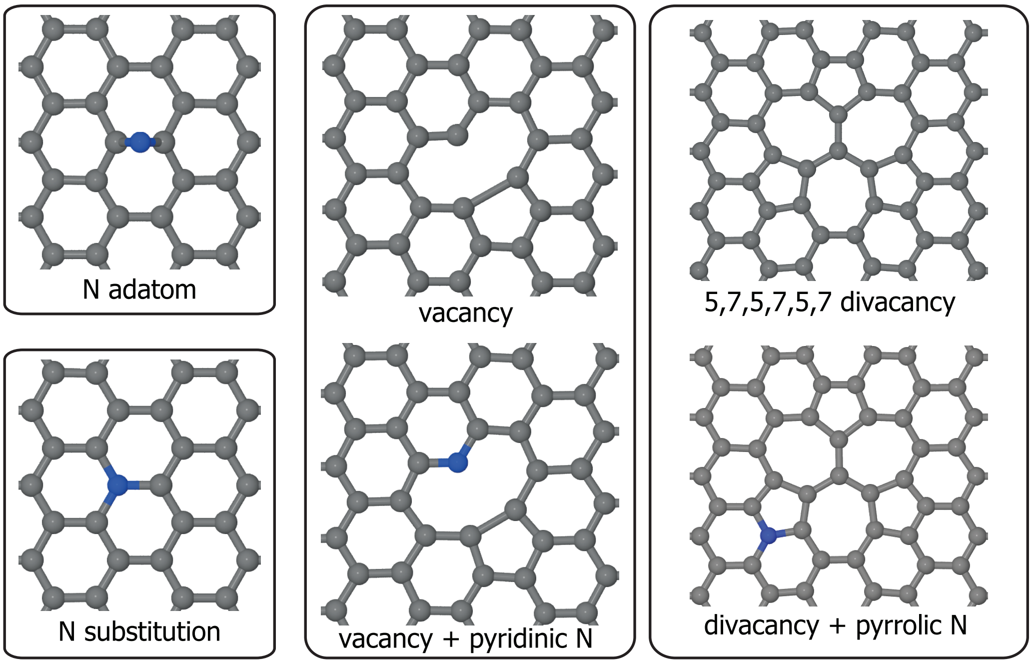

Figure 4.8: Proposed structures of nitrogen groups in graphene based on DFT calculations. Structural models generated by P. Brommer.

the graphene, forming extended topological defects within the film. Examples of these are highlighted in red. The defects are likely to cluster in the graphene lattice again to minimise energy [185]. Finally, the defects highlighted in purple are most likely monovacancies.

To summarise the XPS and TEM, dosing graphene on copper with atomic oxygen results in the formation of epoxide groups on the graphene surface. In contrast, dosing with atomic nitrogen forms a mixture of environments — substitution, atomic, and pyrrolic/pyridinic environments associated with individual defects and with extended topological defects. The next section addresses the effect these functional groups have on the electronic structure of graphene.

4.2.4 Changes in electronic structure upon functionalisation

Figure 4.9 shows the evolution of the ARPES of graphene on copper upon oxygen dosing. The top panel in each column show a slice at constant energy near the Fermi energy; the middle, a slice 600 meV below the Fermi energy; and the bottom panels show cuts indicated by the dashed line. The pristine graphene shows two undoped Dirac cones as described in chapter 3. After dosing, the most obvious change is the gradual broadening and disappearance of the graphene bands. From fitting, there is no evidence of a change in doping and or of a band gap opening. These details are shown in table 4.2. By the final dose the bands are no longer visible indicating a clear reduction in the graphene's electronic quality.

Figure 4.10 shows ARPES after dosing with atomic nitrogen. As in the case for atomic oxygen, the most obvious change is the deterioration of the graphene π band. However, here there are also changes in the doping. After 10 s dose, the Dirac crossing appears at a lower binding energy: fitting gives a crossing at $E - E_F = 210 \pm 20$ meV. For the 30 s dose, the bands are more diffuse, but can still be fit, and the doping remains unchanged within experimental uncertainty ($E - E_F = 190 \pm 40$ meV). Although there is evidence of doping, from these spectra it is unclear whether a band gap has opened. Fitting the intensity in a band of constant momentum — an energy dispersion curve (EDC) — around the Dirac point shows no drop in intensity. Therefore, these results suggest no band gap.

From the extent of the shift of the Fermi level, the carrier concentration per unit cell can be calculated using equation 1.8 [7]. From this, the effective charge per dopant atom can be calculated, which is also shown in table 4.2. The values shown here show how little charge is contributed to the graphene lattice by the dopant species. This highlights how important the pyrrolic/pyridinic environments are in the functionalised graphene; their p-type doping counteracts the n-ype doping from the substitutional groups, and reduces the overall doping of the graphene lattice.

For both atomic oxygen and atomic nitrogen dosing, the most significant effect is the disappearance of the graphene π bands after 60 and 120 s respectively. This can be attributed to localisation of the electronic states caused by the disorder introduced into the graphene lattice. This would have the effect of further broadening the electronic states in reciprocal space, consistent with what is shown here. This has in fact been shown before for graphene when adding other functional groups to the surface: for example in the case of covalently attaching hydrogen to the

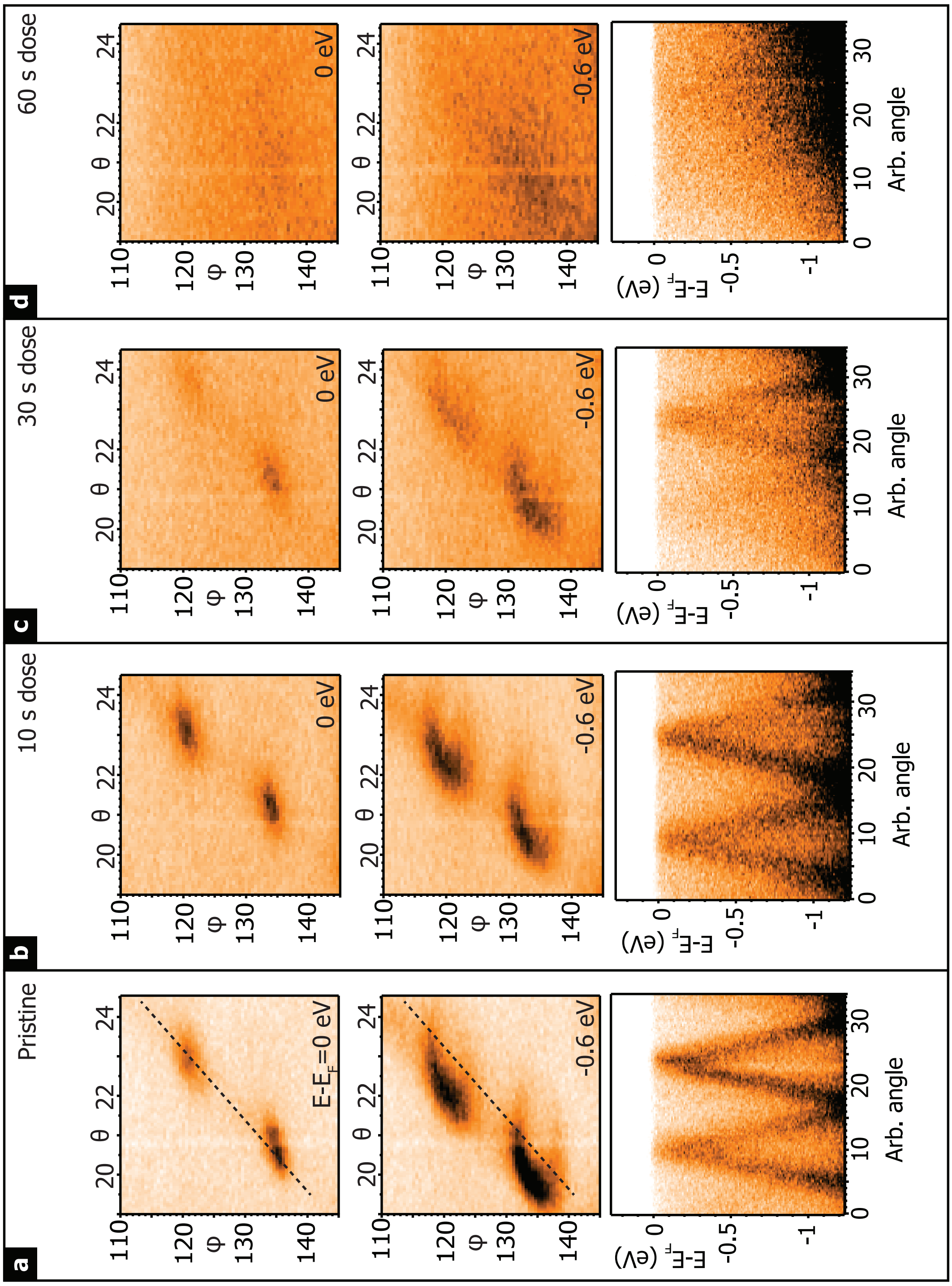

Figure 4.9: ARPES from atomic oxygen dosed graphene. The Dirac cone of pristine graphene is clear in (a). The dominant effect of dosing is the gradual disappearance of the graphene π-band.

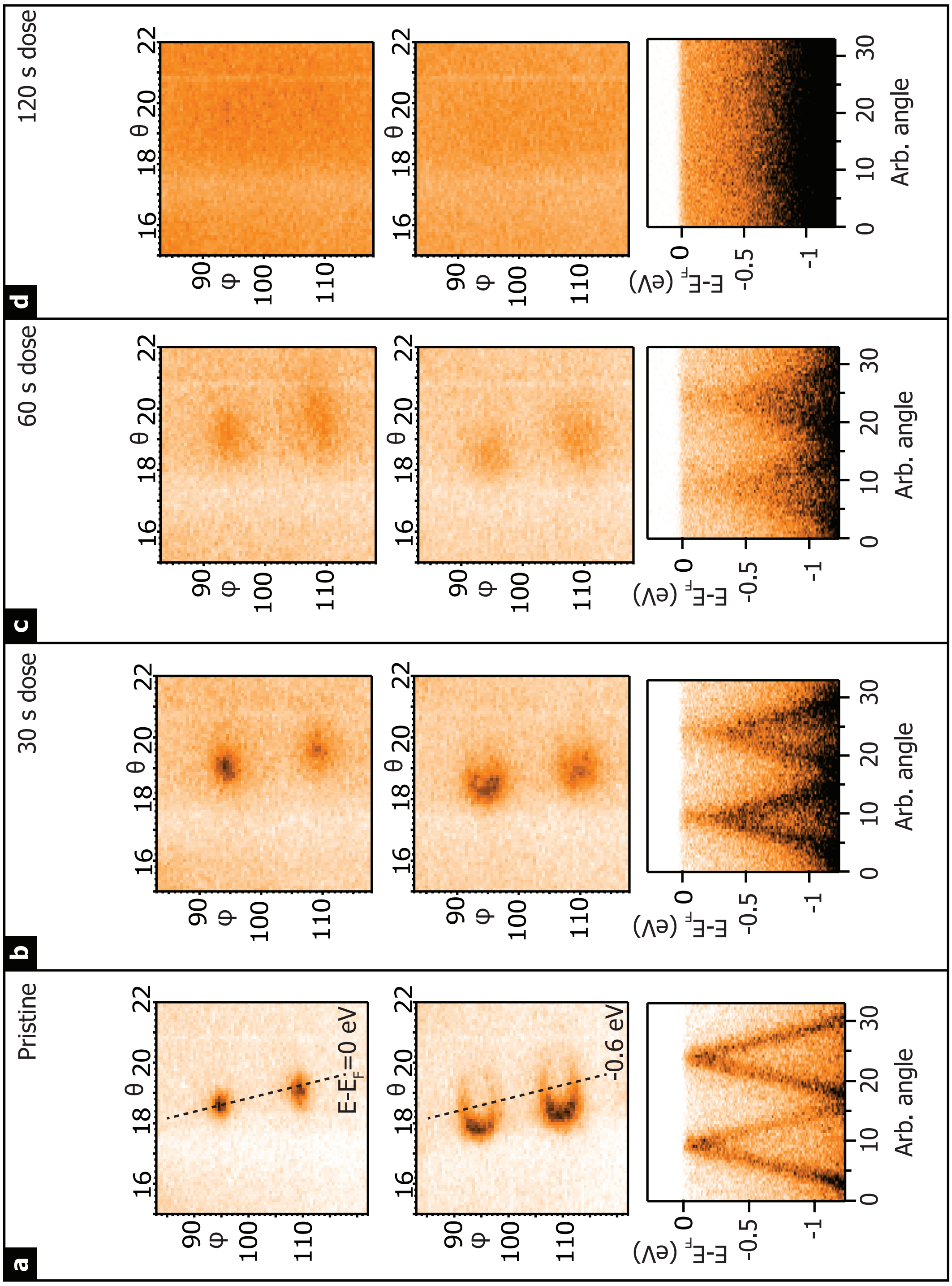

Figure 4.10: ARPES from atomic nitrogen dosed graphene. For pristine graphene (a) the Dirac cone of graphene is clear. After dosing, the intensity in these bands becomes weaker and more diffuse (b) and (c), until after 120 s dose (d), the bands are gone.

Dose	Atomic concentration	$E_D - E_F$ (meV)	Carrier concentration per unit cell (e)	Effective charge per atom (e)
Pristine	—	0 ± 10	—	—
10 s O	0.7 %	0 ± 10	—	—
30 s O	3.1 %	0 ± 10	—	—
60 s O	5.0 %	—	—	—
Pristine	—	20 ± 10	$(2 \pm 1) \times 10^{-5}$	—
30 s N	1.6 %	-210 ± 20	$-(2.2 \pm 0.4) \times 10^{-3}$	-0.07 ± 0.01
60 s N	2.6 %	-190 ± 20	$-(1.8 \pm 0.8) \times 10^{-3}$	-0.04 ± 0.02
120 s N	4.4 %	—	—	—

Table 4.2: Summary of the electronic effects of dosing with atomic species.

surface [186] and after exposing graphene to ozone [187]. Overall, the dominant electronic effect of disordered, covalently attached functionalisation is to convert graphene from a semi-metal to an electronically localised system.

ARPES measurements rely on the emission angles of photoexcited electrons, and so can be sensitive to the topography of the surface. A roughening of the surface caused by the functionalisation would present as a broadening in angle (and so in reciprocal space) of the electronic bands, as seen previously for graphene supported on different substrates [188]. However, after functionalisation, LEED patterns were shown to be unchanged by the functionalisation, suggesting that the graphene topography was not dramatically changed. The effect seen here, therefore, is strictly a change to the electronic structure of graphene and not a change to its surface structure.

Further to localisation, small amounts of nitrogen were measured to electron dope the graphene by ≈ 200 meV. In the most simplistic picture, the group V element would be expected to donate electrons to the carbon lattice, and the doping would be directly related to the dopant concentration. However, this is not what is seen here, and this is likely because a range of nitrogen environments are present. These environments were identified earlier using DFT, and these calculations can be used to determine the amount of charge they each would transfer to the graphene lattice [189].

From XPS measurements, it was possible to determine the relative abun-

Defect	$E_D - E_F$ (meV)	Effective charge per defect (e)
Epoxide	15	0.0004
Nitrogen adatom	90	0.015
Nitrogen substitution	-390	-0.28
Monovacancy	60	0.0007
Monovacancy with pyridinic	330	0.19
7,5,7,5,7,5 divacancy	750	1.0
Divacancy with pyrrolic	460	0.38

Table 4.3: DFT-calculated charge-contributions from each defect type.

dance of each defect type present in the lattice. These abundances can then be used with the effective charge per defect to calculate the total charge contribution from N atoms to the graphene lattice. Doing this estimates the overall charge contribution to be slight p-doing.

However, the ARPES results demonstrate n-doping, the opposite of what would be expected. One explanation lies in the clustering of defects, as already seen in the TEM results. These have already suggested that it is more energetically favourable to have multiple N atoms associated with a single defect. The effect of this would be to reduce the effective charge per N atom from those that are in the vacancy environments, and so reduce their overall charge contribution to the graphene lattice. Overall, this implies that extended topological defects can play an important role graphene doping.

The DFT calculations also give an insight into why doping was not seen after dosing with atomic oxygen. The epoxide group is calculated to contribute almost no charge to the graphene lattice, and so no band shift is expected if only these groups were present.

From this section, in conclusion, the covalently functionalised graphene on copper foils have been examined by ARPES to determine the effect of the functionalisation on the electronic structure. In the case of atomic oxygen, the epoxy groups do not transfer charge to the graphene — consistent with DFT — but do cause a disorder-induced metal-to-insulator transition. This effect is also seen for the multi-nitrogen-environment graphene, where again the disorder has caused localised electronic states. However, in contrast to oxygen, n-doping is seen at low levels of functionalisation, caused by the cumulative balance of charge transferred from the nitrogen groups.

4.2.5 Reversibility of functionalisation

One of the motivations for studying covalent functionalisation of graphene is that it is inevitable in some production routes. Therefore the reversibility of functionalisation is worth studying. There has already been some evidence that the functionalisation is reversible in the previous sections: the TEM of epoxide functionalised graphene did not show the expected coverage, suggesting they are mobile under — or have been removed by — the electron beam. This is supported by DFT calculations that indicated these groups are weakly bound [184].

Figure 4.11 shows the effect of annealing on the oxygen dosed graphene. Panel (a) shows the C1s region in XPS. Here the epoxide peak has decreased significantly, but has not been removed completely, suggesting most of groups have been removed, but not all. Measuring the intensity of the graphene peak and epoxide peak indicates a functionalisation of 0.6 at%, compared to 5.0 at% after the 60 s dose. There is no shift in the binding energy, so the remaining groups should be epoxides; a change in environment would have likely caused a shift in binding energy. As well as this, the graphene peak has become sharper, indicating some return to pristine graphene.

Figure 4.11(b) shows the O1s evolution. The O1s post-annealing resembles that before dosing, but with some key changes. The most noticeable is the removal of the lower binding energy components, those often associated with copper environments. There is still some oxygen present in carbon-associated environments at the higher binding energies, but as before, these are not seen in the C1s. It is therefore not clear what is happening to the oxygen after this annealing from observing the O1s region. The role of this oxygen in graphene grown on copper is becoming an increasingly relevant area of research [58] and interpreting the O1s here is left for future work. However, from the C1s, it appears that the majority of the oxygen

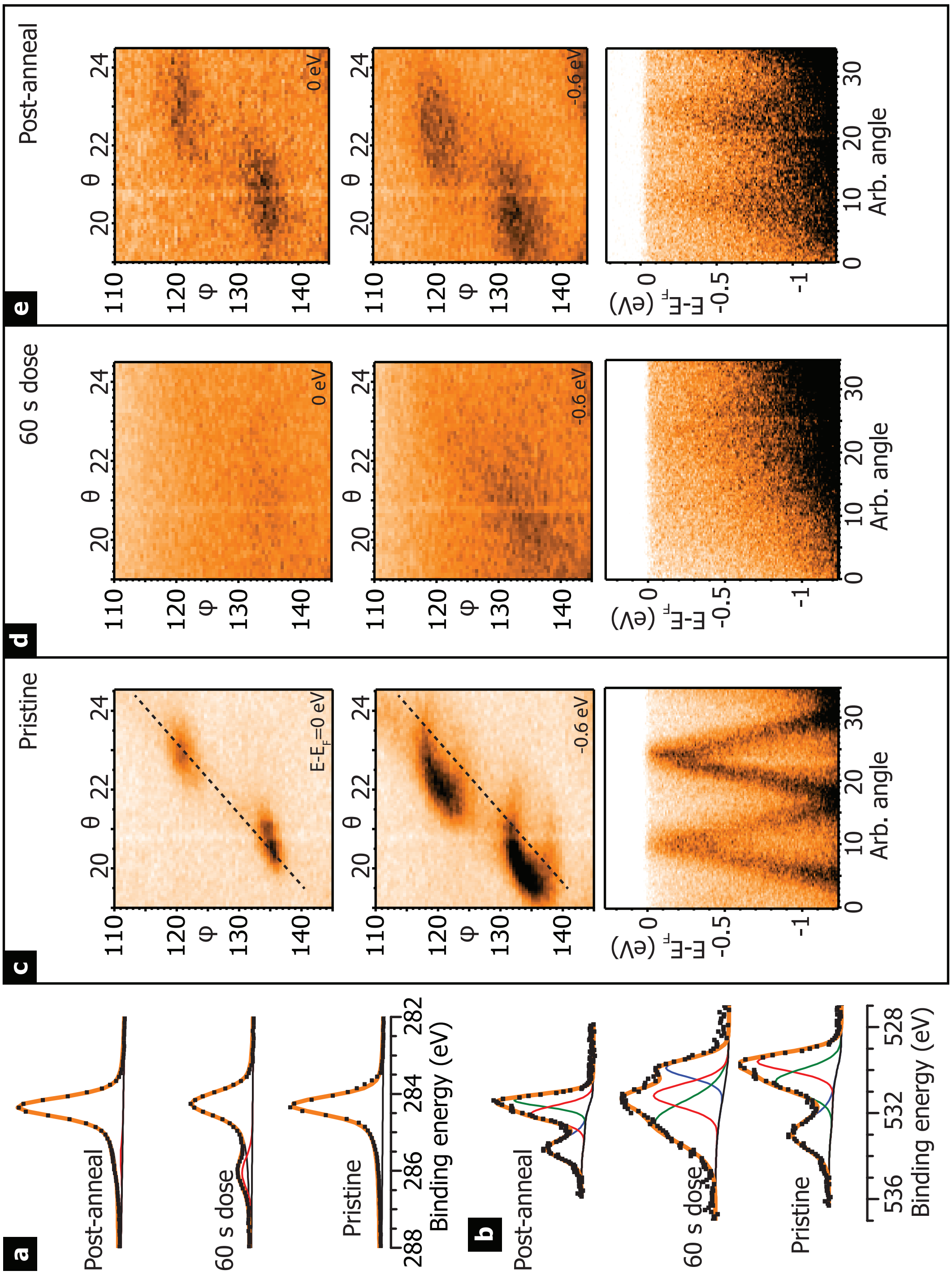

Figure 4.11: (a) C1s and (b) O1s XPS regions of pristine graphene, oxygen dosed graphene and then after annealing. The epoxide group is dramatically reduced in the C1s region. ARPES of (c) pristine graphene, (b) graphene dosed with 60 s of oxygen, and (d) after annealing. Here the bands have partially recovered.

introduced as epoxide groups has been removed by annealing, which is consistent with previous reports for graphene on SiC [169].

Panels (c) to (e) of figure 4.11 show the evolution of the ARPES data through the treatment. Panel (e) shows that after annealing there is some slight recovery of the band structure, as indicated by the diffuse points of intensity in the constant energy slices. Taking a cut across these, the bands are barely visible; the electronic structure is only slightly recovered after this level of functionalisation, suggesting disorder is still present within the lattice. This disorder is unlikely to arise solely from epoxide groups. After annealing, the epoxide coverage is at 0.6 at%, a comparable amount to that after the 10 s dose, at which the bands were much more visible. This points to the annealing forming other types of oxygen environments and defects, which have a more significant impact on the electronic structure.

For the case of nitrogen, figure 4.12 shows XPS from the pristine graphene, after dosing, and finally after post-annealing. In the C1s (panel (a)), little has changed after post-annealing the sample. The nitride peak has shifted towards a lower binding energy, but remains broad, and suggests there is still a range of environments present within the graphene.

There is more insight from the N1s region, shown in panel (b). Here the most significant change is the removal of the lowest binding energy component, that associated with atomic nitrogen. As the weakest bonded group (as suggested by DFT), and considering what happens to oxygen bonded in this way, the removal of this environment is not surprising. There is also a small shift in the pyrrolic/pyridinic peak to 398.0 ± 0.1 eV, which would perhaps indicate that more pyridinic environments were being formed.

The final feature is an increase in the substitutional environment, coupled with a decrease in the pyridinic/pyrrolic environment. This effect on nitrogen groups has been seen before [190]. In this paper, Scardamaglia et al. implanted nitrogen using ion bombradment into graphene films. They observed a range of nitrogen environments including pyrrolic/pyridinic and substitutional nitrogen. When graphene films were annealed, the proportion of substitutional nitrogen increased at

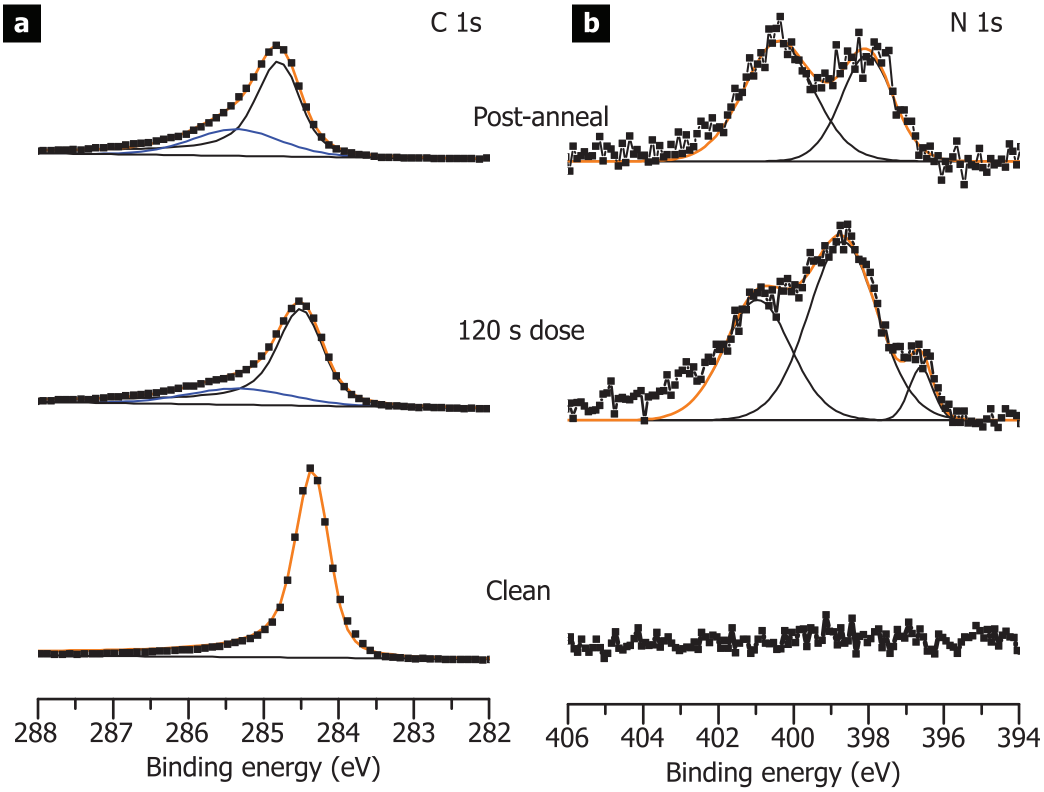

Figure 4.12: (a) C1s and (b) N1s XPS regions of pristine graphene, nitrogen dosed graphene and then after annealing.

the expense of other groups. This suggests that annealing could be used to tailor the nitrogen environments in the graphene film, and, in this case, increase the amount of substitional nitrogens, thus increasing the n-doping. However, the results presented here suggest that the some of the nitrogen will be present in extended topological defects, which are stable and so more difficult to remove. Therefore, again, caution should be used when using the addition of atomic species on graphene as a route to tuning its electronic properties.

The epoxide groups appear to be much easier to remove than the nitrogen functionalisation, particularly the defect associated pyrollic/pyridinic and substitutional groups. For the defect-associated groups, acTEM showed the graphene lattice had reconstructed into a series of 5 and 7 membered rings. These structures are stable and cannot be easily removed, which explains why the chemical structure of the graphene has changed so little after annealing.

It would be interesting to see the effect the anneal has had on the electronic structure of nitrogen-dosed graphene. Unfortunately, this was not done because of the time constraints inherent in synchrotron-based experiments. However, by observing what has happened to the oxygen ARPES, it is unlikely that the electronic structure will have recovered fully after annealing; there is still a significant defect peak in the C1s, much more than for oxygen dosing where the bands had barely recovered. It would also be interesting to observe these changes in the TEM, to try to deduce what has caused the shift in the pyrrolic/pyridinic peak. However, this also remains for future work.

4.2.6 Reversibility of graphene oxide

In the previous section evidence suggested that oxygen functionalisation became irreversible after about 5 at%. Significantly higher levels of fuctionalisation are present in graphene oxide (GO), which, has a C:O ratio of typically 2:1 when fully oxidised [67]. In this section acTEM is used to examine the physical structure of GO both before and after attempts to remove the oxygen functionalisation. GO grids for acTEM were prepared as described in section 2.1.3.

Figure 4.13(a) shows acTEM of a GO covered TEM grid. Regular contrast features are present in the image and an FFT demonstrates the hexagonal lattice present in this area. The spacings are consistent with graphene confirming the presence of a graphene backbone. Further, there is only a single set of hexagonal spots, which points to only a single-layer of GO in this region.

Along with the graphene lattice, there are other contrast features. On most of the surface, the graphene backbone is covered by amorphous features of heavy contrast (highlighted in blue). These can be attributed to the functional groups decorating the graphene backbone, as well as oxidative debris that is present on as-produced GO. In contrast, figure 4.13(b) shows a base-washed GO (bwGO) covered grid. In this image the amount of heavy contrast features is reduced, supporting the removal of the oxidative debris by base-washing.

In addition to the oxidative debris are the presence of holes (shown in red) and defects (shown in green) in the graphene lattice for both aGO and bwGO. These include extended topological defects within the graphene lattice. It had been suggested that the reduction process causes the extended topological defects [191], however, these results show that they are intrinsic to GO, but that they are often hidden in HRTEM by the adsorbed debris. Combined with the observation of extended topological defects in nitrogen-functionalised graphene shown earlier, these results suggest that the defects are a feature in many types of highly functionalised graphenes.

It is possible to try to reduce GO with chemical and heat treatments. After coating a TEM grid with GO, it was exposed to hydrazine vapours for 12 hours, by sealing 60 μL of hydrazine in a petri dish with the grid, which was then placed on a hotplate at $60°$C. After this, the grid was heated in air on a hotplate for 2 hours at $200°$C.

Figure 4.13(c) shows acTEM of a GO coated grid after this treatment. An FFT again shows the graphene backbone is present. However, here the graphene lattice is much clearer in the image, and there are significantly fewer contrast features on the surface. This is consistent with the removal of functional groups and adsorbed

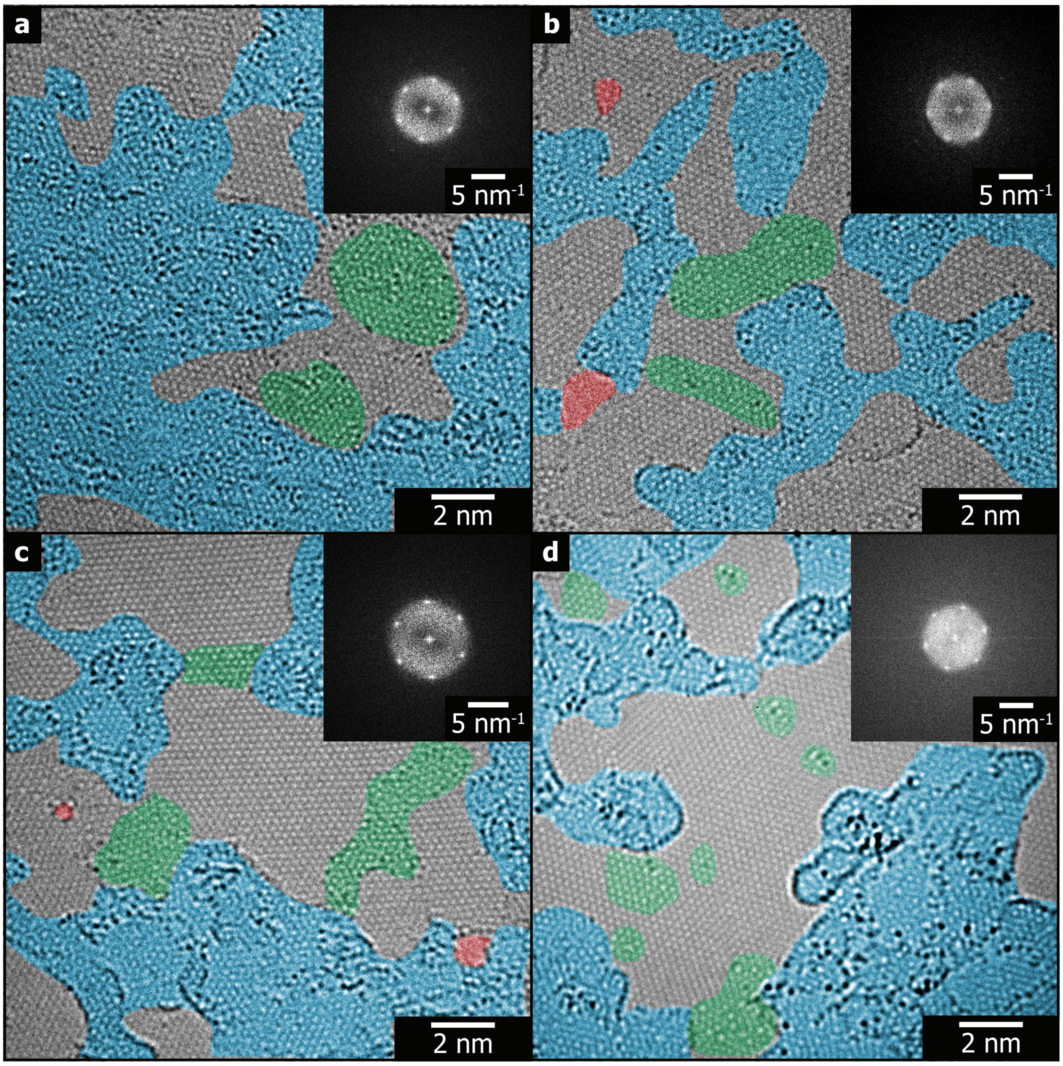

Figure 4.13: acTEM of (a) aGO, (b) GO after base-washing (bwGO), (c) after attempts to reduce aGO, and (d) graphene after 6 minutes of atomic oxygen dosing. In all images the graphene lattice is clear, as shown by the inset FFTs. For aGO, the amorphous regions (highlighted in blue) indicate the presence of oxidative debris, which is reduced in bwGO. After reduction, even more of the graphene backbone is clear, consistent with the removal of functional groups. However, extended defects are still present in the GO (green), confirming that functionalisation can cause surface reconstructions that are harder to remove. These defects are also present in graphene that has been dosed with atomic oxygen for 6 minutes.

debris from the surface. On the other hand, there are still areas where extended topological defects are present. This suggests that, just like in the case for atomic nitrogen, these types of structures are much harder to revert to a pristine graphene lattice.

As a comparison, a graphene coated TEM grid was exposed to atomic oxygen for 6 minutes to increase the level of functionalisation. Images of this grid are shown in figure 4.13(d). This image shows the graphene lattice, also shown by the FFT of this area, along with polymer residue from the transfer. As well as these features, there are now the extended topological defects that were obeserved in the GO images. This suggests that, after this level of functionalisation, extended defects are formed in the lattice.

In summary, this section has shown that after higher levels of oxygen functionalisation, like those seen in GO, extended topological defects are seen in the graphene lattice. These defects are much harder to remove with chemical and heat treatments. Therefore, the functionalisation has irreversibly altered the homogeneous, van der Waals graphene surface. GO and rGO are the most widely used forms of graphene because they are easy and cheap to make, and so these results suggest that care should be taken when using these forms of graphene, especially when considering the imporant differences between rGO and pristine graphene.

4.3 Conclusions

Covalent functionalisation of graphene has attracted attention as a route to modifying graphene's properties, such as opening a band gap or increasing it's chemical reactivity. Also, functionalisation is an inevitable consequence of some production routes. For both of these reasons, understanding how covalently bonded species affect graphene is important. This chapter presented the clean, controlled functionalisation of graphene with atomic oxygen and nitrogen in UHV. The effect this had on the chemical, physical and electronic structure was discussed.

In the case of atomic oxygen, low levels of functionalisation formed epoxide groups on the graphene surface. This had a deleterious effect on the graphene π-band structure, which, by 5 at% functionalisation, could not be observed. However, there was no apparent doping or opening of a band gap. These changes were attributed to a localisation of the electrons, causing a metal-insulator transition at even low levels of functionalisation. Post-annealing suggests this is reversible, and that the band structure is recoverable, but only for lower than 5 at% functionalisation.

On the other hand, atomic nitrogen formed a range of environments with substitutional, adatom and defect-associated pyrrole/pyridinic groups present. The result of this was a removal of the graphene band structure, again associated to localisation from defects introduced into the graphene lattice. However, unlike atomic oxygen, there was n-type doping of the graphene after 1 at% functionalisation. DFT calculations supported charge transfer from the donor nitrogen species.

For post-annealing nitrogen-doped graphene, full characterisation is left for future work, but it is not easily reversed: XPS showed only the removal of the weakly bonded adatom groups, while the rest remained. The difficulty of removing the pyrrole and pyridinic groups is related to the formation of vacancies that reconstructed into 5- and 7-membered rings, and to extended topological defects in the graphene lattice. These structures are energetically harder to remove, along with substitutional nitrogen groups. This suggests caution should be used when using the addition of atomic species to alter the electronic properties of graphene.

Finally, for atomic oxygen, there was evidence that the chemical functionalisation became irreversible after about 5 at%. Chemically functionalised graphene in the form of GO has reported C:O ratios of up to 2:1, much greater than the reversible 5 at%. At this level of functionalisation, extended topological defects are present that are harder to remove with chemical and heat treatments. These defects irreversibly alter the chemical and physical structure of graphene, and are also present in reduced GO. This is important for van der Waals epitaxy because, after this level of functionalisation, graphene is no longer a homogeneous, van der Waals surface. This will change how functionalised graphene interacts compared to pristine graphene. How this affects the growth of molecular overlayers is highlighted in the next chapter.

Chapter 5

Vanadyl-phthalocyanine thin films grown on graphene with elevated substrate temperature.

5.1 Introduction

Organic electronic devices are intensively studied as a way of reducing the cost, both financial and environmental, of the vast electronics industry [80], [81], [192]. Organic semiconductors (OSCs) have been used as the active layers in organic photovoltaics (OPVs) [82] and as the source-drain channel in organic thin film transistors (OTFTs) [81], [193]. While these devices show promise for replacing their inorganic counterparts, more performance optimization is needed.

Performance improvements can come from adjusting the structure of the OSC molecules in the active layer: both the crystallography and the morphology of the OSC have a direct impact on the charge transport mobility [92]. For example, single crystals of organic molecules generally perform better than polycrystalline films, which suffer from charge-scattering and charge-trapping at grain boundaries [194], [195].

The structure within OSC films is dependent on the deposition method and conditions, and the interactions between the substrate and OSC. Here organic molecular beam deposition (OMBD) [86] is used, where the OSC is sublimed in ultra-high vacuum (UHV) forming a molecular beam that deposits directly onto the growth substrate. OMBD has the advantage of controlling the substrate temperature during deposition, which offers the chance to control the film morphology [90], [103].

Increasing the temperature of the substrate during OMBD can lead to more crystalline films [91]. The OSC morphology and crystallinity are also dependent on the substrate; for example order-inducing layers such as CuI [103] or para-sexiphenyl (p-6P) [95] have been used to control the orientation of MPcs.

This chapter presents the OMBD of VOPc onto CVD-grown graphene on copper and demonstrates the effect of elevated substrate temperatures on the morphology and crystallinity of the thin film. At elevated temperatures, the VOPc forms large grains on the graphene surface, with the VOPc becoming more crystalline at higher temperatures. Low-dose aberration-corrected transmission electron microscopy (acTEM) shows that the large grains are single-crystals of VOPc, with the molecules oriented perpendicular to the substrate. This is in contrast to growth at ambient temperatures, where the film is composed of randomly orientated grains. At both ambient and elevated temperatures there is no epitaxial ordering relative to the graphene. Alongside this, deposition under similar conditions on substrates such as silicon oxide and graphene oxide results in much smaller VOPc grain sizes. These observations highlight the impact of elevated substrate temperatures during deposition on the morphology and crystallinity of OSC thin films, and the potential importance of the van der Waals surface of graphene for the deposition of high-performance organic electronic devices.

5.2 Results and Discussion

5.2.1 Controlling VOPc crystal grain size with elevated substrate temperatures during deposition

First the morphology of the VOPc films as a function of substrate temperate during deposition is presented. In UHV, VOPc was sublimed from a solid source forming a molecular beam that deposited onto the graphene on copper substrates at constant flux, with separate control of the substrate temperature. The deposition time was adjusted to give a 50 nm thick film at room temperature (RT, 26°C), and then kept constant for each other temperature.

Figure 5.1 shows AFM images of VOPc on graphene coated copper foils deposited at different substrate temperatures, but under otherwise identical conditions. After deposition at 26°C the VOPc has formed a uniform grainy film. A similar morphology is observed for 75°C. At 125°C the morphology changes and discrete islands are formed with areas of exposed substrate between them. At 155°C the islands increase in size and the surface coverage is reduced, a trend that continues at 175°C.

Average island sizes and percentage coverages for each deposition temperature are presented in figure 5.1(f). The island size can be measured for higher temperatures by thresholding the AFM images. For the grainy films seen at lower temperatures, an estimate of the grain size can be gained from the correlation length measured by the height-height correlation function (HHCF) calculated from the AFM images [196]. The HHCF, $H(\boldsymbol{\tau})$, can be written

$$H(\boldsymbol{\tau}) = \left\langle \left[h(\mathbf{x}) - h(\mathbf{x} - \boldsymbol{\tau}) \right]^2 \right\rangle \tag{5.1}$$

Where $h(\mathbf{x})$ and $h(\mathbf{x} - \boldsymbol{\tau})$ are the heights of the sample at two points separated by the displacement vector, $\boldsymbol{\tau}$. This displacement vector is usually directed along the fast scan direction when calculating the HHCF for AFM images, and so becomes a scalar (1D) function. The distribution is assumed to be Gaussian and thus fit with a

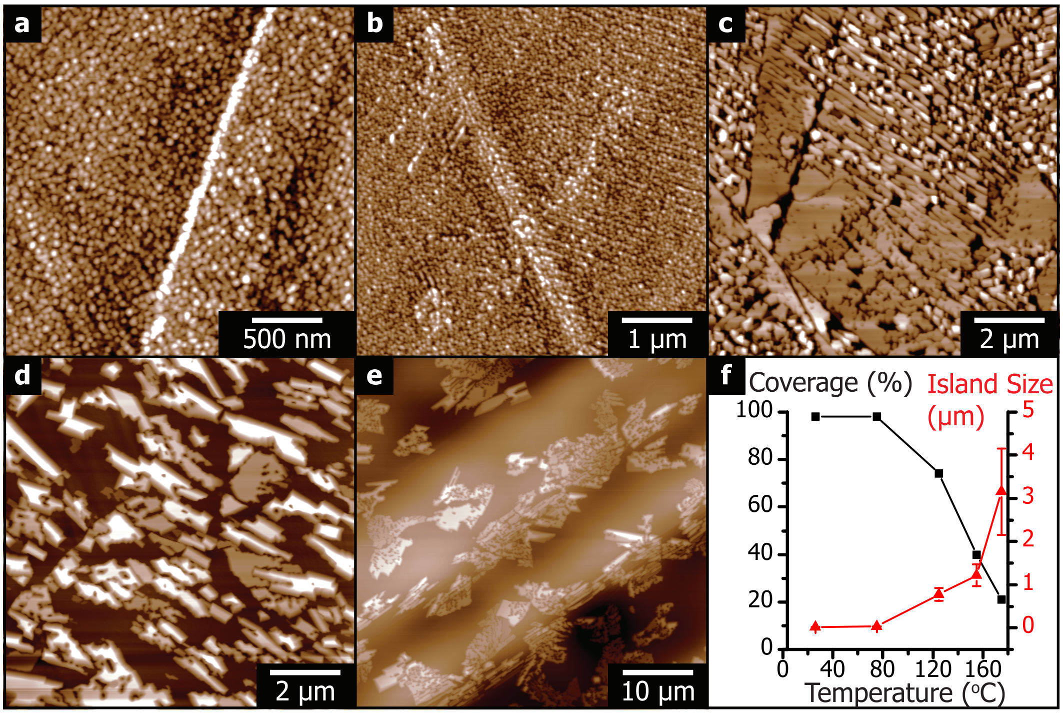

Figure 5.1: AFM showing morphology changes of VOPc with increasing substrate temperature. At ambient temperature (a) the film is grainy, with a similar morphology at 75°C (b). At 125°C substrate temperature (c) discrete crystallites have formed with clear boundaries. At higher temperatures — 155°C (d) and 175°C (e) — the islands increase in size but reduce in number, causing a lower surface coverage. These changes are summarized in average island size and surface coverage statistics in (f). Full height scales are: (a) 20 nm, (b) 20 nm, (c) 30 nm, (d) 50 nm, (e) 800 nm.

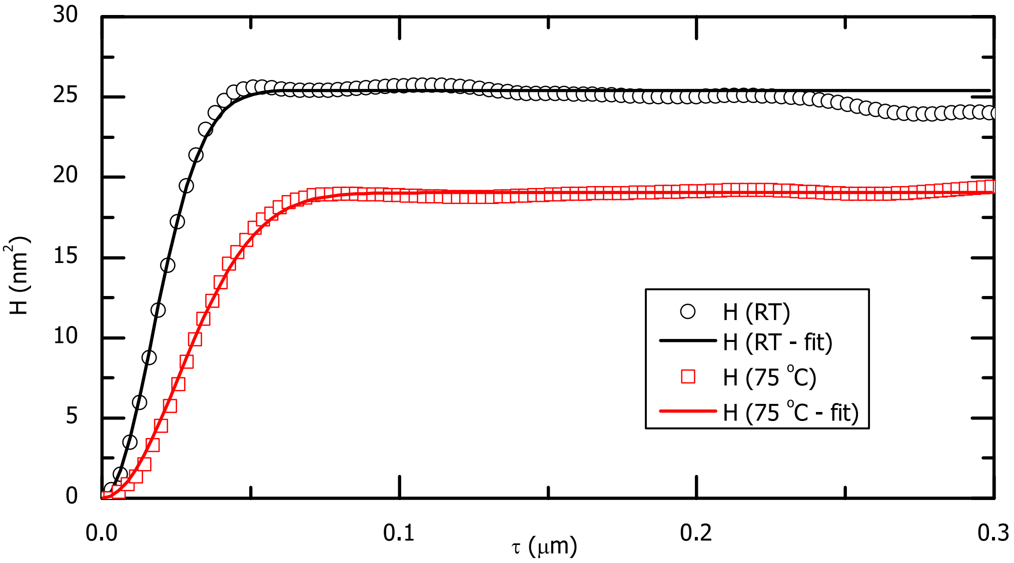

Figure 5.2: HHCFs calculated from AFM images of VOPc deposited onto graphene at room temperature (RT) and at 75°C. The distribution is fit with a Gaussian HHCF which yields the following for the correlation length: $\xi = (23.7 \pm 0.2)$ nm for the RT film and (36.3 ± 0.2) nm for the 75°C film.

function of the form

$$H'(\tau) = 2\sigma^2 \left[1 - \exp\left(\frac{\tau}{\xi}\right)^2 \right] \tag{5.2}$$

where σ is the surface roughness, and ξ the correlation length. It is this correlation length that provides a measure of the grain size of the film. The HHCF is calculated from the images using Gwyddion [197].

Figure 5.2 shows HHCFs calculated from films deposited at 26°C and at 75°C. These are fit with Gaussian HHCF functions (equation 5.2), and yield $\xi = (23.7 \pm 0.2)$ nm for the RT film and (36.3 ± 0.2) nm for the 75°C film. These measurements were repeated across different images and gave values of (22 ± 3) nm for the film deposited at 26°C. For 75°C a larger correlation length of (37 ± 3) nm is found, showing an increase in grain size.

Figure 5.1(f) shows how the typical island size increases from 10s of nanometers at 26°C to around a micrometre at 155°C. Concomitant with this, the percentage of the surface covered by VOPc drops from an almost continuous film at 26°C and

$75°$C, to only (21 ± 2) % coverage at $175°$C. In the higher temperature growth with isolated islands, AFM investigations showed no evidence of VOPc on the graphene between the islands, indicating an island (Volmer-Weber) growth process.

The morphological changes can be understood qualitatively by considering the growth dynamics. After adsorbing, the molecules either diffuse until they desorb, attach to an existing grain, or form a new nucleation site. On a homogeneous surface, the nucleation density is proportional to the deposition rate and inversely proportional to the diffusivity of the molecules on the surface [198]. If the deposition rate is constant, the nucleation density is determined by the diffusivity of molecules on the surface, which is typically governed by an Arrhenius factor and so strongly dependent on temperature. At lower temperatures, diffusivity is low and the nucleation density is high, resulting in a grainy film morphology. As the substrate temperature increases, the diffusivity is higher and so the nucleation rate is lower, resulting in larger islands. In addition, at even higher temperatures the rate of desorption becomes significant, hence the decreased coverage at $175°$C.

The VOPc island size here is larger than that reported on p-6P on silicon oxide [91], despite a lower surface temperature during deposition. This indicates that high quality OSC thin film deposition is readily achieved on graphene without the requirement for order-inducing layers.

5.2.2 Effect of substrate temperature on crystallinity of VOPc thin films

High-resolution X-ray diffraction (XRD) was used to determine the crystallographic changes with increasing substrate temperature, as shown in figure 5.3. Peaks due to the polycrystalline copper are observed at every temperature, and vary across samples. The low cost copper foils used for graphene growth are polycrystalline and, although predominant crystallographic orientations are normally observed (as shown in chapter 3), others are often present. For the sample deposited at $26°$C, there is a single peak in the diffraction pattern at 2θ $=(50.40 \pm 0.05)°$, indexed as the Cu(200) planes from the copper foil substrate, whilst on other samples a peak at $2\theta = (43.23 \pm 0.05)°$, assigned to Cu(111) planes, is also seen.

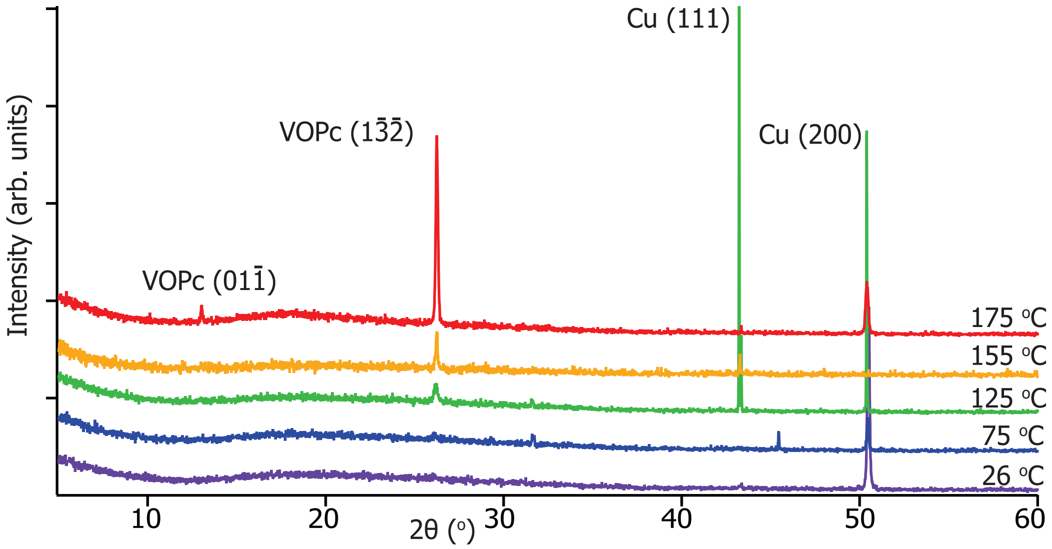

Figure 5.3: X-ray diffraction from films deposited on substrates at ambient and elevated temperatures. At ambient temperature (purple) only diffraction from the polycrystalline copper is seen. At higher temperatures, a peak at $2\theta = (26.23 \pm 0.05)°$ appears and increases with increasing temperature. This peak is assigned to VOPc$(1\bar{3}\bar{2})$ planes. At the highest temperature (175°C - red) diffraction from VOPc $(01\bar{1})$ planes appears.

The XRD shows clear differences in the crystallography of VOPc with substrate temperature. At 26°C no peaks are apparent that are attributable to VOPc. However, at 75°C and higher, diffraction peaks corresponding to the VOPc crystal structure are apparent in the diffraction pattern. The single peak at $2\theta = (26.23 \pm 0.05)°$, which increases in relative intensity with increasing substrate temperature, can be indexed to the $(1\bar{3}\bar{2})$ plane of VOPc. A previous study of VOPc deposited at elevated temperatures onto CuI also showed $(1\bar{3}\bar{2})$ planes in XRD measurements [103]. These planes correspond to the VOPc ligand-plane perpendicular to the surface, in an edge-on orientation. This geometry is in contrast to previous reports on the planar MPc CuPc, which has been shown to stack face-on on graphene [199].

In summary XRD shows that the crystallinity increases with increasing substrate temperature and determines the macroscopically averaged orientation of the VOPc relative to the substrate.

5.2.3 Determination of molecular crystallography

The nanoscale crystallography of the VOPc grains was investigated by low-dose TEM diffraction and acTEM imaging. Graphene was transferred to SiN TEM grids using a formvar support, that was then cleaned off with chloroform, acetone, and heating. TEM analysis of VOPc deposited at $155°$C on a graphene grid is shown in figure 5.4, with panel (a) showing a low-magnification image. The VOPc island morphology on the free-standing graphene is similar to that on graphene on copper. However, the island sizes are smaller, likely due to the effects of the residue from the transfer process; transfer residue is known to affect the growth of OSCs on transferred graphene [200]. TEM of graphene after transfer to SiN supports is shown in figure 5.5. The majority of the graphene surface is exposed pristine graphene. Elsewhere across the film, there are amorphous remnants from the transfer process; this is most likely formvar that has not been completely removed by the cleaning process. This is assumed to be present on only one side of the graphene, and so VOPc was deposited on the reverse, to try and minimize the influence of the amorphous material. No defects were observed in the graphene after the transfer process.

Figure 5.4(b) shows a low-dose, selected-area electron diffraction pattern from the discrete island highlighted in white in figure 5.4(a). The pattern shows sharp diffraction spots that are indicative of crystalline VOPc and are consistent with the molecules being ordered close to the $[1\bar{3}\bar{2}]$ direction relative to the graphene surface, as suggested by the XRD measurements. Molecular models of this orientation are given in figures 5.4(d) and (e). A simulated diffraction pattern from this proposed structure is shown in panel (c) and matches well with the experimental pattern, with the spots closest to the direct beam being those due to the (110) and $(\bar{1}\bar{1}0)$ planes as marked. The electron diffraction pattern is from a single orientation of VOPc suggesting that the island is a single crystal.

The crystallographic orientation of the underlying graphene can be found by electron diffraction after longer exposures (as shown in figure 5.6). Analysis of many VOPc islands showed no preferential orientations between the VOPc and graphene. This indicates that there is no epitaxial relation between VOPc

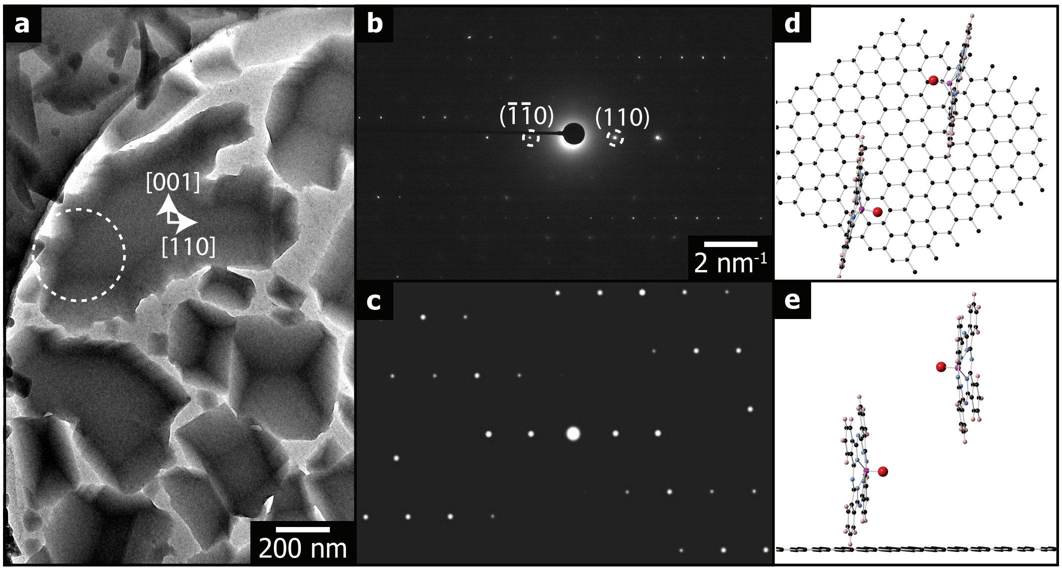

Figure 5.4: TEM of VOPc deposited at 155°C onto graphene on a TEM grid. (a) is a low-magnification image that shows darker contrast features on graphene with a similar morphology to that seen when VOPc is deposited onto graphene on copper. (b) is a diffraction pattern from the region indicated with the white circle in (a). This pattern is consistent with VOPc molecules in the $(1\bar{3}\bar{2})$ direction, with a predicted pattern for this orientation shown in (c). Molecular models of this crystal structure are shown in (d) and (e), and the VOPc crystal directions are shown on the image in (a).

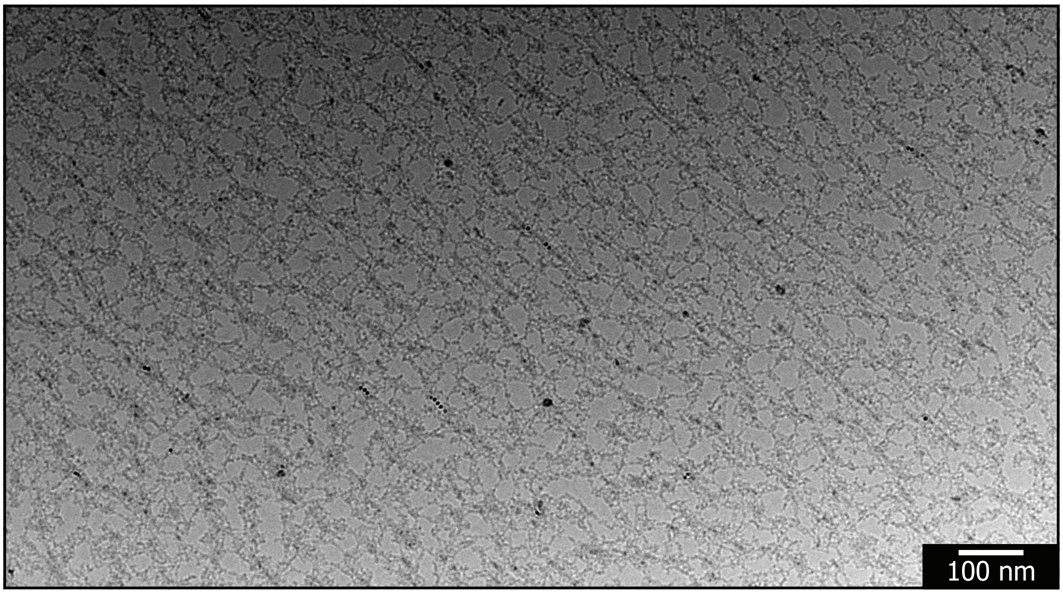

Figure 5.5: A low-magnification acTEM image of graphene after transfer to a SiN TEM support. Contrast in this image results from amorphous remnants from the transfer procedure, with holes representing freely suspended graphene.

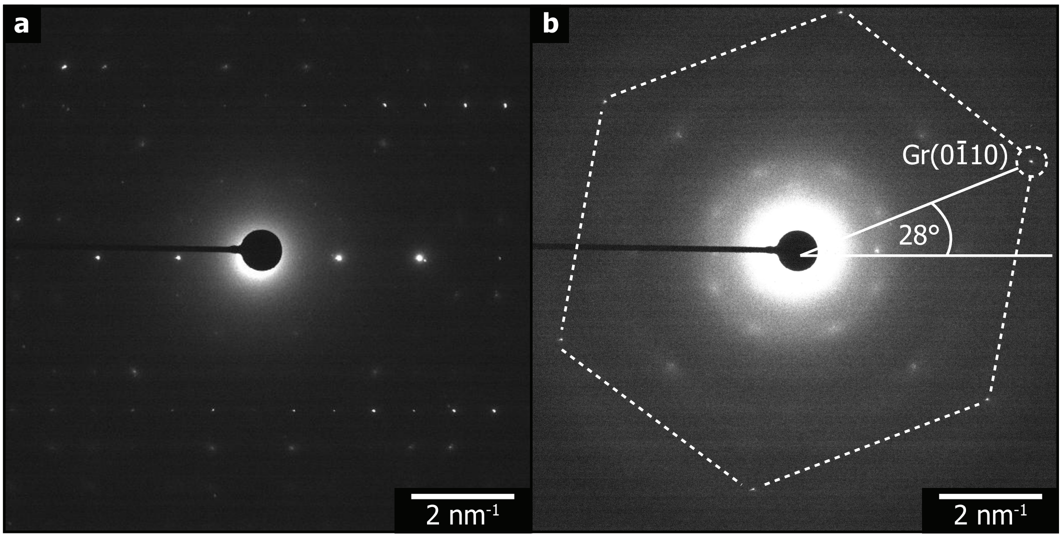

Figure 5.6: Measuring the VOPc orientation relative to graphene. (a) TEM diffraction from within a single VOPc grain. (b) after electron exposure, the intensity of the VOPc diffraction spots has significantly reduced, and the graphene diffraction spots become more visible. The relative angle between VOPc (110) and graphene $(0\bar{1}10)$ is $28°$ as marked.

and graphene: the VOPc molecules have an edge-on arrangement relative to the graphene but each island has a random in-plane orientation.

Further insight into the crystallographic arrangement within the islands can be gained from high resolution imaging. Figure 5.7 shows low-dose acTEM of VOPc deposited on graphene at $155°$C. The high resolution images resolve the lattice planes, as in figure 5.7(b), which is from two separate islands. Fast Fourier transforms (FFTs) from regions within each island show distinct spots, which in areas 1 and 2 correspond to lattice spacings consistent with the (110) and $(\bar{1}\bar{1}0)$ planes as expected from the electron diffraction pattern. The two regions demonstrate the change of orientation between islands. Multislice TEM image simulations of the molecular orientations shown in figure 5.4 are also shown in figure 5.7 and again match well with the experimental images.

The lattice resolution images in areas 1 and 2, are from near the edge of the islands, as marked. In the region closer to the centre of the island, area 3, the FFT shows spots from (110) planes and further spots that can be identified as from (221)

planes of VOPc. These arise from molecules stood up on the graphene surface but that are tilted by 2° from the $[1\bar{3}\bar{2}]$ direction. Molecules oriented in this way are only seen near the centre of the crystalline island and could be indicative of a small amount of strain within the islands due to thermal stress on cooling, although this could be an imaging artefact caused by the electron beam damage.

Ambient temperature deposited films

TEM analysis of VOPC films deposited at room temperature shows a very different nanoscale crystallography to the single crystal islands at high temperature. The granular film morphology shown in the bright field TEM image in figure 5.8 is consistent with that observed in AFM, with grain sizes of order 10s of nanometres across. Panel (b) shows a low-dose selected-area electron diffraction pattern from the area circled in white: the hexagonal spots due to the underlying graphene can be resolved (and are indexed) as well as rings due to VOPc. The rings indicate no epitaxial alignment relative to the graphene; the grain size is smaller than the film thickness so it is not easily possible from the electron diffraction to determine the orientation of the VOPc at the graphene surface. However, high resolution images, figure 5.8(c), confirm that the grains are crystalline.

5.2.4 VOPc deposition on graphene oxide

As well as being dependent on the growth temperature, the island size and nucleation density are dependent on the substrate-molecule interaction. For comparison, the morphology of VOPc deposited onto graphene oxide (GO) and silicon oxide is presented next.

Figure 5.9 shows AFM of VOPc/GO/SiO_2. This shows a surface covered with islands that are roughly 50 nm across, which can be assigned to the VOPc deposition. In the centre of the image, these islands appear lighter than on the outside. This is due to a GO flake in the centre that is increasing the height of islands. There is also a subtle change in the morphology of the VOPc islands between the GO surface and the SiO_2 surface, examined quantitatively by calculating HHCFs for both regions.

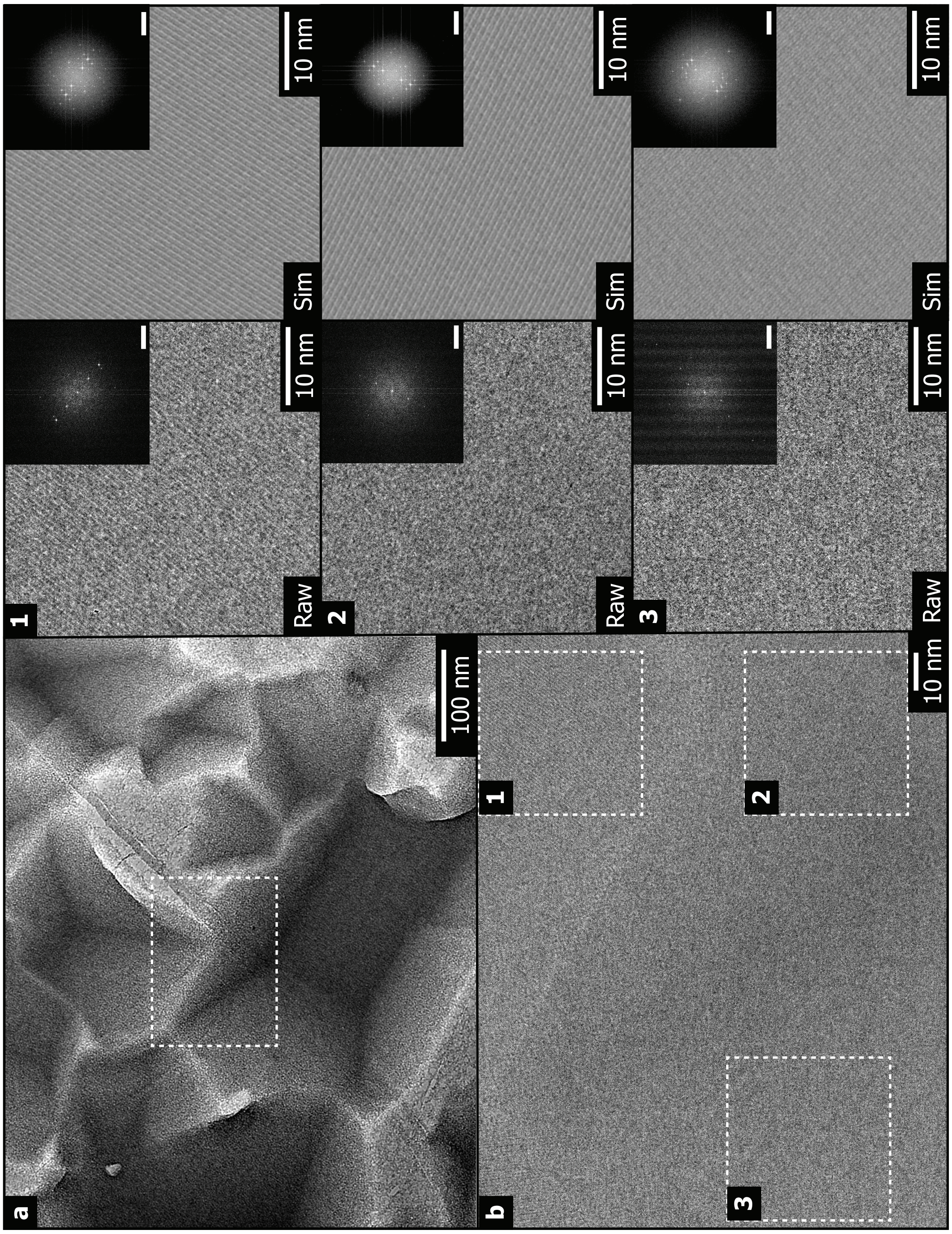

Figure 5.7: acTEM of VOPc deposited onto a graphene coated TEM grid at 155°C. (a) shows a low-magnification image. (b) is a higher magnification image of the region marked in (a). Sections of this image are highlighted in the right panes, with FFTs inset. Next to these are multislice simulations of the expected crystal structure, again with their FFTs inset. The FFT scale bars are 2 nm^{-1}.

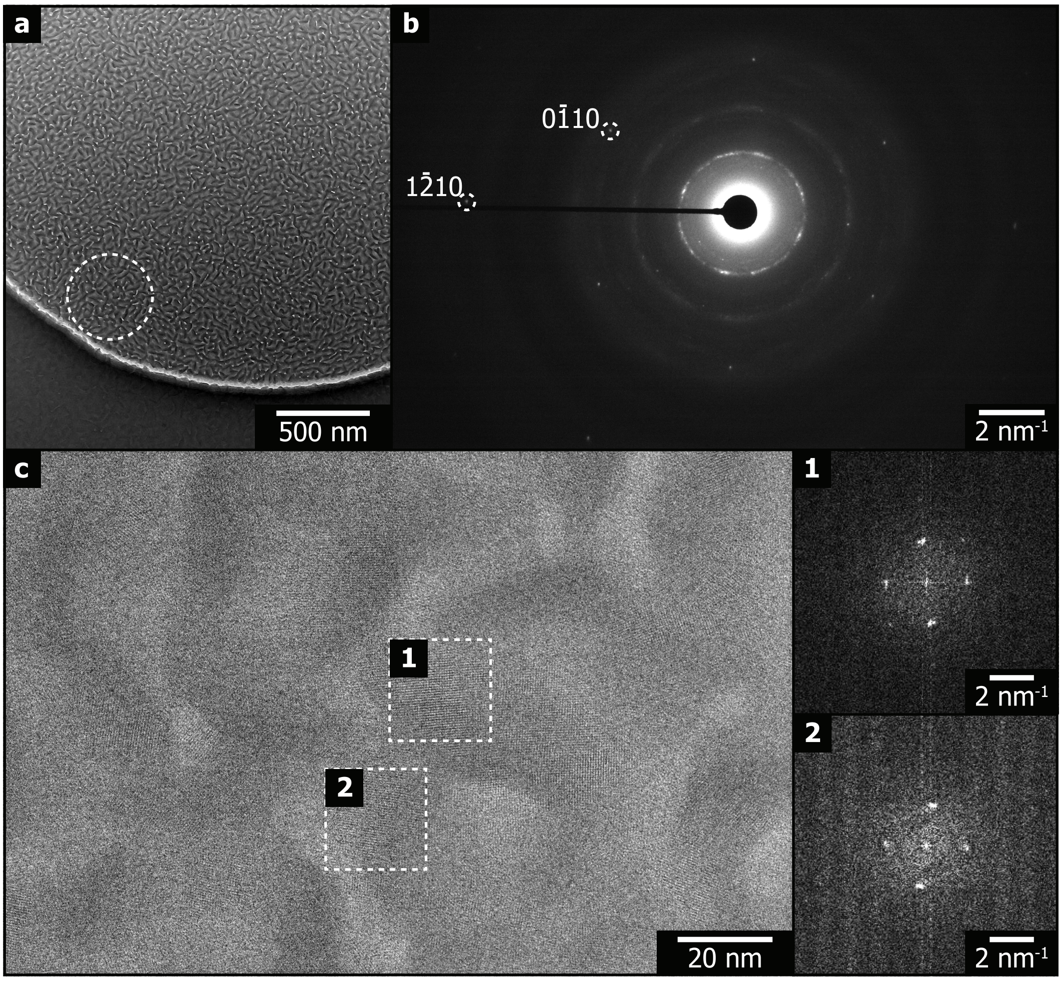

Figure 5.8: TEM of a VOPc film deposited onto graphene at 26°C. (a) shows a low-magnification image of a VOPc coated region. The film morphology is similar to that observed in AFM measurements. (b) is a diffraction pattern from the region marked in (a). The graphene spots are labelled. Also present are rings indicating a polycrystalline VOPc film. (c) is high magnification image, with FFTs of the marked regions. These show that within the film there are crystalline domains around 10 nm across.

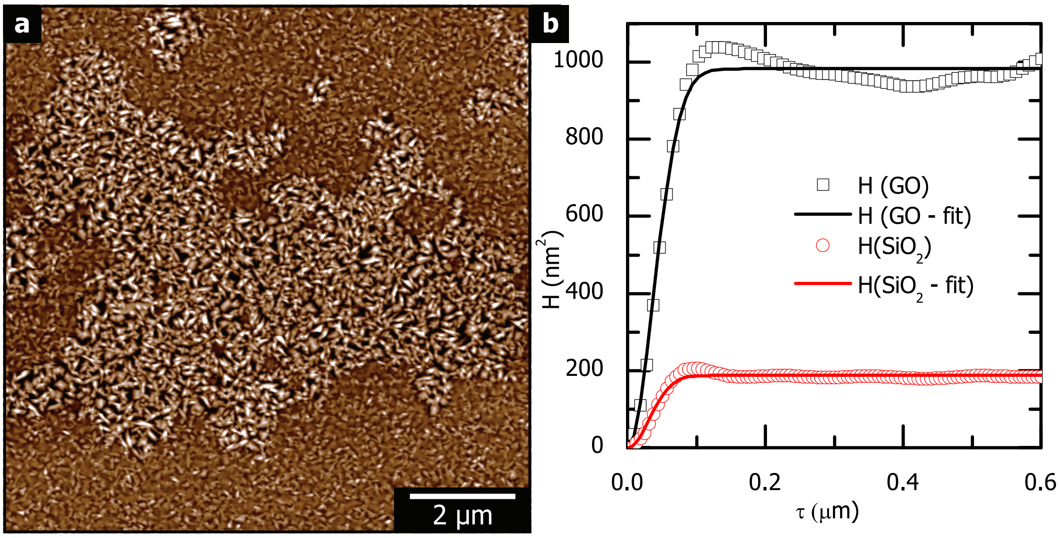

Figure 5.9: (a) AFM of GO on SiO_2 after deposition of VOPc at 155°C. The height increase (lighter) in the centre of the image shows the presence of a layer of GO. 70 nm full height scale. (b) HHCF calculated from the GO and SiO_2 regions. Fit parameters for these are shown in table 5.1.

Substrate at 155°C	ξ [nm]	σ [nm]
GO	54 ± 3	22.0 ± 0.4
SiO_2	44 ± 4	9.7 ± 0.3

Table 5.1: HHCF fitting parameters from the GO and SiO_2 regions of figure 5.9(a). A small but significant increase in the correlation length suggests larger grains on GO than SiO_2.

The HHCFs calculated for both regions are shown in figure 5.9(b). The parameters of the fits from both distributions are shown in table 5.1. The correlation length (ξ) increases slightly for GO compared to SiO_2. This suggests that there are larger grains on the GO than on the SiO_2. This increase would be consistent with the GO surface promoting faster diffusion and encouraging larger grains in comparison to SiO_2. These are, however, much smaller than the grains on graphene, demonstrating the important effect of the surface functionalisation of GO in reducing this diffusion when compared to graphene.

The roughness parameter (σ) increases from (9.7 ± 0.3) nm on SiO_2 to (22.0 ± 0.4) nm on the GO. This roughness change is also clear in the AFM image, with shallower gaps between the VOPc islands on SiO_2 than GO. For both GO and SiO_2, the morphology is quite different from those on graphene deposited under the same conditions. This is primarily associated with the heterogeneous surface of GO and SiO_2 compared to graphene.

Figure 5.10 shows TEM of VOPc deposited onto GO on a lacy carbon support at a substrate temperature of $155°$C. Panel (a) shows a low-magnification TEM image. The dark area around the outside of the image is the copper mesh support. Inside this, the darker contrast of the lacy carbon support is clear, as well as holes in the support. There are islands of darker contrast covering the support and these are islands of deposited VOPc. At the top of the image, these islands can be seen on the holes in the support, and these are islands that have been deposited onto freely suspended GO. The edge of this flake can be seen by the change in coverage.

Figure 5.10(b) shows an increased magnification image. In this image it is clear the VOPc islands are deposited onto the virtually transparent GO support. The islands are generally smaller than those deposited onto graphene, and there are two distinct morphologies present: along with the roughly square islands seen before, there are also long, thin islands, not observed on the graphene supports. Finally, panel (c) shows the diffraction pattern from a single VOPc island. This pattern is consistent with patterns seen for VOPc molecules on graphene, suggesting the molecules are adopting the same structure as for when deposited onto graphene, the $(1\bar{3}\bar{2})$ orientation.

VOPc was also deposited onto a GO covered lacy carbon support with ambient substrate temperature, and this is shown in figure 5.11. Panel (a) shows the lacy carbon support covered with a dark contrast film. This film is incomplete and missing in the top left and bottom right of these images. These holes are regions with no GO support. Higher magnification images of the film (b) show a thin film with grains around 10 nms in size. These grains are VOPc, and they seem to display the same morphology as those deposited at ambient temperature on a graphene surface. Finally, a diffraction pattern in panel (c) shows spots consistent with graphene, with >3 hexagonal arrays of spots representing >3 layers of GO in this region. Within these spots are rings, which represent VOPc. The rings in the diffraction pattern

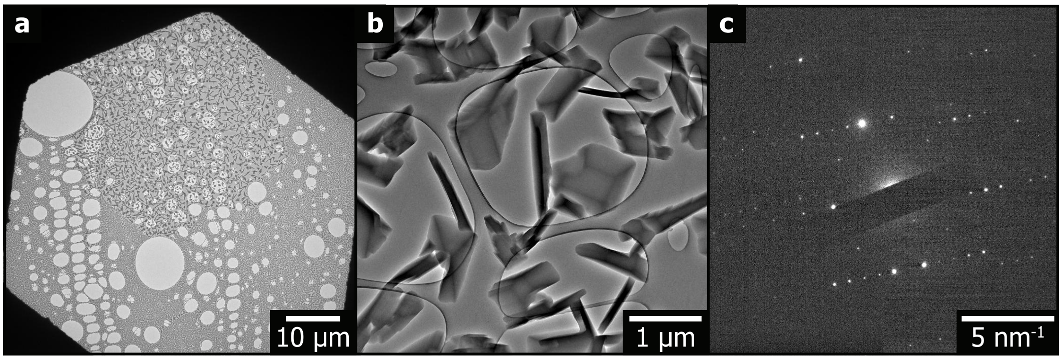

Figure 5.10: VOPc deposited onto GO on a lacy carbon support at 155°C. (a) low magnification image where a hexagonal GO flake is visible covering the support at the top of the image. (b) higher magnification image of islands of VOPc on GO. (c) diffraction pattern, suggesting the same molecular orientation as for the films deposited on graphene.

show the polycrystalline nature of VOPc deposited onto GO at ambient temperatures.

The comparison between suspended GO and GO supported on silicon oxide shows the importance of the underlying substrate: graphene and GO films follow the substrate topography, and for rough substrates such as silicon oxide that results in local strain and curvature in the film that increases interactions with molecules. This in turn reduces the molecule's diffusion rate, and hence increases the nucleation rate. By comparison graphene on copper is locally atomically flat, as shown in previous STM investigations [159], which aids the increase in OSC grain size. However, at larger scales facets do appear, and inspection of the AFM images of the high temperature depositions in figure 5.1 suggests that the VOPc islands form along facets on the Gr/Cu surface. This suggests that the VOPc grain size on graphene could be increased further still by using a flatter substrate, such as hexagonal boron nitride.

5.3 Conclusions

In summary, single crystals of VOPc several micrometres across can be grown on CVD-grown graphene using elevated substrate temperatures of 155°C. This is in

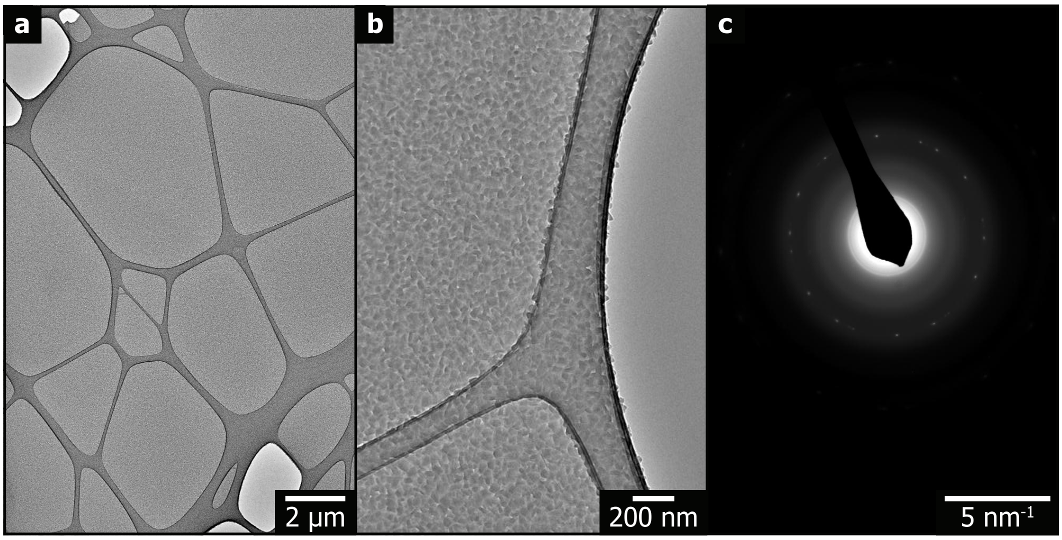

Figure 5.11: VOPc deposited onto GO on lacy carbon support at ambient temperature. (a) low-magnification image demonstrating VOPc coverage where GO is present; holes in the top left and bottom right are empty. (b) higher-magnification of VOPc covered GO sheet. The grains are again 10s of nms across. (c) a diffraction pattern from a typical region. There are approximately 3 distinct sets of graphene spots, indicating roughly 3 sheets of GO in this region. There are also rings present, suggesting a polycrystalline VOPc film.

contrast to deposition on graphene at ambient temperatures, where VOPc grains grow to only 10s of nanometers across. No epitaxial relationship is observed between the deposited VOPc molecules and the graphene, so the increase in grain size is not directly linked to van der Waals epitaxy. However, it is due to the van der Waals nature of the graphene surface and demonstrates a further advantage of using van der Waals substrates like graphene with OSC thin films: the weak interaction encourages high diffusion rates, which promote ordered OSC films.

Moreover, these large grains form only on the homogeneous graphene surface; on the heterogeneous surfaces of graphene oxide and silicon oxide, grain sizes are an order of magnitude smaller. This reduced grain size is likely caused by a reduction in diffusivity of molecules during the growth process. This lower diffusivity is a result of the surface functionalisation and roughness of the substrate.

van der Waals epitaxy of OSCs on graphene can only be achieved for a limited set of molecules. However, these results show that the weak interaction between graphene and molecules should promote the formation of more ordered OSC films without the need for order-inducing layers. To capitalize on this, it will be important to utilize clean graphene (with little surface functionalisation), and to minimise the roughness of the underlying substrate.

Chapter 6

Monolayer to thin film transition in supramolecular assemblies on graphene.

6.1 Introduction

Supramolecular assembly is intensively studied as a route to bottom-up synthesis of nanomaterials, among other areas [104]. In these assemblies, molecules or ions interact through non-covalent forces (like van der Waals and hydrogen bonding) to create macroscopic structures. In many examples, the substrate also plays a role in the self-assembly, which again interacts with the overlayers through non-covalent forces [107], [201].

Traditionally, self-assembly of organic molecules has been studied with STM [106], [114]. This gives accurate structural information at the molecular scale when studying self-assembly on conductive substrates like highly ordered pyrolytic graphite (HOPG) or Au(111) [106]. However, it is difficult to get information about the out-of-plane structure from STM, and so studying anything more than a monolayer is challenging.

In this chapter the self-assembly of trimesic acid (TMA) and terephthalic acid (TPA) is studied. By depositing these molecules in UHV directly onto freely suspended graphene, TEM can be used to study simultaneously the crystallography of graphene and the molecules, and how the 2D assembly transitions to the 3D structure. This is different for each molecule studied here, despite their chemical similarity: 2D supramolecular assembly of TMA results in a chicken-wire form, with further layers growing in registry of this template up to a film thickness of 20 nm. On the other hand, 2D supramolecular assembly of TPA forms a brickwork structure, but thin films show a clear transition to the bulk 3D structure, producing fibres on the surface that grow with increasing thickness. In both cases, the graphene substrate causes epitaxial growth of the molecular layers, but one that is much stronger for thin films of TMA than for TPA. This provides another example of van der Waals epitaxy in graphene heterostructures.

6.2 Results and Discussion

6.2.1 Monolayer structure of TMA and TPA

First, the monolayer structure of TMA and TPA on graphene was investigated using STM. This work was undertaken by Prof. Giovanni Costantini's group, but is included here to aid comparison with TEM. Both molecules were deposited by OMBD in UHV onto graphene-coated copper foils. Deposition for all samples was performed by Dr Luis Alves Perdigao. TPA or TMA molecules were loaded into a crucible within a chamber that was then evacuated to 10^{-5} mbar. The crucible was heated to $\approx 270°$C, which was adjusted to keep the deposition rate constant at 0.01 nm/s. The graphene foils (at ambient temperature) were then placed in front of the molecular beam for the deposition time.

For STM measurements, the deposition time was 6 minutes. The foils were then removed and imaged in ambient STM under a drop of heptanoic acid; when imaged without heptanoic acid, the molecular films are often too thick and too mobile to acquire clear images by STM.

Figure 6.1(a) shows STM of TMA on graphene-coated copper. There are

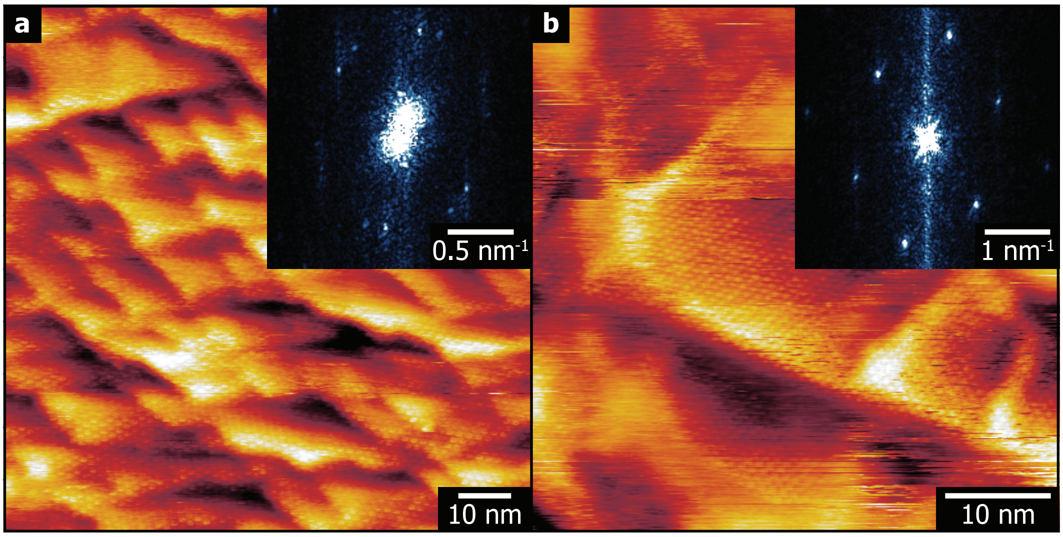

Figure 6.1: STM of TMA (a) and TPA (b) on graphene-coated copper foils. For both films, the presence of the copper facets is clear in larger scale structures. Along with this are pointlike features that are highlighted in the inset FFTs. For TMA, a pair of hexagonal arrays of spots is present, indicating two orientations of the chicken-wire structure. For TPA, the spots demonstrate a brickwork structure. STM parameters for: (a) $V = -1.3$ V, $I = 0.05$ nA; and (b) $V = -1.5$ V, $I = 0.08$ nA. Images taken by O. De Luca.

height edges visible in the scan with a pitch of around 5 nm and these represent the faceting of the graphene-copper surface, as discussed in chapter 3. Along with the copper topography, there are regular pointlike features across the surface. These are seen more clearly in the inset FFT, which shows two hexagonal arrays of spots, with a separation between the pair of $(14 \pm 2)^\circ$. In other regions, half-and-half images were taken — where both the overlayer (TMA) and substrate (graphene) can be resolved in different halves of the same STM image by changing the tunnelling parameters halfway through a scan. This allows STM images to be calibrated from the known graphene lattice underneath. The lattice spacings of the TMA spots was measured as (1.66 ± 0.06) nm. A hexagonal array with this spacing is consistent with TMA taking on the chicken-wire structure [109], [110], [202], with two different in-plane orientations.

Figure 6.1(b) shows TPA deposited and imaged under the same conditions as for TMA. Again the graphene-copper topography is clear from the facet-like height changes. Regular pointlike features are also visible, and these are again highlighted in the inset FFT. Again, from half-and-half images, the lattice parameters are found to be $a_1 = 0.95 \pm 0.1$ nm and $a_2 = 0.72 \pm 0.6$ nm, with the angle $\gamma = (52 \pm 4)^\circ$ between them. These lattice parameters are consistent with the TPA brickwork seen before for TPA on HOPG and on graphene on Pt(111) [113].

In summary, STM shows that a monolayer of TMA forms a pair of chicken-wire structures that are rotated by $(14 \pm 2)^\circ$ relative to one another. For TPA, a single-orientation of the monolayer brickwork structure is seen in images of this scale.

6.2.2 Thickness calibration for thin film deposition of TMA and TPA

To investigate thin films of TMA and TPA molecules, longer deposition times were used. The thicknesses of these films were measured using AFM. Figure 6.2 shows measurements of film thickness for the TMA and TPA depositions onto graphene on copper. Panel (a) is a tapping mode AFM topography image of an 18 minute-deposition film of TPA on graphene on copper after a trench has been cut into the film. The trench is cut by repeatedly scanning a smaller region in contact mode. The deflection setpoint — and hence the force exerted by the tip onto the surface — is gradually increased until the images appear unchanged after repeated scans; this demonstrates that the mobile material has moved and that the harder graphene-coated copper surface is now being imaged. After this, the larger area can be imaged in tapping mode, which preserves the film.

Figure 6.2(a) shows a film with fibrous features (discussed later in section 6.2.6) that indicates the presence of the TPA thin film. There are also diagonal height changes across the image, which show the faceting of the graphene-copper surface underneath. In the centre of the image is a dark rectangle, which represents a sharp decrease in height, and is assigned to the trench. Around this rectangle are white regions (increases in height), and these represent the material moved to the edges of the trench during the cutting.

The height changes around the trench are more clearly seen from the line

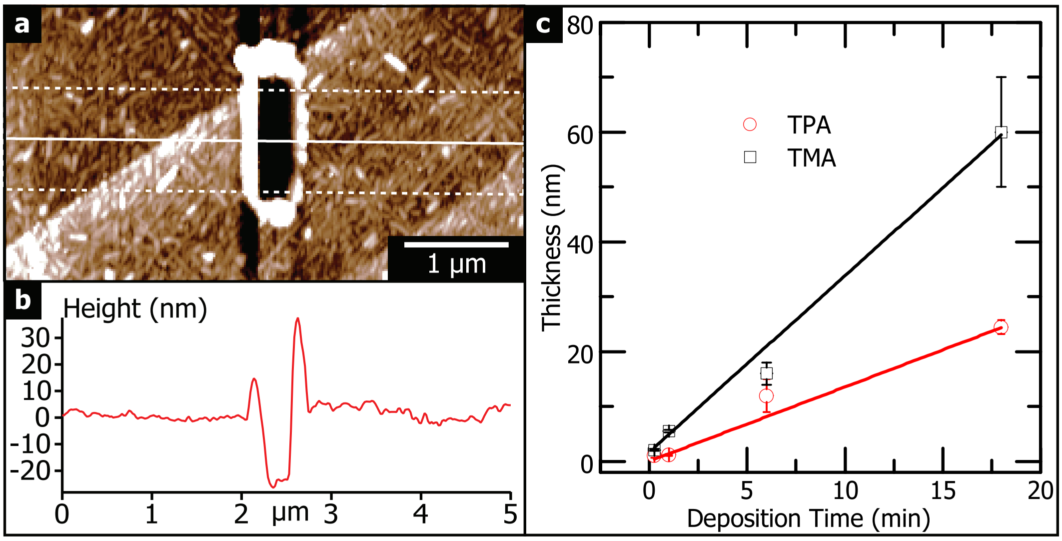

Figure 6.2: Measuring the thickness of TMA and TPA thin films. Tapping mode AFM (a) of an 18 minute-deposition of TPA on graphene on copper, shows a trench cut in the film to measure the thickness. A height profile of the trench (b) is used to measure the thickness as 27 ± 2 nm. These measurements are repeated for each deposition time for both molecules and the results are shown in (c).

profile of the white boxed region indicated in (a), which is shown in panel (b). The line profile shows the TPA surface as almost flat, the depth of the trench at the centre, and the height of the removed material around the edges. The film thickness here is measured as 27 ± 2 nm.

Figure 6.2(c) shows the results of these measurements on each deposition time used for both TMA and TPA. Both films increase linearly with time, demonstrating the constant deposition rate for each. However, even though the deposition rate was consistent for all films (as measured by a quartz crystal microbalance (QCM)), the TMA films are thicker than the TPA films at each deposition time.

6.2.3 Electron diffraction from TMA thin films

TEM diffraction was used to investigate the ordering of TMA thin films deposited onto graphene. Graphene was transferred to SiN TEM grids using the procedure described in section 2.1, using a fromvar support, which was later removed by submerging in chloroform, then acetone, then drying with a critical point dryer. The

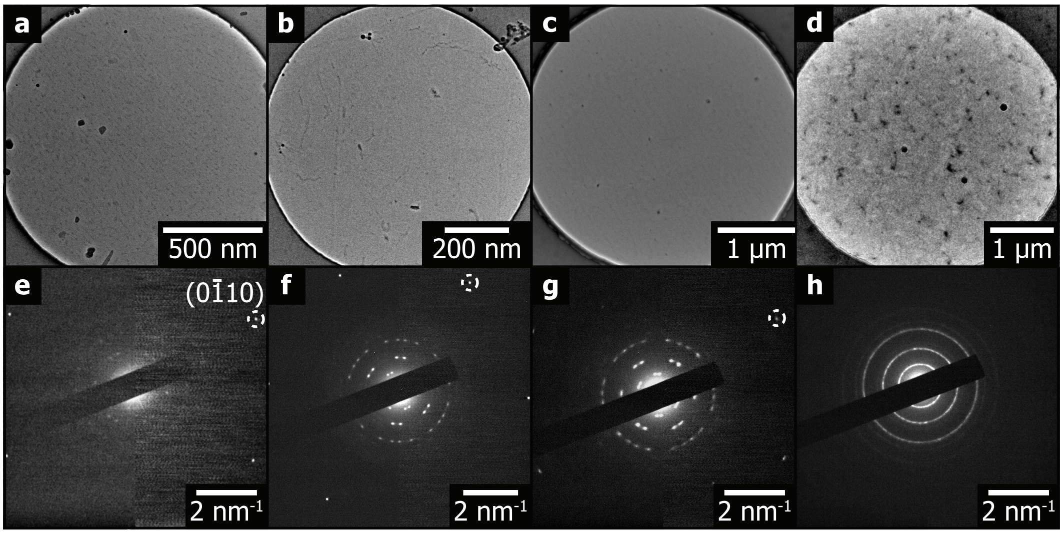

Figure 6.3: TEM imaging of 15 seconds-deposition (a), 1 minute-deposition (b), 6 minute-deposition (c), and 18 minute-deposition (d), deposited onto graphene coated TEM grids. (e)-(f) shows the corresponding electron diffraction patterns with the graphene $(0\bar{1}10)$ spot labelled in each. The hexagonal arrays of spots from the chicken-wire TMA structure are present up to 18 minutes deposition, when these are replaced by polycrystalline rings with the same spacings.

grids were heated for 2 hours on a hotplate. After this, the grids were loaded into UHV with a molecular source. A QCM was used to stabilise the rate of deposition and the grids were placed in the molecular beam for the deposition time. This was varied between 15 seconds and 18 minutes to produce films of different thickness. Once the deposition was complete, the grids were removed from UHV and transferred to the TEM.

Figure 6.3 (a)-(d) show low-magnification images of the TMA coated graphene TEM grids of increasing deposition time: (a) 15 seconds, (b) 1 minute, (c) 6 minutes, and (d) 18 minutes. At the edges of the images the darker contrast from the SiN is clear, and the hole in the centre is graphene coated. Within this hole there are darker contrast features often seen for pristine graphene-coated TEM grids, and are assumed to be remnants from the transfer.

From these images alone, there appears to be little evidence of the TMA film. However, after 18 minutes deposition time there is darker contrast across the hole, which could point to a thicker film. In all cases, the lack of clear features in these

Deposition time	a_1 (nm)	a_2 (nm)	γ (°)
Monolayer (STM)	1.66 ± 0.02	1.7 ± 0.1	60 ± 1
15 seconds	1.64 ± 0.02	1.64 ± 0.02	60 ± 1
1 minute	1.64 ± 0.02	1.64 ± 0.02	60 ± 1
6 minutes	1.65 ± 0.02	1.65 ± 0.02	60 ± 1
18 minutes	1.64 ± 0.02	1.64 ± 0.02	60 ± 1

Table 6.1: Lattice parameters for each thickness of TMA on graphene. The parameters are consistent with the chicken-wire structure for each film thickness.

images suggests the TMA does not form any distinct structures after deposition, and instead forms a uniform thin film.

In panels (e)-(h), selected-area (500 nm aperture) diffraction patterns for each thickness are shown. For all films except 18 minutes, a hexagonal array of spots with spacings consistent with graphene can be seen at the edges of the patterns. This points to a single layer of graphene in these regions. These spots are not visible in the 18 minute film because diffraction from the thick film dominates the intensity.

Along with the graphene spots, there are other diffraction spots at smaller spacings. The corresponding lattice parameters for these spacings are shown in table 6.1. The lattice parameters were consistent within uncertainty for each thickness. The spacings and symmetry point to the chicken-wire structure for TMA. Further, there are two dominant orientations of the structure across the selected-area electron diffraction pattern. These two orientations were always seen at the same relative orientation to the $(0\bar{1}10)$ graphene spots. Patterns of this form were the only type observed and there is no evidence of the flower structure from these patterns.

For the 18 minute-deposition the diffraction pattern is different. There are now rings in the pattern, and the rings have spacings that correspond with the spots seen in the thinner films. This suggests that the same TMA chicken-wire structure is still present, but instead of just two in-plane orientations, many orientations are formed. This results in the polycrystalline rings seen in the diffraction pattern.

To understand more about the structure of the films, high-resolution TEM can be used. Before that, however, it is necessary to understand the effect of the electron dose on the films.

6.2.4 Critical electron dose for TMA thin films

The use of electron microscopy to study organic thin films is restricted by the lifetime of the organic molecules, and their supramolecular structure, under the electron beam. To quantify this lifetime, diffraction patterns from organic thin films can be analysed to find the critical dose — defined as the dose after which the diffraction spot intensity has been reduced by a factor 1/e, and the structure is believed to have been significantly damaged.

Figure 6.4(a) to (d) show four images from a sequence of diffraction patterns that were recorded continuously over 38 seconds, with a diffraction pattern acquired every 0.3 seconds, from a 1 minute-deposition of TMA. The time of each image is in the bottom left corner. Throughout the exposure, the dose rate was kept constant at $(1.3 \pm 0.3)\ \mathrm{e}^{-}\mathrm{\AA}^{-2}\mathrm{s}^{-1}$. The spots previously attributed to TMA are clear, as are those from graphene. From the series it is apparent that the TMA diffraction spots reduce in intensity with increasing dose time, and are not visible after 33 seconds.

The intensity in a diffraction peak can be quantified by summing the intensity in a small box around the diffraction peak, and then subtracting this value by the average background intensity at the same radius. This is repeated for each image in the sequence. Three diffraction peaks for the TMA are chosen, one from each order of the diffraction pattern, and one diffraction peak for the graphene. The resulting intensities are plotted against exposure time in figure 6.4(e).

For the graphene diffraction spot, the intensity remains constant throughout the exposure. This suggests only negligible damage to the graphene lattice during this exposure. Despite an accelerating voltage of 200 kV, the dose is three orders of magnitude lower than what would be expected to damage graphene [203], [204], and so graphene is preserved on these timescales.

On the other hand, for all the TMA diffraction peaks there is an exponential decrease in intensity. This demonstrates a disruption to the crystal structure of the TMA layer. After the total exposure, there are no diffraction spots, consistent with a disordered material. The most likely cause of this damage is radiolysis from the

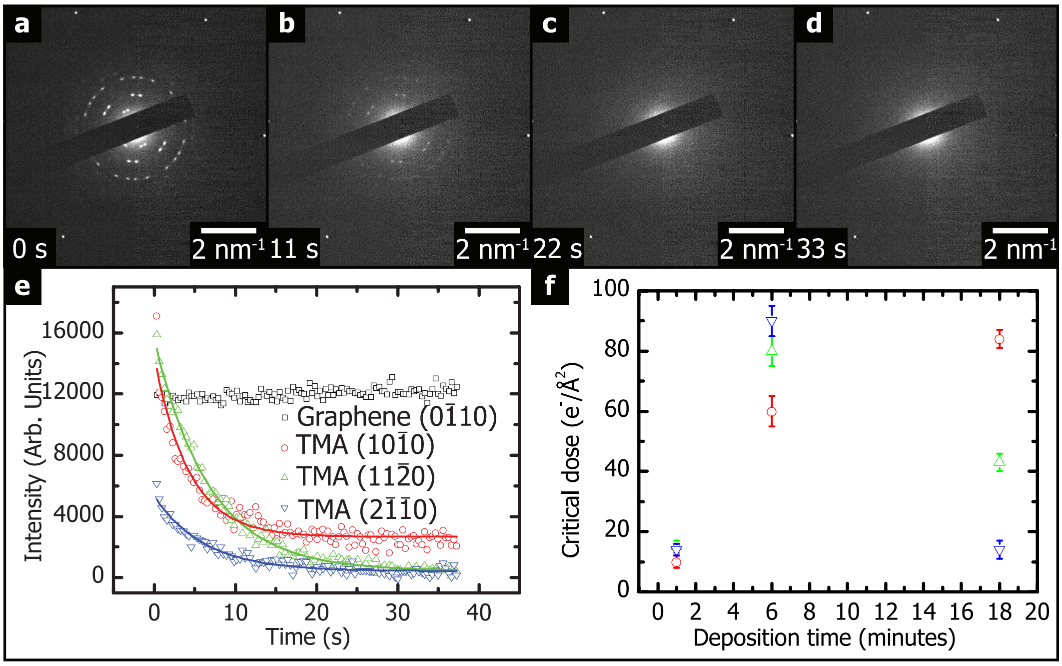

Figure 6.4: Measuring the critical electron dose for TMA thin films. (a)-(d) shows diffraction patterns from a series taken from the same area with increasing time. Plotting the intensity of the diffraction spots, (e), shows exponential decays of intensity, caused by the damage from the electron beam. The characteristic time of the decay — the critical dose — is plotted for the 1, 6 and 18 minute-depositions in (f).

electron beam: the TMA layers are unlikely to be able to dissipate charge introduced by the electron beam, and ionisation damages the crystal structure [205], [206].

The intensity decays in figure 6.4(e) are fit with exponentials of the form

$$y = A \exp\left(-\frac{x}{T_C}\right) + y_0 \tag{6.1}$$

with A, y_0 and T_C free parameters. T_C is then the critical time, which is related to the critical dose as $D_C = D \times T_C$, with $D = (1.3 \pm 0.3)\ \mathrm{e}^{-}\mathrm{\AA}^{-2}\mathrm{s}^{-1}$ the measured dose rate as before. The critical dose is calculated for each diffraction spot from the 1 minute-deposition film and the results plotted in panel (f). Also plotted are those calculated for the thicker TMA films. A critical dose was not calculated for the 15 second-deposition because the intensity is too weak to provide an accurate measure.

For the thicker films, different decay rates are seen for different diffraction spots. One explanation for this is that damage occurs at different rates to different crystallographic planes. Effects of this kind have been seen before for copper phthalocyanine thin films [207]. In this case, some diffraction spots even increased in intensity during the exposure to the electron beam. This was explained by the formation of a different atomic structure in the film that was more resilient to the electron dose, termed a relatively stable matrix. These matrices form as the films are damaged by the electron beam. Therefore, certain structures within the film could be more stable than others.

Another explanation is that the intensities immediately after exposure to the beam are the most important to finding the critical dose, but are also experimentally the hardest to capture. To improve on this, the low-dose techniques used here would need to be developed to minimise the damage caused to the film before information is captured.

The thickness dependence of the critical dose provides an insight into the damage mechanism of the organic films. A thicker film would increase the interaction volume for the high-voltage electrons, and so a faster damage rate would be expected. At the same time, a thicker film has more structure to be damaged, and

Deposition time	Critical electron dose ($\mathrm{e}^{-}\mathrm{\AA}^{-2}$)	
	TMA	TPA
1 minute	13 ± 3	40 ± 20
6 minutes	100 ± 50	130 ± 50
18 minutes	50 ± 40	60 ± 20

Table 6.2: Critical electron doses for thin films of TMA and TPA.

so ultimately, the critical dose should not depend on thickness. However, here there does seem to be a higher critical dose for thicker films for TMA, suggesting a more complicated mechanism than this simple one.

In contrast to what is seen for TMA, a 15 second-deposition of TPA displays a remarkably different behaviour under the electron radiation. At low dose rates ($\approx 1\ \mathrm{e}^{-}\mathrm{\AA}^{-2}\mathrm{s}^{-1}$ used for diffraction patterns) the TPA structure was stable for > 20 minutes (a critical dose $> 1200\ \mathrm{e}^{-}\mathrm{\AA}^{-2}$), which is significantly more robust than the TMA 15 second-deposition film. However, under imaging with higher doses ($\approx 100\ \mathrm{e}^{-}\mathrm{\AA}^{-2}\mathrm{s}^{-1}$) the film was damaged in comparable times. This can be explained by considering the radiolysis damage mechanism. For low electron dose rates, the charge created by the electron beam can be transported away efficiently by the graphene support without causing damage. This phenomenon has been seen before: 2D semiconductors encapsulated in graphene remain stable under the electron beam for much greater times [208]. Thicker films are not able to transport this charge away efficiently and so suffer increased damage. On the other hand, for larger electron dose rates, the charge created is greater than what can be effectively removed, and damage occurs.

In summary, the critical electron dose was measured for thin films of TMA and TPA, with the results summarised in table 6.2. There was no discernible difference in critical electron dose between films of TMA and TPA. The large uncertainties on these measurements reflect the difficulty of measuring critical electron dose for these delicate samples.

6.2.5 High-resolution TEM of TMA thin films

HRTEM can be used to gain more insight into the structure of TMA on graphene. The procedure to acquire HRTEM was as described in section 2.2.3. The electron dose rate at the increased magnification was tuned so that the thin film would be exposed to the critical dose in a 0.3 second camera exposure; this was $\approx 60\ \mathrm{e}^{-}\mathrm{\mathring{A}}^{-2}\mathrm{s}^{-1}$ for the 1 minute-deposition film.

Figure 6.5 shows HRTEM of a 1 minute TMA deposition on a graphene coated TEM grid. The image in panel (a) is noisy because of the low dose of electrons used. However, an FFT calculated from the large white box shows spots, which demonstrates that there is sufficient signal to determine structural features. This FFT resembles that seen in diffraction patterns of the same films: the same pair of hexagonal spots is present and the spacings are consistent with those measured from the diffraction patterns. This suggests TMA is present in this region in the chicken-wire structure.

FFTs from smaller regions are shown in the bottom panels of figure 6.5. These FFTs each show the same hexagonal array as before (with the same spacings), but crucially, not as a pair. The single array of spots shows that there are regions in the TMA thin film that are $\gtrsim 10$ nm across that present only one TMA orientation. Region 1 shows one of these orientations, while regions 2 and 3 display the other.

From the HRTEM images, it is clear that TMA forms columns that are $\gtrsim 10$ nm across that contain a single in-plane orientation of TMA. The question remains as to how the TMA molecules stack within this column. Recent DFT work has suggested that TMA molecules would stack face-on, but with the carboxylic acid groups taking alternating orientations [209]; this arrangement was found preferable to one where the molecules stacked with a single orientation of the carboxylic acid group. However, it is not possible from these TEM images to distinguish between these two arrangements.

The TEM diffraction and high resolution images together show that there are a pair of in-plane orientations. Further, by taking diffraction patterns across many different graphene grains (with different in-plane orientation themselves) it is clear

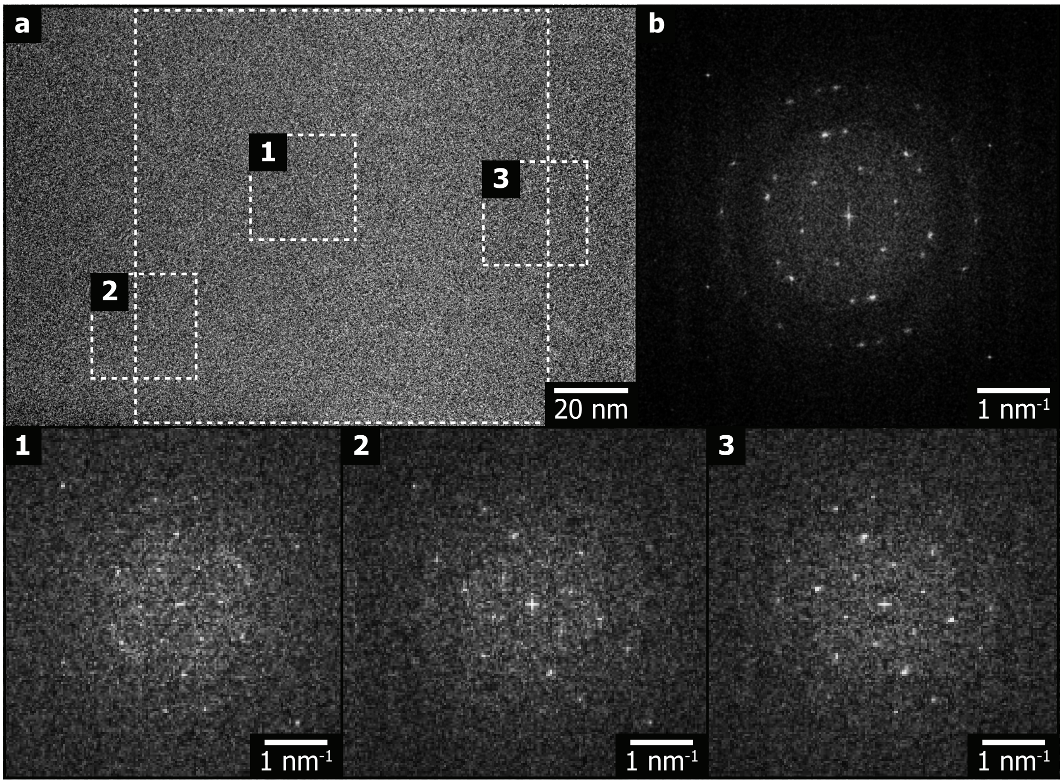

Figure 6.5: HRTEM of the 1 minute-deposition of TMA on graphene. The image (a) demonstrates substantial noise due to the low-electron dose used, but features are clear from an FFT, (b), taken from the large white box. The same pair of hexagonal arrays of spots again demonstrates the chicken-wire TMA structure. FFTs taken from smaller regions (lower panels) demonstrate regions where only a single orientation is present.

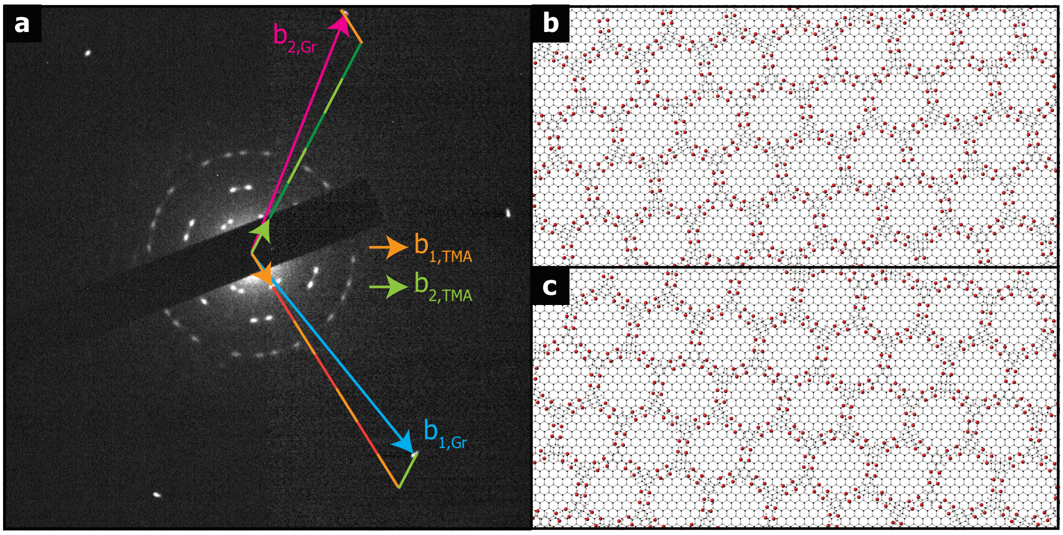

Figure 6.6: The TMA-graphene structure summarised. The 1 minute-deposition diffraction pattern (a) is labelled with reciprocal lattice vectors of TMA and graphene. These demonstrate how the TMA-graphene epitaxy arises, and results in the two structures shown in (b) and (c). Crystal models by Z. Laker.

the TMA structure has a symmetry relative to the graphene lattice. The different orientations are seen in separate domains and so this points to an epitaxial link between the TMA structure and the graphene substrate.

This epitaxial link can be understood by considering the relationship between the reciprocal lattice vectors of graphene and TMA. Figure 6.6(a) shows a diffraction pattern from another region of the 1 minute-deposition TMA film; this pattern demonstrates the same pair of TMA orientations as seen before. The reciprocal lattice vectors of graphene and TMA are overlaid onto the pattern.

From this figure there is a clear relationship between the reciprocal lattice vectors: TMA reciprocal lattice vectors can be combined to form a vector equivalent to the graphene reciprocal lattice vectors. This combination can be represented as

$$\begin{pmatrix} b_{1,\mathrm{Gr}} \\ b_{2,\mathrm{Gr}} \end{pmatrix} = \begin{pmatrix} 7 & -1 \\ 1 & 6 \end{pmatrix} \begin{pmatrix} b_{1,\mathrm{TMA}} \\ b_{2,\mathrm{TMA}} \end{pmatrix} \tag{6.2}$$

The other TMA orientation is then symmetrically equivalent. Models of these two orientations of TMA on graphene are shown in (b) and (c) of figure 6.6. This arrangement has been seen before for monolayers of TMA on HOPG using STM [201]. In this paper, the same epitaxy matrix as found here was proposed.

The fact that this epitaxial structure is seen in films up to (16 ± 2) nm thick demonstrates that the monolayer structure of TMA templates out of the plane. The chicken-wire TMA structure is formed with two orientations in the monolayer due to interactions with the graphene substrate. Subsequent TMA molecules then stack on to this structure, and the epitaxial alignment templates out to (16 ± 2) nm. While subsequent layers acquire the in-plane orientation of the previous layers, it is not clear from these images what registry these layers take.

HRTEM can also help to understand the thicker, 18 minute-deposited TMA film. Figure 6.7(a) shows a HRTEM image (taken under similar conditions as figure 6.5) of an 18 minute-deposition of TMA on graphene. Periodic features are present again, which are highlighted in an FFT (b) of the large white box in (a). The FFT shows spots that have the same spacings as seen before, suggesting the presence of TMA in a chicken-wire structure. However, there are now more than two hexagonal arrays present. Note that the spots do not have the same relative intensity around the FFT, and this is most likely caused by drift during the exposure. The increased number of spots suggests polycrystalline in-plane orientations, agreeing with diffraction patterns from the same films.

It is also possible to take FFTs from smaller regions as before. In the FFT of region 1, a single set of hexagonal spots is clear, but with another orientation weakly present. This suggests that the templating structure is still dominant in some small regions. However, now other orientations can be seen elsewhere, as demonstrated by FFTs of the other regions.

The two preferred orientations are not dominantly visible in the diffraction patterns of the 18 minute-deposition film. This suggests that soon after the 6 minute-deposition point, new and random in-plane orientations appear, rather than just a continuation of the templating of the original orientations. These new orientations also appear to template upwards, as shown by the presence of discrete spots in the FFTs of the 18 minute-deposition: random in-plane orientations across the

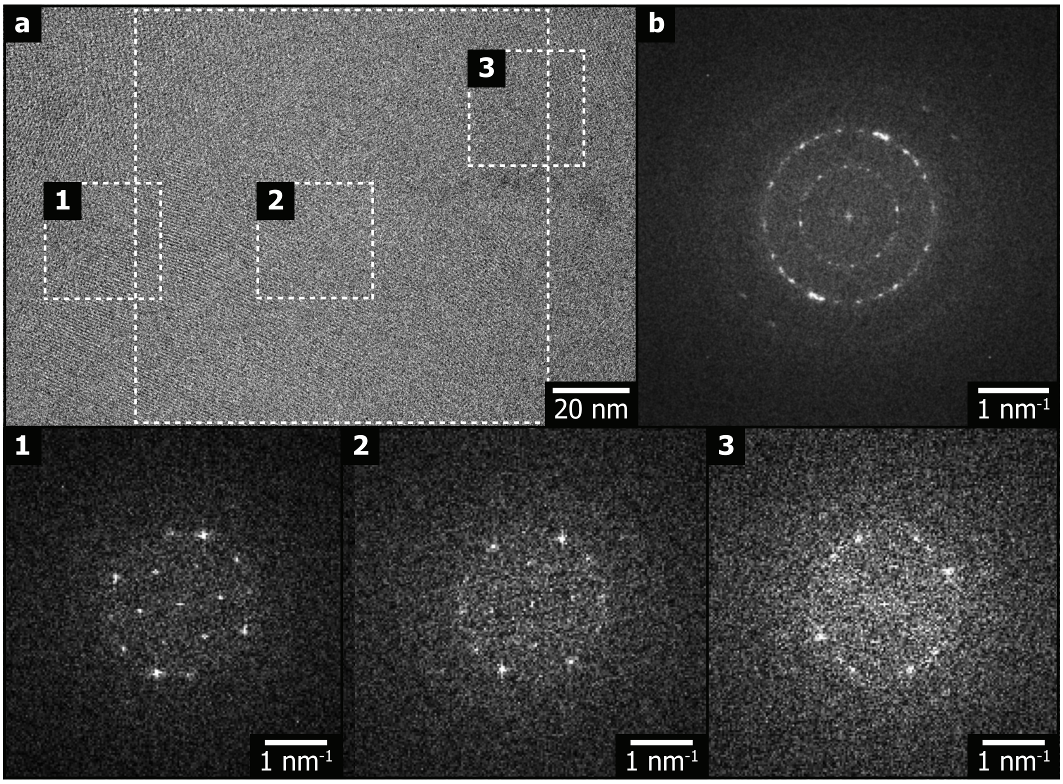

Figure 6.7: HRTEM of the 18 minute-deposition of TMA. The image (a) and the FFT (b) from the large white box demonstrate the polycrystalline nature of the TMA at this thickness. Not all the smaller regions demonstrate single orientations, suggesting randomly orientated grains are present across the film.

film would present as rings or arcs in the HRTEM image FFTs. Therefore, it appears that the TMA templating can continue the epitaxial relationship to graphene up to (16 ± 2) nm, but after that, new orientations appear, that themselves can template as the film grows.

In summary, a monolayer of TMA assembles into a chicken-wire structure with two preferred orientations relative to the graphene surface. As the film thickness increases, this monolayer chicken-wire assembly templates up through the film, with the epitaxial relationship still present for films up to ≈ 20 nm thick. After this, the TMA molecules still assemble into a chicken-wire structure, but now with random in-plane orientation. The structures seen here do not resemble the bulk structure for TMA, which contains non-planar pleats of molecules that would be seen in diffraction patterns [210].

6.2.6 Structural analysis of thin films of TPA on graphene

Next, the investigation of TPA is presented. TPA was deposited onto graphene coated SiN grids using the same procedure as before. Figure 6.8 shows TEM of a 15 second-deposition, a 1 minute-deposition, a 6 minute-deposition and finally an 18 minute-deposition of TPA. Panels (a)-(d) show low magnification images of graphene coated holes after TPA deposition. After 15 seconds, there is little contrast other than remnants from the graphene transfer. After 1 minute, the remnants are still present, but along with these there are fibres also visible, which are approximately 100 nm long. These fibres are orientated in different directions. After the 6 minute-deposition, the fibres have greater contrast, suggesting they are now thicker. Finally after the 18 minute-deposition the fibres are darker still, suggesting a further increase in thickness. These fibre features are assigned to the TPA thin films, and demonstrate that, unlike TMA (which demonstrates a layer-by-layer, or Frank-van der Merwe growth), TPA is arranging into three-dimensional structures after deposition, and so displays a layer-plus-island growth mode, or Stranski-Krastanov growth.

Panels (e)-(h) show the corresponding diffraction patterns for each TPA film thickness. For each deposition, the graphene spots are clear. As well as these, there

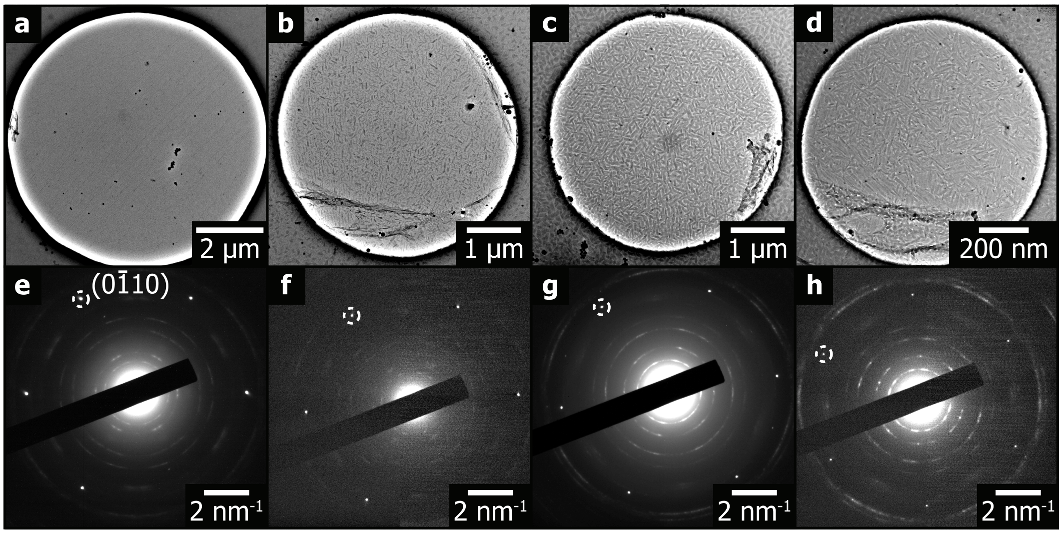

Figure 6.8: TEM imaging of 15 second-deposition (a), 1 minute-deposition (b), 6 minute-deposition (c), and finally 18 minute-deposition (d), of TPA deposited onto graphene coated TEM grids. These images show fibrous features, demonstrating the morphology of TPA thin films. (e)-(f) shows electron diffraction patterns from each thickness. These show the TPA structures have some epitaxial relationship to the graphene (the $(0\bar{1}10)$ spot is labelled in each), but that this is much weaker than for TMA.

are other spots present in the patterns. These are assigned to diffraction from the TPA lattice.

There is a noticeable decrease in the intensity of the diffraction spots for TPA, relative to those for the same deposition time as TMA. This can partially be explained by the fact that TPA displayed thinner films than TMA for the same deposition time (see figure 6.2). However, the comparative lack of order in the TPA films also weakens the diffraction intensity: the TPA peaks appear as arcs rather than spots, suggesting that the ordering is weaker for TPA than TMA. More insight into the thin film structure is found from HRTEM, presented next.

Figure 6.9 shows HRTEM of a 1 minute-deposition of TPA on graphene, with (a) the image and (b) the FFT from the large white box in (a). The spacings of the spots in this region are (1.33 ± 0.05) nm^{-1} for the inner and (1.65 ± 0.05) nm^{-1} for the outer spots, which are consistent with those measured from the diffraction patterns.

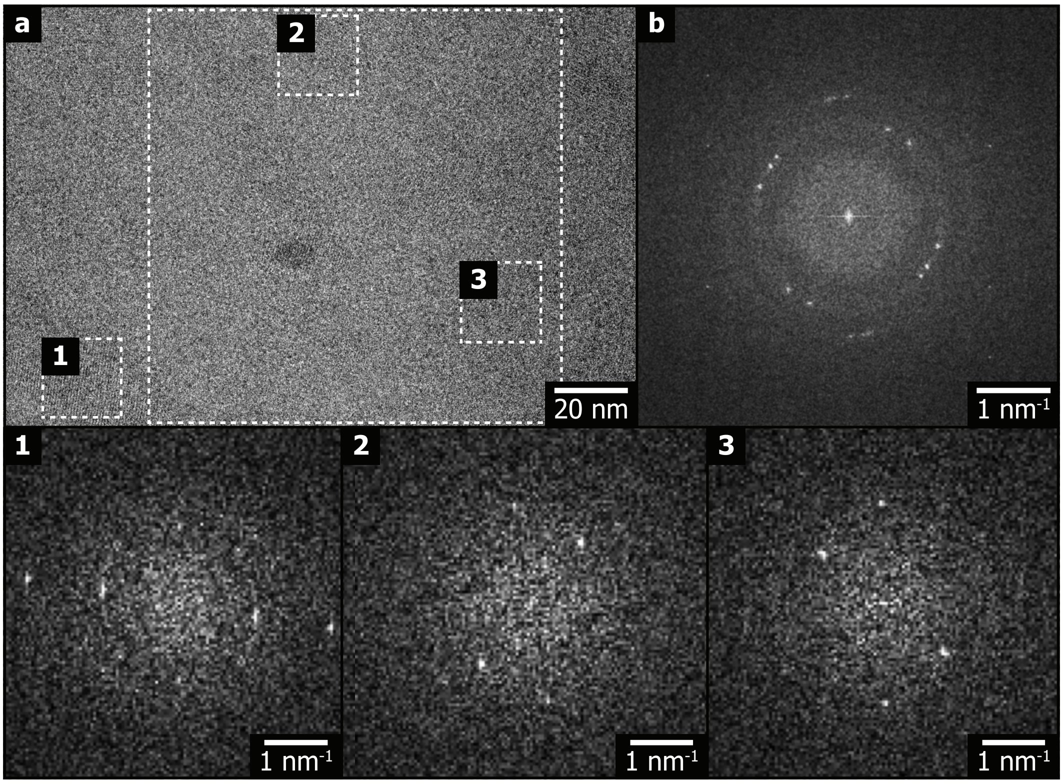

Figure 6.9: HRTEM of the 1 minute-deposition of TPA. The image (a) and FFT from the large white box (b) suggest multiple orientations of the TPA bulk structure. FFTs from smaller regions demonstrate how smaller regions show only one orientation, again demonstrating domains within the thin film that are ≈ 20 nm across.

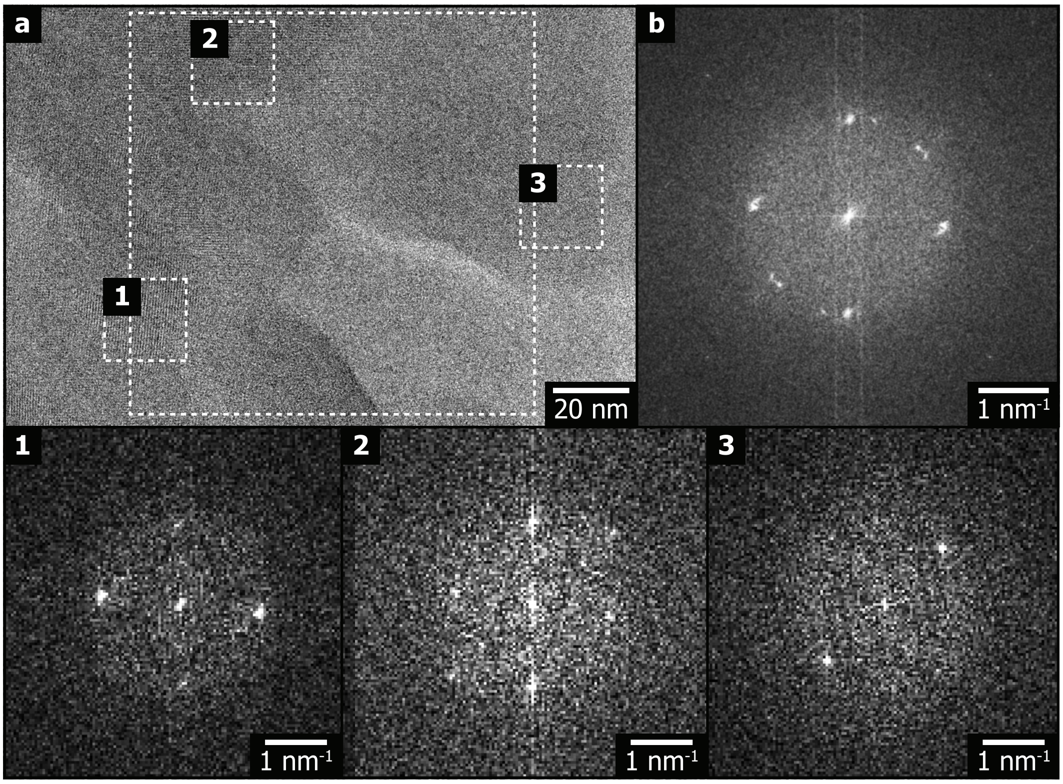

Figure 6.10: HRTEM of the 18 minute-deposition of TPA. The image (a) and FFT (b) from the large white box demonstrate one dominant orientation, suggesting large TPA grains in the thicker films. FFTs from smaller regions 1 and 3 highlight the different TPA orientations, and the FFT from region 2 shows a region where the smaller lattice parameter can be measured.

The lower panels of figure 6.9 show FFTs from smaller regions within the film. These FFTs show spots from a single orientation of the TPA, which demonstrates the domains within the thin film: there are regions $\approx$ 20 nm across that contain a single orientation, similar to that seen for the TMA films. From these regions it is also possible to measure the angle between a_1 and a_2 as γ =53 $\pm$ 2°.

Figure 6.10 shows HRTEM of the 18 minute-deposition film. The spacings of the FFT of this region are (1.38 ± 0.05) nm^{-1}, again consistent with the diffraction patterns. Smaller FFTs demonstrate the ordering across the film, demonstrating that the film still contains domains at this thickness. Even though in some regions the outer spots are less visible, in others the angle γ can still be measured.

Combined the electron diffraction and HRTEM can give the lattice structure

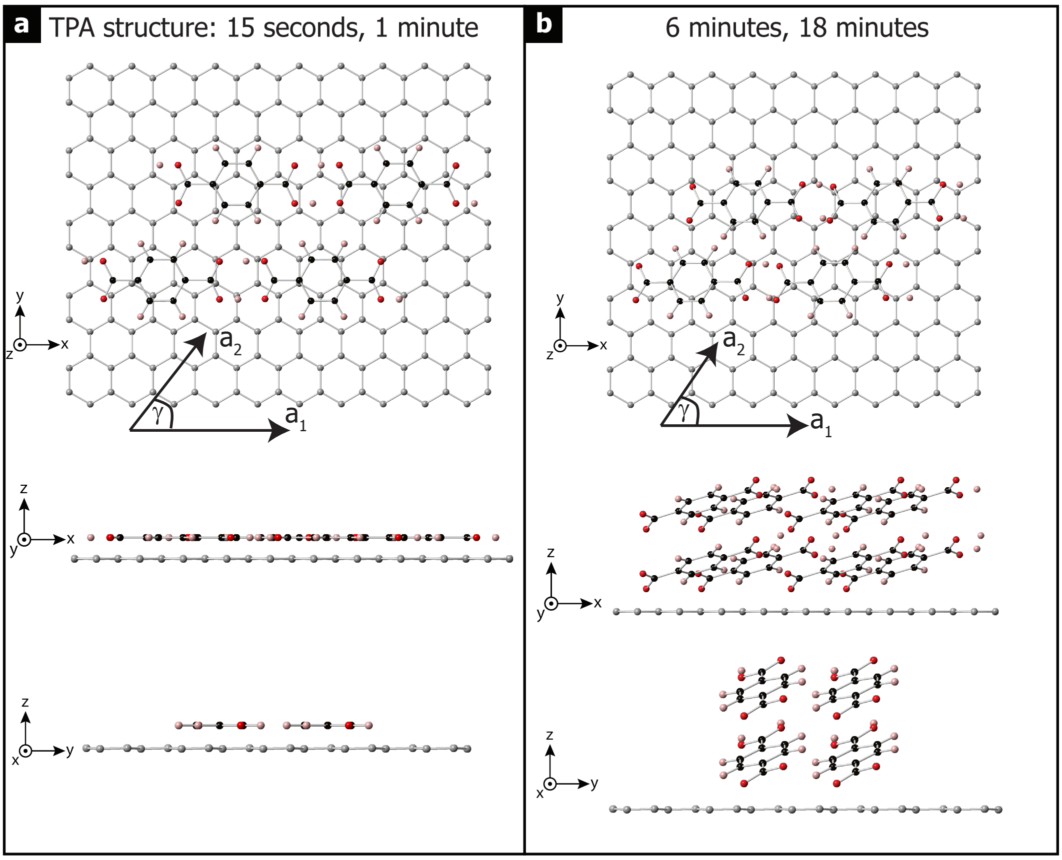

Figure 6.11: Structural models of TPA on graphene. (a) shows the brickwork structure seen for the 15 second and 1 minute-deposition films (as well as that seen in the STM), while (b) demonstrates the structure for the 6 and 18 minute-deposition films. Crystal models by Z. Laker.

for TPA deposited on graphene for different thickness. These are summarised in table 6.3. For the 15 seconds-deposition and 1 minute-deposition, the TPA appears to acquire a structure like the brickwork structure seen in the STM, which is demonstrated by molecular models shown in figure 6.11(a).

For the 6 minute-deposition and 18 minute-deposition, there is a noticeable reduction in the a_1 and a_2 lattice parameters and an increase in the angle γ. These lattice parameters suggest a structure that is closer to the bulk structure for TPA measured previously [211]. In this bulk structure, TPA molecules are tilted off the surface (as shown in figure 6.11(b)), which allows them to pack more closely than in the monolayer brickwork structure.

Deposition time	a_1 (nm)	a_2 (nm)	γ (°)
Monolayer (STM)	0.95 ± 0.01	0.72 ± 0.02	52 ± 4
15 seconds	0.95 ± 0.02	0.74 ± 0.02	50 ± 2
1 minute	0.90 ± 0.02	0.72 ± 0.02	53 ± 2
6 minutes	0.85 ± 0.02	0.62 ± 0.02	57 ± 2
18 minutes	0.86 ± 0.02	0.60 ± 0.02	56 ± 2
Bulk projection [211]	0.92 ± 0.01	0.65 ± 0.01	52 ± 2

Table 6.3: Lattice parameters for each thickness of TPA on graphene. The parameters are consistent with the bulk structure for TPA. There is a reduction in the a_2 lattice vector for the 6 minute-deposition and above, suggesting a more closely packed structure for the thicker films.

In summary, for thin films of TPA of 1 minute-deposition and below there is evidence that TPA molecules are ordered into a brickwork structure, consistent with that seen in the STM of the monolayer. Then for the 6 minute-deposition and above, the TPA molecules form into a bulk-like structure consistent with previous reports. This is supported by low-magnification images that show fibre-like features across the surface. These fibre-like features grow in size as the thickness of the film increases.

It is also clear that epitaxy is still present in the films. This points to an interaction between the graphene and TPA molecules at the first layer of molecules, that then seeds the growth for further layers. However, the ordering of the diffraction spots is much weaker than for TMA thin films, suggesting a weaker interaction between molecules through the layers, likely due to the different growth mode, and that the molecules do not arrange face-on to the graphene surface.

6.3 Conclusions

In conclusion, TMA and TPA deposited onto freely-suspended graphene demonstrate different out-of-plane growth and self assembly, as summarised in figure 6.12. On the one hand, a monolayer of TMA assembles in the chicken-wire structure, with two preferred orientations relative to the graphene substrate. This epitaxy then propagates up through to a film thickness of ≈ 20 nm, with distinct ordering seen

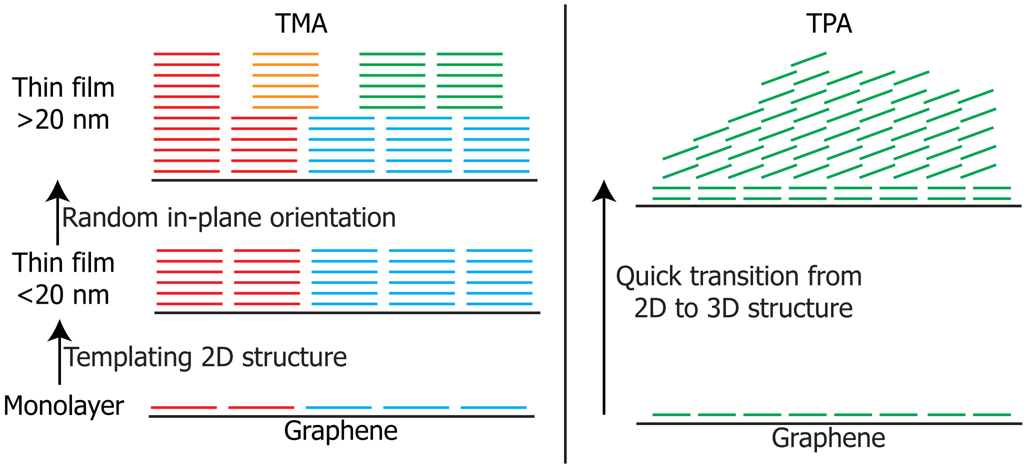

Figure 6.12: Summary of self-assembly seen for TMA and TPA. For TMA, the monolayer assembles into two in-plane orientations of the chicken-wire structure. This then templates through the film up to ≈ 20 nm. For thicker films, random in-plane orientations of the chicken-wire structure are seen. For TPA, the brickwork structure is observed at the monolayer. For thicker films, the assembly quickly transitions to a bulk-like 3D structure.

throughout. This ordering forms as domains of ≈ 20 nm across running through the full thickness. After this, the TMA molecules retain the chicken-wire structure, but acquire different in-plane orientations, and the epitaxial ordering is no longer visible. TPA, on the other hand, forms the characteristic brickwork structure on the graphene surface at the monolayer. However, for thin films, TPA rapidly transitions from a 2D to a 3D morphology, forming fibre-like structures on the surface that display a bulk-like structure. Like TMA, TPA does display epitaxial ordering to the graphene substrate, but this ordering is much weaker. It does, however, define the orientation of the bulk-like TPA thin films, and so weak epitaxy is seen even for the thickest films

Chapter 7

Conclusions and Future Work

This thesis aimed to examine the role of van der Waals epitaxy in graphene heterostructures. The impact of van der Waals forces was investigated across different heterostructures: graphene growth on copper via chemical vapour deposition; functionalisation of the graphene, the effect this has on its structure, and if it is reversible; how organic semiconducting molecules grow on graphene, and how surface functionalisation disrupts this growth; and finally how hydrogen-bonded networks interact with graphene, and how this interaction affects the transition from 2D, surface-driven assembly to 3D films.

First, in chapter 3, the interaction between graphene and copper during CVD growth was presented. Structural feedback between the graphene overlayer and copper substrate caused a mismatch epitaxy of $\pm 8^\circ$ between graphene and the [001] direction of the predominant Cu(100) surface. This in turn was related back to faceting of the copper into (n10) facets only underneath graphene. Despite this epitaxial relationship, only a weak interaction between the two was observed: angle-resolved photoemission spectroscopy showed a pristine graphene band structure, with no charge transfer from the copper substrate.

The nature of the graphene-copper interaction is still attracting much interest. The weak interaction between the two found here enabled the decoupling of the graphene from the substrate, but by annealing to a higher temperature of 550°C, n-doping of 350 meV was seen. The origin of this transition is still not well understood and needs further investigation.

In chapter 4, graphene was functionalised with atomic oxygen and nitrogen, and the chemical, physical and electronic properties were investigated. For the case of oxygen, the atomic species formed epoxide groups across the surface, which caused a disappearance of the graphene electronic band structure. There was no charge transfer and no band gap was induced. Atomic nitrogen formed a range of environments: adatoms, substitutionals, and pyrrolic/pyridinic nitrogen were all seen. The latter of these environments are often associated with defects and were correlated to extended topological defects in the graphene lattice. The addition of atomic species caused the disappearance of the graphene band structure through localisation for only small amounts (≈ 5 at%) for both oxygen and nitrogen. For smaller amounts of functionalisation, no charge transfer is seen for atomic oxygen. On the other hand, for atomic nitrogen, 200 meV n-doping is seen.

The reversibility of the functionalisation was also different: epoxides groups were almost fully removed from the surface after an anneal to $200°$C, but this resulted in only a partial recovery of the band structure. For nitrogen, only the nitrogen adatoms were removed by annealing, demonstrating the difficulty of reverting graphene with extended topological defects back to a pristine lattice. However, the band structure of the nitrogen doped film was not investigated because of the inherent time constraints in synchrotron measurements. How the band structure is affected after this effort to reverse would be interesting.

Further work on functionalisation would be to see if dopants could be tailored to alter charge-transfer to graphene without a significant negative impact on the electronic structure. Removing functionalisation is also receiving significant interest as GO is currently the cheapest form of graphene and is industrially available. Are there ways to remove this functionalisation and return to the pristine graphene lattice?

The final chapters presented investigations of graphene-molecule heterostructures. In chapter 5, vanadyl-phthalocyanine was deposited onto graphene. Films deposited at elevated substrate temperatures of $155°$C showed crystals of several micrometres across, as opposed to 10s of nanometres across when deposited at ambient temperatures. Further, when deposited onto graphene oxide the VOPc crystals were an order of magnitude smaller, caused by an interruption of the molecules diffusivity by the surface functionalisation. This highlights the importance of the weakly interacting, van der Waals surface of graphene, even when epitaxy is not the result.

This then opens many avenues of research for graphene as a substrate for organic electronics. A lot of work has focused on epitaxy as a route to improve device performance but perhaps device improvements could come from exploiting the weak interaction of graphene. Other OSCs could present as even larger crystals, and the device improvements this could offer are yet to be explored. The focus should also be on keeping the graphene surface pristine to enable large crystal growth, especially when using transferred graphene or reduced graphene oxide, as is often the case in these devices.

Finally, the role of graphene as a substrate for molecular self-assembly was investigated. Hydrogen-bonded networks of both trimesic acid (TMA) and terephthalic acid (TPA) were formed on graphene through deposition in UHV. TEM was then used to study the transition from the 2D network to the 3D structure, with differences between the two, despite their chemical similarity. For TMA, a chicken-wire structure was seen at the monolayer, with two orientations separated by 14°. This monolayer structure templated through with increasing thickness, until, after over ≈ 20 nm, they arranged in the same chicken-wire structure but with random in-plane orientations. On the other hand, TPA formed a brickwork arrangement on the graphene surface for the first few layers, but after this, formed a structure close to that reported for the bulk. In both cases, van der Waals epitaxy defined the molecules orientation on the graphene surface.

For supramolecular assembly, it is interesting to see two different behaviours for two similar molecules. This difference was revealed using electron microscopy to examine these hydrogen-bonded networks, something that is still quite new. Therefore, there are still many outstanding questions. The microscopy techniques used in this thesis were relatively primitive, and greater and more detailed information could be available in the future. Improvements could come from data collection, with even more microscope automation to minimise the dose used to only those that contribute to images; or with equipment better suited to using low-electron doses, like has been used in biological studies. There is also scope for further image processing, to combine the diffraction and imaging to extract even more information about the structure. Further, for the molecular systems themselves, it would be interesting to see if there were molecules that could template further. This could be approached by attempting to understand what causes the transition from the templated monolayer to a random or bulk structure. TEM would certainly be a valuable tool in this area.

As the interest in graphene heterostructures increases, it is growth processes that will ultimately provide the most direct route to technologically viable applications. Understanding the role of the van der Waals graphene surface — free of dangling bonds and weakly interacting — will be key. For this reason, van der Waals interactions, and the epitaxy that they can sometimes drive, is likely to feature prominently in the future of graphene heterostructures.

Bibliography

[1] G. E. Moore, "Cramming more components onto integrated circuits", *Proceedings of the IEEE*, vol. 86, no. 1, pp. 82–85, 1998. DOI: `10.1109/JPROC.1998.658762`.

[2] I. L. Markov, "Limits on fundamental limits to computation", *Nature*, vol. 512, no. 7513, pp. 147–154, 2014. DOI: `10.1038/nature13570`.

[3] K. S. Novoselov, A. K. Geim, S. V. Morozov, D Jiang, Y Zhang, S. V. Dubonos, I. V. Grigorieva, and A. A. Firsov, "Electric field effect in atomically thin carbon films.", *Science*, vol. 306, no. 5696, pp. 666–669, 2004. DOI: `10.1126/science.1102896`.

[4] K. S. Novoselov, V. I. Falko, L Colombo, P. R. Gellert, M. G. Schwab, and K Kim, "A roadmap for graphene", *Nature*, vol. 490, no. 7419, pp. 192–200, 2012. DOI: `10.1038/nature11458`.

[5] A. K. Geim and I. V. Grigorieva, "Van der Waals heterostructures.", *Nature*, vol. 499, no. 7459, pp. 419–25, 2013. DOI: `10.1038/nature12385`.

[6] J. Warner, F. Schaffel, M. Rummeli, and A. Bachmatiuk, *Graphene: Fundamentals and emergent applications*. Elsevier, 2012.

[7] A. H. Castro Neto, F. Guinea, N. M. R. Peres, K. S. Novoselov, and A. K. Geim, "The electronic properties of graphene", *Reviews of Modern Physics*, vol. 81, no. 1, pp. 109–162, 2009. DOI: `10.1103/RevModPhys.81.109`.

[8] R. R. Nair, P Blake, A. N. Grigorenko, K. S. Novoselov, T. J. Booth, T. Stauber, N. M. R. Peres, and A. K. Geim, "Fine structure constant defines visual transparency of graphene", *Science*, vol. 320, no. 5881, pp. 1308–1308, 2008. DOI: `10.1126/science.1156965`.

[9] C. Lee, X. Wei, J. W. Kysar, and J. Hone, "Measurement of the elastic properties and intrinsic strength of monolayer graphene", *Science*, vol. 321, no. 5887, pp. 385–388, 2008. DOI: `10.1126/science.1157996`.

[10] J. S. Bunch, A. M. van der Zande, S. S. Verbridge, I. W. Frank, D. M. Tanenbaum, J. M. Parpia, H. G. Craighead, and P. L. McEuen, "Electromechanical resonators from graphene sheets.", *Science*, vol. 315, no. 5811, pp. 490–493, 2007. DOI: `10.1126/science.1136836`.

[11] M. Pumera, "Graphene-based nanomaterials for energy storage", *Energy & Environmental Science*, vol. 4, no. 3, p. 668, 2011. DOI: `10.1039/c0ee00295j`.

[12] Y. Shao, J. Wang, H. Wu, J. Liu, I. A. Aksay, and Y. Lin, "Graphene based electrochemical sensors and biosensors: a review", *Electroanalysis*, vol. 22, no. 10, pp. 1027–1036, 2010. DOI: `10.1002/elan.200900571`.

[13] F Schedin, A. K. Geim, S. V. Morozov, E. W. Hill, P Blake, M. I. Katsnelson, and K. S. Novoselov, "Detection of individual gas molecules adsorbed on graphene", *Nature Materials*, vol. 6, no. 9, pp. 652–655, 2007. DOI: `10.1038/nmat1967`.

[14] Y. Wu, K. A. Jenkins, A. Valdes-Garcia, D. B. Farmer, Y. Zhu, A. A. Bol, C. Dimitrakopoulos, W. Zhu, F. Xia, P. Avouris, and Y.-M. Lin, "State-of-the-art graphene high-frequency electronics", *Nano Letters*, vol. 12, no. 6, pp. 3062–3067, 2012. DOI: `10.1021/nl300904k`.

[15] Y.-M. Lin, C. Dimitrakopoulos, K. A. Jenkins, D. B. Farmer, H.-Y. Chiu, A. Grill, and P. Avouris, "100-GHz transistors from wafer-scale epitaxial graphene.", *Science*, vol. 327, no. 5966, p. 662, 2010. DOI: `10.1126/science.1184289`.

[16] L. Gomez De Arco, Y. Zhang, C. W. Schlenker, K. Ryu, M. E. Thompson, and C. Zhou, "Continuous, highly flexible, and transparent graphene films by chemical vapor deposition for organic photovoltaics", *ACS Nano*, vol. 4, no. 5, pp. 2865–2873, 2010. DOI: `10.1021/nn901587x`.

[17] A. C. Ferrari, F. Bonaccorso, V. Fal'ko, K. S. Novoselov, S. Roche, P. Boggild, S. Borini, F. H. L. Koppens, V. Palermo, N. Pugno, J. A. Garrido, R. Sordan, A. Bianco, L. Ballerini, M. Prato, E. Lidorikis, J. Kivioja, C. Marinelli, T. Ryhänen, A. Morpurgo, J. N. Coleman, V. Nicolosi, L. Colombo, A. Fert, M. Garcia-Hernandez, A. Bachtold, G. F. Schneider, F. Guinea, C. Dekker, M. Barbone, Z. Sun, C. Galiotis, A. N. Grigorenko, G. Konstantatos, A. Kis, M. Katsnelson, L. Vandersypen, A. Loiseau, V. Morandi, D. Neumaier, E. Treossi, V. Pellegrini, M. Polini, A. Tredicucci, G. M. Williams, B. Hee Hong, J.-H. Ahn, J. Min Kim, H. Zirath, B. J. van Wees, H. van der Zant, L. Occhipinti, A. Di Matteo, I. A. Kinloch, T. Seyller, E. Quesnel, X. Feng, K. Teo, N. Rupesinghe, P. Hakonen, S. R. T. Neil, Q. Tannock, T. Löfwander, and J. Kinaret, "Science and technology roadmap for graphene, related two-dimensional crystals, and hybrid systems", *Nanoscale*, vol. 7, no. 11, pp. 4598–4810, 2015. DOI: `10.1039/C4NR01600A`.

[18] Y. Kubota, K. Watanabe, O. Tsuda, and T. Taniguchi, "Deep ultraviolet light-emitting hexagonal boron nitride synthesized at atmospheric pressure.", *Science*, vol. 317, no. 5840, pp. 932–934, 2007. DOI: `10.1126/science.1144216`.

[19] Q. H. Wang, K. Kalantar-Zadeh, A. Kis, J. N. Coleman, and M. S. Strano, "Electronics and optoelectronics of two-dimensional transition metal dichalcogenides.", *Nature nanotechnology*, vol. 7, no. 11, pp. 699–712, 2012. DOI: `10.1038/nnano.2012.193`.

[20] C. R. Dean, A. F. Young, I Meric, C Lee, L Wang, S Sorgenfrei, K Watanabe, T Taniguchi, P Kim, K. L. Shepard, and J Hone, "Boron nitride substrates for high-quality graphene electronics.", *Nature nanotechnology*, vol. 5, no. 10, pp. 722–726, 2010. DOI: `10.1038/nnano.2010.172`.

[21] C. R. Dean, A. F. Young, P. Cadden-Zimansky, L. Wang, H. Ren, K. Watanabe, T. Taniguchi, P. Kim, J. Hone, and K. L. Shepard, "Multicomponent fractional quantum hall effect in graphene", *Nature Physics*, vol. 7, no. 9, pp. 693–696, 2011. DOI: `10.1038/nphys2007`.

[22] A. V. Kretinin, Y Cao, J. S. Tu, G. L. Yu, R Jalil, K. S. Novoselov, S. J. Haigh, A Gholinia, A Mishchenko, M Lozada, T Georgiou, C. R. Woods, F Withers, P Blake, G Eda, A Wirsig, C Hucho, K Watanabe, T Taniguchi, A. K. Geim, and R. V. Gorbachev, "Electronic properties of graphene encapsulated with different two-dimensional atomic crystals", *Nano Letters*, vol. 14, no. 6, pp. 3270–3276, 2014. DOI: `10.1021/nl5006542`.

[23] M. I. B. Utama, Q. Zhang, J. Zhang, Y. Yuan, F. J. Belarre, J. Arbiol, and Q. Xiong, "Recent developments and future directions in the growth of nanostructures by van der Waals epitaxy.", *Nanoscale*, vol. 5, no. 9, pp. 3570–3588, 2013. DOI: `10.1039/c3nr34011b`.

[24] U. W. Pohl, Ed., *Epitaxy of Semiconductors: Introduction to Physical Principles*. Springer, 2013.

[25] D. G. Schlom, L.-Q. Chen, C.-B. Eom, K. M. Rabe, S. K. Streiffer, and J.-M. Triscone, "Strain tuning of ferroelectric thin films", *Annual Review of Materials Research*, vol. 37, no. 1, pp. 589–626, 2007. DOI: `10.1146/annurev.matsci.37.061206.113016`.

[26] A. Koma, "Van der Waals epitaxy - a new epitaxial growth method for a highly lattice-mismatched system", *Thin Solid Films*, vol. 216, no. 1, pp. 72–76, 1992. DOI: `10.1016/0040-6090(92)90872-9`.

[27] A. K. Debnath, S. Samanta, A. Singh, D. K. Aswal, S. K. Gupta, J. V. Yakhmi, S. K. Deshpande, A. K. Poswal, and C. Sürgers, "Growth of iron phthalocyanine nanoweb and nanobrush using molecular beam epitaxy", *Physica E: Low-Dimensional Systems and Nanostructures*, vol. 41, no. 1, pp. 154–163, 2008. DOI: `10.1016/j.physe.2008.06.022`.

[28] M. I. B. Utama, Z. Peng, R. Chen, B. Peng, X. Xu, Y. Dong, L. M. Wong, S. Wang, H. Sun, and Q. Xiong, "Vertically aligned cadmium chalcogenide nanowire arrays on muscovite mica: a demonstration of epitaxial growth strategy", *Nano Letters*, vol. 11, no. 8, pp. 3051–3057, 2011. DOI: `10.1021/nl1034495`.

[29] X. Yuan, L. Tang, S. Liu, P. Wang, Z. Chen, C. Zhang, Y. Liu, W. Wang, Y. Zou, C. Liu, N. Guo, J. Zou, P. Zhou, W. Hu, and F. Xiu, "Arrayed van der Waals vertical heterostructures based on 2D GaSe grown by molecular beam epitaxy", *Nano Letters*, vol. 15, no. 5, pp. 3571–3577, 2015. DOI: `10.1021/acs.nanolett.5b01058`.

[30] J. Kim, C. Bayram, H. Park, C.-W. Cheng, C. Dimitrakopoulos, J. A. Ott, K. B. Reuter, S. W. Bedell, and D. K. Sadana, "Principle of direct van der Waals epitaxy of single-crystalline films on epitaxial graphene", *Nature Communications*, vol. 5, p. 4836, 2014. DOI: `10.1038/ncomms5836`.

[31] Y. J. Hong, W. H. Lee, Y. Wu, R. S. Ruoff, and T. Fukui, "Van der Waals epitaxy of InAs nanowires vertically aligned on single-layer graphene", *Nano Letters*, vol. 12, no. 3, pp. 1431–1436, 2012. DOI: `10.1021/nl204109t`.

[32] O. Lang, Y. Tomm, R. Schlaf, C. Pettenkofer, and W. Jaegermann, "Single crystalline GaSe/WSe2 heterointerfaces grown by van der Waals epitaxy. ii. junction characterization", *Journal of Applied Physics*, vol. 75, no. 12, pp. 7814–7820, 1994. DOI: `10.1063/1.356563`.

[33] H. Ago, H. Endo, P. Solís-Fernández, R. Takizawa, Y. Ohta, Y. Fujita, K. Yamamoto, and M. Tsuji, "Controlled van der Waals epitaxy of monolayer MoS2 triangular domains on graphene", *ACS Applied Materials & Interfaces*, vol. 7, no. 9, pp. 5265–5273, 2015. DOI: `10.1021/am508569m`.

[34] J. A. Miwa, M. Dendzik, S. S. Gronborg, M. Bianchi, J. V. Lauritsen, P. Hofmann, and S. R. Ulstrup, "Van der Waals epitaxy of two-dimensional MoS2-graphene heterostructures in ultrahigh vacuum", *ACS Nano*, vol. 9, no. 6, pp. 6502–6510, 2015. DOI: `10.1021/acsnano.5b02345`.

[35] F. Withers, O. Del Pozo-Zamudio, A. Mishchenko, A. P. Rooney, A. Gholinia, K. Watanabe, T. Taniguchi, S. J. Haigh, A. K. Geim, A. I. Tartakovskii, and K. S. Novoselov, "Light-emitting diodes by band-structure engineering in van der waals heterostructures", *Nature Materials*, vol. 14, no. 3, pp. 301–306, 2015. DOI: `10.1038/nmat4205`.

[36] K. R. Paton, E. Varrla, C. Backes, R. J. Smith, U. Khan, A. OâĂŹNeill, C. Boland, M. Lotya, O. M. Istrate, P. King, T. Higgins, S. Barwich, P. May, P. Puczkarski, I. Ahmed, M. Moebius, H. Pettersson, E. Long, J. Coelho, S. E. OâĂŹBrien, E. K. McGuire, B. M. Sanchez, G. S. Duesberg, N. McEvoy, T. J. Pennycook, C. Downing, A. Crossley, V. Nicolosi, and J. N. Coleman, "Scalable production of large quantities of defect-free few-layer graphene by shear exfoliation in liquids", *Nature Materials*, vol. 13, no. 6, pp. 624–630, 2014. DOI: `10.1038/nmat3944`.

[37] T. Seyller, A. Bostwick, K. V. Emtsev, K. Horn, L. Ley, J. L. McChesney, T. Ohta, J. D. Riley, E. Rotenberg, and F. Speck, "Epitaxial graphene: a new material", *Physica Status Solidi (B) Basic Research*, vol. 245, no. 7, pp. 1436–1446, 2008. DOI: `10.1002/pssb.200844143`.

[38] C. Ratsch and J. A. Venables, "Nucleation theory and the early stages of thin film growth", *Journal of Vacuum Science & Technology A: Vacuum, Surfaces, and Films*, vol. 21, no. 5, S96, 2003. DOI: `10.1116/1.1600454`.

[39] C. Mattevi, H. Kim, and M. Chhowalla, “A review of chemical vapour deposition of graphene on copper”, English, *J. Mater. Chem.*, vol. 21, no. 10, pp. 3324–3334, 2011. DOI: 10.1039/C0JM02126A.

[40] A. Reina, S. Thiele, X. Jia, S. Bhaviripudi, M. S. Dresselhaus, J. a. Schaefer, and J. Kong, “Growth of large-area single- and bi-layer graphene by controlled carbon precipitation on polycrystalline Ni surfaces”, *Nano Research*, vol. 2, no. 6, pp. 509–516, 2010. DOI: 10.1007/s12274-009-9059-y.

[41] H Ago, Y Ogawa, M Tsuji, S Mizuno, and H Hibino, “Catalytic growth of graphene: toward large-area single-crystalline graphene”, English, *Journal of Physical Chemistry Letters*, vol. 3, no. 16, pp. 2228–2236, 2012. DOI: 10.1021/jz3007029.

[42] S. Nie, W. Wu, S. Xing, Q. Yu, J. Bao, S.-S. Pei, and K. F. McCarty, “Growth from below: bilayer graphene on copper by chemical vapor deposition”, *New Journal of Physics*, vol. 14, no. 9, p. 093 028, 2012. DOI: 10.1088/1367-2630/14/9/093028.

[43] A. E. Karu and M. Beer, “Pyrolytic formation of highly crystalline graphite films”, *Journal of Applied Physics*, vol. 37, no. 5, pp. 2179–2181, 1966. DOI: 10.1063/1.1708759.

[44] T. A. Land, T Michely, R. J. Behm, J. C. Hemminger, and G Comsa, “STM investigation of single layer graphite structures produced on Pt(111) by hydrocarbon decomposition”, *Surf. Sci.*, vol. 264, pp. 261–270, 1992.

[45] J. Coraux, A. T. N’Diaye, C. Busse, and T. Michely, “Structural coherency of graphene on Ir(111)”, *Nano letters*, vol. 8, no. 2, pp. 565–570, 2008. DOI: 10.1021/nl0728874.

[46] X. Li, W. Cai, J. An, S. Kim, J. Nah, D. Yang, R. Piner, A. Velamakanni, I. Jung, E. Tutuc, S. K. Banerjee, L. Colombo, and R. S. Ruoff, “Large-area synthesis of high-quality and uniform graphene films on copper foils.”, *Science*, vol. 324, no. 5932, pp. 1312–1314, 2009. DOI: 10.1126/science.1171245.

[47] L. Zhao, M. Levendorf, S. Goncher, T. Schiros, L. Pálová, A. Zabet-Khosousi, K. T. Rim, C. Gutiérrez, D. Nordlund, C. Jaye, M. Hybertsen, D. Reichman, G. W. Flynn, J. Park, and A. N. Pasupathy, “Local atomic and electronic structure of boron chemical doping in monolayer graphene”, *Nano Letters*, vol. 13, no. 10, pp. 4659–4665, 2013. DOI: 10.1021/nl401781d.

[48] A. Srivastava, C. Galande, L. Ci, L. Song, C. Rai, D. Jariwala, K. F. Kelly, and P. M. Ajayan, “Novel liquid precursor-based facile synthesis of large-area continuous, single, and few-layer graphene films”, *Chemistry of Materials*, vol. 22, no. 11, pp. 3457–3461, 2010. DOI: 10.1021/cm101027c.

[49] B. Zhang, W. H. Lee, R. Piner, I. Kholmanov, Y. Wu, H. Li, H. Ji, and R. S. Ruoff, “Low-temperature chemical vapor deposition growth of graphene from toluene on electropolished copper foils.”, *ACS Nano*, vol. 6, no. 3, pp. 2471–6, 2012. DOI: 10.1021/nn204827h.

[50] Z. Li, P. Wu, C. Wang, X. Fan, W. Zhang, X. Zhai, C. Zeng, Z. Li, J. Yang, and J. Hou, “Low-temperature growth of graphene by chemical vapor deposition using solid and liquid carbon sources”, *ACS Nano*, vol. 5, no. 4, pp. 3385–3390, 2011. DOI: 10.1021/nn200854p.

[51] S. Bae, H. Kim, Y. Lee, X. Xu, J.-S. Park, Y. Zheng, J. Balakrishnan, T. Lei, H. Ri Kim, Y. I. Song, Y.-J. Kim, K. S. Kim, B. Özyilmaz, J.-H. Ahn, B. H. Hong, and S. Iijima, “Roll-to-roll production of 30-inch graphene films for transparent electrodes”, English, *Nature Nanotechnology*, vol. 5, no. 8, pp. 574–578, 2010. DOI: 10.1038/nnano.2010.132.

[52] G.-H. Lee, R. C. Cooper, S. J. An, S. Lee, A. van der Zande, N. Petrone, A. G. Hammerberg, C. Lee, B. Crawford, W. Oliver, J. W. Kysar, and J. Hone, “High-strength chemical-vapor-deposited graphene and grain boundaries”, *Science*, vol. 340, no. 6136, pp. 1073–1076, 2013. DOI: 10.1126/science.1235126.

[53] R. Grantab, V. B. Shenoy, and R. S. Ruoff, “Anomalous strength characteristics of tilt grain boundaries in graphene.”, *Science*, vol. 330, no. 6006, pp. 946–948, 2010. DOI: `10.1126/science.1196893`.

[54] O. V. Yazyev and S. G. Louie, “Electronic transport in polycrystalline graphene”, *Nature Materials*, vol. 9, no. 10, pp. 806–809, 2010. DOI: `10.1038/nmat2830`.

[55] Q. K. Yu, L. A. Jauregui, W. Wu, R. Colby, J. F. Tian, Z. H. Su, H. L. Cao, Z. H. Liu, D. Pandey, D. G. Wei, T. F. Chung, P. Peng, N. P. Guisinger, E. A. Stach, J. M. Bao, S.-S. S. Pei, and Y. P. Chen, “Control and characterization of individual grains and grain boundaries in graphene grown by chemical vapour deposition”, *Nature Materials*, vol. 10, no. 6, pp. 443–449, 2011. DOI: `10.1038/nmat3010`.

[56] Z. Yan, Z. Peng, and J. M. Tour, “Chemical vapor deposition of graphene single crystals.”, *Accounts of chemical research*, vol. 47, no. 4, pp. 1327–37, 2014. DOI: `10.1021/ar4003043`.

[57] Y. A. Wu, Y. Fan, S. Speller, G. L. Creeth, J. T. Sadowski, K. He, A. W. Robertson, C. S. Allen, and J. H. Warner, “Large single crystals of graphene on melted copper using chemical vapor deposition”, *ACS Nano*, vol. 6, no. 6, pp. 5010–5017, 2012. DOI: `10.1021/nn3016629`.

[58] Y. Hao, M. S. Bharathi, L. Wang, Y. Liu, H. Chen, S. Nie, X. Wang, H. Chou, C. Tan, B. Fallahazad, H Ramanarayan, C. W. Magnuson, E. Tutuc, B. I. Yakobson, K. F. McCarty, Y.-W. Zhang, P. Kim, J. Hone, L. Colombo, and R. S. Ruoff, “The role of surface oxygen in the growth of large single-crystal graphene on copper”, *Science*, vol. 342, no. 6159, pp. 720–723, 2013. DOI: `10.1126/science.1243879`.

[59] H. Zhou, W. J. Yu, L. Liu, R. Cheng, Y. Chen, X. Huang, Y. Liu, Y. Wang, Y. Huang, and X. Duan, “Chemical vapour deposition growth of large single crystals of monolayer and bilayer graphene”, *Nature Communications*, vol. 4, p. 2096, 2013. DOI: `10.1038/ncomms3096`.

[60] X. Chen, P. Zhao, R. Xiang, S. Kim, J. Cha, S. Chiashi, and S. Maruyama, “Chemical vapor deposition growth of 5mm hexagonal single-crystal graphene from ethanol”, *Carbon*, vol. 94, pp. 810–815, 2015. DOI: `10.1016/j.carbon.2015.07.045`.

[61] H. Tetlow, J. Posthuma de Boer, I. J. Ford, D. D. Vvedensky, J. Coraux, and L. Kantorovich, “Growth of epitaxial graphene: theory and experiment”, *Physics Reports*, vol. 542, no. 3, pp. 195–295, 2014. DOI: `10.1016/j.physrep.2014.03.003`.

[62] B. Hu, H. Ago, Y. Ito, K. Kawahara, M. Tsuji, E. Magome, K. Sumitani, N. Mizuta, K.-i. Ikeda, and S. Mizuno, “Epitaxial growth of large-area single-layer graphene over Cu(111)/sapphire by atmospheric pressure CVD”, *Carbon*, vol. 50, no. 1, pp. 57–65, 2012. DOI: `10.1016/j.carbon.2011.08.002`.

[63] J. D. Wood, S. W. Schmucker, A. S. Lyons, E. Pop, and J. W. Lyding, “Effects of polycrystalline copper substrate on graphene growth by chemical vapor deposition”, *Nano Letters*, vol. 11, no. 11, pp. 4547–4554, 2011. DOI: `10.1021/nl201566c`.

[64] W. S. Hummers and R. E. Offeman, “Preparation of graphitic oxide”, *Journal of the American Chemical Society*, vol. 80, no. 6, pp. 1339–1339, 1958. DOI: `10.1021/ja01539a017`.

[65] D. R. Dreyer, S. Park, C. W. Bielawski, and R. S. Ruoff, “The chemistry of graphene oxide”, *Chemical Society Reviews*, vol. 39, no. 1, pp. 228–240, 2010. DOI: `Doi10.1039/B917103g`.

[66] D. R. Dreyer, A. D. Todd, and C. W. Bielawski, “Harnessing the chemistry of graphene oxide.”, *Chemical Society reviews*, vol. 43, no. 15, pp. 5288–5301, 2014. DOI: `10.1039/c4cs00060a`.

[67] J. P. Rourke, P. A. Pandey, J. J. Moore, M. Bates, I. A. Kinloch, R. J. Young, and N. R. Wilson, “The real graphene oxide revealed: stripping the oxidative

debris from the graphene-like sheets”, *Angewandte Chemie International Edition*, vol. 50, no. 14, pp. 3173–3177, 2011. DOI: 10.1002/anie.201007520.

[68] H. A. Becerril, J. Mao, Z. Liu, R. M. Stoltenberg, Z. Bao, and Y. Chen, “Evaluation of solution-processed reduced graphene oxide films as transparent conductors”, *ACS Nano*, vol. 2, no. 3, pp. 463–470, 2008. DOI: 10.1021/nn700375n.

[69] C. Gómez-Navarro, R. T. Weitz, A. M. Bittner, M. Scolari, A. Mews, M. Burghard, and K. Kern, “Electronic transport properties of individual chemically reduced graphene oxide sheets”, *Nano Letters*, vol. 7, no. 11, pp. 3499–3503, 2007. DOI: 10.1021/nl072090c.

[70] G. Eda, G. Fanchini, and M. Chhowalla, “Large-area ultrathin films of reduced graphene oxide as a transparent and flexible electronic material”, *Nature Nanotechnology*, vol. 3, no. 5, pp. 270–274, 2008. DOI: 10.1038/nnano.2008.83.

[71] I. Jung, D. A. Dikin, R. D. Piner, and R. S. Ruoff, “Tunable electrical conductivity of individual graphene oxide sheets reduced at ’low’ temperatures”, *Nano Letters*, vol. 8, no. 12, pp. 4283–4287, 2008. DOI: 10.1021/nl8019938.

[72] C. K. Chua and M. Pumera, “Chemical reduction of graphene oxide: a synthetic chemistry viewpoint.”, *Chemical Society reviews*, vol. 43, no. 1, pp. 291–312, 2014. DOI: 10.1039/c3cs60303b.

[73] D. C. Elias, R. R. Nair, T. M. G. Mohiuddin, S. V. Morozov, P Blake, M. P. Halsall, A. C. Ferrari, D. W. Boukhvalov, M. I. Katsnelson, A. K. Geim, and K. S. Novoselov, “Control of graphene’s properties by reversible hydrogenation: evidence for graphane”, *Science*, vol. 323, no. 5914, pp. 610–613, 2009. DOI: 10.1126/science.1167130.

[74] H. Wang, T. Maiyalagan, and X. Wang, “Review on recent progress in nitrogen-doped graphene: synthesis, characterization, and its potential applications”, *ACS Catalysis*, vol. 2, no. 5, pp. 781–794, 2012. DOI: 10.1021/cs200652y.

[75] Y.-F. Lu, S.-T. Lo, J.-C. Lin, W. Zhang, J.-Y. Lu, F.-H. Liu, C.-M. Tseng, Y.-H. Lee, C.-T. Liang, and L.-J. Li, “Nitrogen-doped graphene sheets grown by chemical vapor deposition: synthesis and influence of nitrogen impurities on carrier transport”, *ACS Nano*, vol. 7, no. 8, pp. 6522–6532, 2013. DOI: 10.1021/nn402102y.

[76] A. L. M. Reddy, A. Srivastava, S. R. Gowda, H. Gullapalli, M. Dubey, and P. M. Ajayan, “Synthesis of nitrogen-doped graphene films for lithium battery application”, *ACS Nano*, vol. 4, no. 11, pp. 6337–6342, 2010. DOI: 10.1021/nn101926g.

[77] C. Zhang, L. Fu, N. Liu, M. Liu, Y. Wang, and Z. Liu, “Synthesis of nitrogen-doped graphene using embedded carbon and nitrogen sources”, *Advanced Materials*, vol. 23, no. 8, pp. 1020–1024, 2011. DOI: 10.1002/adma.201004110.

[78] G.-H. Lee, C.-H. Lee, A. M. van der Zande, M. Han, X. Cui, G. Arefe, C. Nuckolls, T. F. Heinz, J. Hone, and P. Kim, “Heterostructures based on inorganic and organic van der Waals systems”, *APL Materials*, vol. 092511, 2014. DOI: 10.1063/1.4894435.

[79] P. M. Beaujuge, J. M. J. Fréchet, and J. M. J. Fr, “Molecular design and ordering effects in pi-functional materials for transistor and solar cell applications.”, *Journal of the American Chemical Society*, vol. 133, pp. 20 009–29, 2011. DOI: 10.1021/ja2073643.

[80] M. Mas-Torrent and C. Rovira, “Role of molecular order and solid-state structure in organic field-effect transistors”, *Chemical Reviews*, vol. 111, no. 8, pp. 4833–4856, 2011. DOI: 10.1021/cr100142w.

[81] C. Wang, H. Dong, W. Hu, Y. Liu, and D. Zhu, “Semiconducting pi-conjugated systems in field-effect transistors: a material odyssey of organic electronics.”, *Chemical reviews*, vol. 112, no. 4, pp. 2208–67, 2012. DOI: 10.1021/cr100380z.

[82] M. G. Walter, A. B. Rudine, and C. C. Wamser, “Porphyrins and phthalocyanines in solar photovoltaic cells”, *Journal of Porphyrins and Phthalocyanines*, vol. 14, no. 09, pp. 759–792, 2010. DOI: `10.1142/S1088424610002689`.

[83] S.-C. Lo and P. L. Burn, “Development of dendrimers: macromolecules for use in organic light-emitting diodes and solar cells”, *Chemical Reviews*, vol. 107, no. 4, pp. 1097–1116, 2007. DOI: `10.1021/cr050136l`.

[84] J. Du, S. Pei, L. Ma, and H.-M. Cheng, “25th anniversary article: carbon nanotube- and graphene-based transparent conductive films for optoelectronic devices”, *Advanced Materials*, vol. 26, no. 13, pp. 1958–1991, 2014. DOI: `10.1002/adma.201304135`.

[85] X. Li, H. Wang, J. T. Robinson, H. Sanchez, G. Diankov, and H. Dai, “Simultaneous nitrogen doping and reduction of graphene oxide”, *Journal of the American Chemical Society*, vol. 131, no. 43, pp. 15 939–15 944, 2009. DOI: `10.1021/ja907098f`.

[86] S. Kowarik, A. Gerlach, and F. Schreiber, “Organic molecular beam deposition: fundamentals, growth dynamics, and in situ studies”, *Journal of Physics: Condensed Matter*, vol. 20, no. 18, p. 184 005, 2008. DOI: `10.1088/0953-8984/20/18/184005`.

[87] S. R. Forrest, “Ultrathin organic films grown by organic molecular beam deposition and related techniques.”, *Chemical Reviews*, vol. 97, no. 6, pp. 1793–1896, 1997. DOI: `10.1021/cr941014o`.

[88] G. Guillaud, J. Simon, and J. Germain, “Metallophthalocyanines”, *Coordination Chemistry Reviews*, vol. 178-180, pp. 1433–1484, 1998. DOI: `10.1016/S0010-8545(98)00177-5`.

[89] G. de la Torre, C. G. Claessens, and T. Torres, “Phthalocyanines: old dyes, new materials. putting color in nanotechnology”, *Chem. Commun.*, no. 20, pp. 2000–2015, 2007. DOI: `10.1039/B614234F`.

[90] L. Li, Q. Tang, H. Li, and W. Hu, “Molecular orientation and interface compatibility for high performance organic thin film transistor based on vanadyl phthalocyanine.”, *The Journal of Physical Chemistry B*, vol. 112, pp. 10 405–10, 2008. DOI: `10.1021/jp800879g`.

[91] H. Wang, D. Song, J. Yang, B. Yu, Y. Geng, and D. Yan, “High mobility vanadyl-phthalocyanine polycrystalline films for organic field-effect transistors”, *Applied Physics Letters*, vol. 90, no. 25, p. 253 510, 2007. DOI: `10.1063/1.2751103`.

[92] B. P. Rand, D. Cheyns, K. Vasseur, N. C. Giebink, S. Mothy, Y. Yi, V. Coropceanu, D. Beljonne, J. Cornil, J.-L. Brédas, and J. Genoe, “The impact of molecular orientation on the photovoltaic properties of a phthalocyanine/fullerene heterojunction”, *Advanced Functional Materials*, vol. 22, no. 14, pp. 2987–2995, 2012. DOI: `10.1002/adfm.201200512`.

[93] P. Sullivan, T. S. Jones, A. J. Ferguson, and S. Heutz, “Structural templating as a route to improved photovoltaic performance in copper phthalocyanine/fullerene (c60) heterojunctions”, *Applied Physics Letters*, vol. 91, no. 23, p. 233 114, 2007. DOI: `10.1063/1.2821229`.

[94] R. W. I. de Boer, M. E. Gershenson, A. F. Morpurgo, and V Podzorov, “Organic single-crystal field-effect transistors”, *Physica status solidi (a)*, vol. 201, no. 6, pp. 1302–1331, 2004. DOI: `10.1002/pssa.200404336`.

[95] J. Yang and D. Yan, “Weak epitaxy growth of organic semiconductor thin films.”, *Chemical Society reviews*, vol. 38, no. 9, pp. 2634–45, 2009. DOI: `10.1039/b815723p`.

[96] H. Ying Mao, R. Wang, Y. Wang, T. Chao Niu, J. Qiang Zhong, M. Yang Huang, D. Chen Qi, K. Ping Loh, A. Thye Shen Wee, and W. Chen, “Chemical vapor deposition graphene as structural template to control interfacial molecular orientation of chloroaluminium phthalocyanine”, *Applied Physics Letters*, vol. 99, no. 9, p. 093 301, 2011. DOI: `10.1063/1.3629812`.

[97] J. Mao, H. Zhang, Y. Jiang, Y. Pan, M. Gao, W. Xiao, and H.-J. Gao, "Tunability of supramolecular kagome lattices of magnetic phthalocyanines using graphene-based moire patterns as templates", *Journal of the American Chemical Society*, vol. 131, no. 40, pp. 14 136–14 137, 2009. DOI: `10.1021/ja904907z`.

[98] C. H. Lee, T. Schiros, E. J. G. Santos, B. Kim, K. G. Yager, S. J. Kang, S. Lee, J. Yu, K. Watanabe, T. Taniguchi, J. Hone, E. Kaxiras, C. Nuckolls, and P. Kim, "Epitaxial growth of molecular crystals on van der Waals substrates for high-performance organic electronics", *Advanced Materials*, vol. 26, no. 18, pp. 2812–2817, 2014. DOI: `10.1002/adma.201304973`.

[99] P. A. Pandey, L. A. Rochford, D. S. Keeble, J. P. Rourke, T. S. Jones, R. Beanland, and N. R. Wilson, "Resolving the nanoscale morphology and crystallographic structure of molecular thin films: F16CuPc on graphene oxide", *Chemistry of Materials*, vol. 24, pp. 1365–1370, 2012. DOI: `10.1021/cm300073v`.

[100] X. Zhang, Y. Feng, S. Tang, and W. Feng, "Preparation of a graphene oxide-phthalocyanine hybrid through strong pi-pi interactions", *Carbon*, vol. 48, no. 1, pp. 211–216, 2010. DOI: `10.1016/j.carbon.2009.09.007`.

[101] J. Zhu, Y. Li, Y. Chen, J. Wang, B. Zhang, J. Zhang, and W. J. Blau, "Graphene oxide covalently functionalized with zinc phthalocyanine for broadband optical limiting", *Carbon*, vol. 49, no. 6, pp. 1900–1905, 2011. DOI: `10.1016/j.carbon.2011.01.014`.

[102] J. Malig, N. Jux, D. Kiessling, J. J. Cid, P. Vázquez, T. Torres, and D. M. Guldi, "Towards tunable graphene/phthalocyanine-PPV hybrid systems", *Angewandte Chemie - International Edition*, vol. 50, pp. 3561–3565, 2011. DOI: `10.1002/anie.201003364`.

[103] A. J. Ramadan, L. A. Rochford, D. S. Keeble, P. Sullivan, M. P. Ryan, T. S. Jones, and S. Heutz, "Exploring high temperature templating in non-planar phthalocyanine/copper iodide (111) bilayers", *J. Mater. Chem. C*, vol. 3, no. 2, pp. 461–465, 2015. DOI: `10.1039/C4TC02116A`.

[104] J. W. Steed, D. R. Turner, and K. J. Wallace, *Core Concepts in Supramolecular Chemistry and Nanochemistry*. Wiley, 2007.

[105] J.-M. Lehn, "Supramolecular chemistry: from molecular information towards self-organization and complex matter", *Reports on Progress in Physics*, vol. 67, no. 3, pp. 249–265, 2004. DOI: `10.1088/0034-4885/67/3/R02`.

[106] A. G. Slater (née Phillips), P. H. Beton, and N. R. Champness, "Two-dimensional supramolecular chemistry on surfaces", *Chemical Science*, vol. 2, no. 8, pp. 1440–1448, 2011. DOI: `10.1039/c1sc00251a`.

[107] A. J. Pollard, E. W. Perkins, N. A. Smith, A. Saywell, G. Goretzki, A. G. Phillips, S. P. Argent, H. Sachdev, F. Müller, S. Hüfner, S. Gsell, M. Fischer, M. Schreck, J. Osterwalder, T. Greber, S. Berner, N. R. Champness, and P. H. Beton, "Supramolecular assemblies formed on an epitaxial graphene superstructure", *Angewandte Chemie - International Edition*, vol. 49, no. 10, pp. 1794–1799, 2010. DOI: `10.1002/anie.200905503`.

[108] S. A. Svatek, O. R. Scott, J. P. Rivett, K. Wright, M. Baldoni, E. Bichoutskaia, T. Taniguchi, K. Watanabe, A. J. Marsden, N. R. Wilson, and P. H. Beton, "Adsorbate-induced curvature and stiffening of graphene", *Nano Letters*, vol. 15, no. 1, pp. 159–164, 2015. DOI: `10.1021/nl503308c`.

[109] S. Griessl, M. Lackinger, M. Edelwirth, M. Hietschold, and W. M. Heckl, "Self-assembled two-dimensional molecular host-guest architectures from trimesic acid", *Single Molecules*, vol. 3, no. 1, pp. 25–31, 2002. DOI: `10.1002/1438-5171(200204)3:1<25::AID-SIMO25>3.0.CO;2-K`.

[110] M. Lackinger, S. Griessl, W. M. Heckl, M. Hietschold, and G. W. Flynn, "Self-assembly of trimesic acid at the liquid-solid interface - a study of solvent-induced polymorphism", *Langmuir*, vol. 21, no. 11, pp. 4984–4988, 2005. DOI: `10.1021/la0467640`.

[111] M. Lackinger, S. Griessl, T. Markert, F. Jamitzky, and W. M. Heckl, “Self-assembly of benzene-dicarboxylic acid isomers at the liquid solid interface: steric aspects of hydrogen bonding”, *The Journal of Physical Chemistry B*, vol. 108, no. 36, pp. 13 652–13 655, 2004. DOI: `10.1021/jp048248o`.

[112] Y.-G. Kim, S.-L. Yau, and K. Itaya, “In situ scanning tunneling microscopy of highly ordered adlayers of aromatic molecules on well-defined Pt(111) electrodes in solution: Benzoic acid, terephthalic acid, and pyrazine”, *Langmuir*, vol. 15, no. 22, pp. 7810–7815, 1999. DOI: `10.1021/la990464e`.

[113] R. Addou and M. Batzill, “Defects and domain boundaries in self-assembled terephthalic acid (TPA) monolayers on CVD-grown graphene on Pt(111)”, *Langmuir*, vol. 29, no. 21, pp. 6354–6360, 2013. DOI: `10.1021/la400972k`.

[114] S. De Feyter and F. C. De Schryver, “Two-dimensional supramolecular self-assembly probed by scanning tunneling microscopy.”, *Chemical Society reviews*, vol. 32, no. 3, pp. 139–150, 2003. DOI: `10.1039/b206566p`.

[115] W. Zhang, A. Nefedov, M. Naboka, L. Cao, and C. Wöll, “Molecular orientation of terephthalic acid assembly on epitaxial graphene: NEXAFS and XPS study”, *Physical Chemistry Chemical Physics*, vol. 14, no. 29, p. 10 125, 2012. DOI: `10.1039/c2cp23748b`.

[116] M. C. Daniel and D. Astruc, “Gold nanoparticles: assembly, supramolecular chemistry, quantum-size-related properties, and applications toward biology, catalysis, and nanotechnology”, *Chemical Reviews*, vol. 104, no. 1, pp. 293–346, 2004. DOI: `10.1021/cr030698+`.

[117] J. Park, H. Zheng, W. C. Lee, P. L. Geissler, E. Rabani, and A. P. Alivisatos, “Direct observation of nanoparticle superlattice formation by using liquid cell transmission electron microscopy”, *ACS Nano*, vol. 6, no. 3, pp. 2078–2085, 2012. DOI: `10.1021/nn203837m`.

[118] D. B. Carlson and J. E. Evans, “Low-dose imaging techniques for transmission electron microscopy”, in *The Transmission Electron Microscope*, InTech, 2012, pp. 3–22. DOI: `10.5772/36614`.

[119] U. Kaiser and M. Stöger-Pollach, “Foreword to the special issue low-voltage electron microscopy”, *Ultramicroscopy*, vol. 145, pp. 1–2, 2014. DOI: `10.1016/j.ultramic.2014.05.002`.

[120] M. Haruta and H. Kurata, “Direct observation of crystal defects in an organic molecular crystals of copper hexachlorophthalocyanine by STEM-EELS”, *Scientific Reports*, vol. 2, pp. 2–5, 2012. DOI: `10.1038/srep00252`.

[121] J. B. Gilchrist, T. H. Basey-Fisher, S. C. E. Chang, F. Scheltens, D. W. Mccomb, and S. Heutz, “Uncovering buried structure and interfaces in molecular photovoltaics”, *Advanced Functional Materials*, pp. 6473–6483, 2014. DOI: `10.1002/adfm.201400345`.

[122] E. Montoya, S. Bals, M. D. Rossell, D. Schryvers, and G. Van Tendeloo, “Evaluation of top, angle, and side cleaned FIB samples for TEM analysis”, *Microscopy Research and Technique*, vol. 70, no. 12, pp. 1060–1071, 2007. DOI: `10.1002/jemt.20514`.

[123] P. Blake, E. W. Hill, A. H. Castro Neto, K. S. Novoselov, D. Jiang, R. Yang, T. J. Booth, and A. K. Geim, “Making graphene visible”, *Applied Physics Letters*, vol. 91, no. 6, p. 063 124, 2007. DOI: `10.1063/1.2768624`.

[124] R. Brydson, Ed., *Aberration-corrected analytical transmission electron microscopy*. Wiley, 2011.

[125] P. J. Goodhew, F. J. Humphreys, and R. Beanland, *Electron Microscopy and Analysis*. Taylor and Francis, 2001.

[126] H. Hiura, H. Miyazaki, and K. Tsukagoshi, “Determination of the number of graphene layers: discrete distribution of the secondary electron intensity stemming from individual graphene layers”, *Applied Physics Express*, vol. 3, pp. 1–4, 2010. DOI: `10.1143/APEX.3.095101`.

[127] A. Schwartz, M. Kumar, B. Adams, and D. Field, Eds., *Electron Backscatter Diffraction in Materials Science*. Springer, 2009.

[128] D. B. Williams and C. B. Carter, *Transmission Electron Microscopy*. Springer, 2009.

[129] R. Erni, *Aberration-corrected imaging in transmission electron microscopy*. Imperial College Press, 2010.

[130] S. Pennycook, M Varela, C. Hetherington, and A. Kirkland, "Materials advances through aberration-corrected electron microscopy", *MRS Bulletin*, vol. 31, no. 01, pp. 36–43, 2006. DOI: `10.1557/mrs2006.4`.

[131] S. Uhlemann and M. Haider, "Residual wave aberrations in the first spherical aberration corrected transmission electron microscope", *Ultramicroscopy*, vol. 72, no. 3-4, pp. 109–119, 1998. DOI: `10.1016/S0304-3991(97)00102-2`.

[132] M. A. Dyson, "Advances in computational methods for transmission electron microscopy simulation and image processing", PhD thesis, University of Warwick, 2015.

[133] R. F. Egerton, P Li, and M Malac, "Radiation damage in the TEM and SEM", *Micron*, vol. 35, no. 6, pp. 399–409, 2004. DOI: `10.1016/j.micron.2004.02.003`.

[134] R. F. Egerton, "Choice of operating voltage for a transmission electron microscope", *Ultramicroscopy*, vol. 145, pp. 85–93, 2014. DOI: `10.1016/j.ultramic.2013.10.019`.

[135] N. R. Wilson, P. A. Pandey, R Beanland, J. P. Rourke, U Lupo, G Rowlands, and R. A. Römer, "On the structure and topography of free-standing chemically modified graphene", *New Journal of Physics*, vol. 12, no. 12, p. 125 010, 2010. DOI: `10.1088/1367-2630/12/12/125010`.

[136] P. Eaton and P. West, *Atomic Force Microscopy*. Oxford University Press, 2010.

[137] A. J. Marsden, M. Phillips, and N. R. Wilson, "Friction force microscopy: a simple technique for identifying graphene on rough substrates and mapping the orientation of graphene grains on copper.", *Nanotechnology*, vol. 24, no. 25, p. 255 704, 2013. DOI: `10.1088/0957-4484/24/25/255704`.

[138] M Varenberg, I Etsion, and G Halperin, "An improved wedge calibration method for lateral force in atomic force microscopy", *Review of Scientific Instruments*, vol. 74, no. 7, pp. 3362–3367, 2003. DOI: `10.1063/1.1584082`.

[139] K.-S. Kim, H.-J. Lee, C. Lee, S.-K. Lee, H. Jang, J.-H. Ahn, J.-H. Kim, and H.-J. Lee, "Chemical vapor deposition-grown graphene: the thinnest solid lubricant", *ACS Nano*, vol. 5, no. 6, pp. 5107–5114, 2011. DOI: `10.1021/nn2011865`.

[140] E. Gnecco and E. Meyer, *Fundamentals of Friction and Wear on the Nanoscale*. Springer, 2007.

[141] A Nagashima, "Electronic states of monolayer graphite formed on TiC(111) surface", *Surface Science*, vol. 291, pp. 93–98, 1993. DOI: `10.1016/0039-6028(93)91480-D`.

[142] Y. Gamo, A. Nagashima, M. Wakabayashi, M. Terai, and C. Oshima, "Atomic structure of monolayer graphite formed on Ni(111).", *Hyomen Kagaku*, vol. 17, pp. 745–749, 1996. DOI: `10.1380/jsssj.17.745`.

[143] A. Damascelli, Z. Hussain, and Z.-X. Shen, "Angle-resolved photoemission studies of the cuprate superconductors", *Reviews of Modern Physics*, vol. 75, no. 2, pp. 473–541, 2003.

[144] J. Avila, I. Razado-Colambo, S. Lorcy, B. Lagarde, J.-L. Giorgetta, F. Polack, and M. C. Asensio, "ANTARES, a scanning photoemission microscopy beamline at SOLEIL", *Journal of Physics: Conference Series*, vol. 425, no. 19, p. 192 023, 2013. DOI: `10.1088/1742-6596/425/19/192023`.

[145] P. Y. Huang, C. S. Ruiz-Vargas, A. M. van der Zande, W. S. Whitney, M. P. Levendorf, J. W. Kevek, S. Garg, J. S. Alden, C. J. Hustedt, Y. Zhu, J. Park, P. L. McEuen, and D. A. Muller, "Grains and grain boundaries in single-layer

graphene atomic patchwork quilts", *Nature*, vol. 469, no. 7330, pp. 389–392, 2011. DOI: 10.1038/nature09718.

[146] O. V. Yazyev, "Polycrystalline graphene: atomic structure, energetics and transport properties", *Solid State Communications*, vol. 152, no. 15, pp. 1431–1436, 2012. DOI: 10.1016/j.ssc.2012.04.045.

[147] F Hao and D. N. Fang, "Mechanical deformation and fracture mode of polycrystalline graphene: atomistic simulations", *Physics Letters A*, vol. 376, no. 24-25, pp. 1942–1947, 2012. DOI: 10.1016/j.physleta.2012.04.040.

[148] L. A. Jauregui, H. L. Cao, W Wu, Q. K. Yu, and Y. P. Chen, "Electronic properties of grains and grain boundaries in graphene grown by chemical vapor deposition", *Solid State Communications*, vol. 151, no. 16, pp. 1100–1104, 2011. DOI: 10.1016/j.ssc.2011.05.023.

[149] P. Zhao, A. Kumamoto, S. Kim, X. Chen, B. Hou, S. Chiashi, E. Einarsson, Y. Ikuhara, and S. Maruyama, "Self-limiting chemical vapor deposition growth of monolayer graphene from ethanol", *The Journal of Physical Chemistry C*, 2013. DOI: 10.1021/jp400996s.

[150] A. T. Murdock, A. Koos, T. B. Britton, L. Houben, T. Batten, T. Zhang, A. J. Wilkinson, R. E. Dunin-Borkowski, C. E. Lekka, and N. Grobert, "Controlling the orientation, edge geometry, and thickness of chemical vapor deposition graphene", *ACS Nano*, vol. 7, no. 2, pp. 1351–1359, 2013. DOI: 10.1021/nn3049297.

[151] J. Tian, H. Cao, W. Wu, Q. Yu, N. P. Guisinger, and Y. P. Chen, "Graphene induced surface reconstruction of Cu", *Nano Letters*, vol. 12, no. 8, pp. 3893–3899, 2012. DOI: 10.1021/nl3002974.

[152] D. Yoon, Y.-W. Son, and H. Cheong, "Negative thermal expansion coefficient of graphene measured by Raman spectroscopy.", *Nano letters*, vol. 11, no. 8, pp. 3227–3231, 2011. DOI: 10.1021/nl201488g.

[153] H. I. Rasool, E. B. Song, M. J. Allen, J. K. Wassei, R. B. Kaner, K. L. Wang, B. H. Weiller, and J. K. Gimzewski, "Continuity of graphene on polycrystalline copper", *Nano Letters*, vol. 11, no. 1, pp. 251–256, 2011. DOI: 10.1021/nl1036403.

[154] Y. Yang and E. D. Williams, "Carbon-induced faceting of Si(112)", *Surface Science*, vol. 215, no. 1-2, pp. 102–110, 1989. DOI: 10.1016/0039-6028(89)90703-6.

[155] I. Markov, *Crystal Growth for Beginners*. World Scientific, 2008.

[156] Z.-J. Wang, G. Weinberg, Q. Zhang, T. Lunkenbein, A. Klein-Hoffmann, M. Kurnatowska, M. Plodinec, Q. Li, L. Chi, R Schloegl, and M.-G. Willinger, "Direct observation of graphene growth and associated copper substrate dynamics by in situ scanning electron microscopy", *ACS Nano*, vol. 9, no. 2, pp. 1506–1519, 2015. DOI: 10.1021/nn5059826.

[157] L. Hansen, P. Stoltze, K. W. Jacobsen, and J. K. Norskov, "Self-diffusion on copper surfaces", *Physical Review B*, vol. 44, no. 12, pp. 6523–6526, 1991. DOI: 10.1103/PhysRevB.44.6523.

[158] E. Meca, J. Lowengrub, H. Kim, C. Mattevi, and V. B. Shenoy, "Epitaxial graphene growth and shape dynamics on copper: phase-field modeling and experiments", *Nano Letters*, vol. 13, no. 11, pp. 5692–5697, 2013. DOI: 10.1021/nl4033928.

[159] N. R. Wilson, A. J. Marsden, M. Saghir, C. J. Bromley, R. Schaub, G. Costantini, T. W. White, C. Partridge, A. Barinov, P. Dudin, A. M. Sanchez, J. J. Mudd, M. Walker, and G. R. Bell, "Weak mismatch epitaxy and structural feedback in graphene growth on copper foil", *Nano Research*, vol. 6, no. 2, pp. 99–112, 2013. DOI: 10.1007/s12274-013-0285-y.

[160] E. L. Shirley, L. J. Terminello, A Santoni, and F. J. Himpsel, "Brillouin-zone-selection effects in graphite photoelectron angular distributions", *Physical Review B*, vol. 51, no. 19, pp. 13 614–13 622, 1995.

[161] A. L. Walter, S. Nie, A. Bostwick, K. S. Kim, L. Moreschini, Y. J. Chang, D. Innocenti, K. Horn, K. F. McCarty, and E. Rotenberg, "Electronic structure of graphene on single-crystal copper substrates", *Physical Review B*, vol. 84, no. 19, p. 195 443, 2011.

[162] R. Blume, P. R. Kidambi, B. C. Bayer, R. S. Weatherup, Z.-J. Wang, G. Weinberg, M.-G. Willinger, M. Greiner, S. Hofmann, A. Knop-Gericke, and R. Schlögl, "The influence of intercalated oxygen on the properties of graphene on polycrystalline Cu under various environmental conditions", *Phys. Chem. Chem. Phys.*, vol. 16, no. 47, pp. 25 989–26 003, 2014. DOI: `10.1039/C4CP04025B`.

[163] S. Gottardi, K. Müller, L. Bignardi, J. C. Moreno-López, T. A. Pham, O. Ivashenko, M. Yablonskikh, A. Barinov, J. Björk, P. Rudolf, and M. Stöhr, "Comparing graphene growth on Cu(111) versus oxidized Cu(111)", *Nano Letters*, vol. 15, no. 2, pp. 917–922, 2015. DOI: `10.1021/nl5036463`.

[164] C. Lin, N. Tong, W. Yang, R. Zhao, and Z. Hu, "Low energy electron diffraction study of high index copper surfaces underneath graphene", *Applied Surface Science*, vol. 347, pp. 147–154, 2015. DOI: `10.1016/j.apsusc.2015.03.147`.

[165] V. Georgakilas, M. Otyepka, A. B. Bourlinos, V. Chandra, N. Kim, K. C. Kemp, P. Hobza, R. Zboril, and K. S. Kim, "Functionalization of graphene: covalent and non-covalent approaches, derivatives and applications", *Chemical Reviews*, vol. 112, no. 11, pp. 6156–6214, 2012. DOI: `10.1021/cr3000412`.

[166] Y. Wang, Y. Shao, D. W. Matson, J. Li, and Y. Lin, "Nitrogen-doped graphene and its application in electrochemical biosensing", *ACS Nano*, vol. 4, no. 4, pp. 1790–1798, 2010. DOI: `10.1021/nn100315s`.

[167] K. N. Wood, R. O'Hayre, and S. Pylypenko, "Recent progress on nitrogen/carbon structures designed for use in energy and sustainability applications", *Energy & Environmental Science*, vol. 7, no. 4, p. 1212, 2014. DOI: `10.1039/c3ee44078h`.

[168] L. Qu, Y. Liu, J.-B. Baek, and L. Dai, "Nitrogen-doped graphene as efficient metal-free electrocatalyst for oxygen reduction in fuel cells", *ACS Nano*, vol. 4, no. 3, pp. 1321–1326, 2010. DOI: `10.1021/nn901850u`.

[169] M. Z. Hossain, J. E. Johns, K. H. Bevan, H. J. Karmel, Y. T. Liang, S. Yoshimoto, K. Mukai, T. Koitaya, J. Yoshinobu, M. Kawai, A. M. Lear, L. L. Kesmodel, S. L. Tait, and M. C. Hersam, "Chemically homogeneous and thermally reversible oxidation of epitaxial graphene", *Nature Chemistry*, vol. 4, no. 4, pp. 305–309, 2012. DOI: `10.1038/nchem.1269`.

[170] S Doniach and M Sunjic, "Many-electron singularity in X-ray photoemission and X-ray line spectra from metals", *Journal of Physics C: Solid State Physics*, vol. 3, no. 2, pp. 285–291, 1970. DOI: `10.1088/0022-3719/3/2/010`.

[171] A. Pirkle, J. Chan, A. Venugopal, D. Hinojos, C. W. Magnuson, S. McDonnell, L. Colombo, E. M. Vogel, R. S. Ruoff, and R. M. Wallace, "The effect of chemical residues on the physical and electrical properties of chemical vapor deposited graphene transferred to SiO2", *Applied Physics Letters*, vol. 99, no. 12, pp. 2–5, 2011. DOI: `10.1063/1.3643444`.

[172] A. Grüneis, K. Kummer, and D. V. Vyalikh, "Dynamics of graphene growth on a metal surface: a time-dependent photoemission study", *New Journal of Physics*, vol. 11, no. 7, p. 073 050, 2009. DOI: `10.1088/1367-2630/11/7/073050`.

[173] A. Ouerghi, A. Kahouli, D. Lucot, M. Portail, L. Travers, J. Gierak, J. Penuelas, P. Jegou, A. Shukla, T. Chassagne, and M. Zielinski, "Epitaxial graphene on cubic SiC(111)/Si(111) substrate", *Applied Physics Letters*, vol. 96, no. 19, p. 191 910, 2010. DOI: `10.1063/1.3427406`.

[174] A. Barinov, O. B. Malcioglu, S. Fabris, T. Sun, L. Gregoratti, M. Dalmiglio, and M. Kiskinova, "Initial stages of oxidation on graphitic surfaces: photoe-

mission study and density functional theory calculations", *Journal of Physical Chemistry C*, vol. 113, pp. 9009–9013, 2009. DOI: `10.1021/jp902051d`.

[175] T. L. Barr, "Nature of the use of adventitious carbon as a binding energy standard", *Journal of Vacuum Science & Technology A: Vacuum, Surfaces, and Films*, vol. 13, no. 3, p. 1239, 1995. DOI: `10.1116/1.579868`.

[176] D. Yang, A. Velamakanni, G. Bozoklu, S. Park, M. Stoller, R. D. Piner, S. Stankovich, I. Jung, D. A. Field, C. A. Ventrice, and R. S. Ruoff, "Chemical analysis of graphene oxide films after heat and chemical treatments by X-ray photoelectron and micro-Raman spectroscopy", *Carbon*, vol. 47, no. 1, pp. 145–152, 2009. DOI: `10.1016/j.carbon.2008.09.045`.

[177] Z.-H. Sheng, L. Shao, J.-J. Chen, W.-J. Bao, F.-B. Wang, and X.-H. Xia, "Catalyst-free synthesis of nitrogen-doped graphene via thermal annealing graphite oxide with melamine and its excellent electrocatalysis", *Acs Nano*, vol. 5, no. 6, pp. 4350–4358, 2011. DOI: `10.1021/nn103584t`.

[178] D. Wei, Y. Liu, Y. Wang, H. Zhang, L. Huang, and G. Yu, "Synthesis of N-doped graphene by chemical vapor deposition and its electrical properties", *Nano Letters*, vol. 9, no. 5, pp. 1752–1758, 2009. DOI: `10.1021/nl803279t`.

[179] W. Qian, X. Cui, R. Hao, Y. Hou, and Z. Zhang, "Facile preparation of nitrogen-doped few-layer graphene via supercritical reaction", *Acs Applied Materials & Interfaces*, vol. 3, no. 7, pp. 2259–2264, 2011. DOI: `10.1021/am200479d`.

[180] Z. Mo, R. Zheng, H. Peng, H. Liang, and S. Liao, "Nitrogen-doped graphene prepared by a transfer doping approach for the oxygen reduction reaction application", *Journal of Power Sources*, vol. 245, pp. 801–807, 2014. DOI: `10.1016/j.jpowsour.2013.07.038`.

[181] D Usachov, O Vilkov, A Grüneis, D Haberer, A Fedorov, V. K. Adamchuk, A. B. Preobrajenski, P Dudin, A Barinov, M Oehzelt, C Laubschat, and D. V. Vyalikh, "Nitrogen-doped graphene: efficient growth, structure, and electronic properties", *Nano Letters*, vol. 11, no. 12, pp. 5401–5407, 2011. DOI: `10.1021/nl2031037`.

[182] F. Banhart, J. Kotakoski, and A. V. Krasheninnikov, "Structural defects in graphene.", *ACS nano*, vol. 5, no. 1, pp. 26–41, 2011. DOI: `10.1021/nn102598m`.

[183] H. Terrones, R. Lv, M. Terrones, and M. S. Dresselhaus, "The role of defects and doping in 2D graphene sheets and 1D nanoribbons.", *Reports on progress in physics*, vol. 75, no. 6, p. 062 501, 2012. DOI: `10.1088/0034-4885/75/6/062501`.

[184] A. J. Marsden, P. Brommer, J. J. Mudd, M. A. Dyson, R. Cook, M. Asensio, J. Avila, A. Levy, J. Sloan, D. Quigley, G. R. Bell, and N. R. Wilson, "Effect of oxygen and nitrogen functionalization on the physical and electronic structure of graphene", *Nano Research*, 2015. DOI: `10.1007/s12274-015-0768-0`.

[185] J. Kotakoski, A. V. Krasheninnikov, U. Kaiser, and J. C. Meyer, "From point defects in graphene to two-dimensional amorphous carbon", *Physical Review Letters*, vol. 106, no. 10, p. 105 505, 2011. DOI: `10.1103/PhysRevLett.106.105505`.

[186] A. Bostwick, J. McChesney, K. Emtsev, T. Seyller, K. Horn, S. Kevan, and E. Rotenberg, "Quasiparticle transformation during a metal-insulator transition in graphene", *Physical Review Letters*, vol. 103, no. 5, p. 056 404, 2009. DOI: `10.1103/PhysRevLett.103.056404`.

[187] N. Leconte, J. Moser, P. Ordejon, H. Tao, A. Lherbier, A. Bachtold, F. Alsina, C. M. Sotomayor Torres, J.-C. Charlier, and S. Roche, "Damaging graphene with ozone treatment: a chemically tunable metal-insulator transition", *ACS Nano*, vol. 4, no. 7, pp. 4033–4038, 2010. DOI: `10.1021/nn100537z`.

[188] K. R. Knox, A. Locatelli, M. B. Yilmaz, D. Cvetko, T. O. Mentes, M. A. Niño, P. Kim, A. Morgante, and R. M. Osgood, "Making angle-resolved photoemission measurements on corrugated monolayer crystals: suspended exfoli-

ated single-crystal graphene”, *Physical Review B*, vol. 84, no. 11, p. 115 401, 2011. DOI: 10.1103/PhysRevB.84.115401.

[189] P. Brommer and D. Quigley, “Automated effective band structures for defective and mismatched supercells”, *Journal of Physics: Condensed Matter*, vol. 26, no. 48, p. 485 501, 2014. DOI: 10.1088/0953-8984/26/48/485501.

[190] M. Scardamaglia, B. Aleman, M. Amati, C. Ewels, P. Pochet, N. Reckinger, J.-F. Colomer, T. Skaltsas, N. Tagmatarchis, R. Snyders, L. Gregoratti, and C. Bittencourt, “Nitrogen implantation of suspended graphene flakes: annealing effects and selectivity of sp2 nitrogen species”, *Carbon*, 2014. DOI: 10.1016/j.carbon.2014.02.078.

[191] A. Bagri, C. Mattevi, M. Acik, Y. J. Chabal, M. Chhowalla, and V. B. Shenoy, “Structural evolution during the reduction of chemically derived graphene oxide.”, *Nature chemistry*, vol. 2, no. 7, pp. 581–7, 2010. DOI: 10.1038/nchem.686.

[192] P. M. Beaujuge, J. M. J. Fréchet, and J. M. J. Fr, “Molecular design and ordering effects in pi-functional materials for transistor and solar cell applications.”, *Journal of the American Chemical Society*, vol. 133, pp. 20 009–29, 2011. DOI: 10.1021/ja2073643.

[193] D. He, Y. Zhang, Q. Wu, R. Xu, H. Nan, J. Liu, J. Yao, Z. Wang, S. Yuan, Y. Li, Y. Shi, J. Wang, Z. Ni, L. He, F. Miao, F. Song, H. Xu, K Watanabe, T Taniguchi, J.-b. Xu, and X. Wang, “Two-dimensional quasi-freestanding molecular crystals for high-performance organic field-effect transistors”, *Nature Communications*, vol. 5, pp. 1–7, 2014. DOI: 10.1038/ncomms6162.

[194] R. S. Sposili and J. S. Im, “Sequential lateral solidification of thin silicon films on SiO2”, *Applied Physics Letters*, vol. 69, no. 1996, p. 2864, 1996. DOI: 10.1063/1.117344.

[195] J. Rivnay, L. H. Jimison, J. E. Northrup, M. F. Toney, R. Noriega, S. Lu, T. J. Marks, A. Facchetti, and A. Salleo, “Large modulation of carrier transport by grain-boundary molecular packing and microstructure in organic thin films.”, *Nature materials*, vol. 8, no. 12, pp. 952–958, 2009. DOI: 10.1038/nmat2570.

[196] T. Gredig, E. A. Silverstein, and M. P. Byrne, “Height-height correlation function to determine grain size in iron phthalocyanine thin films”, *Journal of Physics: Conference Series*, vol. 417, p. 012 069, 2013. DOI: 10.1088/1742-6596/417/1/012069.

[197] D. Nečas and P. Klapetek, “Gwyddion: An open-source software for SPM data analysis”, *Central European Journal of Physics*, vol. 10, no. 1, pp. 181–188, 2012. DOI: 10.2478/s11534-011-0096-2.

[198] N. N. Nguyen, S. B. Jo, S. K. Lee, D. H. Sin, B. Kang, H. H. Kim, H. Lee, and K. Cho, “Atomically thin epitaxial template for organic crystal growth using graphene with controlled surface wettability”, *Nano Letters*, vol. 15, no. 4, pp. 2474–2484, 2015. DOI: 10.1021/nl504958e.

[199] J. M. Mativetsky, H. Wang, S. S. Lee, L. Whittaker-Brooks, and Y.-L. Loo, “Face-on stacking and enhanced out-of-plane hole mobility in graphene-templated copper phthalocyanine”, *Chem. Commun.*, vol. 50, no. 40, pp. 5319–5321, 2014. DOI: 10.1039/C3CC47516F.

[200] M. Kratzer, B. C. Bayer, P. R. Kidambi, A. Matković, R. Gajić, A. Cabrero-Vilatela, R. S. Weatherup, S. Hofmann, and C. Teichert, “Effects of PMMA-transfer residues on the growth of organic semiconductor molecules on chemical vapor deposited graphene”, *Applied Physics Letters*, vol. 106, no. 10, p. 103 101, 2015. DOI: 10.1063/1.4913948.

[201] J. M. MacLeod, J. A. Lipton-Duffin, D. Cui, S. De Feyter, and F. Rosei, “Substrate effects in the supramolecular assembly of 1,3,5-benzene tricarboxylic acid on graphite and graphene”, *Langmuir*, vol. 31, no. 25, pp. 7016–7024, 2015. DOI: 10.1021/la5048886.

[202] V. V. Korolkov, S. Allen, C. J. Roberts, and S. J. B. Tendler, “Green chemistry approach to surface decoration: Trimesic acid self-assembly on HOPG”, *Journal of Physical Chemistry C*, vol. 116, no. 21, pp. 11 519–11 525, 2012. DOI: `10.1021/jp212388c`.

[203] A. W. Robertson and J. H. Warner, “Atomic resolution imaging of graphene by transmission electron microscopy.”, *Nanoscale*, vol. 5, no. 10, pp. 4079–93, 2013. DOI: `10.1039/c3nr00934c`.

[204] J. C. Meyer, F. Eder, S. Kurasch, V. Skakalova, J. Kotakoski, H. J. Park, S. Roth, A. Chuvilin, S. Eyhusen, G. Benner, A. V. Krasheninnikov, and U. Kaiser, “Accurate measurement of electron beam induced displacement cross sections for single-layer graphene”, *Physical Review Letters*, vol. 108, no. 19, p. 196 102, 2012. DOI: `10.1103/PhysRevLett.108.196102`.

[205] D. C. Bell, M. Mankin, R. W. Day, and N. Erdman, “Successful application of low voltage electron microscopy to practical materials problems”, *Ultramicroscopy*, vol. 145, pp. 56–65, 2014. DOI: `10.1016/j.ultramic.2014.03.005`.

[206] L. F. Drummy, “Electron microscopy of organic-inorganic interfaces: advantages of low voltage”, *Ultramicroscopy*, vol. 145, pp. 74–79, 2014. DOI: `10.1016/j.ultramic.2014.05.001`.

[207] W. Clark, J. Chapman, A. MacLeod, and R. Ferrier, “Radiation damage mechanisms in copper phthalocyanine and its chlorinated derivatives”, *Ultramicroscopy*, vol. 5, no. 1-3, pp. 195–208, 1980. DOI: `10.1016/0304-3991(80)90024-8`.

[208] R. Zan, Q. M. Ramasse, R. Jalil, T. Georgiou, U. Bangert, and K. S. Novoselov, “Control of radiation damage in MoS2 by graphene encapsulation”, *ACS Nano*, vol. 7, no. 11, pp. 10 167–10 174, 2013. DOI: `10.1021/nn4044035`.

[209] F Shayeganfar, “Columnar organization of stack-assembled trimesic acid on graphene”, *Journal of Physics: Condensed Matter*, vol. 26, no. 43, p. 435 305, 2014. DOI: `10.1088/0953-8984/26/43/435305`.

[210] D. J. Duchamp and R. E. Marsh, “The crystal structure of trimesic acid (benzene-1,3,5-tricarboxylic acid)”, *Acta Crystallographica Section B Structural Crystallography and Crystal Chemistry*, vol. 25, no. 1, pp. 5–19, 1969. DOI: `10.1107/S0567740869001713`.

[211] M. Bailey and C. J. Brown, “The crystal structure of terephthalic acid”, *Acta Crystallographica*, vol. 22, no. 3, pp. 387–391, 1967. DOI: `10.1107/S0365110X67000751`.